

# **EXPERIMENTAL, THEORETICAL AND NUMERICAL INVESTIGATION OF NATURAL CONVECTION HEAT TRANSFER FROM HEATED MICROSPHERES IN A SLENDER CYLINDRICAL GEOMETRY**

**Noah Olugbenga Olanrewaju**  
**12079155**

submitted in partial fulfilment of the requirements for the degree  
**DOCTOR OF PHILOSOPHY**  
in the Department of Mechanical and Aeronautical Engineering,  
Faculty of Engineering Built Environment and Information Technology,  
**University of Pretoria.**

**Supervisor: Professor J.F. Slabber**

**Co-supervisor: Professor J.P. Meyer**

**December 2016**

## Abstract

The ability of coated particles of enriched uranium dioxide ( $\text{UO}_2$ ) fuel to withstand high temperatures and contain the fission products in the case of a loss of cooling event is a vital passive safety measure over traditional nuclear fuel requiring active safety systems to provide cooling. As a possible solution towards enhancing the safety of light-water reactors (LWRs), it is envisaged that the fuel in the form of loose-coated particles in a helium atmosphere can be introduced inside Silicon-Carbide nuclear reactor fuel cladding tubes of the fuel elements. The coated particles in this investigation were treated as a bed from where heat was transferred to the cladding tube by means of helium gas and the gas movement was by natural convection. Hence, it is proposed that light-water reactors (LWR) could be made safer by redesigning the fuel in the fuel assembly (see Fig. 1.3b).

As a first step towards the implementation of this proposal, a proper understanding of the mechanisms of heat transfer, fluid flow and pressure drop through a packed bed of spheres during natural convection was of utmost importance. Such an understanding was achieved through a review of existing literature on porous media. However, most heat transfer correlations and models in heated packed beds are for forced convective conditions and as such characterise porous media as a function of Reynolds number only rather than expressing media heat transfer performance as a function of thermal properties of the bed in combination with the various components of the overall heat transfer. The media heat transfer performance considered as a function of thermal properties of the bed in the proposed design is found to be a more appropriate approach than the media as a function of Reynolds number.

The quest to examine the particle-to-fluid heat transfer characteristics expected in the proposed new fuel design led to implementing this research work in three phases, namely experimental, theoretical and numerical simulation. An experimental investigation of fluid-to-particle natural convection heat transfer characteristics in packed beds heated from below was carried out. Captured data readings from the experiment were analysed and heat transfer characteristics in the medium evaluated by applying the first principle heat transfer concept. A basic unit cell (BUC) model was developed for the theoretical analysis and applied to determine the heat transfer coefficient,  $h$ , of the medium. The model adopted a concept in which a single unit of the packed bed was analysed and taken as representative of the entire bed; it related the convective heat transfer effect of the flowing fluid with the conduction and radiative effect at the finite contact spot between adjacent unit cell particles. As a result, the model could account for the thermophysical properties of sphere particles and the heated gas, the interstitial gas effect, gas temperature, contact interface between particles, particle size and particle temperature distribution in the investigated medium. Although the heat transfer phenomenon experienced in the experimental set-up was a reverse case of the proposed fuel design, the study with the achievement in the validation with the

Gunn correlation aided in developing the appropriate theoretical relations required for evaluating the heat transfer characteristics in the proposed nuclear fuel design.

A slender geometrical model mimicking the proposed nuclear fuel in the cladding was numerically simulated to investigate the heat transfer characteristics and flow distribution under the natural convective conditions anticipated in beds of randomly packed spheres (coated fuel particles) using a commercial code. Random packing of the particles was achieved by discrete element method (DEM) simulation with the aid of Star CCM+ while particle-to-particle and particle-to-wall contacts were achieved through the combined use of the commercial code and a SolidWorks CAD package. Surface-to-surface radiative heat transfer was modelled in the simulation reflecting real-life application. The numerical results obtained allowed for the determination of parameters such as *particle-to-fluid heat transfer coefficient*, *Nusselt number*, *Grashof number* and *Rayleigh number*. These parameters were of prime importance when analysing the heat transfer performance of a fixed bed reactor.

A comparison of three approaches indicated that the application of the CFD combined with the BUC model gave a better expression of the heat transfer phenomenon in the medium mimicking the heat transfer in the new fuel design

**Keywords:** nuclear fuel; light-water reactor; porous medium; numerical simulation; natural convection heat transfer

## Acknowledgements

I would like to thank my two promoters, Prof. Johan F. Slabber and Prof. Josua P. Meyer, for their respectable mentorship and many interesting discussions, as well as financial support; it is sincerely appreciated. In addition, I would like to express my gratitude to my wife, Abimbola Aduke, and my children, Titilola, Samuel and Paul, for their understanding, forbearance and endurance during the years I have been away from home for this research work. Lastly, I wish to thank my Heavenly Father and His son our Lord Jesus Christ for giving me the wisdom and potential to add value to this research field.

*If I have seen further, it is only by standing on the shoulders of giants.*

(Sir Isaac Newton)

# Contents

Abstract.....	ii
Acknowledgements.....	iv
Table of contents.....	v
List of figures .....	viii
List of tables.....	xii
Nomenclature .....	xiii
<b>1 Introduction</b> .....	<b>1</b>
1.1 Background .....	1
1.2 Research problem statement.....	3
1.2.1 Traditional fuel and the proposed fuel design.....	3
1.3 Methodology.....	5
1.4 Contribution of the study.....	6
1.5 Proposed nuclear fuel safety enhancement.....	7
1.6 Publications.....	7
1.6.1 Journal papers.....	8
1.6.2 Conference papers.....	9
1.7 Chapter outline.....	9
<b>2 Porous Structure</b> .....	<b>10</b>
2.1 Introduction.....	10
2.2 Analysis of packing regions.....	10
2.2.1 Porosity.....	11
2.2.2 Coordination number.....	15
2.2.3 Coordination flux number.....	17
2.3 Structured (ordered) packing.....	18
2.4 Limitations on defining packing structures with porosity only.....	19
2.5 Conclusion.....	20

<b>3</b>	<b>Convective Heat Transfer in Packed Beds</b>	<b>21</b>
3.1	Introduction.....	21
3.2	Well-known correlations.....	22
3.3	Solid and fluid heat transfer models.....	23
3.4	Conclusion.....	58
<b>4</b>	<b>Test Facility and Experimental Evaluation of Heat Transfer in the.....</b>	<b>58</b>
	<b>Investigating Medium</b>	
4.1	Introduction.....	58
4.2	Facility configuration .....	59
4.3	Particle test sample instrumentation and measurements.....	62
4.4	Uncertainty analysis.....	65
4.5	Experimental evaluation of heat transfer in the test facility.....	66
4.6	Results and discussion.....	68
4.7	Conclusion.....	72
<b>5</b>	<b>Theoretical: Basic Unit Cell Model</b>	<b>73</b>
5.1	Introduction.....	73
5.2	Heat transfer inside the cladding of traditional fuel.....	75
5.3	Development of the basic unit cell (BUC) model for packed beds.....	78
5.4	Temperature distribution within particles.....	78
5.5	Heat transfer at the contact spots.....	83
	5.5.1 Contact area between adjacent particles.....	84
	5.5.2 Contact region between adjacent particles.....	85
	5.5.3 Effective thermal conductivity.....	90
5.6	Porous media heat transfer characteristics.....	93
	5.6.1 Medium under investigation.....	93
	5.6.2 Proposed medium.....	96
5.7	Results .....	99
5.8	Comparison of theoretical analysis with experimental evaluation results.....	102
5.9	Conclusion.....	104
<b>6</b>	<b>Numerical Modelling of Natural Convection Heat Transfer and Transport</b>	<b>105</b>
	<b>in an Enclosed Slender Tube Geometrical Model Containing Heated Microspheres</b>	
6.1	Introduction.....	105

6.2	Heat transfer in models.....	107
6.3	Geometrical models.....	109
6.3.1	Packing of spherical particles in the tube .....	109
6.3.2	CAD operation and contacts creation.....	111
6.4	Mesh design and CFD modelling.....	114
6.4.1	Mesh design.....	114
6.4.2	Interface matching conditions.....	116
6.4.3	Initial state and boundary conditions.....	118
6.4.4	CFD modelling.....	118
6.4.5	Modelling thermal radiation.....	119
6.5	Flow calculation and fields.....	120
6.5.1	Computation of flow within the packed bed.....	120
6.5.2	Flow through packed beds.....	121
6.5.3	Qualitative features of the flow fields.....	122
6.6	Numerical errors and uncertainties.....	124
6.7	Results and discussion.....	124
6.8	Comparison of experimental evaluation, theoretical and CFD results .....	132
6.9	Conclusion.....	133
<b>7</b>	<b>Conclusions and Recommendations</b>	<b>135</b>
7.1	Conclusions.....	135
7.2	Recommendations for further work.....	137
	<b>References.....</b>	<b>139</b>
	<b>Appendix A: Calibrations, Experimental Uncertainty and Measurement of Force for Loading</b>	<b>147</b>
A.1	Thermocouple Calibration and Experimental Uncertainty.....	149
A.2	Pressure Transmitter.....	153
A.3	Contact Force Distribution.....	154
	<b>Appendix B: Programming Codes, Discrete Element Method and Discrete Scheme</b>	<b>157</b>
B.1:	MATLAB Codes.....	157
B.2:	Visual Basic Codes.....	158
B.3:	Discrete Element Method.....	159
B.3:	Discretisation Scheme.....	161

## List of Figures

Figure 1.1	Schematics of traditional fuel in the cladding.....	4
Figure 1.2	Schematics of proposed coated particle fuel design in a SiC cladding tube.....	5
Figure 1.3a	Traditional nuclear fuel assembly.....	5
Figure 1.3b	Proposed new nuclear fuel design.....	5
Figure 2.1	Packing regions defined in the study.....	11
Figure 2.2	Local and average area void fraction.....	12
Figure 2.3	Comparison between radial exponential porosity correlations [28].....	15
Figure 2.4	Comparison between various coordination number models (see Table 2.3)....	17
Figure 2.5	Ordered packing structures [38].....	18
Figure 2.6	Ordered packing structures [40] and [41].....	19
Figure 3.1	Heat transfer mechanisms through a packed bed.....	21
Figure 3.2	Coordinates for the analysis [7].....	24
Figure 3.3	Model [7].....	25
Figure 3.4	Comparison of model with literature data [7].....	27
Figure 3.5	Experimental device.....	28
Figure 3.6	Packed bed section.....	29
Figure 3.7	Straight lines obtained from Eq. (3.18).....	31
Figure 3.8	Nusselt versus Reynolds numbers and compared with other works.....	31
Figure 3.9	Spherical polar coordinate system.....	33
Figure 3.10	Comparison of the [62] results with other correlations .....	36
Figure 3.11	Two-dimensional model.....	38
Figure 3.12	Experimental apparatus.....	40
Figure 3.13	Photograph of Porous Medium.....	41
Figure 3.14	Longitudinal Nusselt number (a) $d = 1.3$ mm, $Re = 300$ ; (b) $d = 1.3$ mm, $Re = 600$ ; (c) $d = 4.2$ mm, $Re = 300$ .....	42
Figure 3.15	Modes of heat transfer in packed beds.....	43

Figure 3.16	The Horton-Rogers-Lapwood problem: infinite horizontal porous layer heated from below.	51
Figure 3.17	Two-dimensional rectangular porous layer held between differently heated side walls (Bejan, 1984).	53
Figure 3.18	Four heat transfer regimes for natural convection in a two-dimensional porous layer heated from the side (Bejan, 1984).	55
Figure 3.19	Local Nusselt number versus local Rayleigh number for a vertical surface with uniform heat flux (Huenefeld and Plumb, 1981).	56
Figure 4.1	Schematic diagram of the experimental set-up.	59
Figure 4.2	Schematic diagram of the experiment cylindrical vessel (for illustration purpose)	60
Figure 4.3	Cylindrical cavity	61
Figure 4.4	Test facility	62
Figure 4.5a	Sliced test particles with foil paper placed in-between	64
Figure 4.5b	Sectional view of instrumented test particle	64
Figure 4.6	Experimental set-up	65
Figure 4.7	Plot of particle temperature against time	68
Figure 4.8	Fluid-to-particle heat transfer at different Rayleigh numbers ( $Pr = 0.689$ )	69
Figure 4.9	Convective particle-to-fluid heat transfer in packed bed thermal energy storage systems at different Rayleigh numbers.	70
Figure 4.10	Variation in Rayleigh number at different Nusselt numbers for convective fluid-to-particle heat transfer ( $N = 4.12$ , $Pr = 0.689$ )	71
Figure 4.11	Effect of Nusselt number on Rayleigh number in packed bed thermal energy storage systems for convective particle-to-fluid heat transfer ( $N = 4.12$ , $Pr = 0.689$ )	71
Figure 5.1	Section through part of the test facility with a particle test sample highlighted	74
Figure 5.2	Fuel rod consisting of cladding tube and fuel pellets	75
Figure 5.3a	Single unit cell	78
Figure 5.3b	Schematic representation of a unit cell consisting of adjacent contact particles	79
Figure 5.4	Control volumes with grid points in the axial direction	80
Figure 5.5	Temperature distribution against particle diameter in an axial direction	82

Figure 5.6	Finite contact spot of smooth contacting spherical surfaces.....	85
Figure 5.7	Heat conduction between two smooth elastic particles in perfect contact..... (Hertzian contact)	86
Figure 5.8	Thermal resistance network for spherical Hertzian contact network..... (Noah <i>et al.</i> , 2015)	88
Figure 5.9	Effect of gas temperature on convective fluid-to-particle heat..... transfer coefficient and on gas thermal conductivity	100
Figure 5.10	Nusselt number in the packed bed as a function of convective ..... fluid-to-particle heat transfer coefficient	101
Figure 5.11	Variation of Nusselt number on the Rayleigh number for fluid-to particle.... heat transfer	102
Figure 5.12	Variation of Nusselt number with Rayleigh number for fluid-to-particle..... heat transfer	103
Figure 6.1	DEM simulated randomly packed particles.....	110
Figure 6.2a	DEM simulation model with gap between two particles and gaps..... between wall and particles	111
Figure 6.2b	DEM simulation centroid coordinate points (x, y, z) in CAD environment... 112	112
Figure 6.2c	Expansion of packed particle diameter for establishment of contacts..... between adjacent particles and between walls and particles using CAD	113
Figure 6.3a	Packed particle subtract (solid region).....	113
Figure 6.3b	Sectional plane of fluid domain after Boolean subtract operation..... (fluid region)	113
Figure 6.4	Threshold of a generated quality mesh depicting particle-to-particle..... contacts in the fixed bed geometrical mode	114
Figure 6.5a	Mesh sensitivity analysis.....	115
Figure 6.5b	Quality meshed geometrical model.....	116
Figure 6.6a	Sectional plane velocity vector plot immediately after starting up the..... simulation run	122
Figure 6.6b	Sectional plane velocity vector plot shortly after starting up the..... simulation run	123
Figure 6.6c	Sectional plane velocity vector plot before the end of the simulation..... process	123
Figure 6.7	Temperature contour plot for packed beds in helium environment..... contained in an enclosed slender cylindrical tube	125

Figure 6.8	Particle temperature profile along axial and radial positions.....	126
Figure 6.9	Effect of convective fluid velocity on particle-to-fluid..... heat transfer coefficient	127
Figure 6.10	Effect of fluid temperature on Grashof number.....	128
Figure 6.11	Surface average fluid velocity against particle temperature along..... packed bed full height	129
Figure 6.12	Nusselt number against surface average gas velocity.....	130
Figure 6.13	Variation of Rayleigh number with gas temperature.....	131
Figure 6.14	Nusselt number against Rayleigh number for particle-to-fluid heat transfer..	132
Figure 6.15	Nusselt number against Rayleigh number.....	133
Figure A.1	Thermocouple calibration set-up.....	150
Figure A.2	PolyScience circulating bath (PD20R-30-A12E) used for calibration.....	151
Figure A-3	Linear equation for each thermocouple at the card channel.....	152
Figure A-4	Pressure transmitter (PT) used.....	153
Figure A-5	Linear equations fitted to pressure transducer data.....	154
Figure A-6	Spring representation of contact force calculations.....	155
Figure A-7	Contact force as a function of height in the test facility.....	156
Figure B-1a	Contact force components between particles.....	160
Figure B-1b	Geometrical parameters and gap between two particles.....	160

## List of Tables

Table 2.1:	Summary of oscillatory porosity correlations in the radial direction.....	13
Table 2.2:	Summary of exponential porosity correlations in the radial direction.....	14
Table 2.3:	Equations for relation between average coordination number and..... porosity [10]	16
Table 2.4:	Comparison of coordination number and porosity with..... different arrangements [31]	18
Table 3.1:	Correlations for the determination of heat transfer in packed beds.....	22
Table 3.2:	Porous medium.....	41
Table 3.3	Experimental review of packed beds heat transfer.....	47
Table 5.1:	Parameters used in determining the heat transfer effect in the medium.....	95
Table A-1	Statistical results for thermocouples.....	152
Table A-2	Calibration data for pressure transmitter.....	153
Table B-1	Parameters for DEM packing.....	161

# Nomenclature

## Roman Symbols

$A$	area, m <sup>2</sup>
$A$	aspect ratio
$A_{rm}$	modified Archimedes number
$a_L$	radius of macrocontact, m
$a$	conductance at faces
$a$	specific surface area, m <sup>-1</sup>
$\mathbf{a}$	face area vector, m <sup>2</sup>
$b$	total generation within the control volume
$b_L$	chord of macrogap, m
$\overline{B}_f$	body force, N
$c_p$	specific heat at constant pressure, J/kg K
$C_A$	gas specific constant
$C$	concentration (kg/kg)
$C_2$	inertial resistance factor
$d$	diameter, m
$D$	tube diameter, m
$d$	distance separating two plates, m
$\partial r_G$	infinitesimal surface elements, m
$D(r)$	sphere profile in the non-contacting region, m
$e$	total number of contact points
$E$	Young's modulus, N/m <sup>2</sup>
$F$	normal contact force, N
$f$	standard profile assumption parameter
$g$	gravity, m/s <sup>2</sup>
$h$	heat transfer coefficient, W/m <sup>2</sup> K
$H_B$	Brinell hardness, Pa
$H$	bed height
$H$	dimensionless heat transfer coefficient
$j_H$	Colburn $j$ -factor
$k$	thermal conductivity, W/m K
$Kn$	Knudsen number, $\Lambda/d$
$k_n$	normal stiffness

---

$K$	permeability, $m^2$
$L$	tube height, m
$m$	reduced mass of particle
$M$	gas rarefaction parameter, m
$M$	bed weight
$n$	coordination flux number
$\overline{N}_c$	average coordination number
$N$	normal part of the force, F (N)
$N$	diameter ratio ( $d_b/d_p$ )
$N_A$	number of particles per unit area, $m^{-2}$
$N_L$	number of particles per unit length, $m^{-1}$
$P$	pressure, $N/m^2$
$P_v$	viscous resistance coefficient
$P_i$	inertial resistance coefficient
$Q$	heat transfer rate, W
$q''$	heat flux, $W/m^2$
$q'''$	heat production per unit volume, $W/m^3$
$R$	thermal resistance, K/W
$R_{cd}^1$	resistance to heat transfer by conduction, K/J
$R_{L,1,2}$	macrocontact thermal resistance, K/W
$r$	radius, m
$r$	radial direction, m
$S_{gen}$	heat source term, Nm
$S$	constant
$S_F$	constant
$S_\emptyset$	scalar source term
$S_b$	surface area of particles, $m^2$
$S_0$	bed cross-section, $m^2$
$S_p$	specific surface area, $m^{-1}$
$T$	temperature, K
$t$	time, sec
$u$	velocity, $ms^{-1}$
$u_o$	superficial gas velocity, m/s
$U$	internal energy, J
$V$	volume, $m^3$
$v$	average fluid velocity, $ms^{-1}$
$V$	intrinsic velocity, $ms^{-1}$
$\dot{v}$	volume flow rate, $m^3s^{-1}$
$\vec{v}$	velocity vector, m/s

$y_o$  height of a flow passage, m  
 $z$  axial direction, m

### Greek symbols

$\beta$  deformation factor,  $1.25 \left(\frac{1-\varepsilon}{\varepsilon}\right)^{10/9}$   
 $\beta$  thermal expansion coefficient, 1/K  
 $\beta_f$  buoyancy force, N  
 $\beta_t$  tangential viscosity parameter (Ns/m)  
 $\alpha$  damping parameter (dimensionless)  
 $\varepsilon$  porosity,  $1 - \frac{V_s}{V_T}$   
 $\alpha_T$  thermal accommodation coefficient  
 $\alpha$  thermal diffusivity,  $k/\rho c_p$  [ $m^2 s^{-1}$ ]  
 $\delta$  distance between two particles, m  
 $\dot{\delta}$  sliding velocity (m/s)  
 $\xi$  thermal radiative emissivity  
 $\sigma$  Stefan-Boltzmann constant ( $W/m^2 K^4$ )  
 $\rho$  density,  $kg/m^3$   
 $\Lambda$  molecular mean free path, m  
 $\kappa$  conductivity ratio,  $k_g/k_p$   
 $\mu$  dynamic viscosity,  $Ns^{-1}m^{-2}$   
 $\mu_c$  friction coefficient  
 $\Gamma$  diffusion coefficient  
 $\Theta$  dimensionless temperature  
 $\Delta$  increment  
 $\vec{\tau}$  stress tensor, Pa  
 $\gamma_g$  ratio of the specific heats of the gas,  $c_p/c_v$   
 $\Psi$  dimensionless parameter,  $\frac{k_p}{4\sigma T_s^3 d_p}$   
 $\psi$  stream function,  $m^2/s$   
 $\nu$  Poisson ratio,  $-\varepsilon_{lateral}/\varepsilon_{axial}$   
 $\nu$  kinematic viscosity,  $m^2s^{-1}$

### Subscripts

$a$  air  
 $b$  bed  
 $c$  contact point  
 $e$  number of adjacent contact particles  
 $eff$  effective

---

$f$	fluid
$g$	gas microgap
$g$	gas
$G$	macrogap
$j$	thermal joint
$L$	macrocontact
max	maximum
$N$	grid point
$m$	number of contact particles at bottom half
$m$	medium
$n$	number of contact particles at top half
$n$	normal
$nu$	nuclear fission
$n, s$	faces, north and south
$s$	solid
$o$	superficial
$p$	particle
$p$	pressure
$P$	node
$R$	radiative
$s$	solid
$S$	grid point
$T$	total
$t$	tangential
cd	pertaining to conduction
rcd	radiative-conductive
cr	rough contact
cp	perfect contact
$Bc$	bottom contact
$Tc$	top contact
BcdR	combined conduction and radiation at the bottom hemisphere
TcdR	combined conduction and radiation at the top hemisphere
$v$	volumetric
$\infty$	at points far from the body

### Superscripts

$c$	contact interface between particles
$G$	interstitial gas
$r$	radiation

t time, sec  
T total

### Non-dimensional Numbers

**Da** Darcy number,  $K/H^2$   
**Gr** Grashof number,  $\frac{g\beta|T_s-T_f|d_p^3}{\nu^2}$   
**Nu** Nusselt number,  $\frac{hd_p}{k_f}$   
**Pr** Prandtl number,  $\frac{\mu c_p}{k_f}$   
**Ra** Rayleigh number,  $\frac{g\beta|T_s-T_f|d_p^3}{\nu^2} \frac{\mu c_p}{k_f}$   
**Re** Reynolds number,  $\frac{\rho u d_p}{\mu}$   
**St** Stanton number,  $\frac{Nu}{Re Pr}$   
**Bi** Biot number,  $\frac{hd_p}{6k_p}$

### Abbreviations

AISI American Iron and Steel Institute  
 BCC body-centred cubic packing  
 CFD computational fluid dynamics  
 DEM discrete element method  
 FCC face-centred cubic packing  
 FEM finite element method  
 FDM finite difference method  
 FVM finite volume method  
 HCN Hertzian contact network  
 HTR high-temperature reactor  
 HTGR high temperature gas-cooled reactor  
 HTTU high temperature test unit  
 HWR heavy-water reactor  
 IAEA International Atomic Energy Agency  
 IBVP initial boundary value problem  
 KTA Kerntechnischer Ausschuss  
 LWR light-water reactors  
 MSUC multisphere unit cell  
 NLTE non-local thermal equilibrium  
 PBMR pebble bed modular reactor  
 PTFE polytetrafluoroethylene  
 RDF radial distribution function

SC	simple cubic packing
SiC	silicon carbide
TAC	thermal accommodation coefficient
TCR	thermal contact resistance
THTR	thorium high temperature nuclear reactor
TRISO	tristructural-isotropic
ZBS	Zehner, Bauer, SchiOnder

### **Coordinates**

$x, y, z$	cartesian coordinates
$r, \theta, \varphi$	spherical coordinates

# 1

## Introduction

---

### 1.1 Background

Nuclear reactors are installations that contain and control sustained nuclear chain reactions [1]. There are fundamentally two types of nuclear reactors. These are research reactors, where the neutrons produced in the fissioning process are the important product, and power reactors, where the heat released in the fissioning process is the important product. The fuel design of the latter type is the focus of the study.

Nuclear reactors produce energy through nuclear processes. In the fission reactors, energy is produced in a controlled way through the splitting of the nucleus of certain fissile elements. The energy released in this process is harnessed as heat in either gas or water, and is used to produce steam. The steam is used to drive the power-generating turbines that produce electricity. Today, there are about 450 nuclear power reactors that are used to generate electricity in about 30 countries around the world [2]. Nuclear reactors can be classified into four types: i) light-water reactors (LWR), ii) heavy-water reactors (HWR), iii) graphite-moderated reactors and iv) fast-breeder reactors. Statistical data from the International Atomic Energy Agency (IAEA) [3] reveals that there are 359 LWRs in 27 countries generating a total of 328.4GWe. Of the world nuclear reactors, 80% are light-water reactors. The waste produced in nuclear power plants, as distinct from other power-generating facilities, is the highly radioactive materials produced in the fuel elements. These are called the fission products. As in other industries, the design and operation of nuclear power plants aim to minimise the likelihood of accidents, and avoid major human consequences when they occur. A central safety problem in the design of a nuclear plant is to ensure in as much as it is possible or practicable, that these fission products remain safely confined at all times during the operation

of the plant, refuelling of the reactor, preparation and shipping of fuel after its use in the reactor core.

There have been three major reactor accidents in the history of commercial nuclear power, namely Three Mile Island (TMI-2), Chernobyl and Fukushima. The reactors of the three accidents were all light-water reactors and one common consequence of these accidents was the melting of the fission product retention barriers of the fuel. In 1979 at Three Mile Island nuclear power plant in the USA, a cooling malfunction caused part of the reactor core to melt down in the Number 2 reactor. On 26 April 1986, at the Chernobyl nuclear power plant complex during the course of a safety system test being carried out just before a routine maintenance outage, Chernobyl Number 4 boiling water pressure tube reactor (RBMK-1000 type) was destroyed as result of a power transient caused by violation of operating rules. The Fukushima Daiichi nuclear disaster was a failure of the emergency core cooling system at the Fukushima I Nuclear Power Plant on 11 March 2011, resulting in a melting of the cores of three of the plant's six boiling water reactors [4]. The failure occurred when the plant was hit by a tsunami triggered by the Tōhoku earthquake [5]. The plant began releasing substantial amounts of radioactive materials beginning on 12 March [5], becoming the largest nuclear incident since the Chernobyl disaster and the second (after Chernobyl) to measure Level 7 on the International Nuclear Event Scale (INES).

LWRs will continue to be the predominant type of reactor for some number of years because of its established and accepted design. Although the generic designs are all accepted by nuclear safety regulators worldwide, the ongoing objective of reactor designers is to improve the general safety characteristics. Current LWR designs have been optimised over decades, and the required improvements cannot be based on mere redesign but will require novel technologies. Recent developments in high temperature gas-cooled reactors (HTGR) with the pebble bed modular reactor (PBMR) being an example have been highly evaluated worldwide forming part of the candidates for the Generation IV reactor systems. With HTGR research and demonstration reactors now operational in Japan and China, renewed interest in these reactors is based primarily on the unique properties of the technology to assure retention of radioactive fission products by the fuel in all postulated event sequences by passive means.

Inherent safety is claimed for HTGR as a result of its design, fuel type and materials used. With the large number of LWRs in existence around the globe and the constant evolution of the

design towards safety enhancement, one important focus area for improvement is the high temperature fission product retention capabilities of the fuel. This study proposes that light-water reactors (LWR) can be made safer by redesigning the nuclear fuel in the cladding tube of the fuel assembly by making use of fuel in the form of coated particles [6]. A proper understanding of the heat transfer phenomena in packed beds of coated particles is therefore essential for successful redesign of such systems and also for modified reactors applying the HTR particle fuel concept.

## **1.2 Research Problem Statement**

The study investigates the heat transfer characteristics under natural convective heat transfer conditions in beds of randomly packed spheres (coated fuel particles). The investigation will help to develop an appropriate model that can suitably be applied to determine the heat transfer characteristics in the medium of the proposed fuel design.

As part of the Institutional Research Theme on Energy (IRT-E) at the University of Pretoria, a project was identified with the objective to investigate the use of Silicon Carbide as cladding material in fuel elements. As an extension of this project, the use of SiC coated uranium microspheres as the fuel material is investigated from a heat transfer point of view.

### ***1.2.1 Traditional fuel and the proposed fuel design***

The fuel cladding tube in LWR is approximately 4 metres long containing many fuel pellets stacked end-to-end to form a fuel rod. The packing structure of the fuel in the tube as depicted in Fig.1.1 is considered to be a simple (rod) with gas contained in the annulus between the pellets and the tube and hence it makes the heat transfer phenomenon in the tube easy and straightforward to calculate as discussed in Chapter 5.

The concept of the new design proposed in the study (see Fig.1.2) is to redesign the nuclear fuel in the form of loose coated particles in a helium atmosphere inside the nuclear fuel cladding tube of the fuel elements (see Fig. 1.3). The coated particle fuel being the heat source forms a bed in the cladding tube, which is closed at both ends. The heat generated by the fuel particles through nuclear fission is transferred to the gas filling the space between particles and interstice between particles and the inside tube walls. The heat transfer from the fuel to the tube is the objective of the investigation.

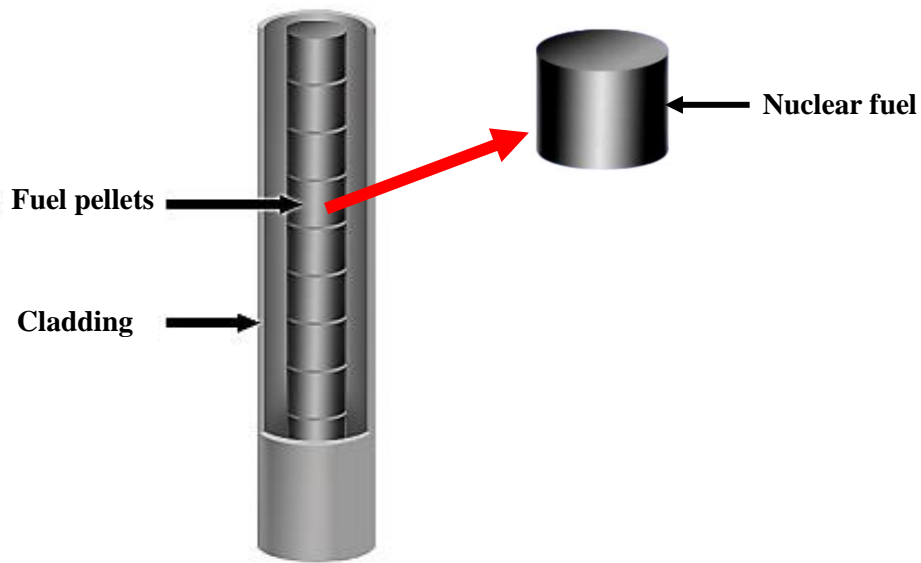


**Figure 1.1** Schematics of traditional fuel in the cladding

By converting the inside of the cladding into a porous medium, it is necessary to evaluate the heat transfer characteristics inside the medium under natural convective heat transfer conditions. To do this, there is the need to examine and confirm the suitability of using existing correlations in determining the heat transfer phenomenon in the medium noting the peculiarity of the medium. In the past, heat transfer correlations for packed beds have been investigated but the applicability of these correlations is mostly limited to the particular bed materials used in developing them. The applicability and accuracy of these correlations are uncertain.

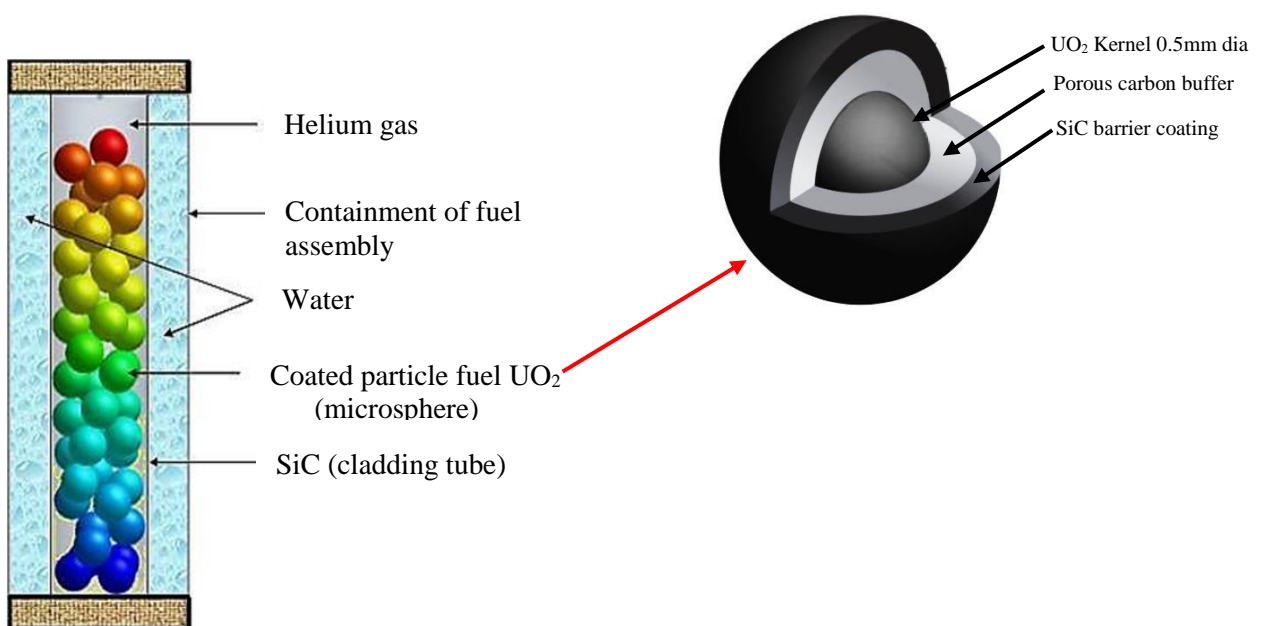


**Figure 1.2** Schematics of proposed coated particle fuel design in a SiC cladding tube

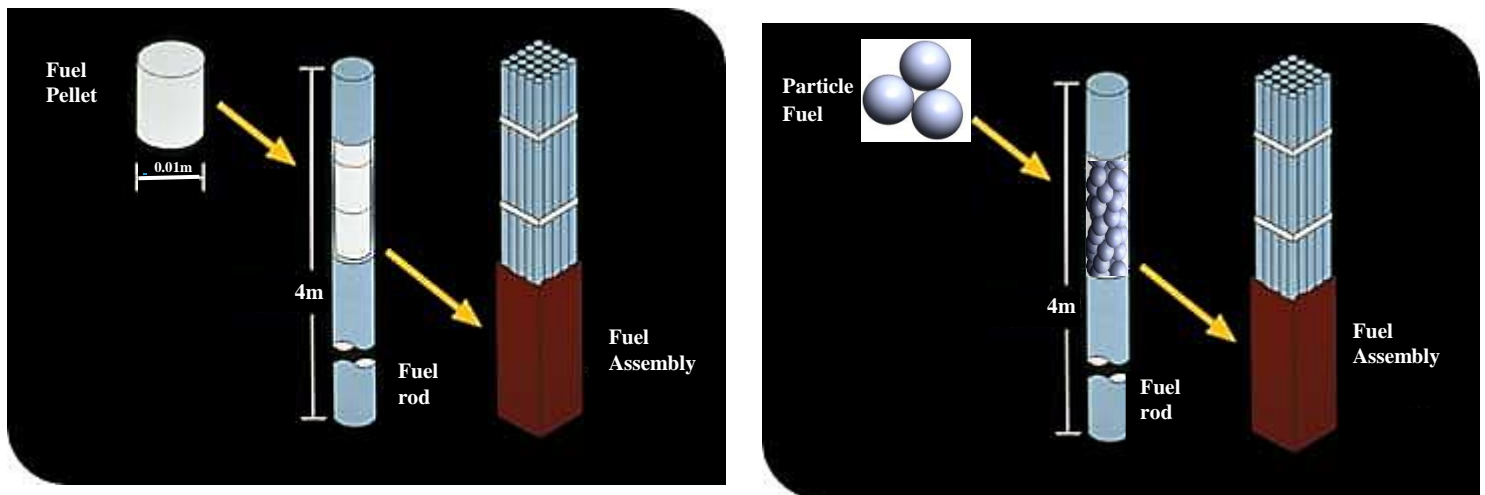


**Figure 1.3** (a) Traditional nuclear fuel assembly (b) Proposed new nuclear fuel design

An earlier review of most models (some of which are discussed in Chapter 3) used in predicting heat transfer in packed beds as presented by [7] reveals that many of the models are highly empirical in nature and applicable under forced convection. It is evident that these correlations do not account for the thermophysical properties of contacting particles and flowing gas, the interstitial gas effect, gas temperature, contact interface between particles, particle size and particle temperature distribution in the medium. This measure is considered vital in heat transfer phenomenon because they are parameters that define the heat transfer effects in the system. The developed correlations are based on flow in the medium. This reason and the one stated earlier annul the suitability of using the developed correlations in the cladding tube. Review and work done by [8], [9] and [10] reveal an increasing use of theoretical modelling in predicting the heat transfer in packed beds. Most work done on heat transfer in porous media summarised by [9], [11] and [12], adopted a microscopic approach considering a finite contact spot between individual particles in the bed and also relating the convective heat effect of the flowing fluid (gas) with the conduction effect between adjacent particles at the contact spot.

### 1.3 Methodology

For adequate investigation of the heat transfer characteristics in the proposed new fuel design, a theoretical model combining both the use of numerical and analytical methods needs to be developed. To do this, a test facility was designed and constructed at the University of Pretoria to investigate the fluid-to-particle natural convection heat transfer characteristics in an enclosed porous medium. The experimental data obtained from the test carried out was analysed and a

basic unit cell model was developed and applied to process the analysed results with the objective of determining the heat transfer characteristics in the medium under investigation.

Although the heat transfer phenomenon experienced in the experimental set-up is a reversed case (i.e. heat being transferred from the hot gas to the colder particles), the knowledge gained from the investigation will help to establish an appropriate theoretical relation required for evaluating the heat transfer characteristics in the proposed nuclear fuel design where the fuel particle is hotter than the gas. Results of heat transfer performance parameters obtained from the medium investigated were validated with the Gunn correlation.

Numerical simulation of a model mimicking the proposed design was later carried out to investigate particle-to-fluid heat transfer characteristics and flow distribution under natural convective conditions anticipated in slender beds of randomly packed heated spheres (coated fuel particles) using CFD simulations. The numerical results obtained allow estimating useful parameters such as *particle-to-fluid heat transfer coefficient*, *Nusselt number*, *Grashof number* and *Rayleigh number*.

## 1.4 Contributions of the Study

The contributions of the study to existing knowledge are in three dimensions:

1. The introduction of the elements of passive safety measures utilised in HTR into the traditional fuel configuration of light-water reactors.
2. Heat transfer characteristics in porous media should not only be associated and resolved through media flow (transport) because very limited and complex flow recirculation may exist in some media, which is the case in this study. For adequate evaluation of media heat transfer characteristics, different models for packed beds with different heat-generating sources should be developed. The heat transfer experienced at the nominal and regional contact regions, by convective and radiative (if applicable) effects must be accommodated in the developed models if heat transfer in packed beds is to be adequately evaluated.
3. The main limitation of heat transfer models in packed beds is the poor knowledge of flow patterns within them; the use of modelling and simulation tools in the study makes it possible

to define not only spatial distribution of involved species, but also temperature and velocity profiles within the bed.

## 1.5 Proposed Nuclear Fuel Safety Enhancement

Accidents resulting in the release of fission products are principally driven by the degradation of the barrier due to excessive temperature. Reactors are normally shut down due to rising fuel temperature but the radioactive fission products keep on generating heat even after shutdown. This residual heat is called decay heat. In ‘conventional’ reactors, heat is removed by active cooling systems such as pumps, which rely on the presence of a coolant such as water. Any such system may fail, and therefore, they are duplicated in conventional reactors to make sure that there will be support, should the first line of defence fail.

The proposed nuclear fuel design in the cladding is tailored towards the concept of high-temperature reactor (HTR) nuclear fuel pebbles. HTR particles of enriched uranium dioxide are coated by three layers: pyrolytic carbon, silicon carbide and pyrolytic carbon (to make them safer). These three layers are to protect the fuel itself in case of a complete loss of cooling [13]. The safety advantage of this proposed fuel design is that it utilises the elements of passive safety to improve the high temperature resistance of LWR fuel. The internationally agreed main safety function to be provided in the design of reactors is as follows [14]:

1. to control the heat production in the fuel by limiting decay heat levels and excessive reactivity excursions;
2. to ensure sufficient heat removal capability (including the options of doing this by passive means, so that the fuel will not exceed the specified limit);
3. to contain the radioactivity from being released to the environment.

The proposed fuel design will enhance the capability of the fuel to withstand high temperature degradation of the containment of the fission products, and thereby, contribute to the last two requirements above.

## 1.6 Publications

Four conference papers from the study have been presented in Europe, the USA and Canada. Three journal articles produced from this work have been submitted to nuclear engineering

journals, two have been published and the third is at the revised stage. The titles of the journal and conference papers are as follows:

### ***1.6.1 Journal papers***

1. O.O. Noah, J.F. Slabber, J.P. Meyer, Numerical simulation of natural convection heat transfer and transport in an enclosed slender tube geometrical model containing heated microspheres. Lead-way toward new nuclear fuel design. Nucl. Eng. Des. NED-D-15-00603R, 2016. (Revised Manuscript submitted on April 29, 2016).
2. O.O. Noah, J.F. Slabber, J.P. Meyer, Modelling a porous region for natural convection heat transfer and experimental validation in slender cylindrical geometries. Journal of Nuclear Technology, **193**(3), 375-390, 2016.
3. O.O. Noah, J.F. Slabber, J.P. Meyer, Investigation of natural convection heat transfer phenomena in packed beds: Lead-way toward new nuclear fuel design. ASME J. Nuclear Engineering and Radiation Science, **1**(4), 2015, 041014-12.

### ***1.6.2 Conference papers***

1. O.O. Noah, J.F. Slabber, J.P. Meyer, Numerical simulation of natural convection heat transfer and transport in packed beds: Mimicking a proposed new nuclear fuel design. *Proceedings of the 2016 24th International Conference on Nuclear Engineering (ICONE24)*, Charlotte, North Carolina, USA, June 26-30, 2016.
2. O.O. Noah, J.F. Slabber, J.P. Meyer, Natural convection heat transfer phenomena in packed bed systems. *Proceedings of ASME International Mechanical Engineering Congress & Exposition*, Montreal, Canada, November 14-20, 2014.
3. O.O. Noah, J.F. Slabber, J.P. Meyer, CFD simulation of natural convection heat transfer from heated microspheres and bottom plate in packed beds contained in slender cylindrical geometries. *Proceedings of the 6th International Conference on Application of Porous Media (InterPore)*, Milwaukee, U.S.A., May 27-30, 2014.

4. O.O. Noah, J.F. Slabber, J.P. Meyer, Experimental evaluation of natural convection heat transfer in packed beds contained in slender cylindrical geometries. *Proceedings of the 5<sup>th</sup> International Conference on Applications of Porous Media (InterPore)*, Cluj-Napoca, Romania, August 25–28, 2013, p. 301-316.

## 1.7 Chapter Outline

Chapter 2 presents a background to the open literature regarding packing structures highlighting near-wall and bulk region radial porosity effects in cylindrical and annular packed beds. Chapter 3 discusses the literature regarding heat transfer and transport through mono-sized randomly packed spheres. Chapter 4 examines the experimental test facility set-up, the use of the data acquisition system in capturing experimental data readings and the experimental evaluation of heat transfer characteristics in the investigating medium. Chapter 5 demonstrates the development of the basic unit cell model and its application to determine the heat transfer characteristics of the medium investigated. The use of the model in this chapter coupled with the knowledge gained from the experimental investigation has greatly aided in establishing a mathematical relation for determining the heat transfer performance in the proposed medium. A numerical simulation mimicking the medium of the proposed nuclear fuel design is carried out in Chapter 6. Conclusions and recommendations on the work done and on the proposed design are covered in Chapter 7.

# 2

## Porous Structure

---

### 2.1 Introduction

The design of high-temperature reactors (HTR) containing spherical fuel elements in the core such as the PBMR requires a thorough knowledge of the mechanisms of heat and mass transfer between the fuel pebbles and the helium coolant as well as the pressure drop of the flowing fluid through the core [15]. This customarily depends on the porous structure present in the packed bed. Most of the difficulties encountered in predicting the effective thermal conductivity have been attributed to the modelling of the microstructure in a porous matrix [16] hence thorough understanding of the structural arrangement in randomly packed beds of spherical fuel particles is crucial before any rigorous heat transfer analysis can be attempted. Realising the importance of the structural arrangement in randomly packed beds, this chapter will therefore focus on the various methods of analysing the porous structure in packed beds.

### 2.2 Analysis of Packing Regions

In the study, two packing regions are identified in the experimental set-up consisting of randomly packed uniform particles contained in a cylindrical cavity. The bulk region is the homogeneous section of the bed. The near-wall region is a significantly close vicinity to the solid walls surrounding the particles and is considered to have a local effect on the flow and heat transfer phenomena as noted by several investigators [17]. The porous structure varies sharply near any wall, as the geometry of the packing is disrupted in this region. This wall effect is composed of two separate components, namely the effect of the side wall (radial direction) and the effect of the top-bottom wall (axial direction), referred to by [18] as the thickness effect. The near-wall region is defined in the study as  $0 \leq z \leq 0.4$  (see Fig. 2.1), where  $z$  is the number of particle diameters away from the wall.

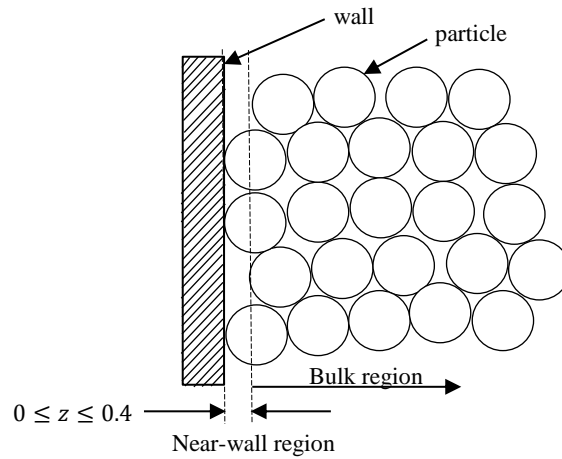


**Figure 2.1** Packing regions defined in the study

### 2.2.1 Porosity

Porosity,  $\varepsilon$ , also known as voidage or void fraction, is defined as the ratio of the void volume through which a fluid can pass relative to the total volume, which includes the volume of the obstruction in the flow path. It is also defined as one minus the packing density  $C$  (solid fraction) and is the most basic parameter for characterising the microstructure in a porous matrix.

$$\varepsilon = \frac{V_{void}}{V_{Total}} = 1 - \frac{V_{solid}}{V_{Total}} \quad (2.1a)$$

$$\varepsilon = 1 - C \quad (2.1b)$$

where  $V_{Total} = V_{solid} + V_{void}$

Total volume fraction: Solid fraction + Void fraction = 1

A number of experimental [19], [20], [21], [22] and theoretical [23], [24] investigations confirm that the porosity in beds of randomly packed uniform spheres varies from the limit of 1.0 at the containing walls, to the average bulk porosity of approximately 0.4 in the homogeneous section of the bed. A homogeneous porosity model is accurate as long as the diameter of the bed is larger than the diameter of the particle [25]. The wall effect is caused by the particles' point of contact with the wall. The transition in the wall porosity towards the constant inner-bed porosity varies. A higher porosity promotes flow along the walls but a higher surface area per unit volume hinders it. Shown in Fig. 2.2 is the measured of radial void

fraction distribution [19] for packed beds of uniform spheres contained by a solid wall and the exponential correlation of [20]. The porosity profile displays the form of a damped oscillation around the mean value. The oscillation period is approximately slightly less than one particle diameter. These oscillations are measurable for four to five particle diameters from the wall with the minimum porosity occurring at a distance of half sphere diameter from the solid wall. The number of particles, the packed height and cylinder diameter determine the overall porosity in the cylindrical container. The porosity used in the study is defined on this basis because of its slender cylindrical geometry. Pressure drop through a porous medium highly depends on the porosity,  $\epsilon$ . The heat transfer coefficient tends to depend more on the specific surface area,  $S_p$ , expressed by Eq. (2.2) [11]:

$$S_p = \frac{6(1 - \epsilon)}{d_p} \tag{2.2}$$

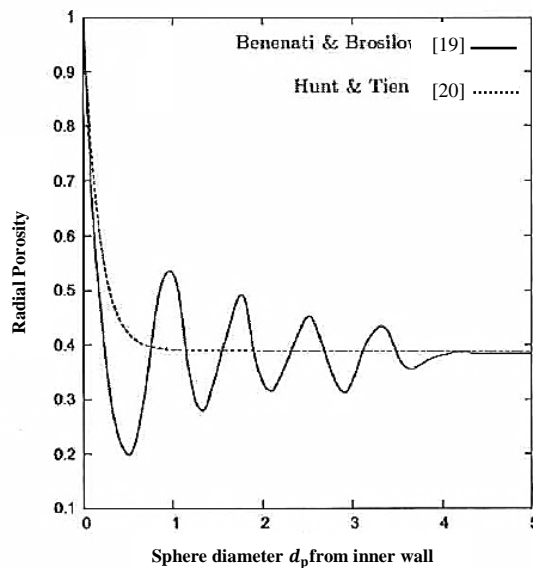


**Figure 2.2** Local and average area void fraction [20]

A good overview of the experimental methods used by various researchers to evaluate the radial voidage variation of packed beds in the bulk and near-wall region is given in [26], [27]. Correlations used to predict the variation in porosity can be classified into two categories: those that attempt to describe the oscillatory behaviour of the variation in the porosity and those that attempt to describe the variation of the averaged porosity using an exponential expression [28].

An overview is given in Table 2.1, summarising the correlations found in literature to describe the oscillatory behaviour of the variation in porosity.

**Table 2.1:** Summary of oscillatory porosity correlations in the radial direction

RESEARCHERS	CORRELATIONS	PARAMETERS
Martin, 1978	$\varepsilon(x) = \begin{cases} \varepsilon_{min} + (1 + \varepsilon_{min})x^2, & -1 \leq x \leq 0 \\ \varepsilon_b + (\varepsilon_{min} - \varepsilon_b)e^{-x/4} \cos\left(\frac{\pi}{C}x\right), & x \geq 0 \end{cases}$	$x = 2 \frac{R-r}{d_p} - 1$ $C = \begin{cases} 0.816 & D/d_p = \infty \\ 0.876 & D/d_p = 20.3 \end{cases}$ $\varepsilon_{min} = 0.245, \quad \text{Bulk porosity } (\varepsilon_b) = 0.385$
Cohen & Metzger, 1981	$\frac{1 - \varepsilon(z)}{1 - \varepsilon_b} = 4.5 \left[ z - \frac{7}{9} z^2 \right] \quad z \leq 0.25$ $\frac{\varepsilon(z) - 1}{1 - \varepsilon_b} = a_1 e^{(-a_2 z)} \cos[a_3 z - a_4] \pi \quad 0.25 < z < 8$ $\varepsilon(z) = \varepsilon_b \quad 8 \leq z \leq \infty$	$z = \frac{R-r}{d_p}$ $a_1 = 0.3463, \quad a_2 = 0.4273$ $a_3 = 2.4509, \quad a_4 = 2.2011$
Ridgeway & Tarbuck, 1968  Kamiuto <i>et al.</i> , 1989	<p>For <math>0 \leq z \leq 0.6</math></p> $\varepsilon(z) = 1 - 3.10036z + 3.70243z^2 - 1.24612z^3$ <p>For <math>0.6 \leq z \leq (R_o - R_i)/2d_p</math></p> $\varepsilon(z) = -0.1865 \exp(0.22z_m^{1.5}) \cos(7.66z_m) + \varepsilon_b$	$z = \frac{r-R_i}{d_p}, \quad R_i \leq r \leq \frac{R_o+R_i}{2}$ $z = \frac{R_o-r}{d_p}, \quad \frac{R_o+R_i}{2} \leq r \leq R_o$ $z_m = z - 0.6$
Mueller, 1992	$\varepsilon(r) = \varepsilon_b + (1 - \varepsilon_b) J_0 \left[ a \frac{r}{d_p} \right] \times \exp \left( -b \frac{r}{d_p} \right)$	$a = \begin{cases} 7.45 - \frac{3.15}{D/d_p} & 2.02 \leq D/d_p \leq 13.0 \\ 7.45 - \frac{11.25}{D/d_p} & 13.0 \geq D/d_p \end{cases}$ $b = 0.315 - \frac{0.728}{D/d_p}, \quad \varepsilon_b = 0.365 + \frac{0.22}{D/d_p}$
De Klerk, 2003	$\varepsilon(x) = 2.14x^2 - 2.53z + 1 \quad z \leq 0.637$ $\varepsilon(z) = \varepsilon_b + 0.29 \exp(-0.6z) \times [\cos(2.3\pi(z - 0.16))] + 0.15 \exp(0.9z) \quad z > 0.637$	$z = \frac{r-R_i}{d_p}, \quad R_i \leq r \leq \frac{R_o+R_i}{2}$ $z = \frac{R_o-r}{d_p}, \quad \frac{R_o+R_i}{2} \leq r \leq R_o$

In the case of [29] correlation, there are various variations and empirical constants for which appropriate values are required. However, [30] demonstrates that the Bessel function of the first kind  $J_0$  does not provide an accurate representation of the void fraction in the near-wall region

between  $0 \leq z \leq 0.5$ . An overview is given in Table 2.2, summarising the correlations found in literature to describe the exponential behaviour in porosity. After careful examination, [28] found that the correlation of [20] gave the best representation of the averaged variation of porosity in the radial direction.

**Table 2.2:** Summary of exponential porosity correlations in the radial direction

RESEARCHERS	CORRELATION
Vortmeyer & Schuster, 1983	$\varepsilon(r) = \varepsilon_o \left[ 1 + C \exp \left\{ -N \frac{r-R_o}{d_p} \right\} \right], \quad R_i \leq r \leq \frac{R_o + R_i}{2}$ $\varepsilon(r) = \varepsilon_o \left[ 1 + C \exp \left\{ -N \frac{R_o-r}{d_p} \right\} \right], \quad \frac{R_o + R_i}{2} \leq r \leq R_o$
Sodre & Parise, 1998	<b>PARAMETER</b>
	$N = \frac{2C\varepsilon_o d_p [1 - \exp(-N(R_o - R_i)/2d_p)]}{(\bar{\varepsilon} - \varepsilon_o)(R_o - R_i)}$ $\bar{\varepsilon} = 0.3517 + 0.387 \frac{d_p}{2(R_o - R_i)}$
White & Tien, 1987	<b>CORRELATION</b>
	$\varepsilon(r) = \left[ 1 + \left\{ \frac{1 - \varepsilon_b}{\varepsilon_b} \right\} \sqrt{1 - \exp \left\{ -2 \frac{r - R_i}{d_p} \right\}} \right]^{-1}$ <p style="text-align: center;"><i>for</i> <math>R_i \leq r \leq \frac{R_o + R_i}{2}</math></p> $\varepsilon(r) = \left[ 1 + \left\{ \frac{1 - \varepsilon_b}{\varepsilon_b} \right\} \sqrt{1 - \exp \left\{ -2 \frac{R_o - r}{d_p} \right\}} \right]^{-1}$ <p style="text-align: center;"><i>for</i> <math>\frac{R_o + R_i}{2} \leq r \leq R_i</math></p>

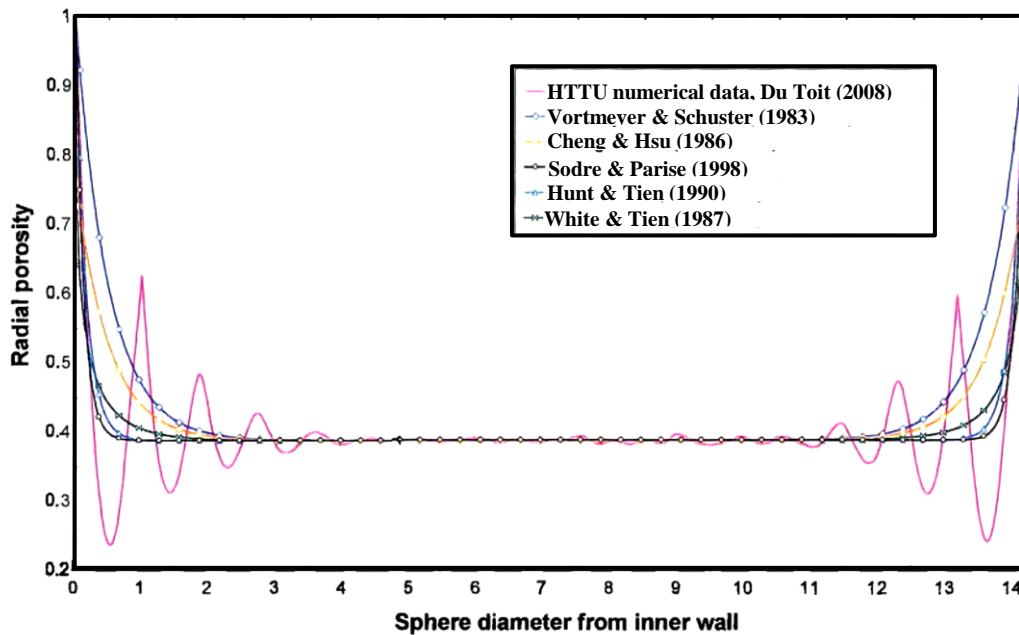


**Figure 2.3** Comparison between radial exponential porosity correlations [28]

## 2.2.2 Coordination Number

The points of contact between a given sphere and adjacent spheres (and in some cases the angular distribution of these points) must be determined. For regular packings, the number of such points, called the coordination number, which is also known as the *kissing number*, is indicative of the packing characteristics at a location; simple cubic, orthorhombic (body-centred cubic), tetragonal-spherominal and rhombohedral (face-centred cubic) packings have six, eight, ten and twelve contact points respectively. Determining the coordination number is very useful for modelling transport phenomena through packed beds as noted by [31]. Experimental studies were conducted by [31] to determine the coordination number for 6.35 mm uniform-sized spheres, concluding that the average coordination number is approximately eight for a randomly packed bed with an average porosity of 0.39.

The frequency distribution of the number of contact points,  $N_i/N$ , in most cases referred to as the average coordination number,  $\overline{N_c}$ , where  $N_i$  is the number of samples that have the number of contact points  $i$  and  $N$  is the total number of samples, is measured and given by [32]. Various researchers, such as [33], [34], [35], have endeavoured to derive correlations that can predict the average coordination number for a given porosity in the bulk region of a randomly packed bed. A summary of all these empirical correlations is presented by [36]. A revised

summary of these correlations is given in Table 2.3. There are significant differences when these correlations are plotted against one another as displayed in Fig. 2.4.

**Table 2.3:** Equations for relation between average coordination number and porosity [10]

RESEARCHERS	CORRELATION	VALIDITY
Rumpf, 1958	$\bar{N}_c = 3.1/\varepsilon$	$(0.2595 \leq \varepsilon \leq 1)$
Meissner <i>et al.</i> , 1964	$\bar{N}_c = 2e^{2.4(1-\varepsilon)}$	$(0.2595 \leq \varepsilon \leq 1)$
Ridgeway & Tarbuck, 1967	$\varepsilon = 1.072 - 0.1193\bar{N}_c + 0.00431\bar{N}_c^2$	$(0.2595 \leq \varepsilon \leq 1)$
Haughey & Beveridge, 1969	$\bar{N}_c = 22.47 - 39.39\varepsilon$	$(\varepsilon \leq 0.5)$
Nakagaki & Sunada, 1968	$\bar{N}_c = 1.61\varepsilon^{-1.48}$	$(\varepsilon \leq 0.82)$
	$\bar{N}_c = 4.28 \times 10^{-3}\varepsilon^{-17.3} + 2$	$(\varepsilon \leq 0.82)$
Smith <i>et al.</i> , 1929	$\bar{N}_c = 26.49 - 10.73/(1 - \varepsilon)$	$(\varepsilon \leq 0.595)$
Gotoh, 1978	$\bar{N}_c = 20.7(1 - \varepsilon) - 4.35$	$(0.3 \leq \varepsilon \leq 0.53)$
	$\bar{N}_c = 36(1 - \varepsilon)/\pi$	$(\varepsilon > 0.53)$
Suzuki <i>et al.</i> , 1981	$\bar{N}_c = 2.812 \frac{(1-\varepsilon)^{-1/3}}{(b/d_p)^2 [1 + (b/d_p)^2]}$ <p>where</p> $(1 - \varepsilon)^{-1/3} = \frac{1 + \left(\frac{b}{d_p}\right)^2}{1 + \left(\frac{b}{d_p}\right) e^{(d_p/b)^2} \text{Erfc}\left(\frac{d_p}{b}\right)}$ $b/d_p = (7.318 \times 10^{-3} + 2.19\varepsilon - 3.357\varepsilon^2 + 3.194\varepsilon^3)$	$(0.2595 \leq \varepsilon \leq 1)$
Yang <i>et al.</i> , 2000	$\bar{N}_c = 2.02 \frac{1 + 87.38(1 - \varepsilon)^4}{1 + 25.8(1 - \varepsilon)^4}$	$(0.39 \leq \varepsilon \leq 1)$
Zhang <i>et al.</i> , 2001	$\bar{N}_c = \frac{1}{0.183 - 659.248(1 - \varepsilon)^{20.961}}$	$(0.37 \leq \varepsilon \leq 0.45)$
Du Toit, 2008	$\bar{N}_c = 25.952\varepsilon^3 - 62.364\varepsilon^2 + 39.724\varepsilon - 2.0233$	$(0.2398 \leq \varepsilon \leq 0.54)$

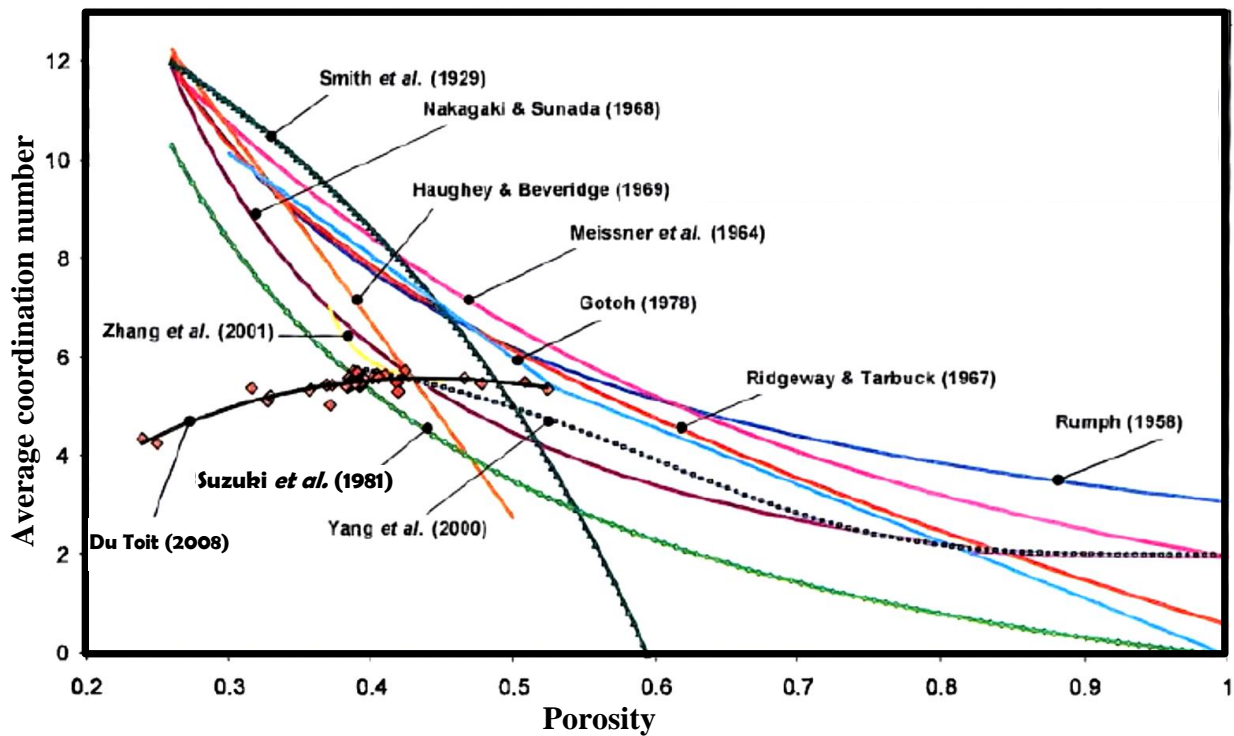


Figure 2.4 Comparison between various coordination number models (see Table 2.3) [28]

One aspect to be noted is that the empirical correlations shown in Table 2.3 are not valid in the near-wall region of a randomly packed bed, although several boundary conditions clearly state its validity up to a porosity of one. The main focus of the researchers was to quantify the bulk region of a packed bed, and therefore, the correlations presented in Table 2.3 are valid up to higher porosities in the bulk region for different types of packings.

### 2.2.3 Coordination Flux Number

An important aspect that is not widely recognised in heat transfer calculations is the actual number of spheres in contact with the sphere under consideration contributing to heat transfer in a certain direction. The parameter,  $n$ , is hereafter referred to as the coordination flux number. In an endeavour to define this value,  $n$ , in a randomly packed bed, [37] argues that for a basic loose packing, the value of  $n$  should be  $n = 1.5$  and for a more dense close packing, the value of  $n$  should be  $4\sqrt{3}$  for a porosity range of  $0.260 \leq \varepsilon \leq 0.476$ . By using contact angles and counting the number of positive and negative contact angles respectively for the particle under consideration, [10] found that approximating the coordination flux number as  $n = \bar{N}_c/2$  would give adequate values for  $n$ . The introduction of this concept is aimed at determining a more

accurate number of spheres in contact with the particle test sample (sphere under consideration) to attain a precise conservative heat transfer balance in packed beds.

### 2.3 Structured (Ordered) Packing

In the open literature, such as presented in [38], ordered packing structures are classified into three different arrangements. These are simple cubic packing (SC), body-centred cubic packing (BCC) and face-centred cubic packing (FCC). Various researchers such as [36] noted that the densest packing arrangement is FCC packing. Table 2.4, Fig. 2.5 and Fig. 2.6 present some important specifications on the various structural arrangements. These structured packing arrangements were used by [39] and [38] to quantify the porous structure in a randomly packed bed for calculating effective thermal conductivity. They argue that if the porosity,  $\varepsilon$ , in a randomly packed bed is within a certain porosity range, the porous structure will be analogous to that of a specific ordered packing structure.

**Table 2.4:** Comparison of coordination number and porosity with different arrangements [31]

TYPE OF PACKING ARRANGEMENT	POROSITY	COORDINATION NUMBER	COORDINATION FLUX NUMBER
SC array	0.476	6	1
BCC array	0.32	8	4
FCC array	0.2595	12	4

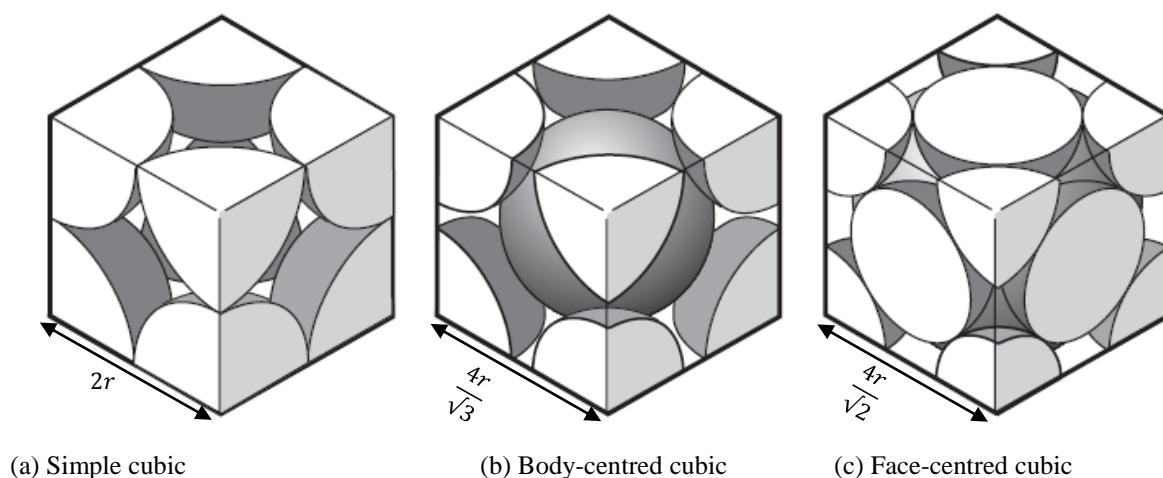


**Figure 2.5** Ordered packing structures [31]

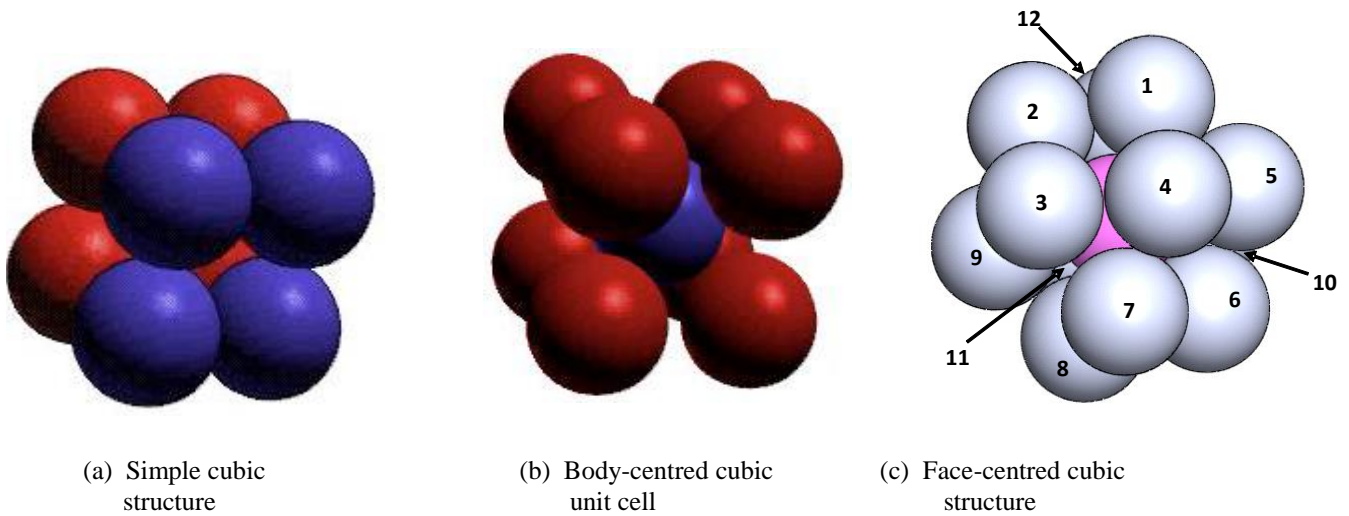


**Figure 2.6** Ordered packing structures [40] and [41]

## 2.4 Limitations on Defining Packing Structures with Porosity Only

In most existing effective thermal conductivity models, the porous structure is commonly quantified using porosity alone. Employing only porosity to quantify the porous structure in the effective thermal conductivity calculations is usually valid on condition that the model is used within specified porosity bounds. The most common simplification associated with these models is to assume some form of ordered packing such as SC, BCC and FCC in order to quantify the porous structure in the bulk and near-wall regions of a randomly packed bed. When considering an ordered packing in the bulk region of a randomly packed bed, it can be presumed that the porous structure is close to SC or BCC with the porosity approaching quantities displayed in Table 2.4. However, the average coordination number of these ordered packings is  $\bar{N}_c = 6$  for SC and  $\bar{N}_c = 8$  for BCC, while in the randomly packed bed used as the basis for the study it is found to be  $\bar{N}_c = 5.6$  from the graph of [36] in Fig. 2.4. This comparison clearly demonstrates that the SC-ordered packing is the best option to use. However, if one considers the coordination flux number, the magnitude for the SC-ordered packing is  $n = 1$ , while for a randomly packed bed in the bulk region, it is actually found to be  $n = \bar{N}_c/2 = 2.8$ . This clearly indicates a significant difference when used in heat transfer calculations. When comparing the near-wall region in a randomly packed bed with a FCC-ordered packing with a porosity of  $\varepsilon = 0.2595$ , important differences are also found. In the numerical porosity calculations for a randomly packed bed presented by [28], it is shown that

the porosity at  $0.5d_p$  away from the wall is  $\varepsilon = 0.2398$ , which is very close to that of the FCC-ordered packing. However, there is a significant difference between the calculated coordination number in a randomly packed bed of  $\bar{N}_c = \pm 4.35$  and that of the FCC-ordered packing at  $N_c = 12$ . Therefore, defining a porous structure using porosity alone is not sufficient.

## 2.5 Conclusion

The structure of a randomly packed bed of spherical fuel particles can be quantified with various methods and tools. In previous work, it was found that the most widely used parameter to quantify the porous structure was porosity. Experimental and numerical procedures were developed and used by [28] to compare porosity variation in the radial and axial directions of a randomly packed bed. It was further found that the coordination number could quantify the porous structure to some extent. The limitations on using porosity as the main parameter to quantify porous structure were also indicated.

# 3

## Convective Heat Transfer in Packed Beds

### 3.1 Introduction

Convective heat transfer in porous media arising in various engineering problems are sometimes induced by a) central internal heat generation [42] as in the SANA test facility, b) heat-generating TRISO particle fuels as in [43] high-temperature reactor (HTR), c) the Horton-Rogers-Lapwood problem heating from below [44], d) heating from the top wall, e) enclosures heated from the side walls. Experimental investigation by various researchers on natural convection in saturated porous medium [45] started with the stability theory applied to an infinite horizontal layer heated from below [44, 46]. Heat transfer in porous media most of the time is a complex issue due to the different parameters involved in the media, such as the bed materials, heat transfer mechanisms, packing structure and heat source (see Fig. 3.1).

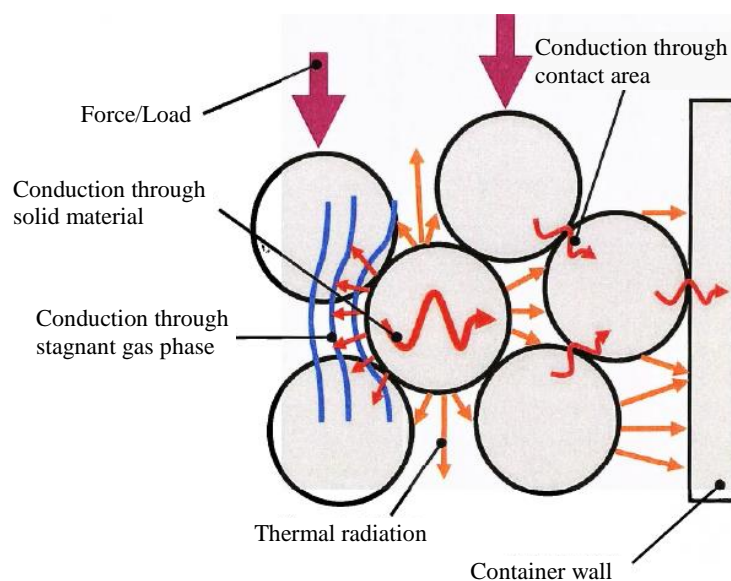


**Figure 3.1** Heat transfer mechanisms through a packed bed

A number of researchers in literature have investigated heat transfer phenomena in different porous media using their own concept or ideology and this has resulted in the development of a number of correlations, mathematical formulae and models in characterising the media. This chapter examines the work done by some researchers from their investigations of the heat transfer effects in different porous media.

### 3.2 Well-known correlations

Correlations commonly employed in literature to characterise the heat transfer in packed beds are those developed by Wakao [47], Gunn [48], Gnielinski [49], German Nuclear Safety Standards Commission [50], Achenbach [51], Dixon [52], Churchill and Chu [53]. A heat transfer correlation for forced convection through pebble beds was proposed by [47] from the study conducted on published heat transfer data by various authors, the experimental set-up for this data was obtained from different geometries and the accuracy of the correlation is uncertain.

The correlation of Gunn [48] for buoyancy-driven flow holds for a porosity range of  $0.35 \leq \varepsilon \leq 1.0$ , and correlates experimental data for a Reynolds number range of  $0 \leq Re_{d_p} \leq 10^5$ .

The correlation of Gnielinski [49] is valid for a Reynolds number in the range  $500 \leq Re_{d_p} \leq 10^3$  and a porosity range  $0.26 \leq \varepsilon \leq 1.0$ . The KTA correlation is only valid for gas-cooled reactor ( $Pr = 0.7$ ) with  $Re$  ranging from 100 to  $10^5$ ,  $0.36 \leq \varepsilon \leq 0.42$ ,  $D/d_p \geq 20$  and  $h/d_p \geq 4$ . Achenbach correlated convective heat transfer for a  $Re > 1$  and a porosity  $\varepsilon$  of 0.387. Correlation by Dixon in heterogeneous medium holds for a Reynolds number range from  $300 \leq Re_{d_p} \leq 3000$ .

**Table 3.1** Correlations for the determination of heat transfer in packed beds

Author	Correlation	Type	Re	Geometry
Wakao <i>et al.</i> , 1978	$Nu_{wak} = 2 + 1.1Pr^{\frac{1}{3}}Re_o^{0.6}$	Heterogeneous particle-to-fluid model	$15 < Re < 850$	Cylindrical bed
Gunn (1978)	$Nu_{d_p} = (7 - 10\varepsilon + 5\varepsilon^2) \left(1 + 0.7Re_{d_p}^{0.2}Pr^{\frac{1}{3}}\right) + (1.33 - 2.4\varepsilon + 1.2\varepsilon^2)Re_{d_p}^{0.7}Pr^{\frac{1}{3}}$	Homogeneous	$0 < Re < 10^5$	Cylindrical bed
Gnielinsk, 1981	$Nu_{gn} = f_s \left[2 + \sqrt{Nu_{lam}^2 + Nu_{turb}^2}\right]$		$500 \leq Re \leq 10^3$	
Dixon (1997)	$Nu_D = 0.523 \left(1 - (D/d_p)^{-1}\right) Pr^{\frac{1}{3}} Re_o^{0.738}$	Heterogeneous wall-fluid model	$300 \leq Re \leq 3000$	

**Table 3.1** (Continued)

Achenbach (1995)	$Nu = [(1.18Re_o^{0.58})^4 + (0.23Re_o^{0.75})^4]^{\frac{1}{4}}$	Heterogeneous particle-to-fluid model	$1 < Re < 10^5$	Cylindrical bed
Churchill-Chu (1975)	$Nu = 2 + \frac{0.600Ra_D^{1/4}}{\left[1 + \left(\frac{0.5}{Pr}\right)^{9/16}\right]^{4/9}}$	Heterogeneous	$Ra_{dp} \leq 10^{11}$	
PBMR KTA (1983)	$Nu_{KTA} = 1.27 \frac{Pr^{1/3}}{\varepsilon^{1.18}} Re^{0.36} + 0.033 \frac{Pr^{1/2}}{\varepsilon^{1.07}} Re^{0.86}$	Homogeneous	$100 < Re < 10^5$	Cylindrical bed

### 3.3 Solid and Fluid Heat Transfer Models

Some existing models accounting for the description of heat transfer performance in porous media at low and high temperatures are discussed in this section.

#### Model 1: Balakrishnan and Pei, 1979 [7]

Balakrishnan and Pei studied analytically the conduction mode of heat transfer in packed beds subject to flowing gases [7]. The analysis of [7] was based on the more realistic assumption of a finite contact spot between the spheres in the bed, the dimensions of which may be obtained from the Hertzian elasticity theory. Moreover, the convective effects of the flowing gas were also incorporated into the analysis of [7] as boundary conditions. The effect of parameters such as contact spot dimensions, packing geometry, Biot modulus (convective effects) and radiation on the conduction mode was examined by [7].

A single sphere in Fig. 3.2 of radius  $r_s = a$  between two planes **A** and **B** was considered by [7], where **A** is at a higher temperature than **B**. Gas, at a bulk temperature of  $t_f$ , flows past the sphere and heat is transferred by conduction through the sphere between the two planes and by convection between the sphere and the gas that surrounds the sphere [7]. The heat flux from Plane **A** to the sphere is  $q_o$  and a heat flux of  $q_1$  leaves the sphere into Plane **B** [7]. The convective flux from the sphere to the gas stream is equal to  $h_{fp}(t - t_f)$ , where  $h_{fp}$  is the convective heat transfer coefficient [7]. There is a finite contact spot between the spheres and each of the other two spheres at Planes **A** and **B** respectively, and the contact radius is given by the Hertz relation [7] in Eq. (3.1).

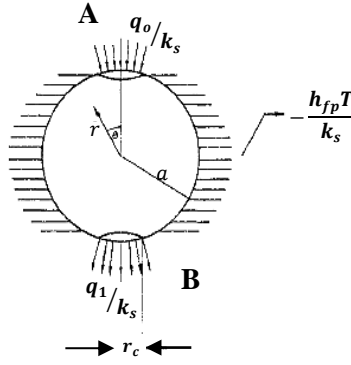


**Figure 3.2** Coordinates for the analysis [7]

$$r_c = \left[ \frac{3}{4} \frac{1 - v^2}{E} F \cdot a \right]^{1/3} \quad (3.1)$$

where radius of sphere  $a = r_s$

By definition, the thermal resistance of the sphere is given by Eq. (3.2) [7]:

$$R_{cd^1} = \frac{T(a, 0) - T(a, \pi)}{\frac{q_0 + q_1}{2} \pi r_c^2} \quad (3.2)$$

The resistance of a cubical volume of Side  $2a$ , just enclosing one of the spheres in the bed, is also  $R_{cd^1}$  (This is because the only solid phase in the cube through which conduction can take place is the sphere) [7]. The effective thermal conductivity of the bed,  $k_{eff}$ , can therefore be defined by a heat balance on the cube (the cube being a part of the bed has the same  $k_{eff}$ ) [7].

$$\frac{\Delta T}{R_{cd^1}} = k_{eff} \cdot [\text{area of cube face}] \cdot \frac{\Delta T}{[\text{height of cube}]} = k_{eff} \cdot (4a^2) \cdot \frac{\Delta T}{2a} \quad (3.3)$$

where  $k_{eff} = \frac{1}{R_{cd^1}(2a)}$

Therefore, the conduction heat transfer per layer of spheres in the bed is [7]:

$$h_{cd} = \frac{k_{eff}}{2a} = \frac{1}{R_{cd^1} 4a^2} \quad (3.4)$$

The corresponding Nusselt number gives:

$$Nu_{cd} = \frac{h_{cd} \cdot 2a}{k_f} = \frac{k_{eff}}{k_f} \quad (3.5)$$

The conduction heat transfer coefficient obtained by Eq. (3.4) is used in obtaining the total heat transfer in packed beds subject to gas flow [7] as analysed below. The validity of the analysis can be confirmed by comparing the total heat transfer thus obtained with experimental data on the total heat transfer of packed beds subject to flowing gas [7].

$$\begin{aligned}
 \text{Total heat transfer} = & \text{axial conduction with convective effects} + \text{convection from bed to fluid} \\
 & + \text{radiation between bed particles} \qquad (3.6)
 \end{aligned}$$

To obtain the total heat transfer coefficient,  $h_t$ , care should be taken that the contributing heat transfer coefficients are based on the same area and temperature difference [7]. Consider Fig. 3.3, the area for axial heat transfer by conduction is the area of the face of a cube just enclosing the sphere of radius  $a$ , i.e.  $4a^2$  (this is the cross-sectional area of the bed per sphere). The temperature driving potential is  $\Delta T$ , which is the temperature difference between Plane A and Plane B, the faces of the cube perpendicular to the direction of heat flow. For the convective mode, the area for heat transfer is the area of the sphere,  $4\pi a^2$ , and the temperature driving force,  $\bar{T}$ , the average temperature difference between the surface of the sphere and the fluid [7]. The total heat transfer coefficient  $h_t$ , is defined on the same basis as  $h_{fp}$  [7], and therefore, from Eq. (3.6):

$$h_t(4\pi a^2)(\bar{T}) = h_{rcd}(4a^2)(\Delta T) + h_{fp}(4\pi a^2)(\bar{T}) \qquad (3.7)$$

To evaluate the total heat transfer, Eq. (3.7) is rewritten as:

$$h_t = h_{rcd} \frac{\Delta T}{\bar{T}} \cdot \frac{1}{\pi} + h_{fp} \qquad (3.8)$$

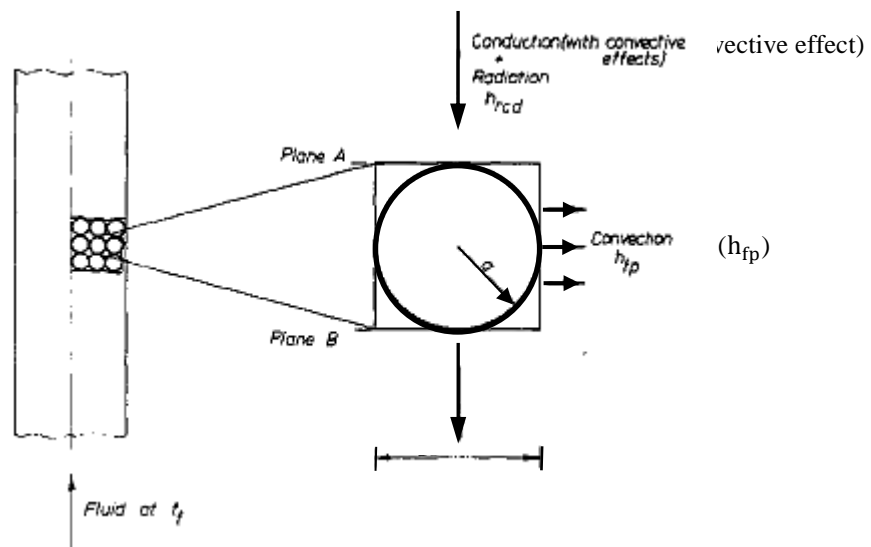


**Figure 3.3** Model [7]

$h_{rcd}$ , is defined as the heat transfer coefficient representing both conduction and radiation [7], it is derived and expressed by Eq. (3.9):

$$h_{rcd} = h_{cd} + h_r \left( \frac{\pi}{4} \right) \quad (3.9)$$

$$h_r = \frac{0.227}{2} \left[ \frac{\bar{T}}{100} \right]^3 \text{ J/m}^2\text{sK} \quad (3.10)$$

$$h_{cd} = \frac{1}{R_{cdi}} = \frac{1}{A_{si}} \quad (3.11)$$

where  $i = 1$  or  $2$  for simple cubic or body-centred cubic geometries respectively. The convective heat transfer coefficient,  $h_{fp}$ , obtained by empirical correlation [54] is expressed in Eq. (3.12):

$$h_{fp} = 0.016 \left[ \frac{k_f}{2a} \right] \cdot [Ar_m]^{0.25} (Re_p)^{0.5} \quad (3.12)$$

where  $Ar_m$  is the modified Archimedes number. The total heat transfer coefficient,  $h_t$ , is then compared with the literature values (see Fig. 3.4) in its dimensionless form as:

$$Nu_t = \frac{h_t \cdot 2a}{k_f} \quad (3.13)$$

In summary, the proposed model is valid under the following conditions [7]: (a) Conduction takes place in the axial direction only. (b) Radiation is restricted to transfer between the bed spheres only. (c) The bed materials are uniform spheres and are perfectly elastic so that the Hertz theory can be used to obtain the contact spot dimensions (to evaluate  $h_{cd}$ ) [7]. This obviously excludes the case where  $2a/D_t$  is large [7]. (d) Values for the convective heat transfer coefficients are available. (e) Adiabatic wall conditions apply.

Fig. 3.4 shows a plot of  $Nu_t$  vs  $Re_p$ . The figure shows the data points of two other studies and the solid lines represent the predictions obtained using the present model of the author. Predicted values based on both the simple cubic and body-centred cubic geometries are shown and it may be noticed that the simple cubic model tends to underestimate and the body-centred cubic to overestimate the total Nusselt number. That is, the actual heat transfer rates are between these two regular packing geometry cases.

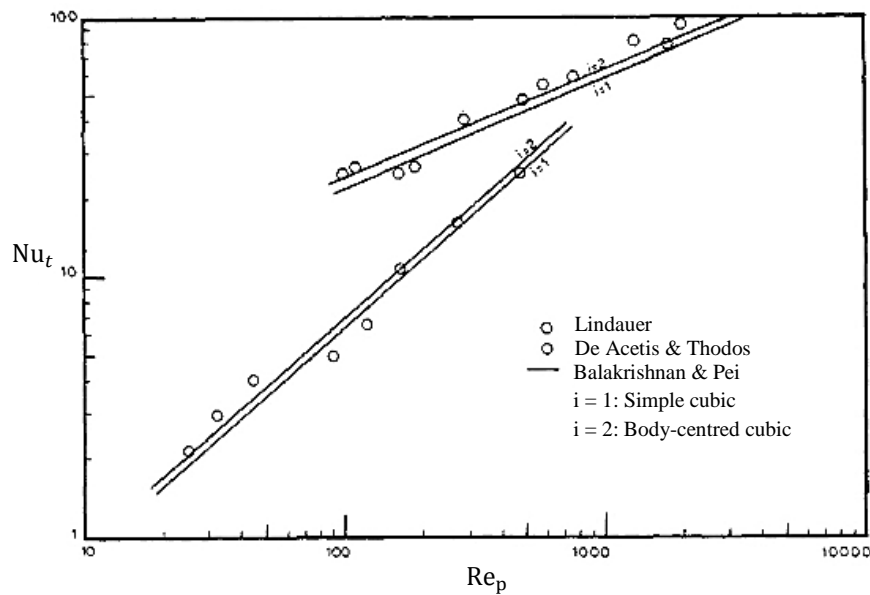


**Figure 3.4** Comparison of model with literature data [7]

Model 2: Souad Messai *et al.* (2014) [56]

Souad Messai *et al.* carried out an experimental study to investigate and evaluate the convective heat transfer coefficient in a cylindrical packed bed of spherical porous alumina particles [56]. The task consisted of proposing a semi-empirical model to avoid excessive instrumentation and time consumption [56]. The measurement of the bed temperature in addition to making simple energy balances led to calculation of the gas-to-particle heat transfer coefficient using a logarithmic mean temperature difference method. These experiments were performed at atmospheric pressure. The operating fluid was humid air. The gas velocity and temperature ranged from 1.7-3 m/s and 120-158 °C respectively. The data obtained was compared with the correlations reported in the literature. It was shown that the proposed model was in reasonable agreement with the correlation of [55]. Despite many proposed researches on experimental investigations of heat transfer coefficients in packed beds at low and average temperatures, few studies have presented a calculation of convective heat transfer coefficients at high temperature (above 120 °C) [56]. A possible application of the proposed model is drying and combustion.

Major correlations proposed in the literature are a function of the dimensionless number, nevertheless, the heat transfer coefficient is shown to be affected by other parameters such as particles and bed characteristics and boundary conditions. Therefore, the application of a general correlation for packed beds is not possible. Moreover, the usual studies are at low and

average temperatures. Therefore, this research attempts to quantify the heat transfer coefficient based on experimental temperature data associated with simple energy balances at high temperature and low Reynolds numbers.

**Experimental set-up**

The experimental device consisted of a thermally isolated cell containing the experimental packed bed, a steam generator, a hot gas heating system, a closed loop for the circulation of humid air ( $P_v = 0.6$  bar), a data acquisition and control unit [56]. A schematic diagram is shown in Fig. 3.5. The circulation of humid air was ensured by a fan. Gas flow rate and velocity in the cell were controlled by adjusting the speed of the fan. A control system allowed setting the gas temperature and vapour pressure. Water vapour was generated continuously in the steam generator and injected into the closed loop through a control valve. The pressure was maintained slightly above atmospheric pressure using a pressure control valve. The cell was an opaque aluminium cylinder. The inside diameter and the length of the cell were approximately 0.18 and 0.32 m respectively.

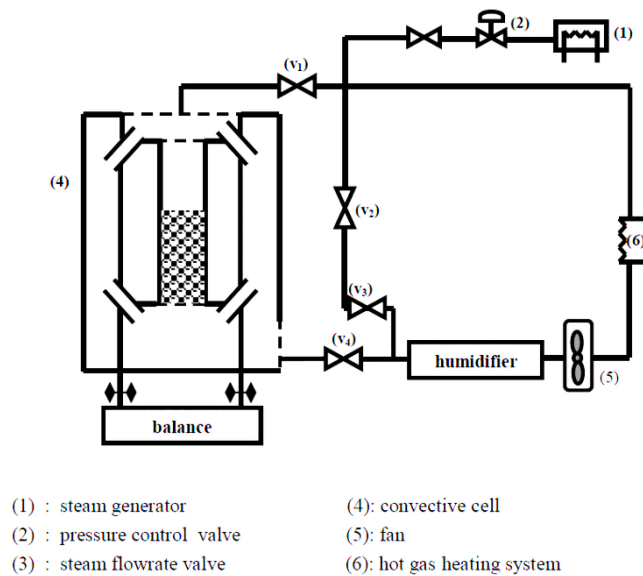


**Figure 3.5** Experimental device [56]

Humid air flowed through the cell containing the packed bed of alumina particles. At the inlet of the cell, a grid ensured a good distribution of humid air. Thermocouples of K-type were placed at different positions in the bed to measure the temperature of the alumina beads [56].

During the packing of the bed in the experimental cell, thermocouples were introduced into the bed at the particle surface in different axial positions. Meanwhile, the experimental equipment was heated to a desired experimental temperature and the steam generator was activated. Steady-state conditions were reached. Then the experimental cell was inserted. The data acquisition system was started immediately after closing the cell door, with continuous measurement of the alumina temperatures at different depths in the bed. The experiment was ended when the alumina particle temperature approached the gas temperature.

### *Gas-to-particle heat transfer performance*

The temperature of the particle surface that is necessary to quantify the heat transfer can be conveniently described in terms of the gas-to-particle heat transfer coefficient [56]. Based on experimental temperature measurements obtained in this work, a simple model was developed considering a steady-state energy balance and assuming the following [56]: i) that the granular medium was homogeneous and isotropic, ii) that the bed porosity was uniform, iii) that the operation was adiabatic, iv) that the bed was considered as a two-phase mixture (solid and gas) [55]. The packed bed was a discontinuous granular medium made of spherical porous particles (solid phase) crossed by humid air (gas phase). Energy balances were made in a bed portion whose height and cross-section were respectively  $dz$  and  $S_0$  as shown in Fig. 3.6.

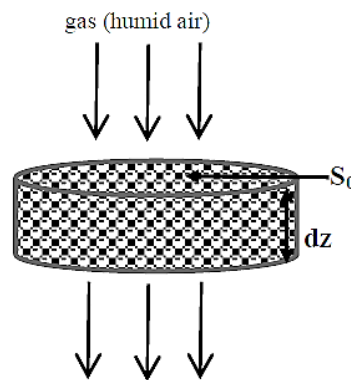


**Figure 3.6** Packed bed section

The solid phase internal energy ( $U_s$ ) is related to the evaporation rate,  $\dot{m}$ , and the gas temperature through applying the conservation of energy [56] in both regions:

$$\frac{dU_s}{dt} = -\dot{m}C_{pg} \frac{dT_g}{dz} dz \quad (3.14)$$

where  $C_{pg}$  and  $T_g$  are the gas specific heat and gas temperature respectively.

For the gas phase, the energy balance is:

$$\dot{m}C_{pg} \frac{dT_g}{dz} = h(T_b - T_g) \frac{dS_b}{dz} \quad (3.15)$$

$h$  is the gas-to-particle heat transfer and  $S_b$  is the total surface area of the particles.

For spherical particles:

$$S_b = \frac{6(1 - \varepsilon)S_0z}{d_p} \quad (3.16)$$

$\varepsilon$  is the porosity and  $d_p$  is the particle diameter. By replacing Eq. (3.14) by Eq. (3.15):

$$\frac{dU_s}{dt} = -h(T_b - T_g) \frac{dS_b}{dz} dz \quad (3.17)$$

Integrating results:

$$\ln \left[ \frac{T_b - T_g}{T_{b0} - T_g} \right] = - \frac{h(1 - \varepsilon)S_0H}{MC_{ps}d_p} t \quad (3.18)$$

$T_{b0}$ ,  $M$ ,  $H$  and  $C_{ps}$  are initial bed temperature, bed weight, bed height and solid specific heat respectively. This equation indicates that a plot of the logarithmic temperature  $\ln((T_b - T_g)/(T_{b0} - T_g))$  versus time should present a straight line with a slope equal to  $h(1 - \varepsilon)S_0H/MC_{ps}d_p$  [56]. The value of  $h$  is obtained from the slope. Fig. 3.7 shows an example of the logarithmic temperature differences versus time for different values of gas velocity. As expected, a family of straight lines is produced. The determination of slopes of these lines leads to the measured heat transfer coefficient, and consequently, the experimental Nusselt number. Fig. 3.8 illustrates the relation between Nusselt and Reynolds numbers for the model developed in the study compared with correlations reported in the literature for a packed bed of spherical porous alumina particles [47, 57 and 58]. It can be seen that a general correlation relating Nusselt number with Reynolds number for different materials with a wide range of physical and transport properties is not possible [56]. This can generally be observed in the literature where the correlation for the heat transfer coefficient of one author working with one material is often at variance with that of another author working with some other materials. In fact, the heat transfer coefficient depends both on the thermal properties of the bed and on the flux rate.

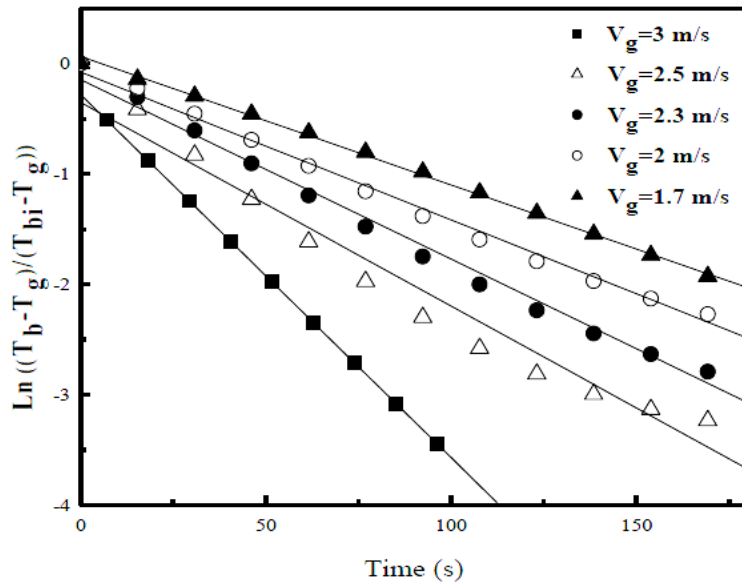


**Figure 3.7** Straight lines obtained from Eq. (3.18) [56]

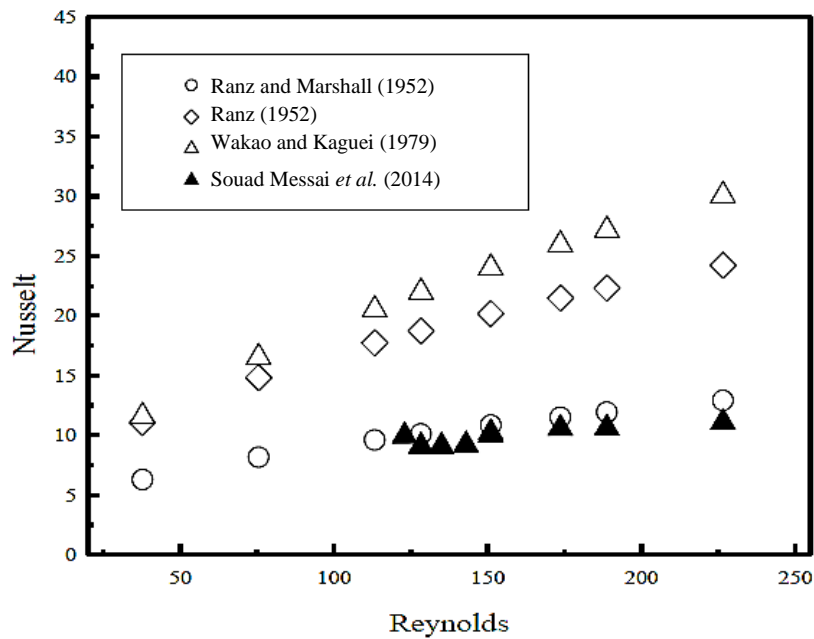


**Figure 3.8** Nusselt versus Reynolds numbers and compared with other works [56]

However, most experimental correlations express it as a function of the Reynolds number. Therefore, the applicability of these correlations is also limited to the particular bed materials used in developing them. Moreover, the thermal properties of the walls (adiabatic or heated) have a significant effect on the conduction mode, and therefore, studies using similar

experimental techniques but different bed materials can also be expected to yield different correlations relating the heat transfer coefficient to Reynolds numbers. A discrepancy of wall heat transfer coefficient values showed by [59] is caused by the non-uniform distribution of gas velocity, gas thermal conductivity, axial distribution of heat and errors in measurement. The correlations of Nusselt number used to validate the study give a  $Re \rightarrow 0$  asymptote of Nusselt equal to 2, which is reasonable for spherical particles. At low Reynolds number, the interfacial convection heat transfer is insignificant compared with other terms in the energy equation, and therefore, the suggested  $Re \rightarrow 0$  asymptote cannot be experimentally verified [11]. As explained above, there are discrepancies in the Nusselt number. This may also be due to some differences in experimental conditions (particle characteristics, height and diameter of the packed bed, boundary conditions). These discrepancies can also be attributed to the position of the thermocouples and errors in the measurement [60-61].

---

### Model 3: Jafarpur and Yovanovich, 1992 [62]

---

Jafarpur and Yovanovich developed a simple approximate analytical method based on a linearisation of the energy equation for the area mean Nusselt number for free convection heat transfer from isothermal spheres for the range of Rayleigh numbers  $0 < Ra < 10^8$  and all Prandtl numbers [62]. In the process of linearisation, the energy equation is reduced to the form of the transient heat conduction equation for which the solution exists. Comparison of the final correlation of Nu against Ra (which is an explicit form of linear superposition of the diffusive limit and boundary layer solution) with other correlations and experimental air data reveals very good agreement with a maximum difference of less than 5% [62].

The study adopted a simple analytical method based on linearisation of the energy equation as well as the usual assumptions made for natural convection problems, i.e. the boundary layer and Boussinesq approximations [62]. In the process of linearisation, the energy equation is reduced to the form of the transient heat conduction equation. These simplifications make otherwise intractable equations amenable to analysis and open a new door to the solution of external natural convection problems [62].

### *Theoretical Analysis*

In processes dealing with free convective heat transfer, the temperature field is linked with the flow; therefore, the non-linear momentum and energy equations are coupled through the

variation of the density [62]. To allow a more convenient procedure for obtaining approximate solutions to these non-linear, coupled governing equations, several simplifying assumptions and various approximation schemes have been used. Boussinesq and boundary layer approximations, as mentioned earlier, are the two widely used simplifying approximations in modelling natural convection heat transfer [62].

***Linearisation of energy equation***

Jafarpur and Yovanovich considered an isothermal sphere of temperature,  $T_s$ , and diameter,  $d_p$ , which was immersed in an extensive quiescent medium at constant temperature,  $T_s$ , [62] as shown in Fig. 3.9. For this time-steady, small-scale problem with zero heat generation and relatively large temperature difference, the Eckert number is taken as zero. The simplified constant property energy equation Eq. (3.19) in the spherical coordinate system  $(r, \theta, \varphi)$  is written as follows:

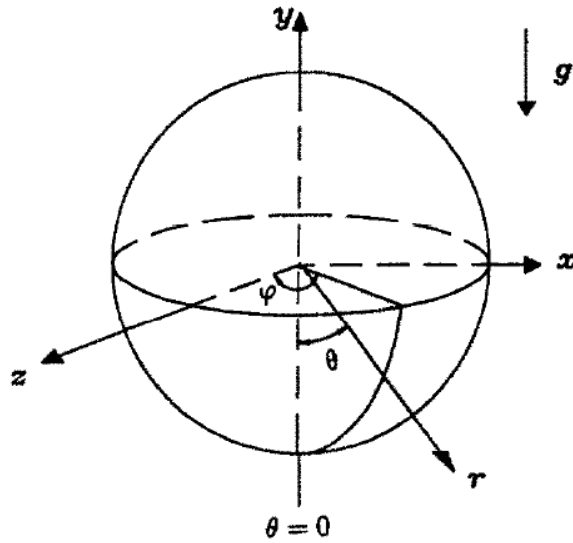


**Figure 3.9** Spherical polar coordinate system [62]

$$\rho c_p \left[ v_r \frac{\partial T}{\partial r} + \frac{v_\theta}{r} \frac{\partial T}{\partial \theta} + \frac{v_\varphi}{r \sin \theta} \frac{\partial T}{\partial \varphi} \right] = k \left[ \frac{1}{r^2} \frac{\partial}{\partial r} \left( r^2 \frac{\partial T}{\partial r} \right) + \frac{1}{r^2 \sin \theta} \frac{\partial}{\partial \theta} \left( \sin \theta \frac{\partial T}{\partial \theta} \right) + \frac{1}{r^2 \sin^2 \theta} \frac{\partial^2 T}{\partial \varphi^2} \right] \quad (3.19)$$

Neglecting conduction in the  $\theta$ -direction, and using the equation,

$$\frac{\partial T}{\partial \varphi} = \frac{\partial^2 T}{\partial \varphi^2} = 0 \quad (3.20)$$

due to the symmetry of the problem, the above energy equation is now expressed by Eq. (3.21):

$$\rho c_p \left[ v_r \frac{\partial T}{\partial r} + \frac{v_\theta}{r} \frac{\partial T}{\partial \theta} \right] = k \left[ \frac{1}{r^2} \frac{\partial}{\partial r} \left( r^2 \frac{\partial T}{\partial r} \right) \right] \quad (3.21)$$

The two terms on the left-hand side of Eq. (3.21) are further approximated by a single equivalent term,  $(V_e/r)(\partial T/\partial \theta)$ , where  $V_e$  is some constant effective velocity yet to be determined [62]. Therefore, the **Linearised energy equation** is written as shown in Eq. (3.22):

$$\rho c_p \frac{V_e}{r} \frac{\partial T}{\partial \theta} = k \left[ \frac{1}{r^2} \frac{\partial}{\partial r} \left( r^2 \frac{\partial T}{\partial r} \right) \right] \quad (3.22)$$

in the region;  $r \geq \frac{d_p}{2}$ ,  $0 \leq \theta \leq \pi$ ,

#### ***Transient conduction-type equation and its solution***

For large Grashof numbers ( $Gr > 10^4$ ), heat transfer occurs in a thin boundary layer [62], therefore,  $r$  in the term appearing on the left-hand side of Eq. (3.22) can be approximated by  $d_p/2$ , thermal diffusivity,  $x = d_p \theta/2$ , distance along the surface from the stagnation point, and  $t = x/V_e = d_p \theta/2V_e$  the effective particle residence time. The Linearised energy equation, Eq. (3.22), can therefore be written as Eq. (3.23):

$$\frac{1}{\alpha} \frac{\partial T^*}{\partial t} = \frac{1}{r^2} \frac{\partial}{\partial r} \left( r^2 \frac{\partial T^*}{\partial r} \right) \quad (3.23)$$

where,  $r \geq d_p/2$ ,  $0 \leq t \leq \pi d_p/2V_e$

$T_\infty$  is the temperature at a point far from the body and  $T^*$  is the dimensionless temperature rise,  $(T - T_\infty)/(T_s - T_\infty)$ . The solution to Eq. (3.23) is given in Eq. (3.24):

$$T^* = \frac{d_p}{2} \frac{1}{r} \operatorname{erfc} \left( \frac{r - \frac{d_p}{2}}{2\sqrt{\alpha t}} \right) \quad (3.24)$$

This consists of the linear superposition of the steady-state solution,  $d_p/2r$ , and the transient solution. The local Nusselt number,  $Nu_{d_p}(\theta)$ , defined as  $h(\theta)d_p/k$ , is related to the local wall heat flux and the overall temperature rise as expressed by Eq. (3.25):

$$Nu_{d_p}(\theta) = \frac{q_s d_p}{(T_s - T_\infty)k} \quad (3.25)$$

The wall heat flux,  $q_s''$ , is determined from the Fourier rate equation

$$q_s'' = -k(T_s - T_\infty) \left. \frac{\partial T^*}{\partial r} \right|_{r=d_p/2} \quad (3.26)$$

which gives

$$q_s'' = \frac{k(T_s - T_\infty)}{d_p/2} + \frac{1}{\sqrt{\pi}} \frac{k(T_s - T_\infty)}{\sqrt{\alpha t}} \quad (3.27)$$

The wall heat flux, Eq. (3.27), consists of the linear sum of two asymptotes: the steady-state value and the transient solution for a half-space. Substituting for  $q_s$  in Eq. (3.25), and setting  $t = d_p\theta/2V_e$ , one obtains the local Nusselt number expressed by Eq. (3.28):

$$Nu_{d_p}(\theta) = 2 + \sqrt{\left(\frac{2}{\pi}\right)} \sqrt{\left(\frac{d_p V_e}{\alpha \theta}\right)} \quad (3.28)$$

Thus, the area-averaged Nusselt number,  $Nu_{d_p} = \frac{1}{2} \int_0^\pi Nu_{d_p}(\theta) \sin\theta \, d\theta$ , becomes:

$$Nu_{d_p} = 2 + 0.714 \sqrt{\left(\frac{d_p V_e}{\alpha}\right)} \quad (3.29)$$

It is worthwhile noting that Eq. (3.29), at this point, is applicable to both forced and free convection heat transfer [62]. This, of course, depends on the type of transformation equation to be used for the effective velocity,  $V_e$ . The equation for the effective velocity applicable to all Prandtl numbers is obtained using the Churchill and Usagi [63] blending technique and is expressed by Eq. (3.30):

$$V_e = \frac{\frac{v}{d_p} (Gr_{d_p}/2Pr)^{1/2}}{\left[1 + \left(\frac{0.5}{Pr}\right)^{n/2}\right]^{1/n}} \quad (3.30)$$

where a value of 9/8 can be used for  $n$  as recommended by Churchill and Chu [53] for their  $f(Pr)$ . Substituting the effective velocity of Eq. (3.30) into Eq. (3.29), the area-averaged Nusselt number,  $Nu$ , becomes:

$$Nu_{dp} = 2 + \frac{0.600Ra_{dp}^{1/4}}{\left[1 + \left(\frac{0.5}{Pr}\right)^{9/16}\right]^{4/9}} \quad (3.31)$$

Finally, in Fig. 3.10, the predictions of free convective heat transfer based on Eq. (3.31) are compared with the results of correlation [64] as well as [65] quasi-steady-state experimental air data. The comparison reveals that the results of the Jafarpur and Yovanovich study are in very good agreement with the experimental data with a maximum difference of 4.3% (which is within the maximum error bounds of the experimental data, reported as 6% [65] and r.m.s of the differences of 0.25).

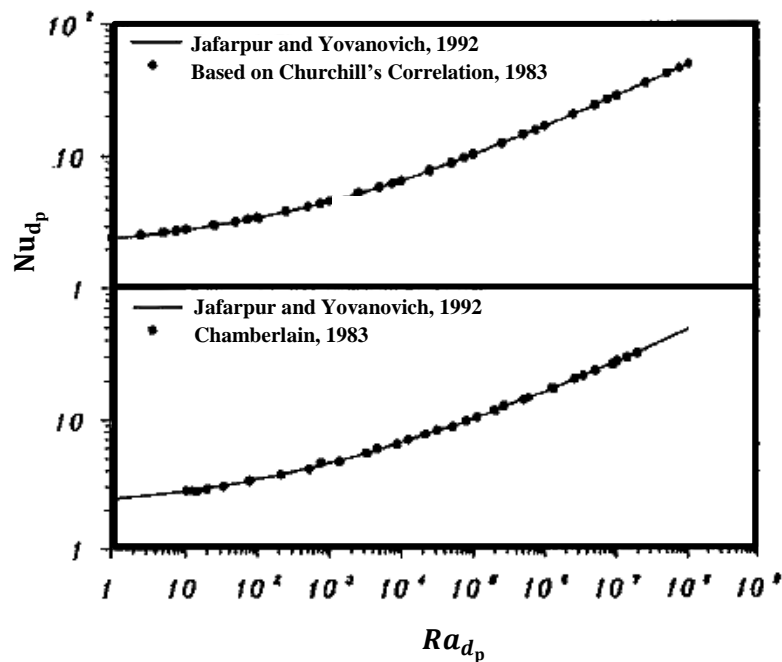


**Figure 3.10** Comparison of the [62] results with other correlations

Model 4: Ichimiya, 1999 [67]

The author proposes a new method to estimate the heat transfer between fluid gas and solid material in a porous medium [67]. In the first stage, the local Nusselt numbers on the heated wall of a flow passage in a porous medium are numerically obtained in advance for the heat

transfer parameter,  $H_a$ , including the volumetric heat transfer coefficient,  $h_v$ , between the fluid and the solid material in a porous medium. In the second stage, the experimental Nusselt numbers on the heated wall are obtained by measuring wall temperatures and heat flux. The volumetric heat transfer coefficient,  $h_v$ , is evaluated by comparing experimental Nusselt numbers with numerical ones [67]. This method also gives the longitudinal characteristics of the heat transfer in a porous medium.

In the new method proposed to evaluate the heat transfer between solid and fluid in a porous medium, the flow field in a porous medium is first analysed in a two-dimensional system [67]. The results are then applied to the energy equation that includes the heat transfer coefficient,  $h$ , between solid and fluid. The volumetric heat transfer coefficient,  $h_v$ , is obtained by comparing the numerical and experimental values of heat transfer on a heated wall of a flow passage without directly measuring the solid and fluid temperatures in a porous medium [67].

### ***Description of the Problem***

The fine structure of a porous medium is very complex. Therefore, the temperatures of solid and fluid cannot be directly measured with sufficient accuracy. In the study by Ichimiya [67], a new method that does not include directly measuring the temperatures of solid and fluid is proposed. This method is based on thermally non-equilibrium convection in a porous medium. In brief, there is a temperature difference between solid and fluid in a porous medium. In the first stage, the flow field in a porous medium and the energy equation including the heat transfer parameter between solid and fluid  $H_a (= h_v y_o^2 / k_a)$  are solved numerically to obtain the Nusselt number on the heated wall of a flow passage. In the next stage, Nusselt numbers on the heated wall are experimentally obtained by measuring the heated wall temperatures. The parameter,  $H_a$ , is determined by adjusting  $H_a$  so that the numerical Nusselt number becomes equal to the experimental one, and the volumetric heat transfer coefficient,  $h_v$ , is evaluated.

Fig. 3.11 shows a two-dimensional model. A parallel plate duct with height,  $y_o$ , is filled with a porous medium of constant porosity along flow direction,  $1 = 10y_o$  (solid lines in Fig. 3.11). Both the upper and lower walls of the duct are heated uniformly (heat flux,  $q''$ ). The working fluid (air in the present case), uniform in temperature, runs into the flow passage. The velocity at the entrance has a fully developed laminar flow distribution.

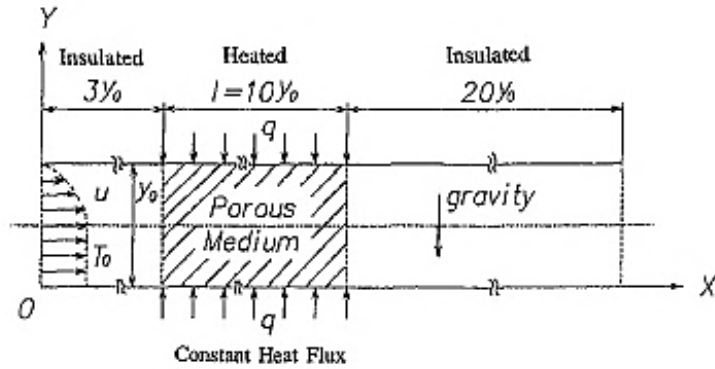


**Figure 3.11** Two-dimensional model [67]

The fluid is released into the atmosphere after achieving fully developed flow conditions after a length of  $20y_0$  from a porous medium. The Nusselt numbers on the heated wall are then compared with numerical values. The flow in a porous medium is assumed to be a non-Darcian flow including the Brinkman viscous term and Forchheimer inertia term [68], [38] to apply this method over a wide range. When the Darcy flow method is applied, both terms in the momentum equation are neglected. The flow velocity is less than sonic velocity and the temperature low enough in order to neglect the effect of thermal radiation; it is also assumed that the flow is steady, laminar and incompressible.

### **Numerical Calculation**

In the numerical calculation, the governing equations of the flow and the energy are written in dimensionless form with the following parameters:

$$\begin{aligned}
 X &= x/y_0, \quad Y = y/y_0, \quad Z = z/y_0, \quad U = u/u_m, \\
 V &= v/u_m, \quad \Psi = \psi/u_m y_0, \quad \Omega = w y_0/u_m \\
 H_a &= h_v y_0^2/k_a, \quad H_p = h_v y_0^2/k_p \\
 \Theta_{a,p,w} &= (T_{a,p,w} - T_a)/(q'' y_0/k_o), \quad Re = 2u_m y_0/v \\
 Pr &= c_p \mu_a/k_a, \quad Gr = g \beta y_0^3 (q'' y_0/k_a)/v^2, \\
 Nu &= 2q'' y_0/\{k_a(T_w - T_o)\}, \quad Da = k/y_0^2,
 \end{aligned} \tag{3.32}$$

Although the porous diameter may be better as a characteristic length, the heat source for convection is the wall of the flow passage. Therefore, the width of the flow passage,  $y_0$ , is used

as a characteristic length. The dimensionless parameters,  $H_a$  and  $H_p$ , are introduced as parameters of the volumetric heat transfer coefficient. The physical meaning of  $H_a$  is a kind of volumetric Nusselt number between solid and fluid (air) in a porous medium. On the other hand, the physical meaning of  $H_p$  is a kind of volumetric Biot number for a solid in a porous medium. The flow equation based on a non-Darcian flow as described in "Description of the Problem" is expressed in Eq. (3.33):

$$\begin{aligned} \frac{1}{\varepsilon^2} \left( \frac{\partial \Psi}{\partial Y} \frac{\partial \Omega}{\partial X} - \frac{\partial \Psi}{\partial X} \frac{\partial \Omega}{\partial Y} \right) - \frac{2}{\varepsilon Re} \left( \frac{\partial^2 \Omega}{\partial Y^2} + \frac{\partial^2 \Omega}{\partial X^2} \right) + \frac{2\Omega}{DaRe} \\ + \frac{C}{Da^{0.5}} \left[ \frac{\partial}{\partial X} \left\{ \left| \frac{\partial \Psi}{\partial X} \right| \left( -\frac{\partial \Psi}{\partial X} \right) \right\} - \frac{\partial}{\partial Y} \left\{ \left| \frac{\partial \Psi}{\partial Y} \right| \left( \frac{\partial \Psi}{\partial Y} \right) \right\} \right] - \frac{4Gr}{Re^2} \frac{\partial \Theta_a}{\partial X} = 0 \end{aligned} \quad (3.33)$$

The coefficient  $C$  in Eq. (3.33) is expressed as the following equation given by (Ergun, 1952):

$$C = (1.75/\sqrt{175})\varepsilon^{-1.5} \quad (3.34)$$

This constant, obtained on the assumption that a small particle bed is a porous medium, is applied to  $10 < U_m D_p / [v(1 - \varepsilon)] < 2000$  in which  $D_p$  is the hydraulic diameter of a particle. The parameter  $U_m D_p / [v(1 - \varepsilon)]$  of a porous medium used in the heat transfer experiment is 133 for  $Re = 300$ . This satisfies the region applicable to Eq. (3.34). Energy equations including the heat transfer between fluid and solid material are applied to each fluid and solid material in a porous medium.

For a fluid section,

$$\frac{\partial \Psi}{\partial Y} \frac{\partial \Theta_a}{\partial X} - \frac{\partial \Psi}{\partial X} \frac{\partial \Theta_a}{\partial Y} - \frac{2\varepsilon}{RePr} \left( \frac{\partial^2 \Theta_a}{\partial X^2} + \frac{\partial^2 \Theta_a}{\partial Y^2} \right) + \frac{2H_a}{RePr} (\Theta_a - \Theta_p) = 0 \quad (3.35)$$

For a solid section,

$$(1 - \varepsilon) \left( \frac{\partial^2 \Theta_p}{\partial X^2} + \frac{\partial^2 \Theta_p}{\partial Y^2} \right) - H_p (\Theta_a - \Theta_p) = 0 \quad (3.36)$$

The dimensionless boundary conditions are as follows:

At the entrance of the flow passage:  $U = -6Y^2 + 6Y$ ,  $V = 0$ ,  $\Theta = 0$

on the wall:  $U = 0$ ,  $V = 0$

on the unheated wall:  $\partial \Theta_a / \partial Y = 0$

on the heated wall:  $\partial \Theta_a / \partial Y = (\lambda_p / \lambda_a) (\partial \Theta_p / \partial Y) = 1$  or  $-1$

at the exit of a flow passage:  $\partial U/\partial X = 0$ ,  $V = 0$ ,  $\partial \theta_a/\partial X = 0$

Numerical calculations are made for the following conditions: the Reynolds number,  $300 \leq Re \leq 600$ ; the heat transfer parameter between fluid and solid,  $100 \leq Ha \leq 50,000$ ; the thermal conductivity ratio,  $RRM = 154$ , which corresponds to the experiment; the Darcy number,  $Da = (2.44 \sim 14.8) \times 10^{-5}$ ; and porosity,  $\varepsilon = 0.87$ . The numerical result is evaluated with the Nusselt number  $Nu$  on the wall of the flow passage defined by Eq. (3.37):

$$Nu = 2q''y_o / [k_a(T_w - T_o)] = \frac{2}{\left[ (T_w - T_o) / \frac{q''y_o}{k_a} \right]} = 2/\Theta_w \quad (3.37)$$

### Heat Transfer Experiment

Fig. 3.12 shows the experimental apparatus corresponding to the model (Fig. 3.11). The properties of the porous medium used are listed in Table 3.2. It was made of alumina-ceramic foam ( $2MgO \cdot 2Al_2O_3 \cdot 5SiO_2$ ) with various porous diameters, permeabilities and Darcy numbers for almost constant porosity  $\varepsilon = 0.87$ .

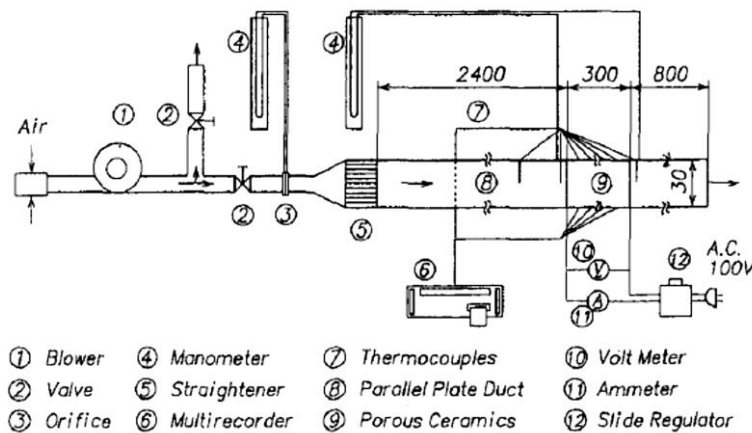


**Figure 3.12** Experimental apparatus [67]

The complex cell and matrix structure (Fig. 3.11) caused the difference in the local heat transfer. In the first stage, it was recognised that the numerical heat transfer without a porous medium [69] agreed with experimental values within 3%. In the next stage, the experiment with a porous medium was performed for  $Re = 300$  and  $600$ .

**Table 3.2** Porous medium [67]

	d (mm)	k (m <sup>2</sup> ) × 10 <sup>8</sup>	ε (%)	Da × 10 <sup>5</sup>
Porous Medium 1	1.3	2.193	87.5	2.44
Porous Medium 2	2.0	3.779	87.0	4.20
Porous Medium 3	4.2	13.324	87.3	14.8

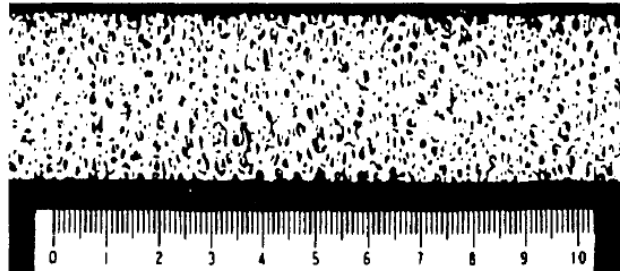


**Figure 3.13** Photograph of Porous Medium [67]

Fig. 3.14(a), (b) and (c) illustrate the numerical Nusselt numbers by solid and broken lines as a parameter of  $H_a$  and the experimental values by solid circles. Fig. 3.14(a) presents the Nusselt numbers for  $d = 1.3$  mm,  $Da = 2.44 \times 10^{-5}$ , and  $Re = 300$ . According to the figure, experimental values agree well with numerical ones for  $H_a = 500$  along the flow direction.

However, in a higher Reynolds number (Fig. 3.14(b),  $Re = 600$ ), the experimental values exceed the numerical ones at the first half and lower at the latter half compared with Fig. 3.14(a). The behaviour of  $H_a$  corresponding to those experimental values is similar to that of the Nusselt numbers described above. When the porous diameter increases (Fig. 3.14(c),  $d = 4.2$  mm),  $H_a$  tends to increase at the latter half. It is recognised that Nusselt numbers on the heated wall and  $H_a$  have a relation to each other. This means that the physical variation in a porous medium affects the heat transfer on the heated wall of a flow passage.

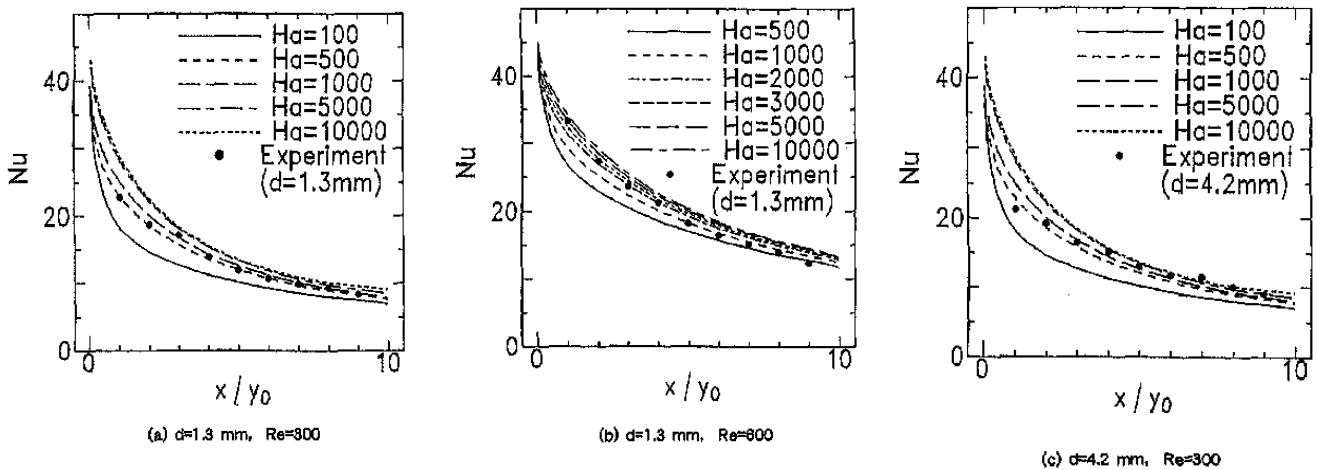


**Figure 3.14.** Longitudinal Nusselt number (a)  $d = 1.3$  mm,  $Re = 300$ ; (b)  $d = 1.3$  mm,  $Re = 600$ ; (c)  $d = 4.2$  mm,  $Re = 300$  [67]

Therefore, the longitudinal variation in the heat transfer between solid and fluid in a porous medium can be evaluated quantitatively corresponding to the local Nusselt numbers on the heated wall.

**Model 5: Adeyanju and Manohar, 2009 [70]**

Adeyanju and Manohar carried out a review of heat transfer in packed beds with the emphasis on both experimental and theoretical techniques [70]. They observed that the two major modes of heat transfer, namely conduction between the particles in the bed and convection between the flowing fluid and the particles, interact with each other. Moreover, at elevated temperatures, heat transfer by radiation will also be an important mode [70]. In many industrial applications, it is found that two or more of the modes mentioned above take place simultaneously. The interaction among the different modes is one of the main reasons for the difficulty in correlating the total heat transfer and analysing the experimental data in this field [70]. Fig. 3.15 depicts the schematic illustration of the modes: (1) wall-to-fluid convection, (2) particle-to-fluid convection, (3) wall-to-particle conduction, (4a) radial particle-to-particle conduction, (4b) axial particle-to-particle conduction, (5a) radiant heat transfer between particles, (5b) radiant heat transfer between wall and particles, (5c) radiant heat transfer between fluid and particles, (6) heat transfer by mixing of the fluid. The fourth mode, namely the conduction between the particles, can be further subdivided into axial and radial directions. In the design of

the packed bed for the thermal storage application, the Biot number should also be kept as low as possible so that the thermal resistance in the solid does not become dominant.

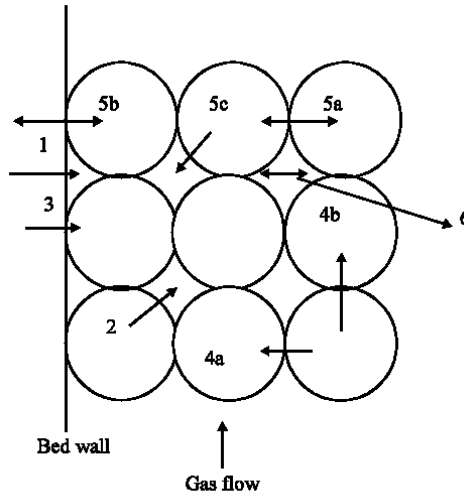


**Figure 3.15** Modes of heat transfer in packed beds [70]

### *Theoretical Investigation*

The first referenced and cited research on heat transfer in packed beds in most studies was by [71]. A number of simplifying assumptions were made by [71] in the process of solving the heat transfer equations for incompressible fluids passing uniformly through a bed of solid particles with perfect conductivity. The derived heat transfer equations are as follows:

$$\frac{(T_s - T_{s,0})}{(T_{f,0} - T_{s,0})} = 1 - e^{-Y-Z} \quad (3.38)$$

$$\sum Y^n M^n(yz) = e^{-Y-Z} \sum Z^n M_n \quad (3.39)$$

$$\frac{(T_f - T_s)}{(T_{f,0} - T_{s,0})} = 1 - e^{-Y-Z} \quad (3.40)$$

$$\sum Y^n M^n(yz) = e^{-Y-Z} \sum Z^n M_n(yz) \quad (3.41)$$

where  $T$  is the temperature (of fluid and solid),  $Y$  and  $Z$  are dimensionless quantities. The solutions of these equations were presented in graphical form, called Schumann curves [70]. Thus, to evaluate the volumetric coefficient of heat transfer using these curves, it is only

necessary to measure exit air temperature and the bed temperature. These curves could be used to evaluate the heat transfer coefficient for a given packed bed exchanging heat with a fluid provided that certain simplifying assumptions made by [71] are satisfied. Schumann's curves were extended by [72] to a wider temperature range. An empirical relation was postulated by [72] for the evaluation of the heat transfer coefficient thus:

$$h_v = \frac{AG^{0.7}T^{0.3}10^{(1.68\varepsilon+3.56\varepsilon^2)}}{d_p^{0.9}} \quad (3.42)$$

where  $h_v$  is the volumetric heat transfer coefficient,  $A$  is the constant dependent on the bed material,  $T$  is the average air temperature, the particle diameter  $d_p$ , the porosity  $\varepsilon$ , and  $G$  is the air mass flow rate. Correlations derived by [72] through the application of dimensional analysis were used to calculate heat transfer coefficient. However, this research was limited to spheres and cannot directly be applied to other geometries of solid particles. Another correlation was presented by [73] for evaluating the heat transfer coefficient between a gas and randomly packed solid spheres. Using the Colburn  $j$ -factor, the correlation was given as:

$$j_H = 0.23/Re_p^{0.3} \quad (3.43)$$

where

$$j_H = St.Pr^{2/3}$$

$$200 < Re_p < 50000 \text{ and } 0.37 < \varepsilon < 0.39$$

The heat transfer between air and packed bed of granitic gravel was investigated by [74]. Unsteady state heat transfer coefficients were correlated with the air mass velocity and particle diameter to obtain the equation:

$$h = 0.652(G/d_p)^{0.7} \quad (3.44)$$

This was evaluated for  $8mm < d_p < 33mm$ ;  $50 < Re_p < 500$  and temperature range of 311 – 394K. It was concluded that the temperature of the entering air had no appreciable effect on the coefficient.

The heat transfer coefficient between smooth spheres of low thermal conductivities and fluids (air and carbondioxide) in packed beds and tubes with diameter of 50.8 and 6.4mm respectively was determined by [75]. The ratio of particles to tube diameters varied from 0.082 – 0.27. Gas

flow rate was of Reynolds number 250 – 3000. The correlation of film heat transfer coefficient was found to be best described by:

$$h = 3.50(k/D_t)e^{-4.6D_p/D_t}(D_p G/\mu)^{0.7} \quad (3.45)$$

by approximation, this reduced to:

$$h = 0.4(k/D_t)(D_p G/\mu)^{0.7} \quad (3.46)$$

or

$$Nu = 0.4Re^{0.7} \quad (3.47)$$

Maximum film coefficient was predicted and verified at a value of  $D_p/D_t$  of 0.153. The dynamic behaviour of beds undergoing heat exchange with air using single and two-phased modes was studied by [76] and [77]. By incorporating factors of axial bed conduction and intra-particle resistance, which [71] ignored, the heat transfer coefficients were evaluated and found to be  $(1 + Bi/5)$  times smaller than those predicted using Schumann curves. [78], [79], [80], [81], [82] and [83] have all worked on various packed beds using air and other gases as fluids and developed correlations involving the heat transfer coefficient. Extensive review of this work was carried out by [84] and [85] and results were compared.

Table 3.3 summarises the experimental conditions, proposed correlations, range of parameters, etc. of the many investigations which were reviewed [70]. Two parameters, the effective or apparent conductivity,  $k$ , and the total heat transfer coefficient,  $h$ , are commonly used to express the heat transfer rates in packed beds [70]. The effective thermal conductivity is an averaged parameter that describes the total thermal performance of the granular medium that constitutes the bed. In other words, the effective conductivity is the conductivity the medium would have were it homogeneous. It should be noted that the effective conductivity is not the same as the conductivity of the material that constitutes the bed. The effective conductivity depends both on the thermal properties of the bed and on the flow rate, but in most experimental correlations, it is generally expressed as a function of the Reynolds number only [70]. This implies that these correlations are valid only for the particular bed materials, which were used in developing them. The other preferred parameter to describe the thermal performance of a packed bed is the total heat transfer coefficient,  $h$ , which is also an average parameter [70]. The total heat transfer coefficient generally incorporates the conduction mode between the bed particles, the convection mode between the bed particles and the flowing

medium, the wall-to-bed conduction and the wall-to-fluid convection. The last two modes can be expected to occur when the walls of the bed are maintained at isothermal conditions [70].

As in the case of the effective conductivity, the total heat transfer coefficient also depends both on the thermal properties of the bed and on the flow rate, but most experimental correlations express it (in dimensionless form) as a function of Reynolds number only [70]. Therefore, the applicability of these correlations is also limited to the particular bed materials used in developing them. The commonly used dimensionless numbers for expressing it are the Colburn  $j$ -factor and the Nusselt number. They are defined as:

$$jh_t = \frac{h_t}{C_{pf}G_f} (Pr_f)^{2/3} \quad (3.48)$$

$$Nu_t = \frac{h_t d_p}{k_f} \quad (3.49)$$

Depending on the experimental technique, it is expected that different modes of heat transfer will contribute to the total heat transfer [70]. For example, in transient experiments performed in beds with adiabatic walls, the modes that contribute are axial conduction and convection between the bed and the fluid. On the other hand, in beds that have heated walls, the significant modes are wall-to-bed and wall-to-fluid heat transfer in addition to the radial conduction and the bed-to-fluid convection. Therefore, depending on the contributing modes, the experimentally obtained correlations relating the total heat transfer rates to the Reynolds number can be expected to show wide variation. Moreover, the thermal properties of the bed have an effect on the conduction mode, and therefore, studies using similar experimental techniques but different bed materials can be expected to yield different correlations relating the heat transfer rates to the Reynolds number.

**Table 3.3** Experimental review of packed beds heat transfer [54]

Authors	System	Reynolds no. range, ( $Re_p$ )	Type of heating	Correlation proposed	Remarks
Balakrishnan and Pei (1974)	Commercial catalyst formulations; (alumina based spheres and cylinders)	300-400	Micro wave heating	$(jh)_p = 0.018 (Fr_{pm})^{-0.5} \times \phi_p^{3.76}$	Use of microwave heating results in uniform temperature throughout the bed eliminating thermal gradients in solid phase and therefore particle conduction. Convective effects truly determined
Baumeister and Bennet (1958)	Air-steel	200-10400	Electrical induction (steady state)	$Jh = 1.09 Re_p$	The bed consisted of 4in. internal diameter. Transite cylinder and the packing 0.155, 0.2495 and 0.3745 in diameter high carbon-chrome alloy steel. The heat transfer, therefore, consists of axial conduction as well as fluid-particle modes.
Bradshaw and Myers (1963)	Air-celite cylinders, etc.	300-2500	Water soaked packing's dried by air at room temp.	$Jh = 2.52 (Re_{pm})^{0.5}$	Data are based on drying experiments. Assumption of constant surface temperature of all the particles is debatable.
Bunnell <i>et al.</i> (1949)	Air-alumina	30-150	Heated airbed wall maintained at boiling point of water	$K_{er}/k_{er} = 5.0 + 0.061 Re_p$	Entering air at 400°C cooled by boiling water-jacket at the walls. $K_{er}$ rad. is therefore, effective radial conductivity. Solid and gas temperatures are claimed to be identical, which is a questionable statement. Bed consisted of 0.125in. diameter alumina cylinders
Coberly and Marshall (1951)	Air-celite	70-300	Steam-heated wall	$K_{er} = 0.018 + 0.00098 Re_p$ (Dimensional equation in British units. Multiply $k_{er}$ obtained from equation by 1.730735 to convert to J/msK)	The gas inlet and outlet and radial and axial temp. have been measured with high response thermo couples. The experimental technique would seem to indicate considerable axial conduction, which has been ignored in the analysis.
Colburn (1931)	Air pebbles, granules, pellets, porcelain balls, etc	G:1-9	Steam-jacketed packed tube	$h = 8a C_p v^{0.2} G^{0.83}$ $a = f(D_p/D_i)$ (Multiply h obtained from equation by 5.678264 to get SI units.)	This study relates to the rate of heat transfer from the wall to the fluid flowing in the packed bed. One of the earliest (1931) studies, it does not consider the gradients within the bed.
De Acetis and Thodos (1960)	Air-catalyst spheres	6.71-1000	Water soaked particle dried by air at rooms temp.	$Jh = 1.1 / (Re_p^{0.41} - 0.15)$	The usual assumption of uniform temp. at the surface of the bed particles, being the wet bulb temp. is used. This could be wrong and the source for the breakdown of the heat and mass transfer analogy.
Eichom and White (1952)	Air + Co <sup>2</sup> and divinyl benzene	58-374	r.f heating	-	Transient temp. measurements are made. While, a constant temperature may be achieved during steady- state measurements resulting in pure fluid-particle mode, during the cooling cycle particle-particle heat transfer will be significant.
Furnas (1930)	Air-iron spheres	120-1200	Heated air	$h = 6.91 \times 10^{-3} \times G_r^{0.75} \times t_r \times G - 1.56$ (Multiply by 5.678264 to get h in SI units)	One of the earlier investigations (1930), temp. of both solids and gases were measured. Test section was 15 cm diameter and 105 cm high, coated with Sil-O- Cel for insulation. Heat transfer therefore consisted of fluid-particle mode and particle-particle mode in axial direction.
Gamson <i>et al.</i> (1943)	air-celite spheres and cylinders	40-4000	Water-soaked packings dried by air	$Jh = 1.064 \times Re_p^{-0.41}$ $Re > 350$ $Jh = 18.1 \times Re_p^{-1.0}; Re_p < 40$	The assumption of wet bulb temperature as the constant surface temperature of the bed is debatable. If true the heat transfer consists of only fluid-particle mode.
Glasser and Thodos (1958)	Air-ceramic/ brass spheres	330-1500 300-4000	Transient heating by regeneration technique; steady-state heating by single electrically heated sphere	$Nu = 1.25 Re_p^{0.56}$ $300 < Re_p < 4000$	In the regenerative technique the surface temp. is quite different from the values at the center. The electrical heating method is perhaps much more accurate.
Gupta and Thodos (1962a)	Existing data	33-6500	Electrical heating of single sphere	$\epsilon jh = 0.0108 + 0.929/Re_p^{0.58} - 0.483$ $Re > 20$	Used existing data in the literature to obtain the correlation
Gupta and Thodos (1962b)	Air-celite spheres	95-2500	Water soaked particles dried by air	$\epsilon jh = 2.06/Re_p^{0.58}$	In this study, mass transfer rates are minimized so as to achieve the direct heat and mass transfer analogy.

**Table 3.3 (Continued)**

Authors	System	Reynolds no. range, ( $Re_p$ )	Type of heating	Correlation proposed	Remarks
Houghen and Piret (1951)	Air-celite spheres	193-2824	Heated air entering the bed	$K_s/C_p \mu = 3.7/\varepsilon \times (Re_p)^{1/3}$	The bed is cooled by water at 60°F. Therefore, there is a radial transport of heat in both phases. Air is flowing downward. $k_s$ values obtained are 20-100 times that of the fluid and 2-15 times that of solid.
Leva (1947)	Air-smooth spheres	500-3408	Heated wall	$h = 0.813k_f/D_i e^{-6(D_p/D_i)}, Re_p^{0.9}$ (Multiply $h$ by 5.678264 to get SI unit values)	Heat is transferred from wall to gases flowing in a packed tube. $D_p/D_i$ . Values ranged from 0.05-0.3. Maximum heat transfer occurred at $D_p/D_i = 0.15$
Leva and Grummer (1948)	Air-smooth spheres	500-3408	Heated wall	$h = 0.813k_f/D_i e^{-6(D_p/D_i)} Re_p^{0.9}$ (Multiply $h$ by 5.678264 to get SI unit values)	Extension of above work for non uniform beds arithmetic average of $D_p$ is used. Nominal $D_p$ for Raschig rings and $D_p$ of equal volume sphere for cylinders.
Leva <i>et al.</i> (1948)	Air-smooth spheres	250-3000	Heat air and $CO_2$ ; bed wall is cooled	$h = 3.5k_f/D_{ix} e^{-4.6(D_p/D_i)}, Re_p^{0.7}$ (Multiply $h$ by 5.678264 to get SI unit values)	Extension of earlier research by Leva. Different equation is obtained for cooling operations. Maximum heat transfer is at $D_p/D_i = 0.153$
Lindauer (1967)	Air-steel and tungsten	23-18200	Electrical resistance heating to produce sinusoidal gas temperature variations.		Cyclic temperature variations are used in the gas phase. This could cause temperature gradients in the solid phase leading up to the question, whether the measured values pertain to the gas-solid mode alone.
Plautz and Johnstone (1955)	Air-glass spheres	100-200	Steam heated wall; entering air at 85°C maintained by heating and cooling coils	$K_{er} = 0.439 + 0.00129 \times Re_p$ $hw = 0.09G_r^{0.75}$ [Multiply $k_{er}$ and $h$ obtained from correlation by 1.730735 and 5.678264, respectively, to get SI unit values.]	Reports both radial effective conductivity and wall transfer coefficient.
Wakao and Kato (1969)	Air-glass		Concentric carborundum electric heater	$K_s/k_f = (k_s/k_f)_{\text{het}} = 0 + 0.707 Nu_s^{0.96} (k_s/k_f)^{1.11}$	The effect of radiative heat transfer in conduction has been evaluated.
Yagi and Kunii (1957)	Air-iron, porcelain, cement clinker, fire brick and Raschig rings		Coaxial electric heater at the center; outside wall is insulated with fire brick.	$K_s/k_f = B + Re_p Pr_f/D$	Model agrees well with data at $Re_p \rightarrow 0$

**Model 6: Nield and Bejan, 2006 [12]**

Summaries of work compiled by Nield and Bejan start with a simple situation in which the medium is isotropic and radiative effects, viscous dissipation and the work done by pressure changes are negligible [12]. Initially, it was assumed that there was local thermal equilibrium so that  $T_s = T_f = T$ , where  $T_s$  and  $T_f$  were the temperatures of the solid and fluid phases respectively. Here, it is assumed that heat conduction in the solid and fluid phases takes place in parallel so that there was no net heat transfer from one phase to another. The fundamentals of heat transfer in porous media are also presented in [86], taking averages over an elemental volume of the medium.

For the solid phase:

$$(1 - \varepsilon)(\rho c)_s \frac{\partial T_s}{\partial t} = (1 - \varepsilon) \nabla \cdot (k_s \nabla T_s) + (1 - \varepsilon) q_s''' \quad (3.50)$$

and for the fluid phase:

$$\varepsilon(\rho c_p)_f \frac{\partial T_f}{\partial t} + (\rho c_p)_f \mathbf{v} \cdot \nabla T_f = \varepsilon \nabla \cdot (k_f \nabla T_f) + \varepsilon q_f''' \quad (3.51)$$

Here, the subscripts  $s$  and  $f$  refer to the solid and fluid phases respectively,  $c$  is the specific heat of the solid,  $c_p$  is the specific heat at constant pressure of the fluid,  $k$  is the thermal conductivity and  $q'''$  [W/m<sup>3</sup>] is the heat production rate per unit volume. In writing Eqs. (3.50) and (3.51), it is assumed that the surface porosity is equal to the porosity. This is pertinent to the conduction terms. For example,  $-k_s \nabla T_s$  is the conductive heat flux through the solid, and thus  $\nabla \cdot (k_s \nabla T_s)$  is the net rate of heat conduction into a unit volume of the solid. In Eq. (3.50), this appears multiplied by the factor  $(1 - \varepsilon)$ , which is the ratio of the cross-sectional area occupied by solid to the total cross-sectional area of the medium. The other two terms in Eq. (3.50) also contain the factor  $(1 - \varepsilon)$ , because this is the ratio of volume occupied by the solid to the total volume of the element. In Eq. (3.51), there also appears a convective term, due to the seepage velocity. It is recognised that  $\mathbf{v} \cdot \nabla T_f$  is the rate of change of temperature in the elemental volume due to the convection of fluid into it, therefore this, multiplied by  $(\rho c_p)_f$ , is the rate of change of thermal energy per unit volume of fluid, due to the convection. Note further that in writing Eq. (3.51), the Dupuit-Forchheimer relationship is used:

$$\mathbf{v} = \varepsilon \mathbf{V}.$$

Setting  $T_s = T_f = T$  and adding Eqs. (3.50) and (3.51), the following can be established:

$$(\rho c_p)_m \frac{\partial T}{\partial t} + (\rho c_p)_f \mathbf{v} \cdot \nabla T = \nabla \cdot (k_m \nabla T) + q_m''' \quad (3.52)$$

where

$$(\rho c)_m = (1 - \varepsilon)(\rho c)_s + \varepsilon(\rho c_p)_f, \quad (3.53)$$

$$k_m = (1 - \varepsilon)k_s + \varepsilon k_f, \quad (3.54)$$

$$q_m''' = (1 - \varepsilon)q_s''' + \varepsilon q_f''', \quad (3.55)$$

are the overall heat capacity per unit volume, overall thermal conductivity and overall heat production rate per unit volume of the medium respectively.

If heat transfer between solid and fluid is allowed (that is, thermal equilibrium does not exist), then Eqs. (3.50) and (3.51) can be replaced by:

$$(1 - \varepsilon)(\rho c)_s \frac{\partial T_s}{\partial t} = (1 - \varepsilon)\nabla \cdot (k_s \nabla T_s) + (1 - \varepsilon)q_s''' + h(T_f - T_s), \quad (3.56)$$

$$\varepsilon(\rho c_p)_f \frac{\partial T_f}{\partial t} + (\rho c_p)_f \mathbf{v} \cdot \nabla T_f = \varepsilon\nabla \cdot (k_f \nabla T_f) + (1 - \varepsilon)q_f''' + h(T_s - T_f), \quad (3.57)$$

where  $h$  is a heat transfer coefficient per unit volume. A critical aspect of using this approach lies in the determination of the appropriate value of  $h$ .

### ***Horton-Rogers-Lapwood Problem***

Starting with the simplest case, that of zero flow through the fluid-saturated porous medium, for an equilibrium state, the momentum equation is satisfied if

$$-\nabla P + \rho_f g = 0 \quad (3.58)$$

Taking the curl of each term yields

$$\nabla \rho_f \times g = 0 \quad (3.59)$$

If the fluid density,  $\rho_f$ , depends only on the temperature,  $T$ , then this equation implies that  $\nabla T \times g = 0$ . It can be concluded that a necessary condition for equilibrium is that the temperature gradient is vertical (or zero). Intra-pore convection may increase effective conductivity of the medium. A special interest in the problem of a horizontal layer of a porous medium uniformly heated from below is thus developed. This problem, the porous-medium analogy of the Rayleigh-B'ernard problem, was first treated by Lapwood and Rogers [44] and independently by Lapwood [46]. With reference to Fig. 3.16, the Cartesian frame is taken with the  $z$ -axis vertically upwards. It is supposed that the layer is confined by boundaries at  $z = 0$  and  $z = H$ , the lower boundary being at uniform temperature  $T_o + \Delta T$  and the upper boundary at temperature  $T_o$ . A layer of thickness,  $H$ , and an imposed adverse temperature gradient,  $\Delta T/H$ , are attained, supposing that the medium is homogeneous and isotropic, that Darcy's law is valid and that the Oberbeck-Boussinesq approximation is applicable, and also making the other standard assumptions (local thermal equilibrium, negligible heating from viscous dissipation, negligible radiative effects, etc.).

$$\nabla \cdot \mathbf{v} = 0 \quad (3.60)$$

$$c_a \rho_o \frac{\partial \mathbf{v}}{\partial t} = -\nabla P - \frac{\mu}{K} \mathbf{v} + \rho_f g \quad (3.61)$$

$$(\rho c)_m \frac{\partial T}{\partial t} + (\rho c_p)_f \mathbf{v} \cdot \nabla T = k_m \nabla^2 T \quad (3.62)$$

$$\rho_f = \rho_o [1 - \beta(T - T_o)] \quad (3.63)$$

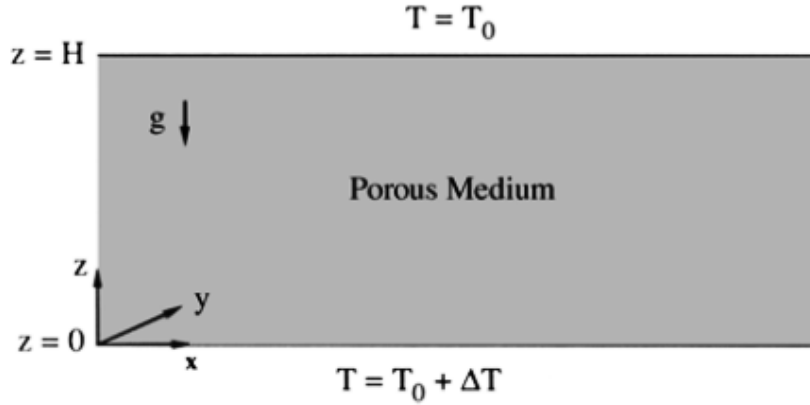


**Figure 3.16** The Horton-Rogers-Lapwood problem: infinite horizontal porous layer heated from below [12]

Given that  $\mathbf{v}$  is the seepage velocity,  $P$  is the pressure,  $\mu$  the dynamic viscosity,  $K$  the permeability,  $c$  the specific heat,  $k_m$  the overall thermal conductivity, and  $\beta$  the volumetric thermal expansion coefficient.

Given that  $\alpha_m$  is a thermal diffusivity defined by:

$$\alpha_m = \frac{k_m}{(\rho c_p)_f} \quad (3.64)$$

where  $\alpha_f = k_f / (\rho c_p)_f$  is the thermal diffusivity of the fluid phase.

$$Ra = \frac{\rho_o g \beta K H \Delta T}{\mu \alpha_m}, \quad Pr_m = \frac{\mu}{\rho_o \alpha_m}, \quad \gamma_a = \frac{c_a K}{\sigma Pr_m H^2}, \quad (3.65)$$

In Eq. (3.65),  $Ra$  is the Rayleigh-Darcy number (or Rayleigh number, for short),  $Pr_m$  is an overall Prandtl number, and  $\gamma_a$  is a non-dimensional acceleration coefficient. In most practical situations, the Darcy number  $K/H^2$  will be small, and consequently,  $\gamma_a$  will be small. Accordingly, take  $\gamma_a = 0$  unless otherwise specified. Note that the Rayleigh-Darcy number is the product of the Darcy number and the usual Rayleigh number for a clear viscous fluid.

***Internal Natural Convection: Heating from the side***

Enclosures heated from the side are mostly representative of porous systems that function while  $v$  is oriented vertically, as in the insulation of buildings, industrial cold-storage installations and cryogenics. Here, the most fundamental aspects of the convection heat transfer process are considered when the flow is steady and in the Darcy regime. Consider the basic scales of the clockwise convection pattern maintained by the side-to-side heating of the porous medium defined in Fig. 3.17. In accordance with the homogeneous porous medium model, the following are considered: the equations for the conservation of mass, Darcy flow and the conservation of energy in the  $H \times L$  space:

$$\frac{\partial u}{\partial x} + \frac{\partial v}{\partial y} = 0 \quad (3.66)$$

$$u = -\frac{K}{\mu} \frac{\partial P}{\partial x} \quad (3.67)$$

$$v = -\frac{K}{\mu} \left( \frac{\partial P}{\partial y} + \rho g \right) \quad (3.68)$$

$$u \frac{\partial T}{\partial x} + v \frac{\partial T}{\partial y} = \alpha_m \left( \frac{\partial^2 T}{\partial x^2} + \frac{\partial^2 T}{\partial y^2} \right) \quad (3.69)$$

By eliminating the pressure  $P$  between Eqs. (3.67) and (3.68) and by invoking the Boussinesq approximation in the body force term  $\rho g$  of Eq. (3.68), a single equation for momentum conservation is obtained:

$$\frac{\partial u}{\partial y} - \frac{\partial v}{\partial x} = -\frac{Kg\beta}{\nu} \frac{\partial T}{\partial x} \quad (3.70)$$

where  $u$  and  $v$  are velocity components along the  $x$  and  $y$  axis,  $T$  is the fluid temperature,  $g$  is the acceleration due to gravity, the permeability  $K$ , the coefficient of volumetric thermal expansion coefficient,  $\beta$ , the kinematic viscosity,  $\nu$ , and the porous-medium thermal diffusivity  $\alpha_m = k_m/(\rho c_p)_f$ . Eqs. (3.66), (3.69) and (3.70) hold in the entire domain  $H \times L$  subject to the boundary conditions indicated in Fig. 3.17.

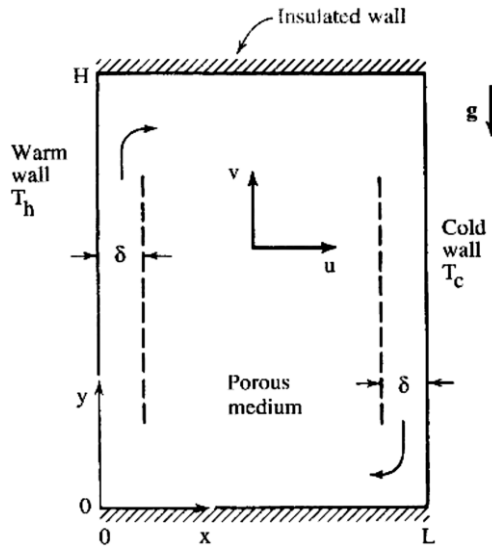


**Figure 3.17** Two-dimensional rectangular porous layer held between differently heated side walls [12]

The four walls are impermeable and the side-to-side temperature difference is  $T_h - T_c = \Delta T$ . Of special interest are the scales of the vertical boundary layers of thickness  $\delta$  and height  $H$ . In each  $\delta \times H$  region, the order-of-magnitude equivalents of Eqs. (3.66), (3.69) and (3.70) are:

$$\text{mass:} \quad \frac{u}{\delta} \sim \frac{v}{H}, \quad (3.71)$$

$$\text{energy:} \quad \left( u \frac{\Delta T}{\delta}, v \frac{\Delta T}{H} \right) \sim \left( \alpha_m \frac{\Delta T}{\delta^2}, \alpha_m \frac{\Delta T}{H^2} \right), \quad (3.72)$$

$$\text{momentum:} \quad \left( \frac{u}{H}, \frac{v}{\delta} \right) \sim \frac{Kg\beta\Delta T}{\nu\delta} \quad (3.73)$$

The mass balance in Eq. (3.71) shows that the two scales on the left-hand side of Eq. (3.72) are of the same order, namely  $v \Delta T / H$ . On the right-hand side of Eq. (3.72), the second scale can be neglected in favour of the first, because the  $\delta \times H$  region is a boundary layer (i.e. slender),

$$\delta \ll H \quad (3.74)$$

In this way, the energy conservation statement (3.72) reduces to a balance between the two most important effects, the conduction heating from the side and the convection in the vertical direction:

$$v \frac{\Delta T}{H} \sim \alpha_m \frac{\Delta T}{\delta^2} \quad (3.75)$$

longitudinal convection      lateral conduction

From the momentum scales in Eq. (3.73), it can be seen that the mass balance in Eq. (3.71) implies that the ratio between  $(u/H)$  and  $(v/\delta)$  is of the order  $(\delta/H)^2$ . The first term on the left-hand side of Eq. (3.73) can be neglected and it is found that the momentum balance reduces to:

$$\frac{v}{\delta} \sim \frac{Kg\beta\Delta T}{\nu\delta} \quad (3.76)$$

Eqs. (3.71), (3.75) and (3.76) imply that the scales of the vertical boundary layer [12] are

$$v \sim \frac{Kg\beta}{\nu}\Delta T \sim \frac{\alpha_m}{H}Ra, \quad (3.77)$$

$$\delta \sim HRa^{-1/2}, \quad (3.78)$$

$$u \sim \frac{\alpha_m}{H}Ra^{1/2} \quad (3.79)$$

where  $Ra$  is the Rayleigh number based on height:

$$Ra = \frac{g\beta KH\Delta T}{\nu\alpha_m} \quad (3.80)$$

The total heat transfer rate from one side wall to the other is simply

$$q' \sim k_m H \frac{\Delta T}{\delta} \sim k_m \Delta T R a^{1/2} \quad (3.81)$$

The heat transfer rate is expressed per unit length in the direction perpendicular to the plane  $H \times L$ . It can be non-dimensionalised as the overall Nusselt number:

$$Nu = \frac{q'}{q'_c} \sim \frac{k_m \Delta T R a^{1/2}}{k_m H \Delta T / L} \sim \frac{L}{H} R a^{1/2} \quad (3.82)$$

in which  $q'_c = k_m H \Delta T / L$  is the true heat transfer rate in the pure conduction limit (i.e. in the absence of convection).

**Side Walls with Uniform Flux and Other Thermal Conditions**

In the field of thermal insulation engineering, a more appropriate description for the side heating of the porous layer is the model where the heat flux  $q''$  is distributed uniformly along the two side walls. In the high Rayleigh number regime (Regime III, Fig. 3.18), the overall Nusselt number is given by [87]

$$Nu = \frac{q''H}{k_m H \overline{\Delta T} / L} = \frac{1}{2} \left( \frac{L}{H} \right)^{4/5} Ra_*^{2/5} \quad (3.83)$$

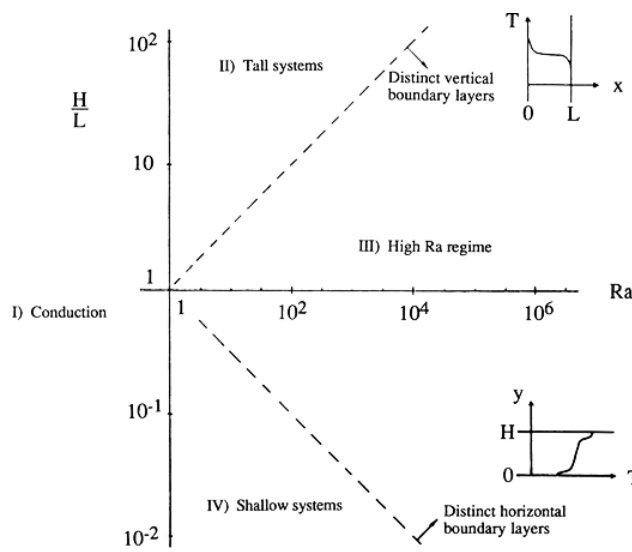


**Figure 3.18** Four heat transfer regimes for natural convection in a two-dimensional porous layer heated from the side [86]

In this  $Nu$  definition,  $\overline{\Delta T}$  is the height-averaged temperature difference that develops between the two side walls,  $(T_h - T_c)$ , while  $Ra_*$  is the Rayleigh number based on the heat flux

$$Ra_* = \frac{g\beta KH^2 q''}{v \alpha_m k_m} \quad (3.84)$$

Eq. (3.83) is based on a matched boundary layer analysis that combines [88] approach with the zero energy flow condition for the top and bottom boundaries of the enclosure [89]. The solution obtained also shows that:

- (i) the vertical boundary layers have a constant thickness of order  $HRa_*^{-1/3}$ ;

- (ii) the core region is motionless and linearly stratified, with a vertical temperature gradient equal to  $(q''/k_m)Ra_*^{-1/5} \left(\frac{H}{L}\right)^{2/5}$ ;
- (iii) the temperature of each side wall increases linearly with altitude at the same rate as the core temperature, and so the local temperature difference between the side walls is independent of altitude; and
- (iv) in any horizontal cut through the layer, there exists an exact balance between the net upflow of enthalpy and the net downward heat conduction.

The conditions that delineate the parametric domain in which Eq. (3.83) and regime III are valid are  $Ra_*^{-1/3} < H/L < Ra_*^{1/3}$ . This solution and the special flow features revealed are supported by numerical experiments performed in the range  $100 = Ra = 5000$  and  $1 = H/L = 10$ , which also are reported in [89].

Experiments on convection about a vertical surface with uniform heat flux were performed by [90], the medium being glass beads saturated with water. They observed that temperature fluctuations occurred when the non-Darcy Grashof number  $Gr^*$  attained a value of about 0.03. Their results are illustrated in Fig. 3.19. The experimental data for the larger beads (diameter 5 mm) are above the predicted values from the Darcy theory, while those of the smaller beads (diameter 1.5 mm) are below the predicted values.

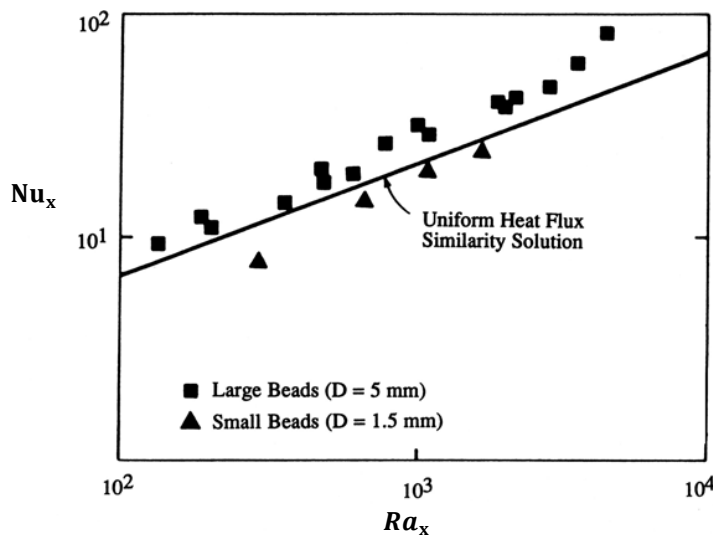


**Figure 3.19** Local Nusselt number versus local Rayleigh number for a vertical surface with uniform heat flux [90]

### **3.4 Conclusion**

This chapter presented some well-known correlations and analysis of models found in open literature, which were used to determine the heat transfer effects in porous media containing mono-sized spheres. It was shown that relatively good accuracy could be obtained with unit cell approaches in the bulk region of a packed bed but adequate thermophysical properties that quantified the heat transfer between particles and fluid in the media were not completely taken into consideration in the development of the analysed models.

# 4

## Test Facility and Experimental Evaluation of Heat Transfer in the Investigating Medium

---

### 4.1 Introduction

Experimental test facilities aimed at measuring the heat transfer characteristics found in open literature are usually case specific and must be fully understood before any attempt can be made to compare simulation models with experimental data. This is particularly true when analysing the porous structure in each experimental set-up as porosity alone cannot sufficiently characterise a porous structure in all the regions. Considering the literature survey presented in Chapter 3, it was found that more experimental researches were conducted with fluid flowing in and out of the medium than heated fluid confined in an enclosed medium. It was also observed that most of the experimental research found in literature was conducted under forced convection compared with the experimental investigation in the study conducted under natural convection.

The test facility used in the study as illustrated below is produced for use in investigating the natural convection fluid-to-particle heat transfer phenomenon in packed beds heated from below. As stated earlier in the thesis, the investigation will aid in better understanding and development of a suitable basic unit cell model that can be used to establish appropriate theoretical relations necessary for the evaluation of natural convection particle-to-fluid heat transfer characteristics in a medium such as the proposed nuclear fuel design. Although adiabatic wall conditions, often used in industrial practice, are assumed in the experiment, it should be noted that this boundary condition is assumed only for experimental purpose to trap substantial heat in the cylinder thereby necessitating a quick rise in helium gas temperature, which may be lost to the environment if the cylinder wall is not highly insulated. This

## Test Facility and Experimental Evaluation of Heat Transfer

assumption is not applicable to the proposed design as heat is expected to be transferred across the cladding to heat up the surrounding waters.

The facility consisted of one test section, a cylindrical enclosed cavity. The test section was divided into three regions; the upstream region, the porous region and the downstream region. The test section consisted of 500 mono-sized randomly packed stainless steel (AISI 304) spheres of 17.46 mm diameter (hereinafter called particles). The cavity outside diameter was 150 mm and the inside diameter 72 mm. The height of the vessel was 760mm while the bed (porous region) was 550 mm high and an axial heat path was generated by an inductively heated steel plate situated at the bottom of the upstream region. The schematic diagram of the experimental set-up is presented in Fig. 4.1.

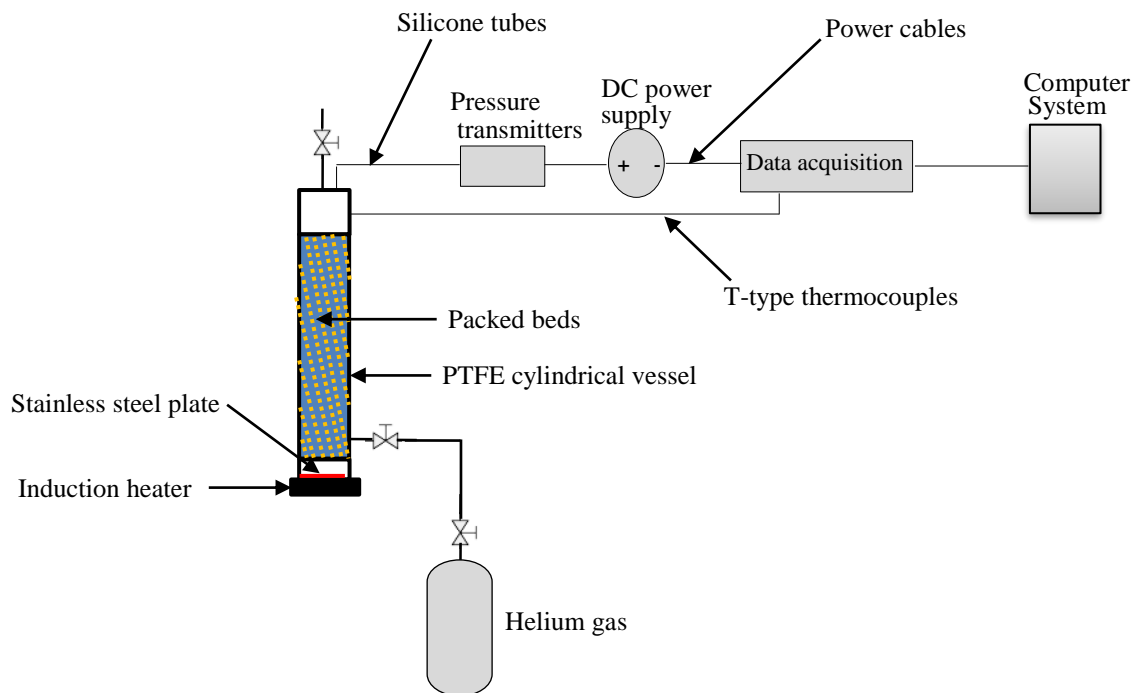


**Figure 4.1** Schematic diagram of the experimental set-up

## 4.2 Facility Configuration

The facility vessel was a vertically orientated and highly insulating polytetrafluoroethylene (PTFE)/Teflon structure, designed to enclose all internals and provide valves to connect with helium gas cylinder for gas supply at inlet and for pressure relief or blowout at the outlet. The vessel contained removable top and bottom lids as main access into the vessel. A wire mesh for

Test Facility and Experimental Evaluation of Heat Transfer

suspending the bed in the tube (see Figs. 4.2 & 4.3) to allow for convectational fluid flow current was placed a little distance vertically above the bottom plate inside the vessel. Miniature holes for the passage of thermocouples and silicon tubes were created on the upper part of the cylinder side wall and on the top lid of the vessel respectively as shown in Fig. 4.4.

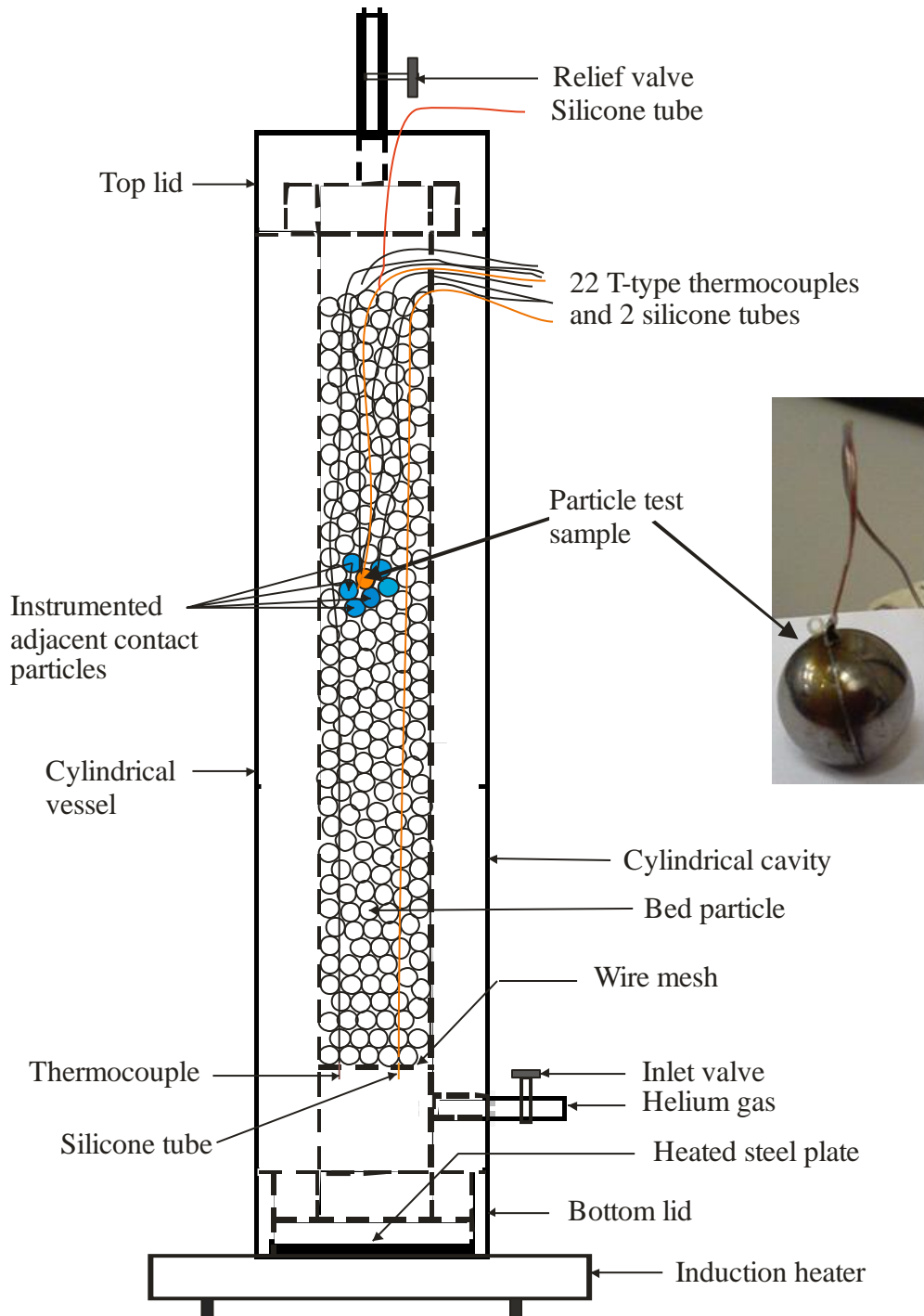


**Figure 4.2** Schematic diagram of the experiment cylindrical vessel (for illustration purpose)

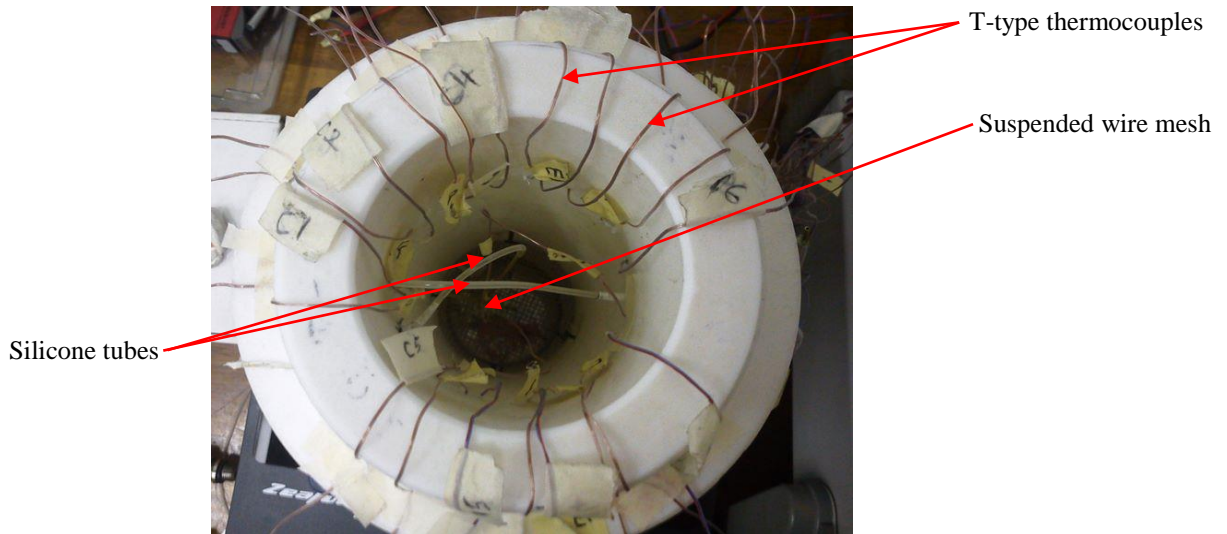


**Figure 4.3** Cylindrical cavity

Heat was generated inside the cavity by means of an electric induction cooktop that inductively heated a steel plate placed inside the vessel located at the bottom of the cavity (see Fig. 4.2). The vessel's material insulation properties and the thick walls (see Fig. 4.3) prevented heat loss both in the radial and axial direction when heat was transported through the beds. Leaks were minimised by tight fitting both lids using silicon tapes at the threaded sides, the tape was also used at the thermocouples and silicon by-pass passages. The particles were poured randomly into the cylinder cavity; nine selected particles were instrumented with logged thermocouples in such a way as to measure temperatures at the surface and central point inside the particle. The instrumented particles were also poured randomly into the container having adjacent contact with each other and identifying one as the particle test sample. Logged thermocouples were also placed in the interstices of the particle test sample (at the void spaces) to measure the average gas temperature neighbouring the particle test sample; silicone tubes connected to pressure transducers were placed below and above the bed (see Fig. 4.2) to measure possible pressure drop across the bed. The air in the cylinder was initially flushed out by running helium gas continuously through the medium for a few seconds while the pressure relief valve stayed open before the cylinder was later finally filled with helium gas and both inlet and relief valves closed.

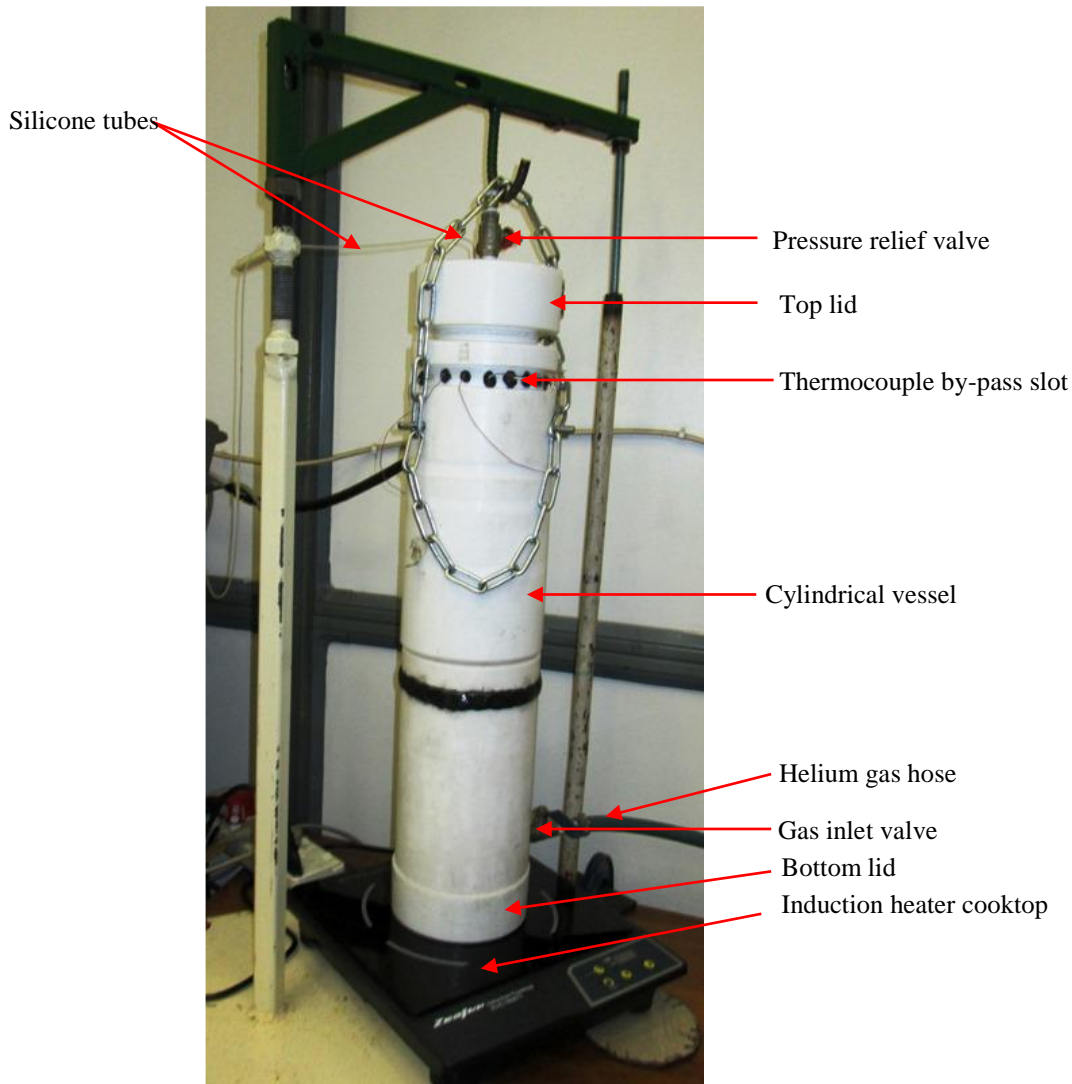


**Figure 4.4** Test facility

Thermal energy entered the packed bed by means of the inductively heated steel plate inside the cylinder cavity, which transferred heat to the helium gas immediately above the plate. Buoyancy-driven convective flow and recirculation took place in the medium due to density change as the gas became hot. The temperature of the bed particles was raised substantially by the hot helium gas after five hours of heating the gas.

### **4.3 Particle Test Sample Instrumentation and Measurements**

Nine particles were selected and identified as test particles. One out of these particles was recognised as the particle test sample. All nine particles were sliced halfway using wire-cutting

## Test Facility and Experimental Evaluation of Heat Transfer

---

technology (see Fig. 4.5a). A PolyScience Circulating Bath PD20R-30-A12E was used for calibrating the T-type thermocouples used in the experimental study before the test particles and particle test sample were instrumented with the thermocouples. The calibration was carried out to determine the relative error associated with each thermocouple. The readout of the thermocouples was compared with the readout of a secondary standard at the same conditions. Using regression, a slope and intercept were determined in order to adjust by appropriate difference to reflect the same readout as that of the secondary to ensure accurate data measurement in the experiment. Areas of the particles instrumented were as follows: the centre point inside each test particle, the top and bottom of each test particle and at opposite sides of each test particle (see Fig. 4.5b). The instrumentation was used for capturing the temperature distribution at different positions on the surface and in the centre point of each test particle as the particles gained heat from the hot gas. This action was necessitated due to the transient heat conduction to be experienced by the particles due to the bottom heat source in the medium. Properties of the particles were taken directly from the manufacturer's tables and consisted solely of the material properties of AISI 304 stainless steel.

The particle test sample was studied in conjunction with the other contacting adjacent test particles. Thermocouples were also placed at the void spaces neighbouring the particle test sample; this enabled the fluid (gas) temperature,  $T_f$ , surrounding the particle test sample to be determined by considering the average temperature. The hot gas temperature and pressure were measured just at the entry (immediately before the mesh wire) of the bed and at the exit of the bed by placing thermocouples and silicon tubes at the mentioned positions. A 34970A Agilent Data Acquisition/Switch Unit was used as a data logger and connected to a computer system to acquire data (see Fig. 4.6). It consist of three 20-channel Armature Multiplexer cards onto which the thermocouples and pressure transducers were connected. The pressure transducers used in the experiments were calibrated to secondary standards as well.

The logger had provision to accommodate three multiplexer cards. Communication between the Agilent Data Acquisition/Switch Unit and computer was established using the USB/GPIB interface 2.0. The Agilent Data Acquisition/Switch Unit converted the measured thermocouple voltage to temperature, using a built-in cold junction static temperature reference. Detailed information regarding the calibration of the thermocouples is provided in Appendix A.1.

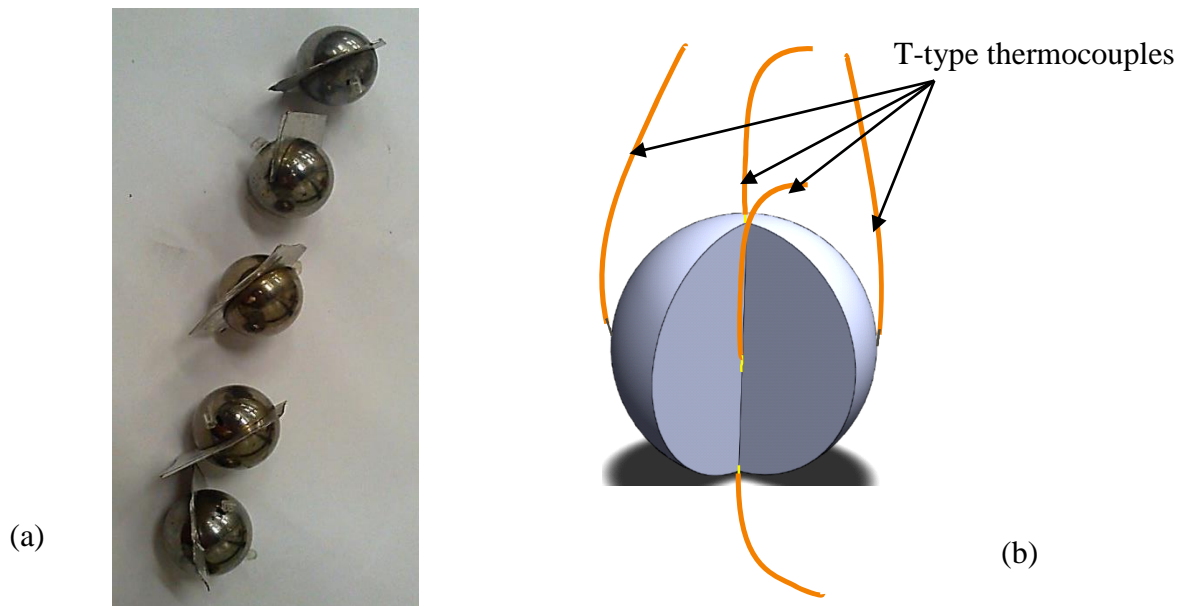


**Figure 4.5** (a) Sliced test particles with foil paper placed in-between (b) Sectional view of instrumented test particle.

Pressure measurements were taken to measure the differential pressure across the bed. Two WIKA Pressure Transmitters model A-10 (see Fig. 4.6) were connected to silicon tubes for measurement of the hot gas pressure at the entry of the bed and at the top of the bed. The pressure transmitters were powered by direct current power supply and the transducers were connected to the multiplexer card in order to log the data onto the computer. Measured voltage readings from the pressure transmitter were converted to gauge pressure using the manufacturer's manual guide. An induction cooker (cooktop) heated the stainless steel plate placed inside the enclosed cylinder cavity by a principle of magnetic induction (see Fig. 4.2 and Fig. 4.4). The heated steel plate heated the helium gas directly above and around its surface. The heat supplied by the cooktop was regulated by digitally varying the temperature output and power consumption using push buttons on the device. A temperature of 160 °C was maintained during the experiment.

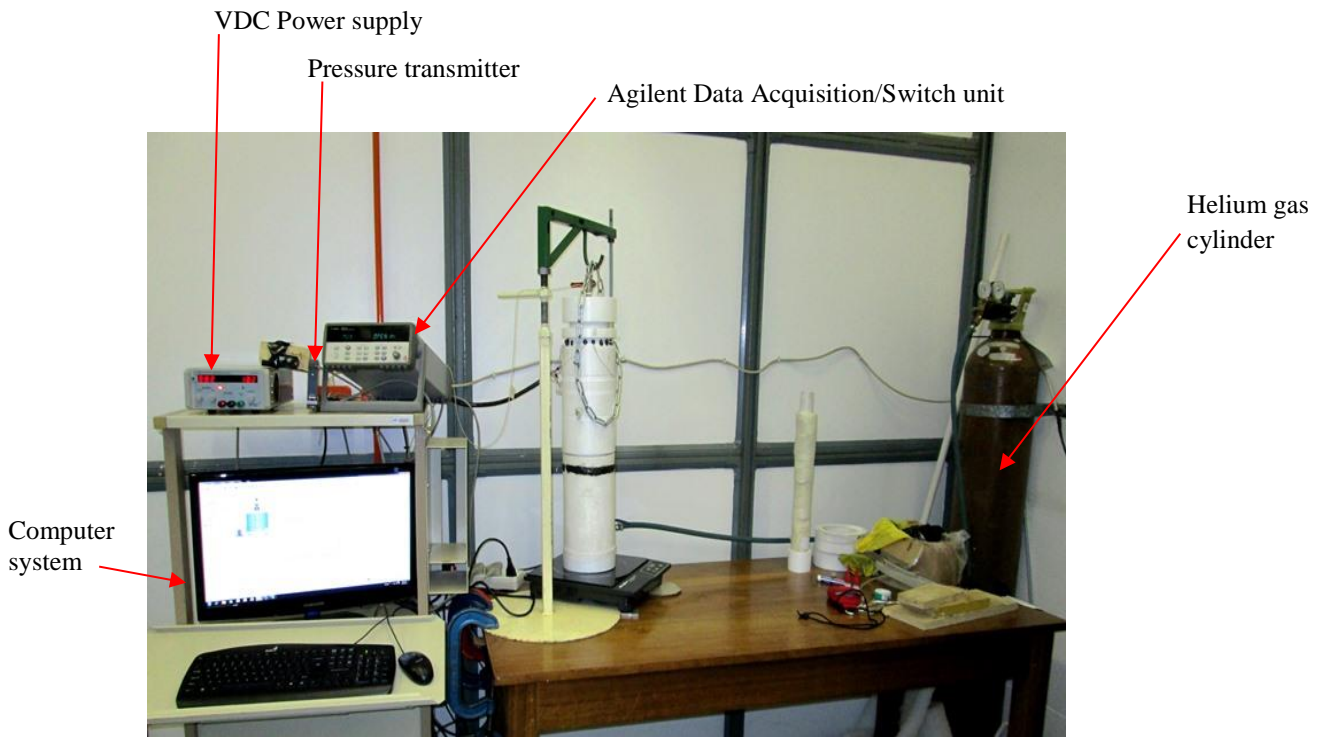


**Figure 4.6** Experimental set-up

## 4.4 Uncertainty Analysis

In general, an uncertainty implies a parameter associated with the result of a measurement, or the combined result of several measurements, which characterises the dispersion or the width of a specific confidence interval. Three different types of uncertainties are considered to contribute to the total uncertainty in the test facility, i.e. statistical variance, instrument uncertainty and drift uncertainty [93]. All instruments as well as measurement loops (i.e. thermocouples) are calibrated before an experiment commences. Measurement loops are calibrated by subjecting the instrument to a known process condition. The readout of the instrument is compared with the readout of a secondary standard at the same conditions. Using regression, a slope and intercept can be determined in order to adjust the field instrument to reflect the same readout as that of the secondary. The slope and intercept of the measurement loops used in the study, shown in **Appendix A.1**. Eq. (4.1), were applied to determine the statistical variance:

$$u(x_{i,statistical}) = \sqrt{\frac{\sum_{i=1}^N (x_i - \bar{x})^2}{N}} \quad (4.1)$$

## Test Facility and Experimental Evaluation of Heat Transfer

where  $x_i$  is the reference temperature value and  $\bar{x}$  the corresponding average measured temperature of  $N$  sample points. The instrument uncertainty,  $u(x_{i,instrument})$ , on the other hand, was obtained from the manufacturer and the drift uncertainty  $u(x_{i,drift})$  was obtained after each major calibration. The uncertainties were then combined to give a total standard uncertainty employing the following formula in Eq. (4.2):

$$u(x_{i,exp}) = \sqrt{[u(x_{i,statistical})]^2 + [u(x_{i,instrument})]^2 + [u(x_{i,drift})]^2} \quad (4.2)$$

Further discussion of this topic is provided in Appendix A.1.

### 4.5 Experimental Evaluation of Heat Transfer in the Test Facility

In the study, an experimental investigation was carried out in the test facility. The investigation was divided in two parts, the first was to investigate the heat transfer characteristics of fluid-to-particle by applying heat through an inductive heated bottom plate to the gas, which heated up the particles. The second part was to consider the medium as a thermal energy storage system, thus creating a particle-to-fluid heat transfer, which discharged stored heat energy in the particle under natural convective condition.

The experimental evaluation of the heat transfer in the investigating medium is achieved by the application of the basic *first principles* heat transfer concept. Considering the particle test sample of mass,  $m$ , volume,  $V_p$ , particle surface area,  $A_p$ , density,  $\rho$ , and specific heat,  $c_p$ , the particle test sample has an initial temperature,  $T_i$ . At time  $t = 0$ , the particles are placed into the medium of temperature,  $T_\infty$ , and heat transfer takes place between the particle and its environment, with a heat transfer coefficient of  $h$ . During a differential time interval,  $dt$ , the temperature of the particle rises by a differential amount,  $dT$ . The energy balance of the particle test sample for the time interval,  $dt$ , is expressed as:

$$\left( \begin{array}{c} \text{Heat transfer into the particle} \\ \text{during } dt \end{array} \right) = \left( \begin{array}{c} \text{Increase in the energy of the particle} \\ \text{during } dt \end{array} \right)$$

$$hA_p(T_\infty - T)dt = mc_p dT \quad (4.3)$$

## Test Facility and Experimental Evaluation of Heat Transfer

---

noting that  $m = \rho V_p$ , and  $dT = d(T - T_\infty)$ . Since  $T_\infty = \text{constant}$ , Eq. (4.3) can be rearranged as:

$$\frac{d(T - T_\infty)}{(T - T_\infty)} = -\frac{hA_p}{\rho V_p c_p} dt \quad (4.4)$$

Integrating from  $t = 0$ , at which  $T = T_i$ , to any time  $t$ , at which  $T = T(t)$ , gives:

$$\ln \frac{T(t) - T_\infty}{T_i - T_\infty} = -\frac{hA_p}{\rho V_p c_p} t \quad (4.5)$$

Taking the exponential of both sides and rearranging, Eq.(4.5) gives:

$$h = -\left( \ln \frac{T(t) - T_\infty}{T_i - T_\infty} \right) \frac{\rho V_p c_p}{A_p t} \quad (4.6)$$

Analysed captured data of the convective and conductive heat transfer at the surface and within the particle test sample was used in the experimental evaluation and representative results obtained from the heat transfer characteristics of the investigated medium. The parameters used in characterising heat transfer in the study are as follows: heat transfer coefficient,  $h$ , the Nusselt number,  $Nu_{d_p}$ , the Grashof number,  $Gr$ , and the Rayleigh number,  $Ra_{d_p}$ . These parameters are of prime importance when analysing the heat transfer performance of a fixed bed system.

$$Nu_{d_p} = \frac{hL_c}{k_f} \quad (4.7)$$

$$Ra_{d_p} = \frac{g\beta|T_s - T_f| L_c^3}{\nu^2} Pr = Gr.Pr \quad (4.8)$$

In Eq. (4.9), the correlation recommended by Nuclear Safety Standard Commission KTA [15] is expressed. It is used to validate results of the heat transfer performance obtained in the medium through the concept adopted for the experimental evaluation.

$$Nu_{KTA} = 1.27 \frac{Pr^{1/3}}{\varepsilon^{1.18}} Re^{0.36} + 0.033 \frac{Pr^{1/2}}{\varepsilon^{1.07}} Re^{0.86} \quad (4.9)$$

$$h = \frac{Nu_{KTA} k_f}{d_p} \quad (4.10)$$

## 4.6 Results and Discussion

Experimental results in Fig. 4.7 reveal a change in particle temperature with time during the process of fluid-to-particle and particle-to-fluid heat transfer.

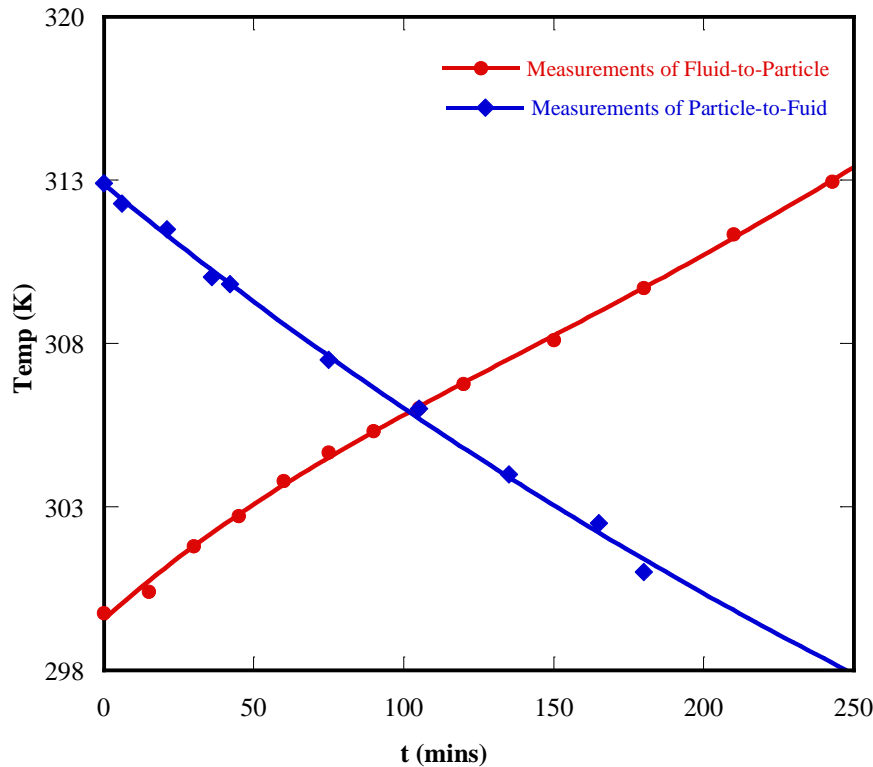


**Figure 4.7** Plot of particle temperature against time

The temperature profile of the particle test sample is shown in Fig. 4.7 as the hot gas heated the particle to create a temperature rise in the particle. A particle temperature drop is seen in the above graph as the particle test sample acted as a thermal energy storage system when it gave up the heat stored in it to the gas of which the temperature had dropped after the heating source was switched off and left for a long time to cool. This created a particle-to-fluid heat transfer, which discharged stored heat energy in the particle under natural convective condition. Results from the experimental investigation carried out reveal the influence of dimensionless parameters (Nusselt, Grashof, Rayleigh and Prandtl numbers), which define the operating conditions encountered in porous media engineering applications. Fig. 4.8 depicts fluid-to-particle heat transfer coefficient at different  $Ra_{dp}$  values. Apparently, the KTA measured values have higher  $h_{fp}$  compared with measured values of Eq. (4.6). The reason is that the KTA correlation was developed for nuclear reactors operating under forced convection while

measurements of Eq. (4.6) were established on temperature difference relations between the particle and the fluid. An equivalent Reynolds number was used in obtaining the KTA measured values in Eq. (4.9) due to the flow recirculation that took place in the medium.

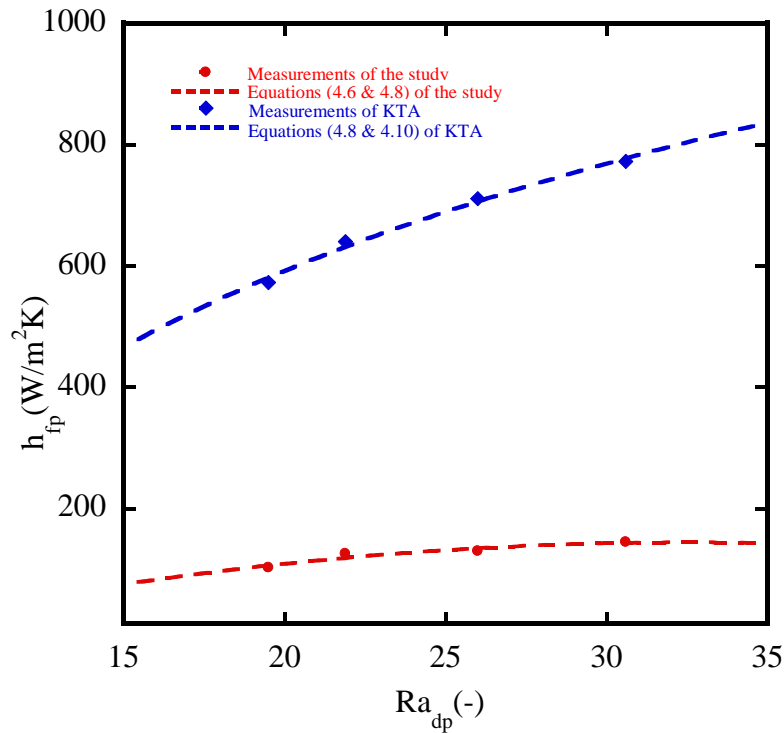


**Figure 4.8** Fluid-to-particle heat transfer at different Rayleigh numbers ( $Pr = 0.689$ )

In Fig. 4.9, the variation of the particle-to-fluid heat transfer coefficient,  $h_{pf}$ , with Rayleigh number,  $Ra_{dp}$ , is illustrated as the stored heat energy in the particles was being transferred/discharged to the fluid. As the particles lost heat to the fluid, the heat transfer effect gradually decreased and after a long time, the particles and fluid would attain almost the same temperature equal to the medium initial ambient temperature before heating commenced, a condition at which  $T_f = T_p$ . A validation using the KTA measured  $h_{pf}$  values of Eq. (4.10) shows a parallel declining profile of gradual heat loss but at a distance apart.

The reason for the high measured values is that the KTA correlation did not have sufficient medium properties that could capture the exact heat transfer phenomena taking place between the particles and the fluid in the medium.

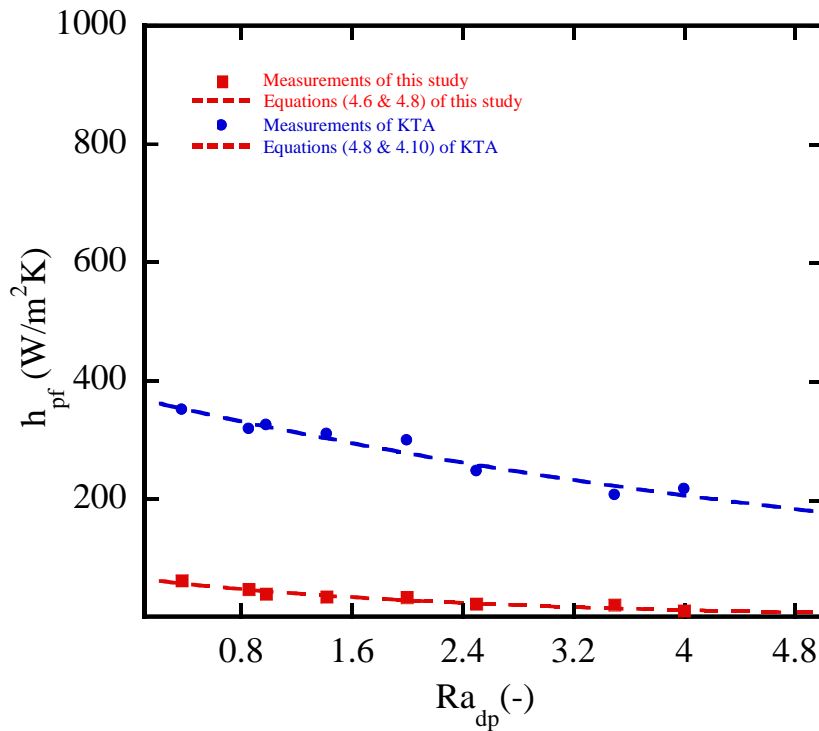


**Figure 4.9** Convective particle-to-fluid heat transfer in packed bed thermal energy storage systems at different Rayleigh numbers.

Heat transfer results for  $N = 4.12$  are presented in Fig. 4.10. The behaviour of the Nusselt number with respect to the Rayleigh number is similar to what has been observed in literature [31] for square annulus. In the present case, the Nusselt number increased gradually with increasing  $Ra_{dp}$ , which is a development of increasing convective mode in the medium. A validation was equally carried out with the KTA correlation.

Fig. 4.11 illustrates the effect of Nusselt number on  $Ra_{dp}$  as the heat energy stored in the particles was being transferred to the fluid under natural convective operating condition. The Nusselt number measured value in Eq. (4.6) is observed to drop to a value close to zero as the particles lost their stored heat energy, the heat transfer from particle-to-fluid continued to decline as the medium returned to its initial start-up condition. Agreement exists when the results are validated with the KTA correlation.

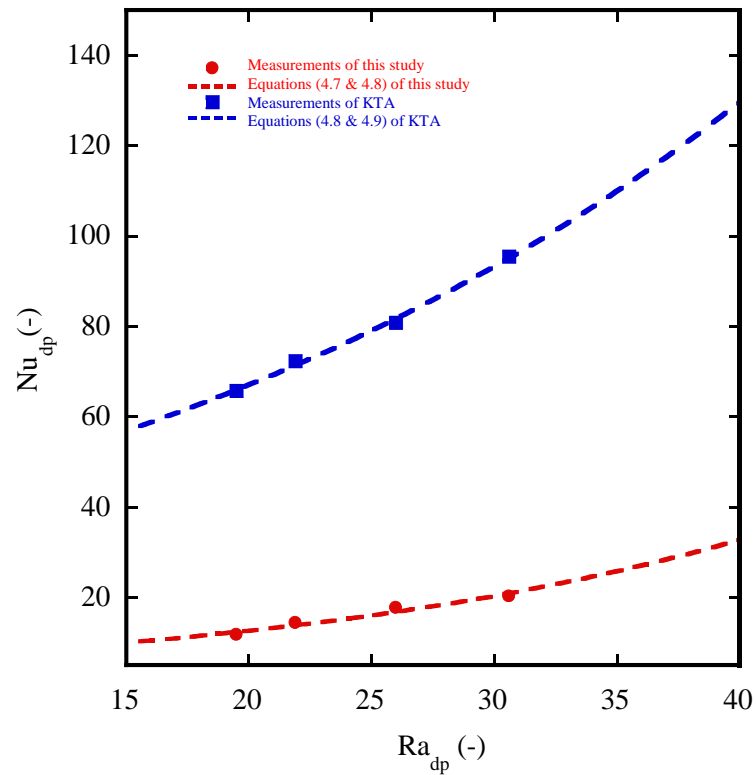


**Figure 4.10** Variation in Rayleigh number at different Nusselt numbers for convective fluid-to-particle heat transfer ( $N = 4.12$ ,  $Pr = 0.689$ )

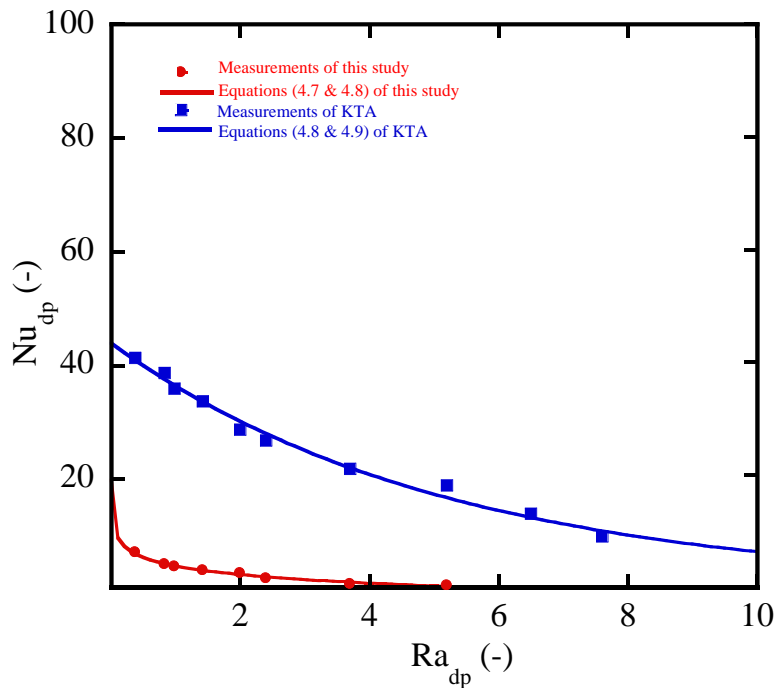


**Figure 4.11** Effect of Nusselt number on Rayleigh number in packed bed thermal energy storage systems for convective particle-to-fluid heat transfer ( $N = 4.12$ ,  $Pr = 0.689$ )

## 4.7 CONCLUSION

The chapter described the experimental test facility set-up and use of data acquisition system in the capturing of experimental data readings. The functions of equipment constituting the set-up and experimental procedure were also discussed. Deliberations on experimental errors and uncertainty were equally made in the chapter. For the porous medium investigated, an experimental procedure used in evaluating the convective heat transfer coefficient of heat exchange between the working fluid and the bed particles was detailed. While a validation of the measured results with correlation recommended by the Nuclear Safety Standard Commission *KTA* agreed with the plot profile of the dimensionless groups, the difference in values was due to the non-consideration of the thermal energy exchange properties (conduction and convection) in the bed by the *KTA* correlation. The concept of the medium investigation was not intended on flow but on heat transfer characteristics between the solids and fluid knowing well that the fluid was buoyancy driven due to temperature variation. Unlike most studies where there was continuous and fresh replacement of cooling fluid, the experimental set-up was tailored towards the proposed fuel design where the fluid was confined to an enclosure.

# 5

## Theoretical: Basic Unit Cell Model

---

### 5.1 Introduction

Chapter 3 presented some correlations and models used for determining the heat transfer performance in packed beds. It demonstrated that much empirical evidence was incorporated into the various models to achieve the desired results in the prediction of the heat transfer performance of the various investigated media. In Chapter 4, the *first principle* heat transfer concept was applied to the experimental evaluation of the heat transfer in the medium investigated.

The focus of this chapter is the development of a suitable theoretical model for evaluating the natural convection heat transfer characteristics in porous media heated by a hot gas through natural convection and that of heat-generating particles. Heat transfer mechanisms that play an active role in packed beds are as follows (see Fig. 5.1): (i) the convective heat transfer from the surface of the packing materials (particles) to the fluid, sometimes referred to as particle-to-fluid mode; (ii) the convective heat transfer from the flowing fluid to the particles, sometimes referred to as fluid-to-particle mode; (iii) the conduction heat transfer between the walls of the bed and the particle interface constituting the bed; (iv) the conduction heat transfer between individual particles in the bed, sometimes referred to as particle-to-particle mode; (v) radiant heat transfer between particles and between particles and the container wall; (vi) radiant heat transfer between fluid and particles [91]. However, the modes are not compartmentalised and will naturally influence one another; for instance, conduction between the particles may be affected by the convection between the particles and the fluid. This interaction among the different modes is one of the main reasons for the difficulty in correlating the total heat transfer and analysing the experimental data obtained. Fundamental heat transfer principles were

applied by [9] to characterise the heat transfer mechanism between two contacting rough solid spherical bodies. The model only dealt with conduction through the contact area between spheres while incorporating surface roughness and conduction through the gas phase at lower temperatures. Good results were obtained from the study when the model was compared with other packings though limited to SC and FCC arrangements. It was suggested that the heat transfer trends obtained in regularly packed beds through the model could be used to study the effect of important parameters involved in randomly packed beds.

However, the new model developed in this chapter will be based on some of the thermal conduction heat transfer principles used by [9]. While [9] concentrates on conduction across the contact region of rough contacting spherical surfaces, this model is developed based on Hertzian (perfect) contacts between the contacting particles since the particle falls within a Brinell hardness of  $H_B < 1.3 \text{ GPa}$  [97]. The newly developed basic unit cell model deals with all the aforementioned heat transfer mechanisms, while distinguishing between short-range thermal radiation, defined as radiation to and from spheres in contact with the sphere under consideration, and long-range thermal radiation, defined as radiation to and from spheres not in direct contact with the sphere under consideration (see Fig. 5.1).

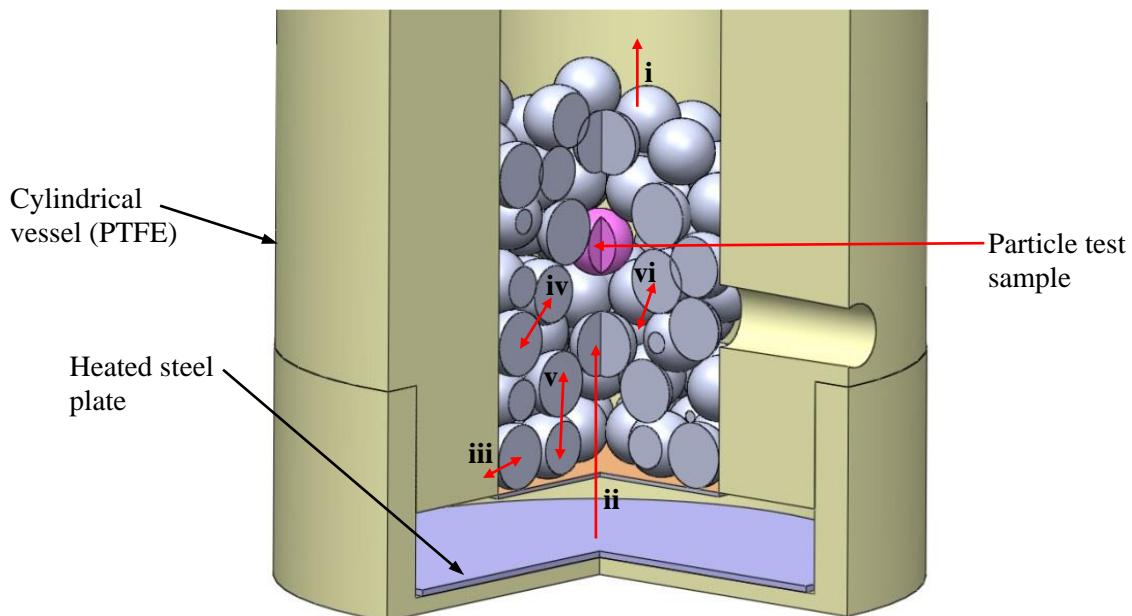


**Figure 5.1** Section through part of the test facility with a particle test sample highlighted. (i) heat transfer by particle-to-fluid mode, (ii) heat transfer by fluid-to-particle mode, (iii) heat transfer between the bed wall and particles, (iv) heat transfer by particle-to-particle mode, (v) radiant heat transfer between particles, (vi) radiant heat transfer between fluid and particles.

**Source:** Noah *et al.*, 2015

## 5.2 Heat Transfer inside the Cladding of Traditional Fuel

In a quest to investigate the particle-to-fluid heat transfer characteristics expected in the proposed new fuel design using the basic unit cell model, it is necessary to examine the heat transfer process that takes place inside the cladding of the traditional fuel of LWR. This will help to not only compare the two but also to give a better understanding of the new design.

In the traditional fuel design, energy is removed from a reactor by two fundamentally different heat transfer processes [92]: conduction and convection. In conduction, heat is transmitted from one location in a body to another due to the temperature difference existing in the body; there is no macroscopic movement of any portion of the body. It is by this mechanism that heat produced in fuel pellets is transferred to the surface of the rod. Heat convection involves the transfer of heat to a moving liquid or gas, again as a result of a temperature difference and the later rejection of this heat at another location. The heat generation rate is not constant inside the fuel pellet being smaller at the centre due to the attenuation thermal neutron flux by the fuel. Thus, the heat conducted to the surface of a fuel rod is carried into the coolant and out of the system by convection. A gap between the pellets and the cladding tube is filled with helium gas to improve the conduction heat transfer from the fuel pellets to the cladding. Consider fuel pellets of radius  $a$  surrounded by cladding of thickness  $b$ , as shown in Fig. 5.2.

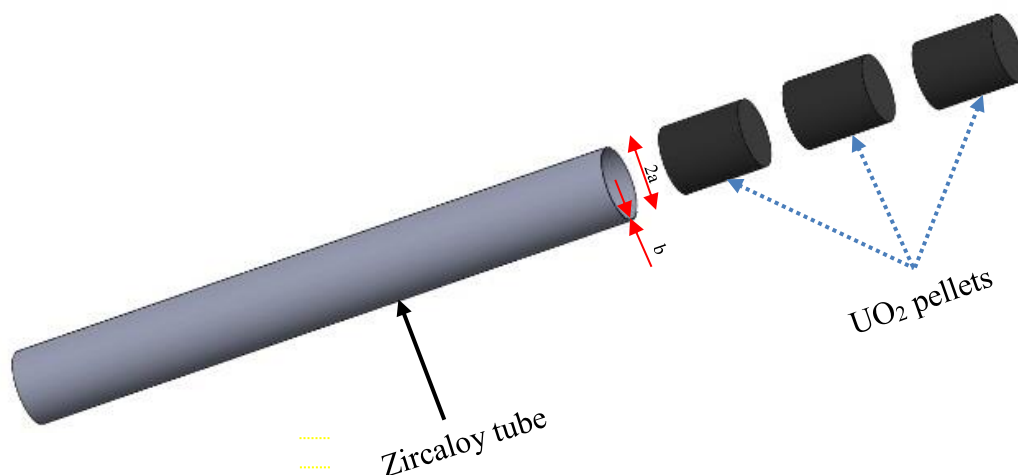


**Figure 5.2** Fuel rod consisting of cladding tube and fuel pellets

Heat is produced at a rate of  $q'''$  per unit volume inside the fuel rod and heat released in the cladding by  $\gamma$ -absorption is very small compared with fission heating, hence it is assumed

negligible. The temperature in the rod is only a function of the distance  $r$  from the axis of the rod, so that in cylindrical coordinates, the heat conduction equation is expressed by Eq. (5.1):

$$\frac{d^2T}{dr^2} + \frac{1}{r} \frac{dT}{dr} + \frac{q'''}{k_{fuel}} = 0 \quad (5.1)$$

The boundary conditions appropriate to this problem are:

(i)  $T$  is non-singular within the rod      (ii)  $T(0) = T_m$

where  $T_m$  is the central temperature of the fuel. The general solution is given in Eq. (5.2):

$$T(r) = -\frac{q'''r^2}{4k_{fuel}} + C_1 \ln r + C_2 \quad (5.2)$$

where  $C_1$  and  $C_2$  are constants. In view of the boundary condition,  $C_1 = 0$  and  $C_2 = T_m$ , thus the temperature within the rod is:

$$T(r) = T_m - \frac{q'''r^2}{4k_{fuel}} \quad (5.3)$$

Consider an arbitrary volume  $V$  of material throughout a portion of which heat is being produced. From the conservation of energy, the rate at which heat is produced within the fuel rod must be equal to the rate at which it flows out of the rod. If this were not the case, the substance would change temperature and therefore would not be in a steady state. In equation form, let the volume of fuel rod be  $V = \pi a^2 H$ :

$$q = \pi a^2 H q''' \quad (5.4)$$

where  $a$  is the fuel pellet radius,  $H$  is the length of the rod and  $q$  is the heat flow out of the rod. Solving for  $q'''$  in Eq. (5.3) and introducing in Eq. (5.4) given that  $r = a$  and  $T_s$  is the surface temperature of the rod, Eq. (5.4) can now be expressed as:

$$q = \frac{T_m - T_s}{1/(4\pi H k_{fuel})} \quad (5.5)$$

In view of Eq. (5.5), the thermal resistance of the fuel is expressed by Eq. (5.6):

$$R_{fuel} = \frac{1}{4\pi H k_{fuel}} \quad (5.6)$$

From Fourier's law, the total heat flowing out of the cladding having a thickness of  $b$  is:

$$q = -2\pi(a + b)Hk_{clad} \frac{dT}{dr} \quad (5.7)$$

evaluated at  $r = a + b$ . Carrying out the differentiation of Eq. (5.7) yields

$$q = \frac{2\pi Hk_{clad}(T_s - T_{clad})}{\ln(1 + b/a)} \quad (5.8)$$

The thermal resistance of the cladding is given to be:

$$R_{clad} = \frac{\ln(1 + b/a)}{2\pi Hk_{clad}} \quad (5.9a)$$

Normally,  $b$  is much less than  $a$ . In this case, since

$$\ln(1 + b/a) \cong \frac{b}{a} \quad (5.9b)$$

Eq. (5.9a) can be written as

$$R_{clad} = \frac{b}{2\pi a Hk_{clad}} \quad (5.10)$$

In terms of the overall temperature difference between the centre of the fuel and the surface of the cladding, the heat flowing out of the rod is:

$$q = \frac{T_m - T_{clad}}{R_{fuel} + R_{gap} + R_{clad}} \quad (5.11)$$

The heat transfer between the fuel pellets and the helium gas contained in the cladding is expressed by Eq. (5.12a):

$$q = \frac{\Delta T}{R_{total_{conv}}} = \frac{T_m - T_g}{h_{pf} A_{total}} \quad (5.12a)$$

The fuel pellet-to-gas heat transfer coefficient is determined from the above equation and expressed in Eq. (5.12b):

$$h_{pf} = \frac{T_m - T_g}{q A_{total}} \quad (5.12b)$$

where  $R_{total_{conv}}$  is the total convective thermal resistance,  $A_{total}$  is the total surface area of the fuel in the cladding and  $T_g$  is the temperature of gas contained inside the cladding.

### 5.3 Development of the Basic Unit Cell (BUC) Model for Packed Beds

The BUC model adopts the concept of a single unit of the packed bed being analysed and taken as representing the entire bed; it relates the convective heat effect of the flowing fluid with the conduction and radiative effect between adjacent particles at the finite contact spot. A unit cell is made up of any identified particle in the bed with adjacent contacting particles (see Fig. 5.3a). The model is an application of conservative heat transfer energy balance within any unit cell in the medium. It brings into account every form of heat exchange that occurs in the unit cell. One vital form of heat exchange intensely dealt with in the model is the conduction mode. To completely resolve the issue of heat transfer by conduction in the unit cell, the model combines both analytical and numerical methods in predicting the conduction mode of heat transfer in packed beds; analytical refers to the use of the concept of thermal contact resistance (TCR) of smooth sphere particles and numerical refers to the use of finite volume method (FVM) to determine the temperature distribution within the particles.

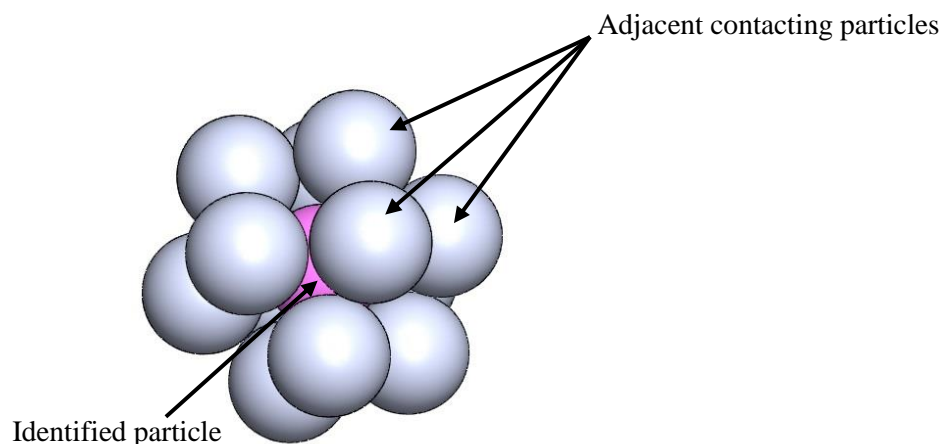


**Figure 5.3a** Single unit cell

### 5.4 Temperature Distribution within Particles

Randomly packed coated nuclear particle fuels in the cladding of the proposed design are expected to exhibit a relatively uniform temperature distribution on the particle fuel surface. Given the uniform heat removal from the particles, it can be expected to have a uniform temperature distribution on the surface. However, in the experiment, temperature distribution was not uniform due to the mode of heat-generating source in the medium and the nature of

heat removal from particle surface. This development creates the need to determine the transient temperature distribution on the test particle surfaces as they are being heated up by the hot gas and neighbouring particles in contact with them.

It is assumed that the inductively heated bottom steel plate temperature increases the temperature of helium gas on the top surface of the plate and the gas starts flowing upwards in an axial direction through the bed pores due to buoyancy and the formation of convective fluid current at the near-wall region. The particle test sample gains heat by convection from the hot gas and conduction from adjacent contact test particles. Fig. 5.3b depicts the particle test sample in contact with a number of test particles at different finite contact spots on its surface, this set-up forms a unit cell in the medium. In the experiment carried out, the thermocouples were positioned at some specified locations to take temperature readings at contact spots and were designed to determine the temperature distribution within each particle as it gained heat. Due to the particle size, it is difficult and unreasonable instrumenting every contact spot on the surface of the particle (see Fig. 5.3b), hence a numerical method is considered to be ideal for this purpose. With the method, the temperature distribution in each control volume on the surface of the particle can be determined. To achieve this objective, a finite volume discretisation implicit scheme can be applied; the scheme is used because of its robustness and unconditional stability as compared with other schemes. A Matlab programme in Appendix B.1 was written and used to assist in the discretisation calculation.

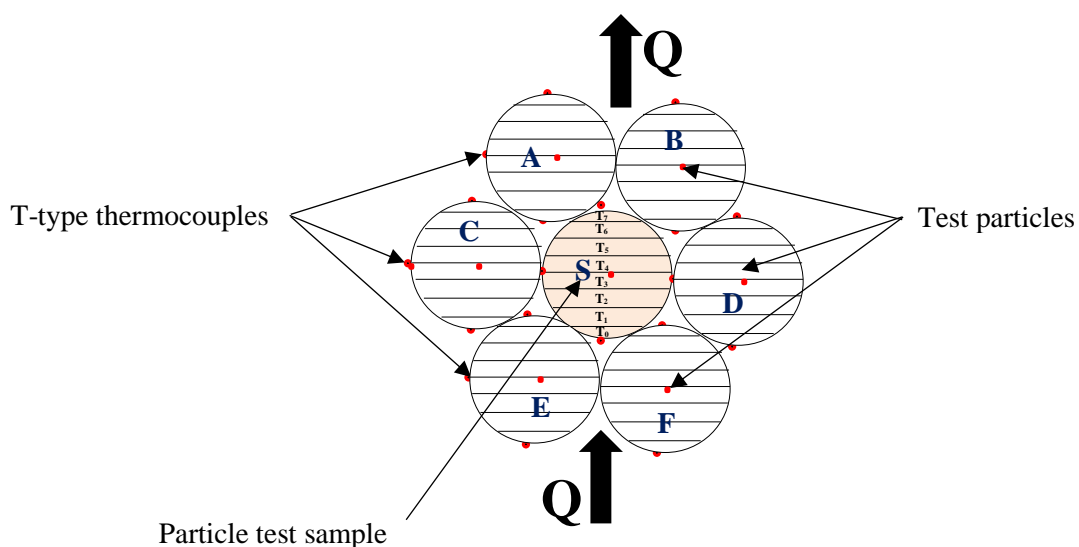


**Figure 5.3b** Schematic representation of contacting adjacent particles

By determining the temperature of the contact spot, the appropriate heat transfer by conduction between adjacent particles at the contact spot can be obtained. The one-dimensional heat conduction equation in a sphere having an internal heat source  $S_{gen}$  is expressed in Eq. (5.13a):

$$\frac{1}{r^2} \frac{\partial}{\partial z} \left( r^2 \frac{\partial T}{\partial z} \right) + \frac{S_{gen}}{k_s} = \frac{1}{\alpha} \frac{\partial T}{\partial t} \quad (5.13a)$$

Considering the radius in an axial direction, Eq. (5.13a) can alternatively be expressed as:

$$k_s \frac{\partial^2 T}{\partial z^2} + S_{gen} = \rho c_p \frac{\partial T}{\partial t} \quad (5.13b)$$

Since the particles do not have an internal heat source  $S_{gen} = 0$  and the equation reduces to

$$k_s \frac{\partial}{\partial z} \left( \frac{\partial T}{\partial z} \right) = \rho c_p \frac{\partial T}{\partial t} \quad (5.14)$$

The temperature distribution determined by numerical method in and on the surface of the test particles and particle test sample is governed by the transient one-dimensional heat conduction equation shown in Eq. (5.14), using the appropriate initial boundary conditions. To determine the temperature distribution within any of the particles, the particle is divided into a number of control volumes as shown in Fig. 5.4, and thereafter, a discretised algebraic equation is established as derived in Eq. (5.21).

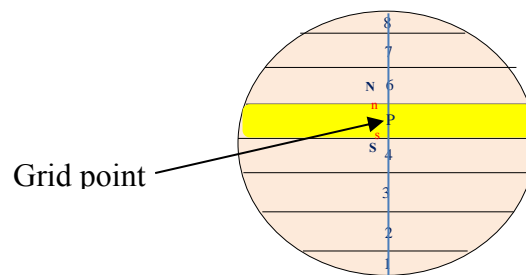


**Figure 5.4** Control volumes with grid points in the axial direction

Integrating the transient one-dimensional heat conduction equation in Eq. (5.14) over a control volume at a time interval  $\Delta t$  gives:

$$\int_t^{t+\Delta t} \int_s^n \frac{\partial(\rho c_p T)}{\partial t} dz dt = \int_t^{t+\Delta t} \int_s^n \frac{\partial}{\partial z} \left( k_s \frac{\partial T}{\partial z} \right) dz dt \quad (5.15)$$

$$\rho c_p [T_P^{t+\Delta t} - T_P^t] \frac{\Delta Z}{\Delta t} = \int_t^{t+\Delta t} \left[ \frac{k_s(T_N - T_P)}{\partial z} - \frac{k_s(T_P - T_S)}{\partial z} \right] dt \quad (5.16)$$

given an analogy and an initial condition;  $t = 0$

$$\int_t^{t+\Delta t} T dt = ((1-f)T^t + fT^{t+\Delta t}) = ((1-f)T^o + fT) \quad (5.17)$$

substituting the analogy in Eq. (5.16) gives:

$$\begin{aligned} & \rho c_p [T_P - T_P^o] \Delta Z \\ &= \left\{ \frac{k_n}{\partial z} [(1-f)T_N^t + fT_N^{t+\Delta t}] - \frac{k_n}{\partial z} [(1-f)T_P^t + fT_P^{t+\Delta t}] \right. \\ & \quad \left. - \frac{k_s}{\partial z} [(1-f)T_P^t + fT_P^{t+\Delta t}] + \frac{k_s}{\partial z} [(1-f)T_S^t + fT_S^{t+\Delta t}] \right\} \Delta t \end{aligned} \quad (5.18)$$

Considering the scheme to be fully implicit, a weighting parameter  $f = 1$  is introduced hence  $a_N = \frac{k_n}{\partial z} f$ ,  $a_S = \frac{k_s}{\partial z} f$ ,  $a_P = a_N + a_S + \rho c_p \frac{\Delta Z}{\Delta t}$ , a discretised algebraic equation can now be established in Eq. (5.21):

$$\begin{aligned} & \rho c_p \frac{\Delta Z}{\Delta t} [T_P - T_P^o] \\ &= \frac{k_n}{\partial z} [(1-f)T_N^o + fT_N] - \frac{k_n}{\partial z} [(1-f)T_P^o + fT_P] \\ & \quad - \frac{k_s}{\partial z} [(1-f)T_P^o + fT_P] + \frac{k_s}{\partial z} [(1-f)T_S^o + fT_S] \end{aligned} \quad (5.19)$$

$$\begin{aligned} & \left( \rho c_p \frac{\Delta Z}{\Delta t} + \frac{k_n}{\partial z} f + \frac{k_s}{\partial z} f \right) T_P \\ &= \frac{k_n}{\partial z} f T_N + \frac{k_s}{\partial z} f T_S + \left( \rho c_p \frac{\Delta Z}{\Delta t} - \frac{k_n}{\partial z} (1-f) - \frac{k_s}{\partial z} (1-f) \right) T_P^o \\ & \quad + \left( \frac{k_n}{\partial z} (1-f) T_N^o + \frac{k_s}{\partial z} (1-f) T_S^o \right) \end{aligned} \quad (5.20)$$

From the above equation, the discretised algebraic equation is expressed as:

$$a_P T_P = a_N T_N + a_S T_S + a_P^o T_P^o + b \quad (5.21)$$

From the discretised algebraic equation derived in Eq. (5.21), it is possible to determine the temperature at the surface of a particle when it makes contact with another particle in the surrounding medium. The conduction heat transfer at contact area spots can then be expressed by using Eq. (5.22):

$$Q_c = k_{eff}^c A_c \frac{dT_i}{dz} \quad (5.22)$$

where  $T_i$  could be  $T_1, T_2, T_3, T_4, \dots$ ;  $T_i$  accounts for the particle surface non-uniform temperature (see Figs. 5.3b & 5.4). The graph in Fig. 5.5 validates the experimental temperature distribution with numerical temperature distribution in the particle test sample along axial direction. Temperatures  $T_0, T_4$ , and  $T_7$  are determined experimentally from the thermocouples embedded in the particles. Temperatures in all the nodes are likewise deduced numerically using the finite volume implicit scheme at a time step of two seconds. The graph in Fig. 5.5 shows an error of less than 1% between experimental and numerical results and is therefore regarded as appropriate for use. The value of  $k_{eff}^c$  used in the above equation is obtained from the expression in Eq. (5.38).

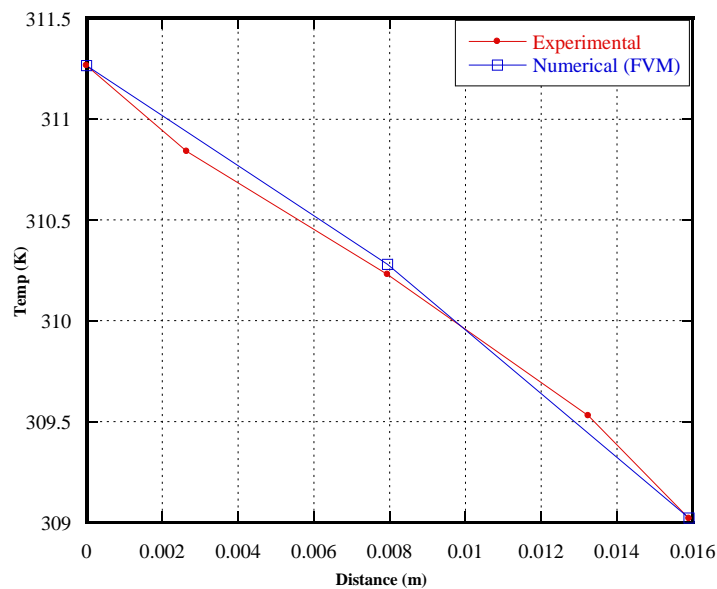


**Figure 5.5** Temperature distribution against particle diameter in an axial direction

In the case of the proposed design, coated particle fuel in the cladding tube will generate heat by nuclear fission. Here, the heat to be generated by nuclear fission in the particle is expected

to be uniformly distributed throughout the volume of the fissile material. The general governing equation for the heat conduction in this case is expressed by Eq. (5.23), hence individual particle surface temperature is assumed uniform and heat transfer by conduction at the contact spot between adjacent coated particle fuels in the cladding tube can be expressed by using Eq. (5.24):

$$\frac{1}{r^2} \frac{\partial}{\partial z} \left( k_s r^2 \frac{\partial T}{\partial z} \right) + S_{gen} = \rho c_p \frac{\partial T}{\partial t} \quad (5.23)$$

$$Q_c = k_{eff}^c A_c \frac{dT}{dz} \quad (5.24)$$

where temperature  $T$  is uniform on each particle surface. The value of  $k_{eff}^c$  used in the above equation is obtained from the expression in Eq. (5.38).

## 5.5 Heat Transfer at the Contact Spots

Conduction in packed beds occurs at the finite contact spot between adjacent particles in the bed; this is sometimes referred to as the particle-to-particle mode. Conduction also exists at the contact spot between the walls of the bed container and the particles constituting the bed. In beds with adiabatic wall conditions, heat transfer may be assumed small or negligible in radial conduction as well as in bed-to-wall contacts. It should be noted that in the case of the proposed nuclear fuel design, conduction in both radial and axial direction exists at the finite contact spot. Adiabatic wall conditions, often used in industrial practice, are assumed only for experimental purposes. It should be noted that this boundary condition is assumed only for experimental purpose to trap substantial heat in the cylinder, thereby necessitating a rise in helium gas temperature, which might have been lost to the environment if the cylinder wall was not highly insulated. This assumption is not applicable to the proposed design as heat is expected to be transferred across the cladding to heat up the surrounding coolant. Consider a particle test sample located at the bulk region in a random packing structure as shown in Fig. 5.1, the particle test sample bottom and top halves are in contact with  $m$  and  $n$  numbers of particles respectively. Values of  $m$  and  $n$  are function of the bed porosity and particle diameters; the values of  $m$  and  $n$  are in the range of 1 to 4 particles [91] as observed in the experiment. The  $m$  and  $n$  particles serve as heat source(s) and sink(s) respectively to the particle test sample. A thorough knowledge of *contact mechanics* and *thermal contact resistance* is

needed in determining the total heat transferred to and from the particle test sample at the contact region of  $m$  and  $n$  contacting particles.

Through the knowledge gained from this investigation, the heat transfer at the finite contact spot between adjacent coated particle fuels in the proposed design is expected to be uniform in both axial and radial directions because the proposed coated particle fuel is a heat-generating source by nuclear fission. Hence the heat will be uniformly distributed across the surface of each particle fuel. In the case of the proposed design, the number of point contacts between a given coated particle fuel and adjacent particle fuels (and in some cases, the angular distribution of these points) must be determined. Various researchers, such as [33], [34] and [35], have endeavoured to derive correlations that can predict the average coordination  $\overline{N}_c$  number for a given porosity in the bulk region of a randomly packed bed. A summary of all the empirical correlations is presented by [36].

### ***5.5.1 Contact area between adjacent particles***

As in [7], [10], [93], [94], [95], [96], the model presented in this study utilises the concept of a finite contact spot between individual particles in the bed; the dimension of the contact spot as shown in Fig. 5.6 is evaluated from the Hertzian theory of elastic contact (contact mechanics application). The Hertzian theory is based on the principle that contacting surfaces are ideally smooth and in perfect contact thus occupying the entire nominal contact area. In this type of contact, it is assumed that the radii of curvature of the contacting bodies are large compared with the radius of the circle of contact; the contacting bodies are in frictionless contact; the surfaces in contact are continuous and non-conforming.

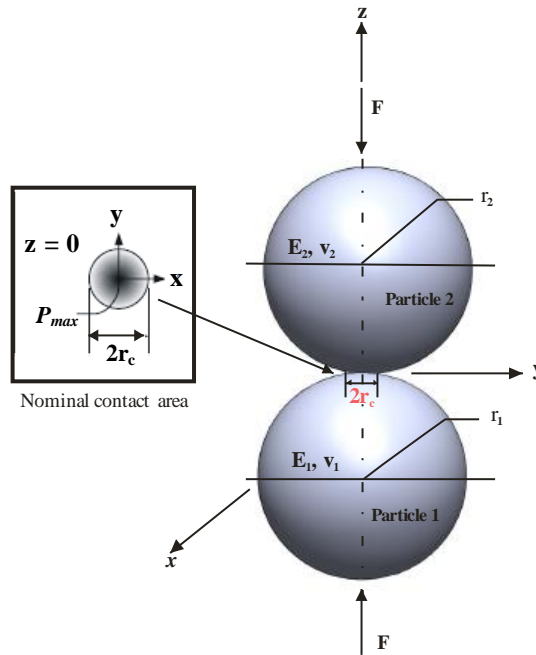


**Figure 5.6** Finite contact spot of smooth contacting spherical surfaces [6]

The area of contact,  $A_c$ , for a circle of radius,  $r_c$ , is given by the Hertz relation [97] in Eq. (5.25), and depends on the normal load,  $F$ , while the maximum contact pressure,  $P_{max}$  at the centre of the circular contact area is given in Eq. (5.26):

$$r_c = \left[ \frac{3}{4} \frac{1 - \nu^2}{E} F \cdot r_p \right]^{1/3} \quad (5.25)$$

$$P_{max} = \frac{3F}{2A_c}, \quad A_c = \pi r_c^2 \quad (5.26)$$

### 5.5.2. Contact region between adjacent particles

The contact region is made up of the nominal contact area found at the contact spot between two adjacent particles and the surrounding gas layer as shown in Fig. 5.7. The heat transferred in an isolated contact region may be used to determine the thermal heat transfer behaviour of the bed. Thermal energy can be transferred across the joint via radiation, conduction through interstitial gas in the gap and conduction through the finite contact spot [9]. Conduction which is predominant at the contact region [98] occurs in rough spherical surfaces via three main paths [9]: microcontacts,  $Q_s$ , the interstitial gas within the microgap,  $Q_g$ , and the interstitial gas within the macrogap,  $Q_G$ .

Microcontacts are discrete spots in the nominal contact area where asperities make *real* contact; it is usually a small fraction or a small percentage of the nominal contact area; microcontacts are generally located far from each other in the nominal contact area, the gap between two microcontacts is referred to as the *microgap* and is filled with interstitial gas. The microgap constitutes a large portion of the nominal contact area. A gap between non-contacting parts of adjacent particles filled with stagnant gas is referred to as the *macrogap*; it is an immediate gas layer surrounding the nominal contact area; both the macrogap and the nominal contact area make up the contact region, most of the heat transfer occurs through the interstitial gas (macrogap).

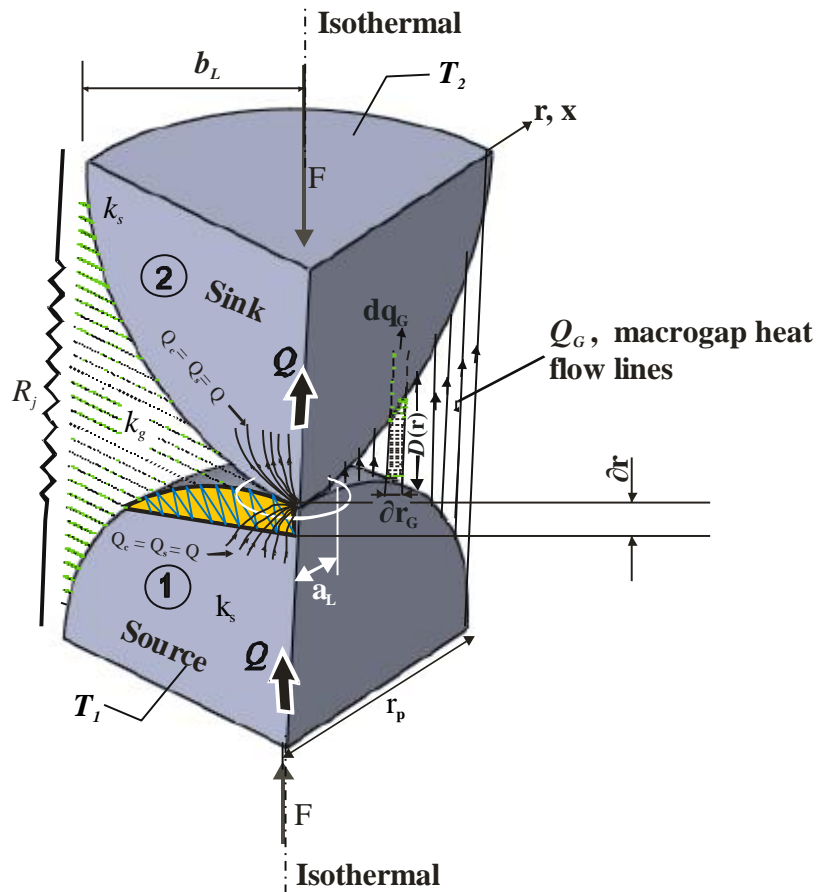


**Figure 5.7** Heat conduction between two smooth elastic particles in perfect contact (Hertzian contact) [6]

The total heat transferred by conduction across the contact region of adjacent particles with particle surfaces of a Brinell hardness of  $1.3 \leq H_B \leq 7.6 \text{ GPa}$  [97] is the summation of the available heat at these paths, which is expressed in Eq. (5.27):

$$Q_{cr} = Q_s + Q_g + Q_G \quad (5.27)$$

The total heat transferred by conduction across the contact region of rough contacting spherical surfaces,  $Q_{cr}$ , is expressed by Eq. (5.28), it is deduced using the *joint thermal resistance*,  $R_j$ , acting at the contact region, a model developed by [9].

The joint thermal contact resistance of rough spherical surfaces with the presence of an interstitial gas contains four thermal resistance components: (i) resistance of the interstitial gas in the microgap,  $R_g$ ; (ii) the thermal resistance of the interstitial gas in the macrogap,  $R_G$ ; (iii) the macrocontact constriction/spreading thermal resistance,  $R_L$  (this is the summation of macrocontact thermal resistance in Spheres 1 and 2,  $R_{L,1}$  and  $R_{L,2}$ ); (iv) the microcontacts constriction/spreading resistance,  $R_s$ . An expression of the total heat transferred across the region relating to the temperature difference across the region and the joint thermal resistance at the contact region is given in Eq. (5.28):

$$Q_{cr} = Q_s + Q_g + Q_G = \frac{\Delta T}{R_j} = \frac{T_1 - T_2}{R_j} \quad (5.28)$$

where  $R_j$  for the rough contact is given in the equation below:

$$R_j = \left[ \frac{1}{\left( \frac{1}{R_s} + \frac{1}{R_g} \right)^{-1} + R_L} + \frac{1}{R_G} \right]^{-1} \quad (5.29)$$

In the study, 15.9 mm diameter stainless steel (AISI 304) spheres are used; the thermal conductivity, specific heat at constant pressure and density are 15.6 W/m·K, 456 J/kg·K and 7913 kg/m<sup>3</sup> respectively and a Brinell hardness of  $H_B < 1.3 \text{ GPa}$ . Hertzian (perfect) contacts are assumed between the contacting particles in this work because the particle falls within a Brinell hardness of  $H_B < 1.3 \text{ GPa}$ . Also for the study, a thermal resistance network will be developed to illustrate thermal resistances present at different parts in the contact region and also to assist in establishing a relation for the joint thermal resistance of particle-to-particle contact in the medium (see Fig. 5.8).

In the case of Hertzian (perfect) contact,  $R_s$ ,  $R_g$  and  $R_L$  are replaced by the Hertzian microcontact,  $R_c$ , [94], due to the surface smoothness of the particle, as shown in Fig. 5.7. The expected temperature drop across the joint usually experienced in rough contact because of

thermal resistance is assumed here in Hertzian contact negligible. The total heat by conduction across the region of adjacent particles in perfect contact  $Q_{cp}$  can then be expressed by Eqs. (5.30) and (5.33). It should be noted that the role played by helium gas in the medium by exhibiting the quality of being a better conducting gas also helps to reduce thermal contact resistance at the particle-to-particle interface.

$$Q_{cp} = Q_c + Q_G \tag{5.30}$$

The joint thermal resistance for Hertzian contact expressed in Eq. (5.31) is made up of two resistance components,  $R_c$  and  $R_G$ , in parallel, as illustrated in the thermal resistance network in Fig. 5.8.

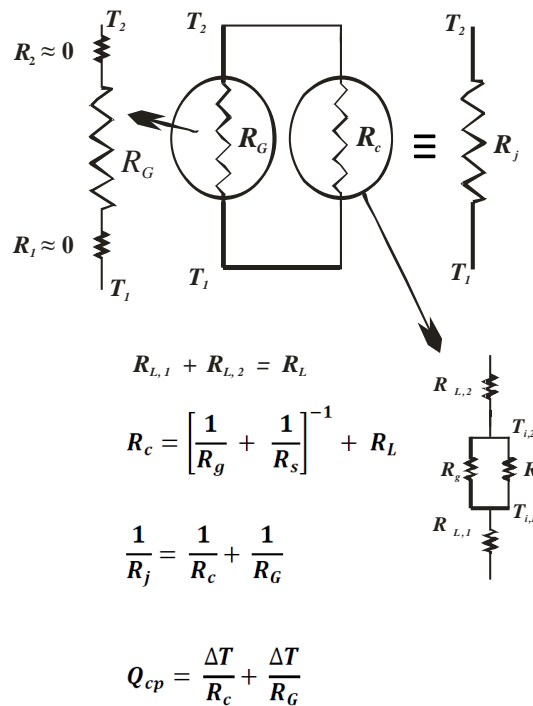


**Figure 5.8.** Thermal resistance for spherical Hertzian contact network [6]

$$R_j = \left[ \frac{1}{R_c} + \frac{1}{R_G} \right]^{-1} \tag{5.31}$$

$$Q_{cp} = Q_c + Q_G = \frac{\Delta T_i}{R_j} = \frac{\Delta T_i}{R_c} + \frac{\Delta T_i}{R_G} \quad (5.32)$$

$$Q_{cp} = Q_c + Q_G = k_{eff}^c \frac{dT_i}{dz} A_c + \frac{\Delta T_i}{\left[ \frac{1}{R_G} \right]^{-1}} \quad (5.33)$$

Heat transfer by conduction through the microcontact (finite contact spot),  $Q_c$ , is determined using the expression in Eq. (5.22). While using an implicit finite volume scheme in obtaining  $T_i$  in the expression for  $Q_c$  in Eq. (5.22), values of  $Q_G$  and  $R_G$  are calculated from the relationships developed by [99] in Eqs. (5.35) and (5.37).

The method developed by [99] is applied to determine  $Q_G$ . The macrogap provides a parallel path for transferring heat from the heat source to the sink. Conduction heat transfer in a gas layer between two parallel plates/surfaces is commonly categorised into four heat flow regimes: continuum, temperature-jump or slip, transition and free molecular. The parameter that characterises the regimes is the Knudsen number,  $Kn = \Lambda/d$ , where  $\Lambda$  and  $d$  are the molecular mean free path and the distance separating the two plates/surfaces respectively. The molecular mean free path expressed mathematically in Eq. (5.34) is defined as the average distance a gas molecule travels before it collides with another gas molecule and it is proportional to the gas temperature and inversely proportional to the gas pressure:

$$\Lambda = C_A \frac{T_g}{P_g} \quad (5.34)$$

where  $T_g$  and  $P_g$  are the gas temperature and pressure respectively, while  $C_A$  is a gas specific constant. The macrogap thermal resistance is considered to provide a parallel path between the heat source and the sink. The macrogap area,  $A_G$ , of the non-contacting region of the solids is divided into infinitesimal surface elements,  $\partial r_G$ , as shown in Fig. 5.7, heat transfer at this region through interstitial gas,  $Q_G$ , is determined using [99] in Eq. (5.35):

$$Q_G = \iint \frac{k_g(T_1 - T_2)}{D(r) + M} dA_G \quad (5.35)$$

$$M = \left( \frac{2 - \alpha_{T1}}{\alpha_{T1}} + \frac{2 - \alpha_{T2}}{\alpha_{T2}} \right) \left( \frac{2\gamma_g}{1 + \gamma_g} \right) \frac{1}{Pr} \Lambda \quad (5.36)$$

where

- $D(r)$  is the sphere profile in the non-contacting region;
- $T_1, T_2$  are the heat source and sink temperatures respectively;
- $d$  is distance between the two isothermal parallel plates/surfaces;
- $\alpha_{T1}, \alpha_{T2}$  are thermal accommodation coefficients (TAC);
- $\gamma_g$  is the ratio of gas specific heats;
- $M$  is the gas parameter.

The thermal accommodation coefficient  $\alpha_T$  represents the extent to which the exchange of energy takes place between the gas and the solid. A value of 0.55 is applicable for helium gas and is used in the study. By using the relation,  $R_G = \Delta T/Q_G$ , the thermal resistance is obtained in [99] Eq. (5.37). The thermal resistance network for a Hertzian contact is represented in Fig. 5.8. The distance ranges,  $a_L$  and  $b_L$ , are the macrocontact radius and chord of the macrogap.

$$R_G = \frac{1}{2\pi k_g} \left[ \int_{a_L}^{b_L} \frac{r dr}{D(r) + M} \right]^{-1} \quad (5.37)$$

### 5.5.3 Effective thermal conductivity

The effective thermal conductivity,  $k_{\text{eff}}$ , is an averaged parameter, which describes the total thermal performance of the granular medium that constitutes the bed. Effective thermal conductivity can be determined in a porous medium by conduction when the fluid phase is stagnant and by buoyancy-induced convection when the fluid phase is in motion. For appropriate determination of the effective thermal conductivity in porous media, three dominating variables are essential: the solid-phase thermal conductivity, the fluid-phase thermal conductivity and the microstructure. The two correlations widely used [100] are the models of [101] and a model based on the original work of [102]. The effective thermal conductivity is considered to consist of three parts, listed below, and the sum gives the total effective thermal conductivity:

- effective thermal conductivity at the contact interface between particles ( $k_{\text{eff}}^c$ );
- effective thermal conductivity due to thermal radiation ( $k_{\text{eff}}^r$ );

- effective thermal conductivity across the stationary fluid phase filling the interstitial voids between contact particles ( $k_{eff}^G$ ).

(i) Effective thermal conductivity across the contact interface between particles: The component of effective thermal conductivity that describes conduction through the particles and across the contact between the particles is predicted by the model in Eq. (5.38) as defined by [103]. The model is expressed as:

$$k_{eff}^c = k_s \left[ \left( \frac{3(1-v^2)}{4E_s} \frac{F d_p}{2} \right)^{1/3} \frac{1}{0.531S} \left( \frac{N_A}{N_L} \right) \right] \quad (5.38)$$

where  $F = P_p \frac{S_F}{N_A}$

- $N_A = 1/d_p^2$  and  $N_L = 1/d_p$  denote the number of particles per unit area and length respectively.
- $S = 1$  and  $S_F = 1$  are constants related to the volumetric arrangement of the particles [38].
- $k_s$  is the solid-phase (particle) thermal conductivity.
- $E_s$  denotes Young's modulus of the particles (solid phase).
- $v$  is the Poisson ratio.
- $P_p$  and  $F$  are the external pressure as a result of the stacked particles and the force responsible for particle deformation due to the accumulated mass of the particles in the bed respectively.

The value of  $k_{eff}^c$  expressed in Eq. (5.38) is used as the effective thermal conductivity across contact interface between particles in Eqs. (5.22), (5.24) and (5.33).

(ii) Effective thermal conductivity due to thermal radiation: The effective thermal conductivity accounting for interstitial void radiation and solid conduction is given by the Zehner-Schlünder equation as modified by [104]:

$$k_{eff}^r = \left[ \left[ 1 - (1 - \varepsilon)^{1/2} \right] \varepsilon + \frac{(1 - \varepsilon)^{1/2}}{2/\xi_s - 1} \frac{\beta + 1}{\beta} \frac{1}{1 + \frac{1}{(2/\xi_s - 1)^\psi}} \right] 4\sigma T_s^3 d_p \quad (5.39)$$

where

$$\beta = 1.25 \left( \frac{1 - \varepsilon}{\varepsilon} \right)^{10/9}$$

$$\psi = \frac{k_p}{4\sigma T_s^3 d_p}$$

Here,

- $\xi_s$  denotes the particle emissivity.
- $\sigma$  is the Stephan-Boltzmann constant.
- $\beta$  as used in Eq. (5.39) is the deformation factor.
- $T_s$  is the solid-phase temperature.
- $\psi$  used in Eq. (5.39) forms part of Damköhler's equivalent thermal conductivity [105] describing the radiative heat transfer.
- $k_p$  is the thermal conductivity of the fuel particle.

Thermal radiation is a heat transfer mechanism that occurs in packed beds at high temperatures; the phenomenon is a complex problem. Radiant heat as shown in Fig. 3.1 can be transferred via three paths: radiation (a) between bed particles, (b) between the bed particles and interstitial gas, and (c) between interstitial gas and the bed wall. The radiant heat transfer between the particles can be analysed as a parallel path to the conduction part. While radiative absorption and emission are major radiative mechanisms in homogeneous media, however, an additional mechanism of scattering is considered if the medium contains inhomogeneities. Summaries of most studies conducted on radiative heat transfer in packed beds are given by [106] and [107].

Thermal radiation heat transfer inside the microgaps is complex and very difficult to characterise [98]. In contrast, [99] derives a ratio between the radiative conductivity and thermal conductance through the contact area between a flat and a spherical surface. They demonstrate that although radiation through the contact area becomes relatively important at higher temperatures, the radiation heat transfer contribution is still far less than that of the

conductance. Therefore, in the study, it is considered that the thermal radiation heat transfer normally occurs in the region between  $r_c \leq r \leq r_p$  for the Hertzian contact network. The heat transfer through thermal radiation is expressed by Eq. (5.42):

$$\frac{1}{r} \frac{\partial}{\partial z} \left( k_{eff}^r r \frac{\partial T}{\partial z} \right) = -\frac{\partial q_R''}{\partial z} \quad (5.40)$$

Integrating both sides

$$k_{eff}^r \frac{\partial T}{\partial z} = -q_R'' \quad (5.41)$$

$$Q_R = A_p \left( k_{eff}^r \frac{\partial T}{\partial z} \right) = -A_p q_R'' \quad (5.42)$$

(iii) Effective thermal conductivity across the stationary fluid phase filling the interstitial voids between the particle: The component of  $k_{eff}^G$  is given in Eq. (5.43):

$$\frac{k_{eff}^G}{k_f} = 1 - \sqrt{1 - \varepsilon} + \frac{2\sqrt{1 - \varepsilon}}{1 - \kappa\beta} \left[ \frac{(1 - \kappa)\beta}{(1 - \kappa\beta)^2} \ln \left( \frac{1}{\kappa\beta} \right) - \frac{\beta + 1}{2} - \frac{\beta - 1}{1 - \kappa\beta} \right] \quad (5.43)$$

where  $\beta$  is the same as in Eq. (5.39) and  $\kappa = k_g/k_p$  is the conductivity ratio. The model is based on a one-dimensional heat flow for conduction through packed beds of spherical particles as defined by [103]. The above correlations are combined to obtain an expression in Eq. (5.44) for the total effective thermal conductivity of the homogeneous section of the packed particle bed:

$$k_{eff}^T = k_{eff}^c + k_{eff}^r + k_{eff}^G \quad (5.44)$$

## 5.6 Porous Media Heat Transfer Characteristics

### 5.6.1 Medium under investigation

Heat transfer analysis between elements with point contact can be quite complicated due to the time-dependent behaviour and the complex geometrical contact arrangement [39]. For a bottom-heated porous medium shown in Fig. 5.1, heated helium gas flows axially upwards and radially outwards due to wall channelling. Consider a particle test sample (which is the particle

under consideration) with adjacent contact test particles in the medium as shown in Fig. 5.1. The particle test sample experiences thermal energy being transferred in or out of it from neighbouring contact particles and gaining heat from hot flowing helium gas (heated from below) thus exhibiting an attribute of a heat collector or heat sink.

Considering the porous medium under investigation, which is isotropic and exhibits non-local thermal equilibrium (NLTE), keeping in mind that heat transfer in the medium occurs between solid and fluid phases, a conservative heat transfer energy balance as shown in Eq. (5.45) is established to determine the heat transfer coefficient obtainable in the medium under investigation. The equation accounts for the heat transfer experienced by the particle test sample with adjacent contact test particles taking into consideration convective, conductive and radiative heat transfer modes occurring around it. In beds with adiabatic wall conditions, the radial conduction as well as the bed-to-wall surface heat transfer may be assumed to be small or negligible. Adiabatic wall conditions, often used in industrial practice, are assumed in this investigation. It should be noted that this boundary condition is assumed only for experimental purposes to trap substantial heat in the cylinder, thereby necessitating a rise in helium gas temperature, which might have been lost to the environment if the cylinder wall was not highly insulated. This assumption is not applicable to the proposed design as heat is expected to be transferred across the cladding to heat up the surrounding water.

$$h_{fp} \left( A_p - \sum_{e=1}^8 A_{c_e} \right) (T_f - T_p) + \sum_{m=1}^4 Q_{m(BcdR)} = (1 - \varepsilon) (V_T \rho_p c_p) \frac{\partial T_p}{\partial t} + \sum_{n=1}^4 Q_{n(TcdR)} \quad (5.45)$$

The left of Eq. (5.45) represents the total heat supplied to the particle test sample while the right-hand side is the heat stored within it plus that which is transferred from it. Heat from adjacent contacting test particles (usually ranging from one to four) below the particle test sample serves as heat source while the particle test sample serves as a heat sink. The reverse is the case for adjacent contact test particles (usually ranging from one to four) above it where the particle test sample supplies heat by conduction through the contact points. The surface area of the particle test sample exposed to convective heat transfer is the difference between the spherical particle total surface area,  $A_p$ , and the sum of  $e$  contact area spots located on the surface of the particle test sample. The factor  $(1-\varepsilon)$  is the ratio of volume occupied by particles to the total volume of the element  $V_T$ . Because the particle test sample and adjacent contact test particles are not in isolation but are in a porous medium, the solid volume fraction  $(1 - \varepsilon)$  of

the solid phase in the above equation is applied. Heat transfer effects in porous media are determined by dimensionless parameters such as the Nusselt, Rayleigh, Prandtl, Grashof and Reynolds numbers. In applying Eq. (5.45) to evaluate the fluid-to-particle heat transfer coefficient,  $h_{fp}$ , in relation to the work under investigation, the heat transfer modes mechanism (natural convection, conduction and radiation) acting in the medium at elevated temperature must be analysed and resolved effectively. Combined conduction and radiation heats transferred to lower half  $Q_{(BcdR)}$  of the particle test sample, and from the upper half  $Q_{(TcdR)}$  of the particle test sample are established in Eqs. (5.46) and (5.47). Incorporating the expressions into Eqs. (5.46) and (5.47) into Eq. (5.45), the values of  $h_{fp}$  for the bed can be determined through the expression in Eq. (5.48):

$$Q_{BcdR} = Q_{cp} + Q_R = \left\{ k_{eff}^c \frac{dT_i}{dz} A_c + \frac{\Delta T_i}{R_G} \right\}_{Bc} - \{A_p q_R''\}_{Bc} \quad (5.46)$$

$$Q_{TcdR} = Q_{cp} + Q_R = \left\{ k_{eff}^c \frac{dT_i}{dz} A_c + \frac{\Delta T_i}{R_G} \right\}_{Tc} - \{A_p q_R''\}_{Tc} \quad (5.47)$$

$$h_{fp} = \frac{(1-\varepsilon) \frac{(\rho c_p V_T)}{\Delta t} [T^{t+\Delta t} - T^t] - \sum_{m=1}^4 \left[ \left\{ k_{eff}^c \frac{dT_i}{dz} A_c + \frac{\Delta T_i}{R_G} \right\}_{Bc} - \{A_p q_R''\}_{Bc} \right]_m + \sum_{n=1}^4 \left[ \left\{ k_{eff}^c \frac{dT_i}{dz} A_c + \frac{\Delta T_i}{R_G} \right\}_{Tc} - \{A_p q_R''\}_{Tc} \right]_n}{(A_p - \sum_{e=1}^8 A_{ce}) (T_f - T_p)} \quad (5.48)$$

Properties of the test particles were taken directly from literature and consist solely of the material and thermal properties of 304 stainless steel (see Table. 5.1).

**Table 5.1** Parameters used in determining the heat transfer effect in the medium

Parameter	Value
Density, $\rho_p$	7913 kg/m <sup>3</sup>
Poisson ratio, $\nu$	0.29
Young's modulus, E	193 GPa
Particle radius, $r_p$	7.95 mm
Thermal diffusivity, $\alpha$	$4.3210 \times 10^{-6} \text{ m}^2 \text{ s}^{-1}$
Thermal conductivity, $k_p$	15.6 W/m K
Thermal conductivity, $k_f$	0.14786 W/m K

**Table 5.1 (Continued)**

<b>Parameter</b>	<b>Value</b>
Number of particles	180
Bed diameter	72 mm
Cylinder height	760 mm
Cylinder wall thickness	38 mm
Prandtl number, Pr	0.689
Specific heat ratio of gas $\gamma_g$	1.667
Molecular mean free path, $\Lambda$	173.6 nm
Thermal accommodation coefficient (TAC)	0.55
Initial enclosed cavity pressure (abs)	86.6 kPa
Induction cooktop power (max)	1800 W

### 5.6.2 Proposed medium

A schematic of the regular 4 metre long light-water reactor (LWR) cladding with fuel pellets is depicted in Fig. 1.1. A possible solution towards enhancing the safety of LWR by re-designing the fuel in the form of loose coated particles in a helium atmosphere inside the nuclear fuel cladding tube is proposed in the study. A schematic of the proposed new fuel design is equally depicted in Fig. 1.2. It is believed that the knowledge gained from the experimental evaluation of the heat transfer phenomenon in packed beds will be found beneficial in the proposed design.

Since the coated particle fuel is a heat-generating source by nuclear fission, the temperature distribution on the surface of each coated particle is expected to be uniform. A situation of steady-state heat generation is applicable in this circumstance. Heat is produced by the  $UO_2$  fuel kernel at the constant rate  $q'''$  [ $W/m^3$ ] per unit volume inside the coating layers. The temperature in the fuel kernel is only a function of the distance,  $r_{fuel}$ , from the centre of the sphere (see Fig. 1.2) so that the heat conduction equation is expressed by Eq. (5.49). A Poisson equation in Eq. (5.50) can be used to represent the one-dimensional steady-state heat conduction of the fuel:

$$\frac{1}{r_{fuel}^2} \frac{\partial}{\partial r} \left( r_{fuel}^2 \frac{\partial T}{\partial r} \right) + \frac{q'''_{gen}}{k_{fuel}} = \frac{1}{\alpha} \frac{\partial T}{\partial t} \quad (5.49)$$

$$\int_{cv} \frac{1}{r_{fuel}^2} \frac{\partial}{\partial r} \left( r_{fuel}^2 \frac{\partial T}{\partial r} \right) dV + \int_{cv} \frac{q_{gen}'''}{k_{fuel}} dV = 0 \quad (5.50)$$

Integrating the governing differential equation in Eq. (5.50) over a control volume (cv) gives the solution expressed by Eq. (5.51) of the heat conduction by the fuel kernel at steady-state heat generation:

$$Q_{fuel} = Q_{nu} = \left( \left[ k_{fuel} \frac{\partial T}{\partial r} \right]_s A_s - \left[ k_{fuel} \frac{\partial T}{\partial r} \right]_n A_n \right) \quad (5.51)$$

The expression in Eq. (5.24) is considered appropriate for the heat transfer by conduction at contact spots between adjacent particle fuels. On this basis, Hertzian (perfect) contacts are assumed between contacting particle fuels. For the proposed design, the thermal resistance network developed in Fig. 5.8 to illustrate the thermal resistances present at different parts in the contact region and to assist in establishing a relation for the joint thermal resistance of particle-to-particle contact in a medium is applicable. Hence the total heat transfer by conduction across the contact region of adjacent particles in perfect contact  $Q_{cp}$  is expressed by Eq. (5.52) for the new design with the assumption that the same magnitude of heat is conducted in both axial and radial directions:

$$Q_{cp} = Q_c + Q_G = k_{eff}^c \frac{dT}{dz} A_c + \frac{\Delta T}{R_G} \quad (5.52)$$

Consider an arbitrary volume,  $V$ , of material throughout a portion of which heat is being produced. From the conservation of energy, the rate at which heat is produced by the fuel kernel,  $Q_{nu}$ , must be equal to the rate at which it flows out. If this were not the case, the substance would change temperature and therefore would not be in a steady state. Hence the conservative heat transfer energy balance in the proposed medium using the basic unit cell model can be expressed by Eq. (5.53):

$$Q_{nu} = (1 - \varepsilon) \frac{(\rho_p c_p V_T) \Delta T}{\Delta t} + \bar{N}_c Q_{cp} + A_p q_R'' + h_{pf} A \Delta T \quad (5.53)$$

Applying the BUC model to the medium of the proposed new fuel design,  $Q_{nu}$  is the heat generated by nuclear fission in the coated particle fuel,  $\bar{N}_c$ , as discussed in Section 2.2.2, is the frequency distribution of the number of contact points, which in most cases is referred to as the average coordination number or average kissing number which is a function of both the bed

porosity and particle diameter. The correlation proposed by [36] in Table 2.3 for  $\bar{N}_c$  expression is applied in this study. The particle-to-fluid heat transfer coefficient,  $h_{pf}$ , developed for the medium of the proposed design, is expressed in Eq. (5.54):

$$h_{pf} = \frac{Q_{nu} - (1 - \varepsilon) \frac{(\rho c_p V_T) \Delta T}{\Delta t} - \left\{ \bar{N}_c \left[ \left( k_{eff}^c \frac{dT}{dz} \right) A_c + \frac{\Delta T}{R_G} \right] - A_p q_R'' \right\}}{(A_p - \bar{N}_c A_c)(T_p - T_f)} \quad (5.54)$$

where  $\varepsilon$ ,  $k_{eff}^c$ ,  $q_R''$ ,  $A_p$ ,  $A_c$  represent the bed porosity, the effective thermal conductivity at the contact interface between particles, the radiative heat flux, the spherical particle total surface area and the area of contact spot respectively. The heat transfer characteristics in this study for the proposed new fuel design under natural convection are evaluated using the particle-to-fluid heat transfer coefficient,  $h_{pf}$ , Nusselt number, Grashof number, Prandtl number and the Rayleigh number. These are expressed in Eqs. (5.55) and (5.56):

$$Nu = \frac{h_{pf} d_p}{k_f} \quad (5.55)$$

$$Ra_{d_p} = \frac{g \beta |T_s - T_f| d_p^3}{\nu^2} Pr = Gr \cdot Pr \quad (5.56)$$

### ***Gunn Correlation***

The Gunn correlation [48] used to validate the heat transfer performance of the medium investigated is expressed in Eq. (5.57):

$$Nu_{d_p} = (7 - 10\varepsilon + 5\varepsilon^2) \left( 1 + 0.7 Re_{d_p}^{0.2} Pr^{1/3} \right) + (1.33 - 2.4\varepsilon + 1.2\varepsilon^2) Re_{d_p}^{0.7} Pr^{1/3} \quad (5.57)$$

valid:  $0 < Re_{d_p} < 10^5$

The Gunn correlation is one of the well-known correlations. The correlation is chosen for the following reasons:

- The particle type used in derivation of the correlation is homogeneous. This is similar to the particle used in the experiment and in the proposed fuel design.

- The correlation is developed to accommodate fluid flow within the range from negligible to very large. This parameter in the correlation is essential as it relates to the experiment and proposed design where flow recirculation is dominant in the media.
- The application of voidage or void fraction (porosity,  $\varepsilon$ ) is another important parameter in the correlation. This aids in providing an understanding of the porous structure in the medium under investigation.

## 5.7 Results

The evaluation of fluid-to-particle natural convection heat transfer in randomly packed beds consisting of microparticles was carried out in a test facility of slender cylindrical geometry. Reference values of thermophysical properties of sphere particle and the interstitial gas effect used for the work in determining the conductive heat transfer mode at the contact region were given in Table 5.1. In the investigation, the Nusselt number, the Rayleigh number and the heat transfer coefficient were the basic parameters used in evaluating the convective heat transfer characteristics in the packed bed considered. The value of these parameters was obtained using the expressions in Eqs. (5.48), (5.51) and (5.52), graphs were plotted to demonstrate the variation of these parameters with one another in an increasing bed temperature. Graphs were also used for validating the theoretical method with the [13] correlation. The graphs in Fig. 5.9 depicted an effect of gas temperature on both fluid-to-particle heat transfer coefficient and thermal conductivity of helium gas. From the figure, it could be seen that the fluid-to-particle heat transfer coefficient increased with a rising gas temperature. Another effect of rising gas temperature in the medium shown in the graph was a slight increase in the gas thermal conductivity.

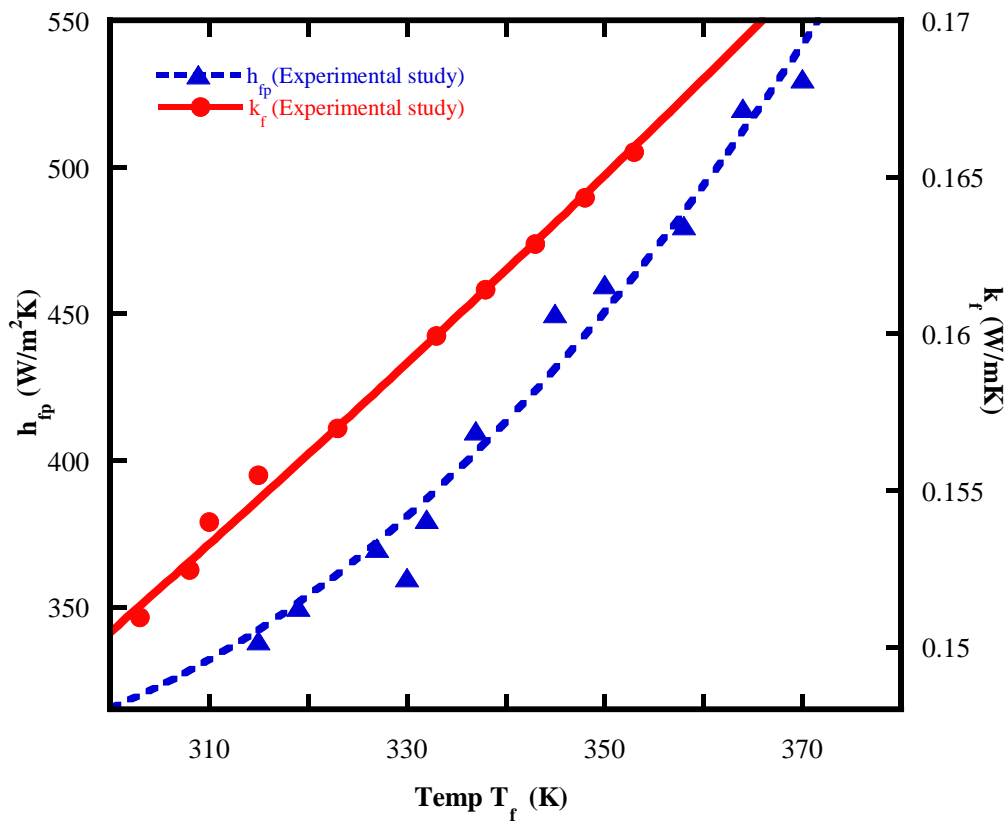


**Figure 5.9** Effect of gas temperature on convective fluid-to-particle heat transfer coefficient and on gas thermal conductivity

Fig. 5.10 is a plot of the Nusselt number as a function of the convective heat transfer coefficient in the bed. Heat transfer coefficient is a quantitative characteristic of convective heat transfer between a gas medium (a fluid) and the solid (particle) surface submerged in the fluid. In heat transfer, at a boundary (surface) within a gas, the Nusselt number (**Nu**) is the ratio of convective to conductive heat transfer across the boundary. From the study, as depicted in the graph, it can be observed that the Nusselt number increases with an increasing heat transfer coefficient as the gas temperature rises.

The significance of the graph is that an increasing Nusselt number corresponds to more active convective heat transfer between a surface and a gas flowing past it. Validation of the study with suitable correlation such as [48] shows good agreement, the difference depicted in the graph when compared with the study may be attributed to the bed materials (type of particle, gas and wall) and nature of heat transfer (i.e. particle-to-fluid, type of convective heat transfer) used in developing the correlation.

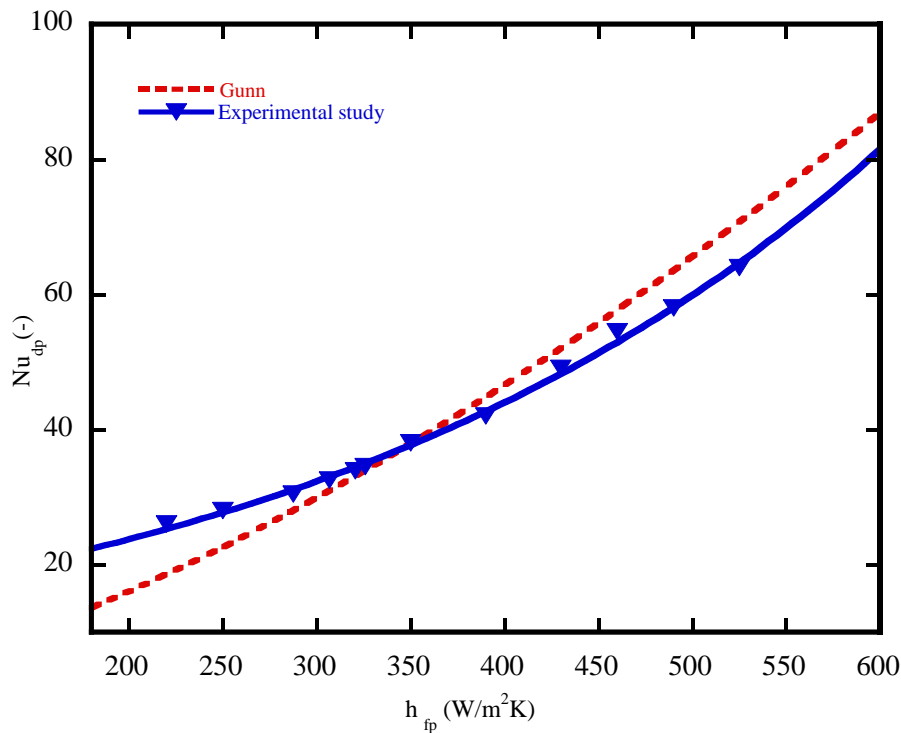


**Figure 5.10** Nusselt number in the packed bed as a function of convective fluid-to-particle heat transfer coefficient

In Fig. 5.11, the variation of Rayleigh number (Ra) with the Nusselt number (Nu) is illustrated. The Rayleigh number is a dimensionless term used in the calculation of natural convection heat transfer in a medium; it is associated with buoyancy-driven flow. Its value in this investigation is determined from the thermophysical properties of the particle test sample and heated helium gas. Parameters needed for determining the Rayleigh number includes the thermal expansion coefficient of the gas, the gas temperature and corresponding viscosity around the particle, the Prandtl number and the particle diameter. Plotted values for Ra in the graph are obtained by inserting these property values, which are mostly temperature dependent, into Eq. (5.56).

Another significant feature shown in Fig. 5.11 is that an increasing Rayleigh number from a relatively low value, as depicted in the graph, is an indication of a rising natural convection heat transfer in the packed bed.

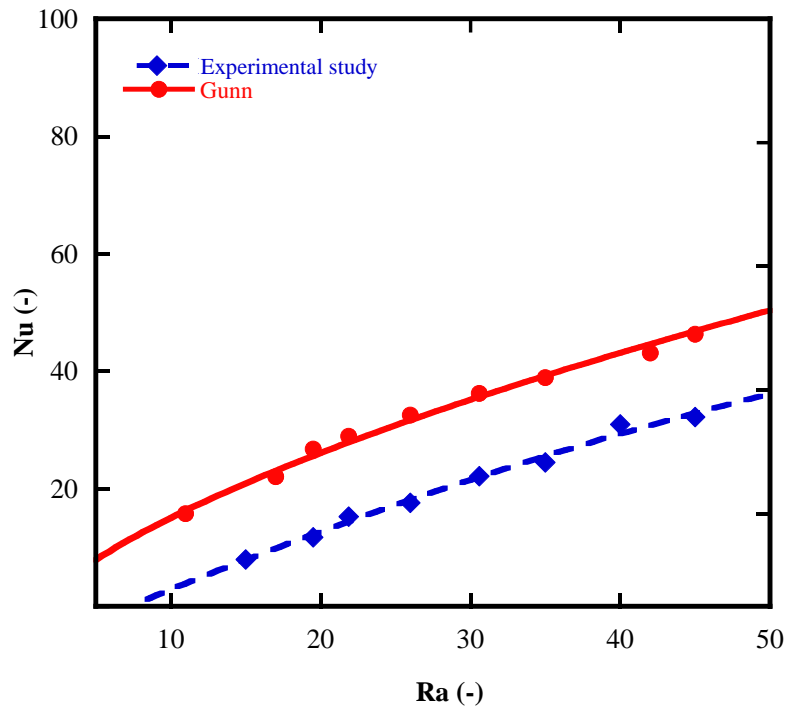


**Figure 5.11** Variation of Nusselt number on the Rayleigh number for fluid-to particles heat transfer

## 5.9 Comparison of Theoretical Analysis and Experimental Evaluation Results

The experimental evaluation of heat transfer in the investigated medium was carried out in Chapter 4 by applying the first principle heat transfer concept to the heat exchange that occurred in the particle test sample and the results obtained forms a representation of the heat transfer characteristics of the investigated medium. This was carried out in isolation from other contacting particles. On the other hand, the basic unit cell model forming the theoretical analysis of the investigation dealt systematically with the heat exchange that was active in and around the same particle test sample putting into consideration contacting particles in the bed and thermal radiation effect at elevated temperatures. A more detailed examination of the particle test sample through the BUC model accounted for the transient heat conduction in the particle test sample along with the various sources of heat at the contact points and at the interstice through the application of different methods, which were not considered in the experimental evaluation process. These differences made the results of the BUC model heat transfer characteristics more dependable compared with results obtained from the experimental evaluation. A conclusive action to provide sufficient assurance of the dependability of the

theoretical analysis is achieved through close examination of the graph in Fig. 5.12 depicting the variation of Nusselt number against the Rayleigh number for the experimental and theoretical results earlier determined in this chapter and the previous one. From the graphs depicted in Fig. 5.12, the Nusselt number for the experimental and theoretical results is observed to rise gradually but with a different profile. The graph of the theoretical Nusselt number is seen to have a similar profile as that of Gunn's correlation results. The profile of the experimental Nusselt number may be attributed to lumped system application assumptions on the particle test sample and the non-consideration of heat source and heat sink phenomenon associated with contacting particles in the investigated configuration. A further rise in the graph of the experimental results after interception with the graph of theoretical results is observed to approach the graph of validating Gunn's correlation [48] results. This development may be attributed to a phenomenon in which the experimental evaluation approach considers the test sample as a single particle in the investigated configuration.

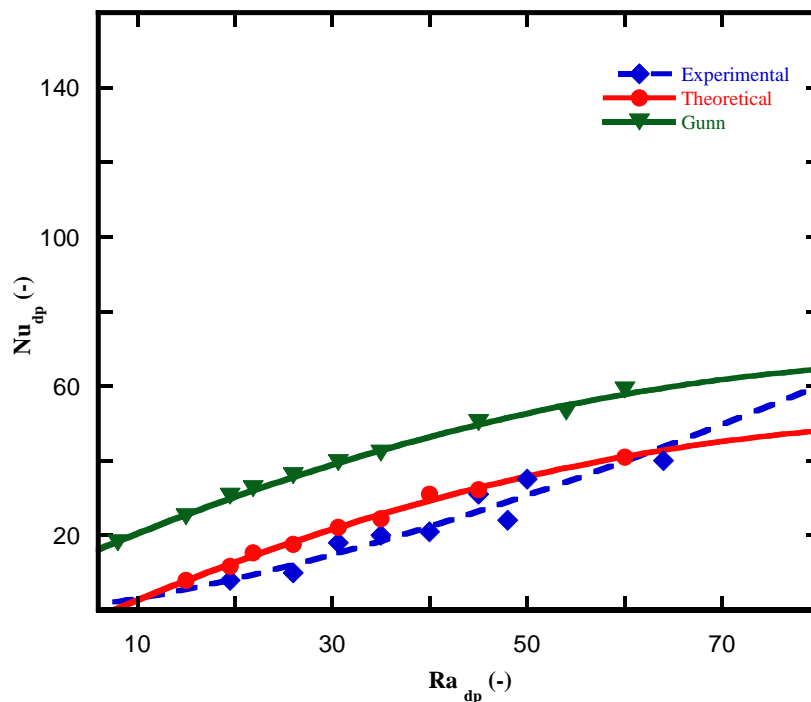


**Figure 5.12** Variation of Nusselt number with Rayleigh number for fluid-to-particle heat transfer

## 5.10 Conclusion

The chapter discussed the heat transfer in the traditional nuclear fuel. The aim of the theoretical analysis was to investigate the heat transfer characteristics in packed beds under natural convection and to validate the results with a suitable correlation such as that of Gunn [48]. The investigation carried out in the bed was done in the bulk region of the bed that formed the major part of the medium. The heat transfer coefficient,  $h_{fp}$ , Nusselt number, Nu, and the Rayleigh number, Ra, were the parameters used in the evaluation and their values were all determined in the bulk region. The results from the study revealed a rising natural convection heat transfer effect between particle surface and the gas flowing past it at an increasing bed temperature. Slightly differing values are likely to be obtained at the near-wall region because of the high porosity associated with this region. Although the heat transfer phenomenon experienced in the theoretical investigation was a reverse case to the real fuel application but for design purpose, the study leads the way in developing a model suitable for evaluating the heat transfer characteristics within the cladding tube with coated particle fuels. In addition, the study has also established the limitations of experimental evaluation approach in determining the heat transfer characteristics in porous media under natural convection.

# 6

## **Numerical Modelling of Natural Convection Heat Transfer and Transport in an Enclosed Slender Tube Geometrical Model Containing Heated Microspheres**

---

### **6.1 Introduction**

Gains from experimental investigations carried out in the study helped significantly in developing a model that can be used in determining particle-to-fluid heat transfer characteristics of the proposed new fuel design in the cladding. The main limitation of heat transfer models in packed beds is the poor knowledge of flow patterns within them; the use of modelling and simulation tools has made it possible to define not only spatial distribution of involved species, but also temperature and velocity profiles within the bed.

Two approaches can be adopted in simulating porous media. The first is the traditional method; it is a direct simulation of spherical packings permeated by fine-scale voids that permit the passage of fluids in a cylindrical vessel. The second is by simulating a porous region whose medium properties are defined; typically, the geometrical model representing the packed bed is specified as a porous region. Lumped parameter effect and other uncertainties including the inability to visualize flow patterns and obtain appropriate velocity profile within the packed beds were part of the limitations identified when this model was simulated in the course of the research work. Simulation results from this approach are just estimates compared with results from direct simulation of spherical packings that are known to be closer to exact solution. Its only advantage is the ability to simulate large-size porous regions using a system with an average-size computational capacity. During this research work, simulations on both approaches were carried out, but in this thesis, only the first simulation approach is reported

because its geometrical model mimics the proposed fuel design contained in the cladding. Simulation results of qualitative features in the medium are seen to depict a convincingly true application.

In recent years, the use of numerical simulation through computational fluid dynamics (CFD) has been growing and this offers the opportunity to predict the heat transfer and fluid flow phenomena in packed beds, thereby providing important reduction of the time required for completing the investigation. The use of CFD limits the number of experiments, accessing information on a large scale which may not be measurable with experimental methods and it is also possible to take into account real physical properties such as high temperature and pressure conditions [108]. Although confronted in the past with microprocessor speed, memory size and computational time, consistent gains over the years in these limiting areas have made highly accurate and computationally expensive computer codes more practical in simulating system behaviour in modern nuclear reactors.

The use of CFD to predict heat or mass transfer coefficients has been applied to many different packed bed configurations but most applications are faced with problems ranging from porosity [109], contact points and accurate meshing of models [110]. In most of the past studies, problems arose as a result of improper meshing of contact points between particles when finite volume methods were used to simulate the flow between particles. The challenge resulted into contracting the particle diameter to permit the CFD calculation but the contraction of spheres increased the porosity of the bed, which affected the pressure drop in the medium. The approach used is detrimental to the quality of the results obtained from such a model. Pressure drop and particle-to-fluid heat and mass transfer in low channel-to-particle diameter ratio were also studied [111], [112], showing that a commercial CFD code can be used to adequately predict particle-to-fluid heat transfer of a single free sphere, and that the CFD code can predict the heat/mass transfer characteristics for packed beds of spherical particles with a channel-to-particle diameter ratio between 1 and 2 with an average error of 15% compared with experimental values. A simple model consisting of three spheres in a tube was later developed to investigate the wall heat transfer coefficients [113]. An extended model by [114] was developed to handle eight spheres, divided into two layers of four spheres without solid-solid contact points. However, [115] incorporated contact points between the solids in a 10-sphere model, which used spherical dead volumes around the contact points. This model showed flow

and heat transfer behaviour that could not be described by the conventional fixed bed model. Simulations were also presented for a model geometry of 44 solid spheres in a tube with tube-to-particle diameter ratio equal to 2 [116]. Velocity field profiles and temperature contours were obtained with emphasis on the wall-particle region. Comparisons were made with measured temperature profiles in a typical experimental set-up with the same geometry. Several correction factors were required to compensate for non-ideal experimental measurements, and for phenomena that were not included in the CFD model. After correction, excellent agreement could be obtained between simulation and experiment.

The study investigated the heat transfer characteristics and flow distribution under natural convective condition, anticipated in beds of randomly packed spheres (coated fuel particles) through the use of CFD simulations. A geometrical model of the bed containing 171 uniformly sized particles randomly packed in an enclosed slender cylindrical tube was modelled and analysed at a particle surface temperature of 700K. A particle surface temperature of 700K is an assumed average working temperature in LWRs. Random packing of the particles was achieved by discrete element method (DEM) simulation with the aid of Star CCM+ commercial code while particle-to-particle and particle-to-wall contacts were achieved through the combined use of the commercial code and a CAD package.

## 6.2 Heat Transfer in Models

The first step in the solution of fixed bed flow and heat transfer problems in complex geometry is to solve the problem of one sphere suspended in an infinite domain of fluid. Basic simulation knowledge of particle-to-fluid heat transfer for a single free sphere in an ‘infinite’ fluid domain is considered necessary for better understanding of simulating packed particles in a tube. Considering a single free sphere in a medium simulated using CFD for particle-to-fluid heat transfer rate,  $Q$ , the temperature of the surface of the particle is set to a surface temperature,  $T_p$ , while the fluid at the boundary of the domain is set to a lower bulk temperature,  $T_\infty$ . Due to the temperature difference between the particle surface and the fluid, heat is transferred from the particle to the fluid. For each simulation, temperature contour plots were analysed, and heat flux through the particle surface was recorded. With this data, the particle-to-fluid average heat transfer coefficient,  $\bar{h}$ , can be determined as expressed by Eq. (6.1):

$$\bar{h} = \frac{\bar{q}''}{T_p - T_\infty} = \frac{\bar{Q}}{\pi d_p^2 (T_p - T_\infty)} \quad (6.1)$$

The average Nusselt number of the single particle is expressed by Eq. (6.2):

$$\overline{Nu} = \frac{\bar{h}d_p}{k_f} = \frac{\bar{Q}}{\pi d_p k_f (T_p - T_\infty)} \quad (6.2)$$

This model works well for simple cases such as a single free sphere, where the temperature difference between the surface and the bulk temperature is well defined. However, it is less applicable to packed beds because the bulk temperature is not easily defined [112]. In packed beds with a constant particle surface temperature, the resistance to heat transfer resides only on the fluid side. Theoretical analysis shows that if axial fluid thermal dispersion is taken into consideration, a conservative heat energy balance equation can be established and the heat transfer coefficient deduced. For packed beds contained in an enclosed tube with a given particle surface temperature,  $T_p$ , like the case under investigation,  $Q_{nu}$  is considered as the heat generated by nuclear fission in the coated particle fuel,  $\bar{N}_c$  is the average coordination number or average kissing number [36], which is a function of both the bed porosity and particle diameter,  $R_G$  is the thermal resistance of the interstitial gas in the macropag.

Considering a basic unit cell in the medium of the proposed new fuel design, the convectonal engineering expression developed in the course of this research work for the particle-to-fluid heat transfer coefficient,  $h_{pf}$  [6], is given in Eq. (6.3). For each simulation, temperature, thermal conductivities and density profiles along the bed were recorded and analysed. With the collected data,  $h_{pf}$  is obtained from Eq. (6.3):

$$h_{pf} = \frac{Q_{nu} - (1 - \varepsilon) \frac{(\rho c_p V_T) \Delta T}{\Delta t} - \left\{ \bar{N}_c \left[ k_{eff}^c \frac{dT}{dz} A_c + \frac{\Delta T}{R_G} \right] - A_p q_R'' \right\}}{(A_p - \bar{N}_c A_c) (T_p - T_f)} \quad (6.3)$$

where  $\varepsilon$ ,  $k_{eff}^c$ ,  $q_R''$ ,  $A_p$ ,  $A_c$  represent the bed porosity, the effective thermal conductivity at the contact interface between particles, the radiative heat flux, the spherical particle total surface area and the area of contact spot respectively.

The heat transfer characteristics in this study under natural convection and as expected for the proposed new fuel design are evaluated using the particle-to-fluid heat transfer coefficient,  $h_{pf}$ , Nusselt number,  $Nu$ , Grashof number,  $Gr$ , Prandtl number,  $Pr$ , and the Rayleigh number,  $Ra$ . These are expressed in Eqs. (6.4) and (6.5):

$$Nu_{d_p} = \frac{h_{pf} d_p}{k_f} \quad (6.4)$$

$$Ra_{d_p} = \frac{g\beta|T_s - T_f| d_p^3}{\nu^2} Pr = GrPr \quad (6.5)$$

## 6.3 Geometrical Models

### 6.3.1 Packing of spherical particles in the tube

Random particle packings can be built by means of different methods. These methods are essentially of two types: deposition algorithms and the dynamic simulation method known as the discrete element method (DEM). Deposition algorithms are generally very quick but provide samples that are mechanically unstable. Furthermore, these algorithms are not suitable for the construction of very dense packings such as a granular bed obtained by deposition under gravity. In this work, a discrete element method simulation was used to construct a densely packed cylindrical sample composed of spherical particles. A geometrical model of the proposed new fuel design was developed with the aid of a commercial CFD code for the DEM simulation (see Fig. 6.1) and a CAD package for creating contact points between adjacent packed particles by expansion of packed bed particle diameter. DEM is an engineering numerical method used to simulate motion of a large number of interacting discrete objects, which are typically solid particles. The DEM model established by [117] is an extension of Lagrangian modelling methodology to include dense particle flows; Star CCM+ uses a classical mechanics method to model DEM, which is based on soft-particle formulation where particles are allowed to develop an overlap [118]. The numerical sample is very similar to the experimental close-packed materials and its solid fraction can be adjusted by the tuning friction or cohesion between particles [119] and [120]. Before the random packing of particles is carried out, a particle and cylinder diameters mimicking the proposed fuel design are chosen.

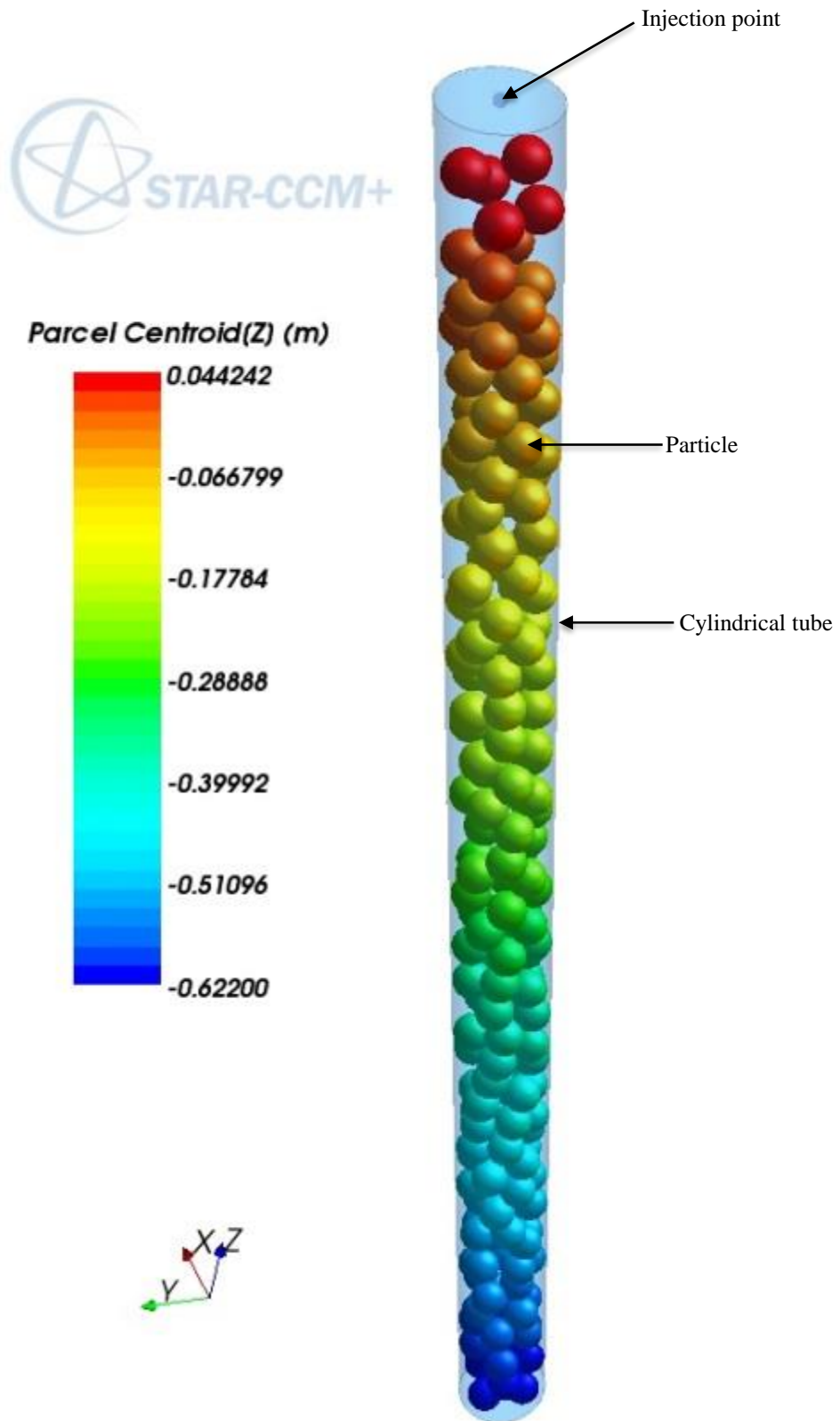


**Figure 6.1** DEM simulated randomly packed particles

Uniform particles of 15.9mm diameter and a cylinder of 40mm diameter were used in this study for the DEM simulation. Particle diameters of 17.46mm and 15.9mm are standard stainless steel (AISI 304) spheres but the latter diameter was chosen to accommodate more particles in the slender tube. A single injector with random point distribution was used to inject particles (raining of particles) into an enclosed tube (see Fig. 6.1). The parcel centroid indicator bar depicted in Fig. 6.1 is the visualisation of the locus of parcel positions in the  $z$ -axis direction. Parcels are a discretisation of the population of particles. Further details on the DEM simulation can be found in Appendix B.3. To establish real particle-to-particle and particle-to-wall contact points, a 0.5% particle diameter expansion was carried out in the study on each bed particle. Convergence problems were not detected during simulation runs.

### 6.3.2 CAD operation and contacts creation

For appropriate volume mesh generation to be carried out on the geometry, some work needed to be done on the DEM simulated randomly packed particles to close up the existing gap between adjacent particles and between the walls and particles (see Fig. 6.2a).

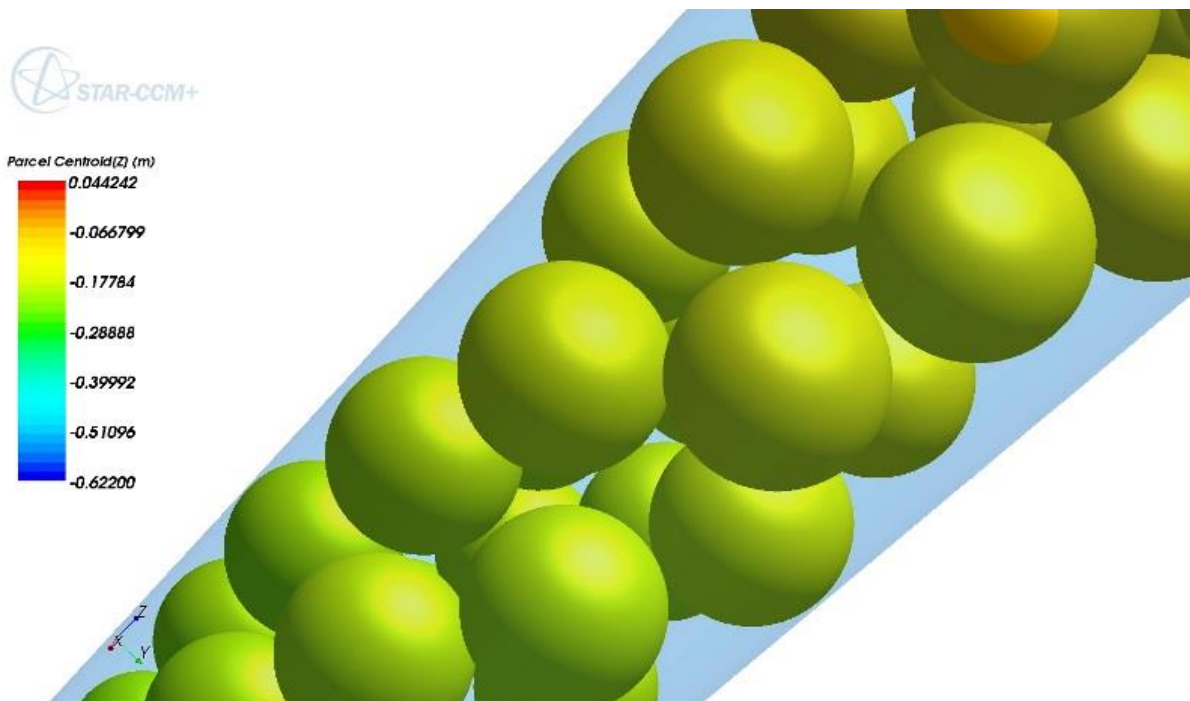


**Figure 6.2(a)** DEM simulation model with gap between two particles and gaps between wall and particles.

The x, y and z centroid coordinate points of all packed particles obtained through the X-Y plot were extracted from the Star CCM+ environment into an Excel spreadsheet. The centroid of all the 171 particles was then imported from the Excel spreadsheet through the use of a macro visual basic programme (see Appendix B.2) into a SolidWorks (CAD) environment (see Fig. 6.2b). Particles with 0.5% diameter increment (expansion to create small overlapping between particles) were drawn on each centroid to generate particle-to-particle and particle-to-wall contacts (see Fig. 6.2c). A Boolean subtract operation was carried out to cut out the packed particles (solid spheres) in the cylinder fluid region. A Boolean operation was done to subtract the spheres (see Fig. 6.3a) from the cylinder leaving empty spherical spaces (void) in the cylinder (see Fig. 6.3b). The cylinder fluid region and the packed particles (subtract), which is herewith referred to as the solid region, were simultaneously exported back to Star CCM+ for surface and volume mesh generation. Heat transfer performance calculations were carried out using the modified particle size.

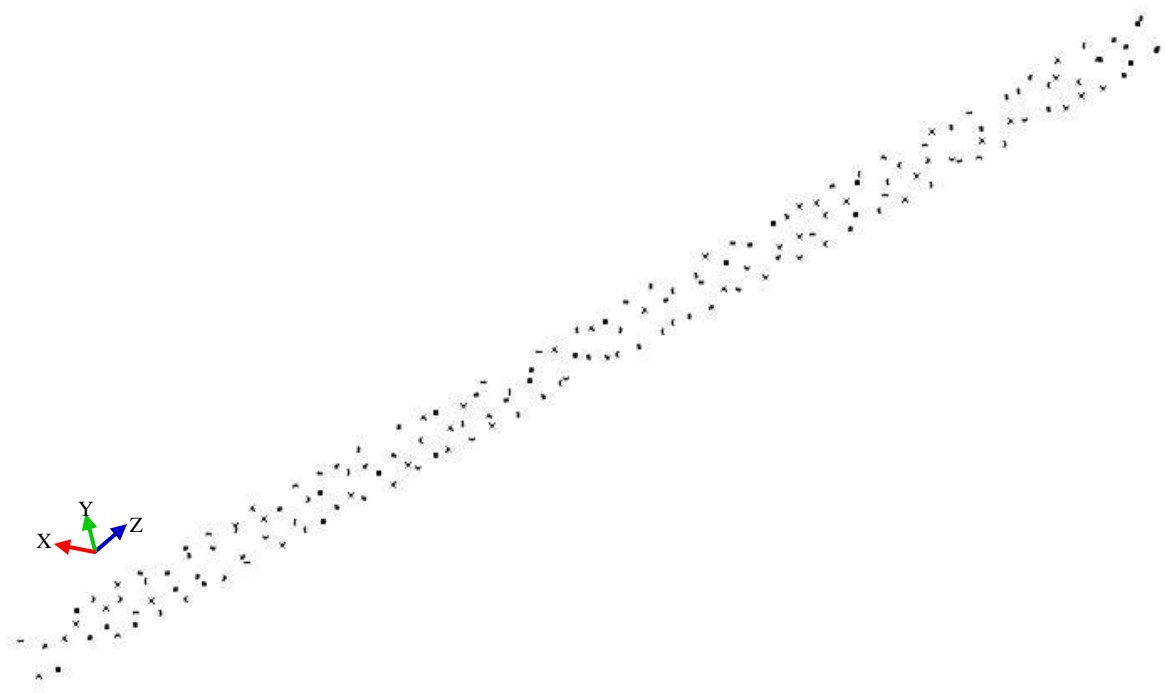


**Figure 6.2(b)** DEM simulation centroid coordinate points (x, y, z) in CAD environment

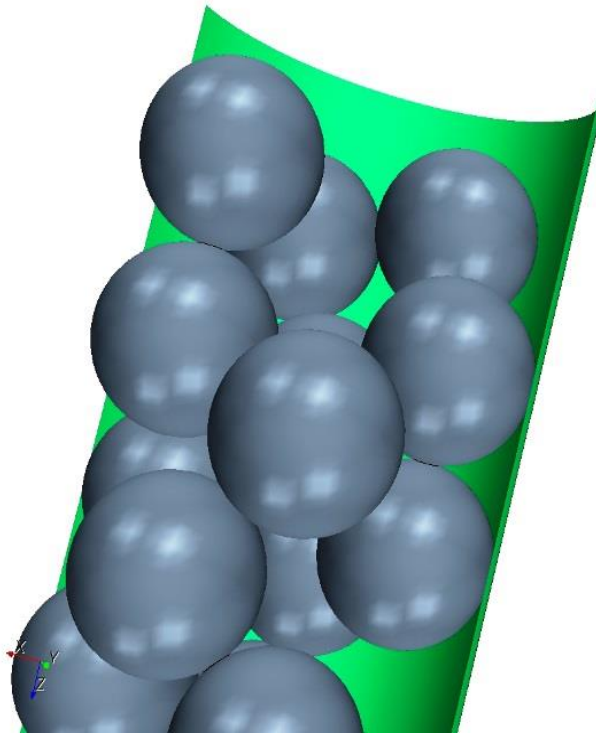


**Figure 6.2(c)** Expansion of packed particle diameter for establishment of contacts between adjacent particles and between walls and particles using CAD

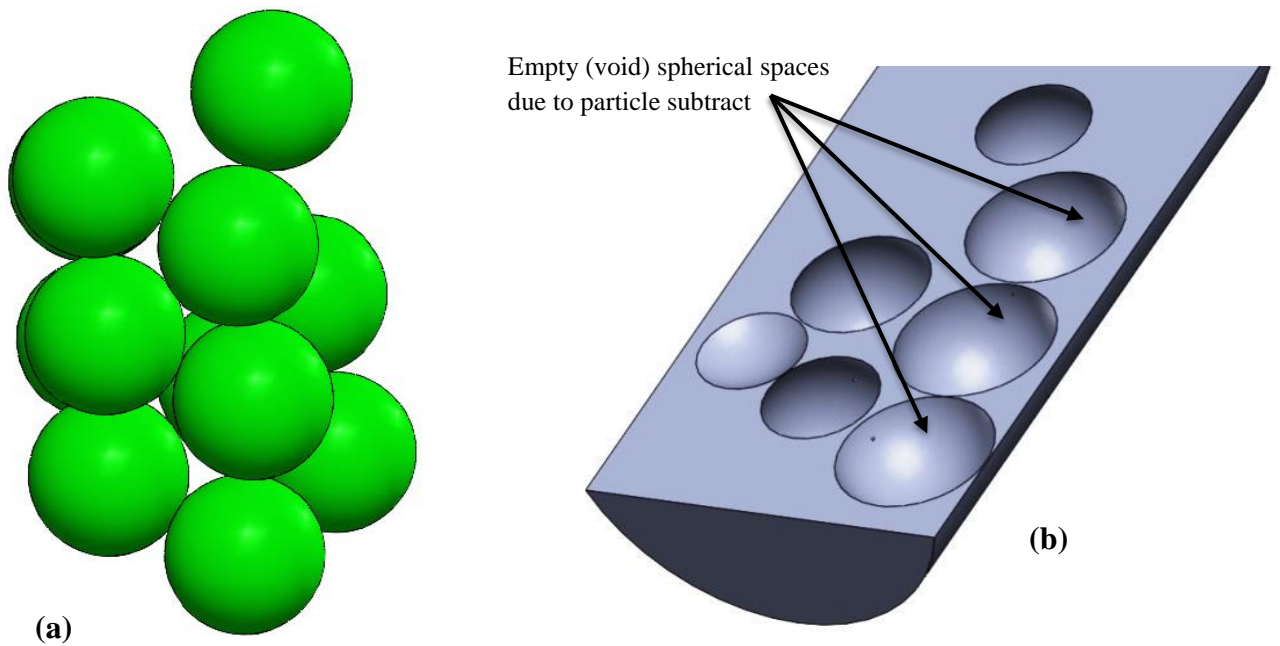


**Figure 6.3** (a) Packed particle subtract (solid region) (b) Sectional plane of fluid domain after Boolean subtract operation (fluid region)

## 6.4 Mesh Design and CFD modelling

### 6.4.1 Mesh design

A mesh is the discretised representation of the computational volume, which the physics solvers use to provide a numerical solution. STAR-CCM+ provides meshers and tools that are used to generate a quality mesh (as can be seen in Fig. 6.4) for various geometries and applications. Mesh quality influences the quality of the numerical results, irrespective of the set-up. Mesh establishes the accuracy of the simulation that has to be chosen with enough detail to describe the simulation processes accurately. The cylinder fluid region and the packed spheres solid region (subtracts) are simultaneously exported back to the commercial code software from the CAD package for surface and volume mesh generation. A polyhedral mesh in conjunction with a prism layer mesh model was used to generate orthogonal prismatic cells next to wall boundaries (see Fig. 6.4). These layers of cells were necessary to allow the solver to resolve near-wall flow accurately. This is critical in determining not only the forces and heat transfer on walls, but also flow features such as separation. On a mesh of given quality and sufficient fineness, higher-order schemes are applied for momentum and energy equations because they yield more accurate results than lower-order schemes.

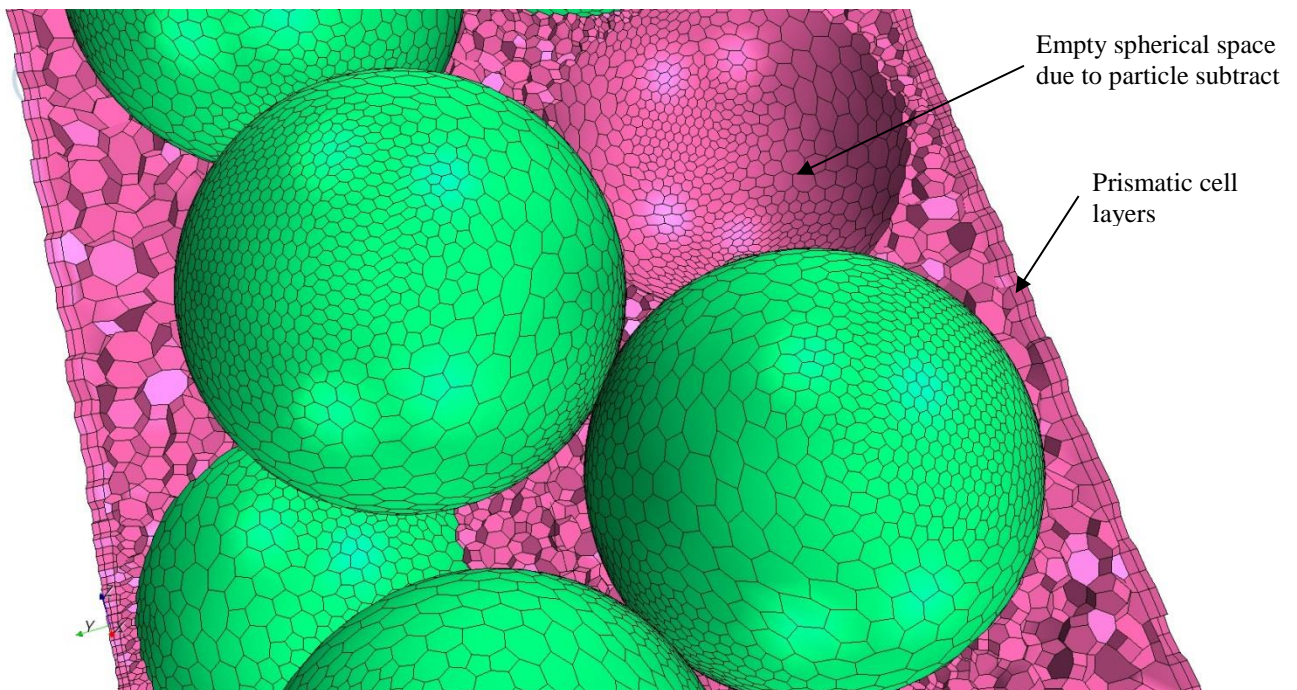


**Figure 6.4** Threshold of a generated quality mesh depicting particle-to-particle contacts in the fixed bed geometrical mode

Grid skewing is an important contributing factor (much more than grid stretching) to the loss in nominal accuracy of the solution. Skewed meshes found around the contact points do not actually create serious problems for laminar solutions, but they make convergence in some specific cases unachievable when simulating turbulent flow. It turned out that the flow velocities, especially in the fluid elements around the contact points, were increasing dramatically, a very typical result for cells that are too skewed.

Concerning the mesh sensitivity analysis, the test consisted of increasing the mesh density at the particle surface in order to properly capture the boundary layer associated problem. When solving steady-state problems on fine meshes, start with a much coarser mesh, and then successively refine the mesh by increasing the mesh density. Refinement enables better resolution of the flow. Meshes should be well designed to resolve important fluid flow features which depend on flow condition parameters such as the grid refinement inside the wall boundary layer. Four grid refinement levels were carried out in this study, from coarse to finer mesh. This was done by varying the mesh density to ensure that the CFD solution did not change with further mesh refinement as the aim of grid refinement was for numerical accuracy that led to a solution closer to the exact solution of a system of equations that implied considerable physical approximations [123] and [124]. For a 1.0mm base size used in the study, four sets of simulation sets were carried out within specified temperature range using varying mesh density and temperature profile results plotted in Fig. 6.5a.

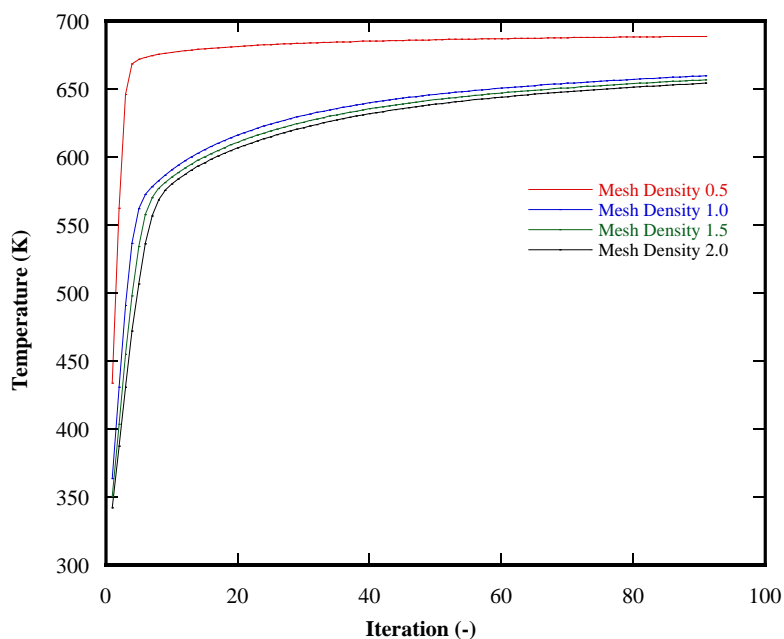


**Figure 6.5a** Mesh sensitivity analysis

It can be seen that as the temperature plot for the mesh density increases from 0.5 to 2.0, the lines move closer and closer indicating a transition from coarse to finer grid mesh refinement, the physical appearance of the mesh geometries also attests to this. Results obtained for the last two finer meshes are almost identical (see Fig. 6.5a). Hence it can be established that simulations had reached an asymptotic solution and the geometry with the last grid refinement level of optimum mesh density 2.0 was used to build the fixed bed model. The chosen geometry had 7,660,356 grid cells, 50,768,855 faces and 44,096,934 vertices (see Fig. 6.5b). From experience, this should be adequate to capture heat transfer phenomena over the particle surfaces. An in-place interface was placed in-between the fluid and the solid region, this allowed for the appropriate transfer of quantities of mass and energy calculated during the simulation.

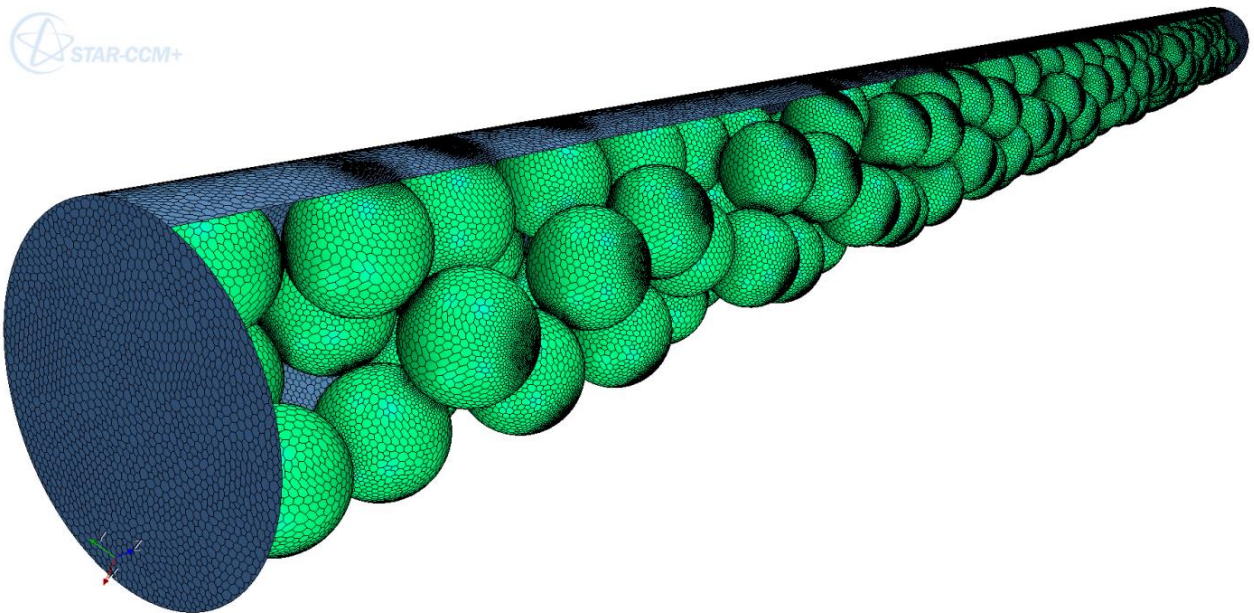


**Figure 6.5b** Quality meshed geometrical model

#### **6.4.2 Interface matching conditions**

The work of [125] was one of the first attempts to study the fluid flow boundary conditions at the interface region stated by [126] and [127]. Understanding the matching conditions for velocity, pressure and temperature at the interface between a solid layer and a free fluid is of

optimal importance in the use of interface between two regions. In the microscopic approach, mass, momentum and energy conservation are clearly satisfied across the interface but not at the macroscopic level. The study employed classical continuity conditions; the following matching conditions need to be satisfied at the interface when continuity of mass, momentum and energy are assumed [128]. The conditions are shown in Eq. (6.6):

$$(u_i^f - u_i^p)n_i = 0 \quad (6.6a)$$

$$(\sigma_{ij}^f - \sigma_{ij}^p)n_j = 0 \quad (6.6b)$$

$$(\tau_{ij}^f - \tau_{ij}^p)t_j = 0 \quad (6.6c)$$

given that  $f$ ,  $p$ ,  $n_i$ ,  $\sigma_{ij}$ ,  $\tau_{ij}$ ,  $t_j$ , represent free fluid, porous medium, unit vector normal to the interface, tangential stress, viscous stress and unit vector in tangential direction respectively. An in-place interface was applied between the solid and fluid region in this work; it was required to link together the two regions (fluid and solid) so that a conformal mesh was created at the common interface planes during the surface and volume meshing process. When used as part of the meshing process, the two boundaries imprinted on one another at the surface remeshing stage to ensure a conformal mesh across the interface where applicable. When applied to a volume mesh, the two boundaries were intersected and, if they were non-conformal, some new discretisation was created. An explicit connection was created between cells on each side of the interface so that mass and/or heat transfer occurred across the intersected area. Pressure was generally assumed continuous across the interface and this required that the normal components of the fluid viscous stress were balanced across the interface [126], but was argued by [129] that in this way, the stress in the solid matrix would not be taken into proper account. Regarding thermal conditions, local thermal equilibrium and the energy conservation were assumed along the interface, as expressed by Eq. (6.7):

$$(T^f - T^p) = 0 \quad (6.7a)$$

$$\left( \frac{\partial T^f}{\partial x_i} - \kappa \frac{\partial T^p}{\partial x_i} \right) n_i = 0 \quad (6.7b)$$

where  $\kappa$  represent the ratio between the conductivity of the fluid and that of the porous medium saturated by stagnant fluid.

With the above assumption, the nodal equations did not need any particular treatment at the interface. The nodes placed along the interface would get adequate contribution from elements placed in the fluid and solid medium [128].

### ***6.4.3 Initial state and boundary conditions***

For a problem to be well posed, boundary conditions must be specified on all solution domain boundaries. Boundary conditions in this study were set the same as the boundary conditions anticipated in the proposed design. The working fluid in the model was specified as helium gas at initial static temperature 293.1 K, static gauge pressure 0.0 Pa and reference pressure 101.325 kPa. The boundary conditions determined the flow and thermal variables on the boundaries of the physical model. The cylinder curved, top and bottom sides were set as walls, and temperature 300K, cylinder wall thermal boundary condition was specified as environment due to expected heat transfer across the cladding tube wall and at no-slip wall conditions. The particles, which formed the solid region, had their surfaces set as wall boundary at 700K and thermal boundary condition specified as convection.

### ***6.4.4 CFD modelling***

Modelling is the mathematical problem formulation of the physics involved in terms of a continuous initial boundary value problem (IBVP). In conducting any CFD modelling, the physics should first be set up for the model. Essentially, the physics models define the primary variables of the simulation and what mathematical formulation will be used to generate the solution. For this modelling, 171 uniformly sized solid particles, 15.98mm particle diameter and 2.503 tube-to-particle diameter ratio geometrical model were used. The particles were randomly packed in a helium gas environment contained in a slender cylindrical tube enclosed at both ends. The space model selected was 3D because the mesh was generated in three dimensions, it described the physical model accurately and was able to handle the flow specifics of the packed bed geometry. For high-pressure simulation, the gas was taken to be Newtonian, in the laminar flow regime and with variable density. Helium gas was selected as the simulation fluid while coated particle surfaces were identified as graphite carbon and a thermal specification of 7500W heat source was applied. The thermal and material properties value of the two porous materials (gas and particles) was available on the Star CCM+ database. The ideal gas law was used for the density temperature dependency and Sutherland's law [118] was used for the thermal conductivity and viscosity temperature dependencies. Gravitational

acceleration is added to the operating conditions of the model. An implicit solver was applied in this implicit unsteady flow simulation. Its function is to control the update at each physical time for the calculation (solution of continuity, momentum and energy equations) and as well to control the time-step size. Segregated fluid energy and segregated models are applied only for implicit unsteady flow. Appropriate numerical parameters (convergence limit, under-relaxation factor, number of iterations/time steps, etc.) were specified to control the calculation. A maximum step criteria of 100,000 was set as convergence limit, under-relaxation factor of 0.45 and time-step size of 0.00008 second were used in this study while simulation is runned at 20 iterations per time step. The gray thermal radiation model was specified for the surface-surface radiation expected at elevated temperatures. Simulations were run in a high-end computer system (see Fig. 6.7) and simulation time ranged from one to 72 hours depending on the studied case.

Numerical convergence of the model was checked based on a suitable diminution of the normalised numerical residuals of computed variables. Residual monitor plots of conserved variables such as the mass/continuity, momentum and energy against the iteration number were very useful for judging the convergence (or divergence) of a solution, and they were created automatically within every simulation. However, it is important to understand both the significance of residuals and their limitations. While it is true that the residual quantity will tend towards a very small number when the solution is converged, the residual monitors cannot be relied on as the only measure of convergence. Other convergence criteria used in the study were creating scalar and vector plots of the entire solution domain or parts of it, and visualising these plots as the solution developed. This technique is useful when comparing with residuals that cannot exhibit a converged solution. It is worthy to note that initial conditions affect convergence path and a converged solution is one that is nearly independent of meshing errors.

#### **6.4.5 Modelling thermal radiation**

A radiation model can be involved in fluid flow and thermal analysis. It is heat transfer by electromagnetic waves; either wave length dependent (multiband radiation) or wave length independent (gray thermal radiation), which purely depends on surface temperatures, material properties, transmission media, and topology of the geometry. If the solid is not interfaced with the fluid domain, radiation is turned on only in the solid. If the solid is interfaced with the fluid domain, the radiation model will be only on the fluid side, and not on the solid. The outside

boundaries of the fluid are made transmissive so that they interact radiatively. Only the fluid boundaries that are interfaced with the solid radiate to ambient.

In modelling thermal radiation for the study, surface-to-surface radiation was modelled on the fluid domain while the outside boundaries of the fluid were made transmissive so that they did radiatively interact. Under this circumstance, the amount of radiation received and emitted by each surface was uniquely defined by the surface's radiation properties and the thermal boundary conditions imposed on it. The surface properties were quantified in terms of emissivity, reflectivity and transmissivity radiation temperature. These properties were not dependent on direction. Min/max temperatures for the fluid and solid continua were set to the same value as appropriate for the run. When radiation properties were invariant with wavelength, the radiation was said to be gray. Gray radiation in this study was modelled using the Gray thermal radiation model selection. The radiation properties were taken to be the same over the entire thermal spectrum, and only a single radiative transfer solution was necessary for the full thermal spectrum.

## 6.5 Flow Calculation and Fields

### 6.5.1 Computation of Flow within the Packed Bed

Energy transport across the porous region is dealt with by specifying the thermal properties of the region in addition to the thermal properties of the fluid passing through it. Computation of flow is achieved by mathematical models based on conservation principles, namely the conservation of mass, momentum and energy governed by the 3D Navier-Stokes equations representing the fluid as a continuum for an arbitrary control volume. Natural convection is generated by the density differences induced by the temperature differences within a fluid system. By using the physical (interstitial) formulation and assuming a general scalar,  $\phi$ , the governing equation in an isotropic porous region expressed in differential form [130] is shown in Eq. (6.8):

$$\frac{\partial(\varepsilon\rho\phi)}{\partial t} + \nabla \cdot (\varepsilon\rho\vec{v}\phi) = \nabla \cdot (\varepsilon\Gamma\nabla\phi) + \varepsilon S_\phi \quad (6.8)$$

Assuming isotropic porosity and single-phase flow, the volume-averaged mass and momentum conservation equations are given by Eqs. (6.9) and (6.10):

$$\frac{\partial(\varepsilon\rho)}{\partial t} + \nabla \cdot (\varepsilon\rho\vec{v}) = 0 \quad (6.9)$$

$$\frac{\partial(\varepsilon\rho\vec{v})}{\partial t} + \nabla \cdot (\varepsilon\rho\vec{v}\vec{v}) = -\varepsilon\nabla p + \nabla \cdot (\varepsilon\vec{\tau}) + \varepsilon\vec{B}_f - \left( \frac{\varepsilon^2\mu}{K}\vec{v} + \frac{\varepsilon^3C_2}{2}\rho|\vec{v}|\vec{v} \right) \quad (6.10)$$

The CFD code solves the full set of discretised Navier-Stokes equations using a finite volume approach as earlier mentioned. In Eq. (6.10),  $\frac{\partial(\varepsilon\rho\vec{v})}{\partial t}$  is the time derivative term, where  $\varepsilon$  is the porosity,  $\rho$  is the density and  $\vec{v}$  is the velocity vector. The last term in Eq. (6.10) represents the viscous and inertial drag forces imposed by the pore walls on the fluid. In the term,  $\mu$  dynamic viscosity,  $K$  permeability,  $\vec{B}_f$  body force,  $\rho$  density,  $\vec{v}$  velocity vector and  $C_2$  is the inertial resistance factor. Porous resistance properties can be specified in several different ways depending on the particular media being modelled and the expected flow conditions through the media. Two methods are widely used when specifying porous resistance, namely the orthotropic viscous resistance method and the isotropic resistance method.

### 6.5.2 Flow through packed beds

In the porous region, the theoretical pressure drop per unit length is determined using the Forchheimer equation [131]. This is represented in Eq. (6.11):

$$\begin{aligned} -\frac{\Delta P}{L} &= \frac{\mu}{K}u_o + \beta\rho u_o^2 \\ &= (P_v u_o + P_i u_o^2) \end{aligned} \quad (6.11)$$

An example of the above Forchheimer equation widely used in porous media flow is the Ergun equation [132], a semi-empirical correlation applicable over a wide range of Reynolds numbers and for many types of packing.

$$-\frac{\Delta P}{L} = \frac{150\mu(1-\varepsilon)^2u_o}{\varepsilon^3d_p^2} + \frac{1.75\rho(1-\varepsilon)u_o^2}{\varepsilon^3d_p} \quad (6.12)$$

where  $u_o$  is the superficial velocity through the porous region,  $\beta$  is thermal expansion coefficient and  $P_i$ ,  $P_v$  are coefficients defining the porous resistance, known as the inertial resistance and viscous resistance respectively. Values for the resistance coefficients can be measured experimentally or derived using various empirical relationships, depending on the

exact nature of the problem. When modelling laminar flow through a packed bed, the second term in Eq. (6.12) is usually dropped resulting in the Blake-Kozeny equation [132].

### 6.5.3 Qualitative features of the flow fields

A velocity vector plot was created by defining a 2D plane. The resulting data set consisted of all the elements that intersected the defined plane, so that the data to be shown was not obscured by elements in front of the plane of view. The velocity vectors were coloured according to their magnitudes, and their lengths were projections of the 3D fluid flow vectors onto the defined plane. Fig. 6.6(a) shows a vertical section over the whole bed height, through the bed centre, and extending to two particle diameters in the radial direction. The section illustrates the bulk gas movement due to fluid temperature difference developed immediately after simulation run, the initial heat supplied to the fluid created a sudden change in the medium gas density.

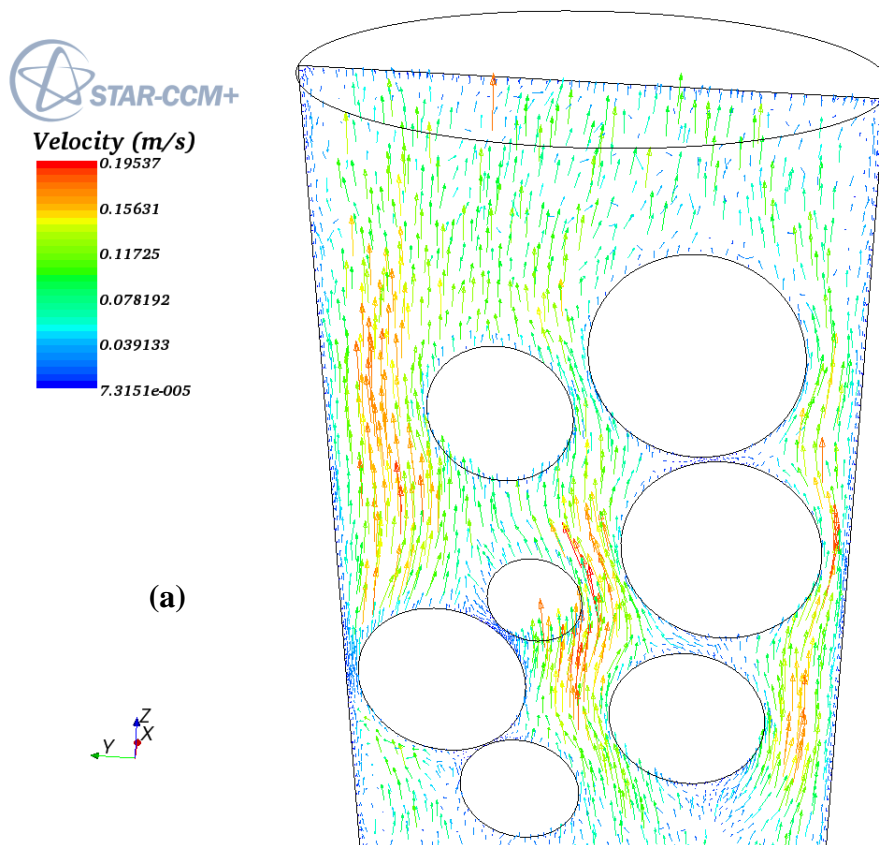


**Figure 6.6(a)** Sectional plane velocity vector plot immediately after starting up the simulation run

A scenario shortly after the simulation run is depicted in Fig. 6.6(b). From the yellow/green contours, the area of highest flow was in the bed centre while noticeable flow recirculation

gradually developed at the extreme corners of the top wall. As the gas temperature increased, flow recirculation at specific locations in the medium became fully developed, as seen in Fig. 6.6(c).

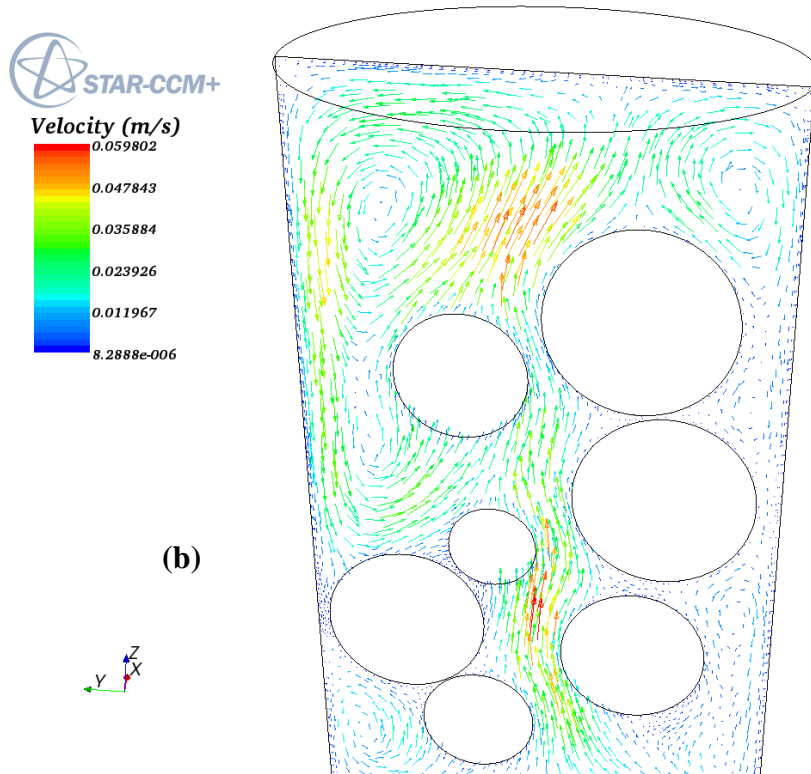


**Figure 6.6 (b)** Sectional plane velocity vector plot shortly after starting up the simulation run

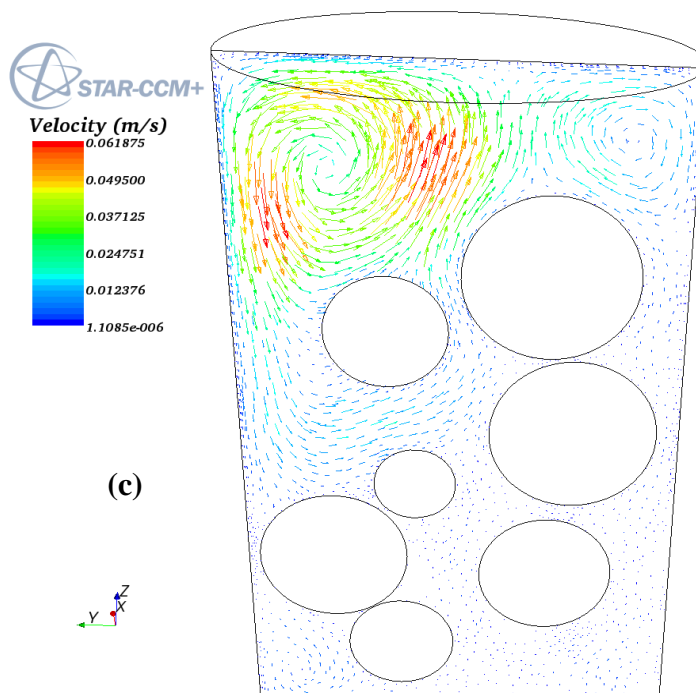


**Figure 6.6(c)** Sectional plane velocity vector plot before the end of the simulation process

With flow recirculation now fully developed, bulk gas movement dropped tremendously in the medium (see Fig. 6.6(c)) as bulk helium gas temperature approached particle surface temperature while simulation progressed towards the end.

## 6.6 Numerical Errors and Uncertainties

Errors and uncertainty are unavoidable aspects of CFD modelling. They can be calculated by different methods; Polynomial chaos method, Wilk's method, etc. These errors and uncertainty could emanate from round-off error (error caused by computational representation of real numbers by means of a finite number of significant digits), iterative convergence error (numerical errors resulting from truncating the iteration of discretised governing equations before final or exact solution is reached), discretisation error (error from representing a function by its values at a discrete set of points), input uncertainty (inaccuracies due to limited information or approximate representation of geometry, boundary conditions, fluid/material properties) and physical model uncertainty (discrepancies between real flows and CFD due to inadequate representation of physical/chemical processes or due to simplifying assumptions in the modelling process). Appropriate measures were taken to reduce some of these errors and uncertainties to the barest minimum during the simulation process as mentioned in the thesis.

## 6.7 Results and discussion

Unlike in HTR where continuous input and output discharge of the cooling fluid is carried out in the reactor, in this analysis both ends of the cladding were closed (see Fig. 1.2) with the working fluid and packed coated particle fuel contained in it. Simulations of HTR performance have been carried out by different authors using different simulation techniques and results analysed. These techniques were looked into before the commencement of this study and the most practicable simulation technique closer to the exact solution was adopted for the study. Results of the CFD simulations were presented first in the form of temperature contour plots and velocity vector plots to illustrate the qualitative features and insight that could be obtained. Following the qualitative discussion, CFD data was extracted to generate parameter plots that define the heat transfer performance in the medium. In this investigation, the heat transfer coefficient,  $h_{pf}$ , Nusselt number,  $Nu$ , Grashof number,  $Gr$ , and Rayleigh number,  $Ra$ , were the basic parameters used in evaluating the convective heat transfer characteristics in the packed bed considered.

Although Fig. 6.7 is modelled in a vertical direction, it is displayed in a horizontal direction for better viewing and description of its temperature contours. The temperature contours for the simulated packed beds are depicted in Fig. 6.7. It can be seen that particle surface temperature in red contours are uniform but the side, top and bottom outer-wall temperatures are non-uniform. On the side walls, the reddish-brown contours show the influence of conduction at each particle-to-wall point contact and the heat spread out by the yellow contours on the side walls from these contacts was due to the influence of the hot helium gas neighbouring the wall boundary along axial direction. The blue/green contours on the outer side wall close to the top and bottom of the tube were influenced by the gas temperature and heat transfer spread out along the tube wall at these two locations. The tube top wall surface located on the extreme left of the modelled diagram had no particle point contact on its surface hence the greenish contours indicate the influence of less dense hot helium gas experiencing recirculation concentrated on one part of the top wall boundary while areas with blue contours indicate the influence of hot gas not experiencing recirculation.

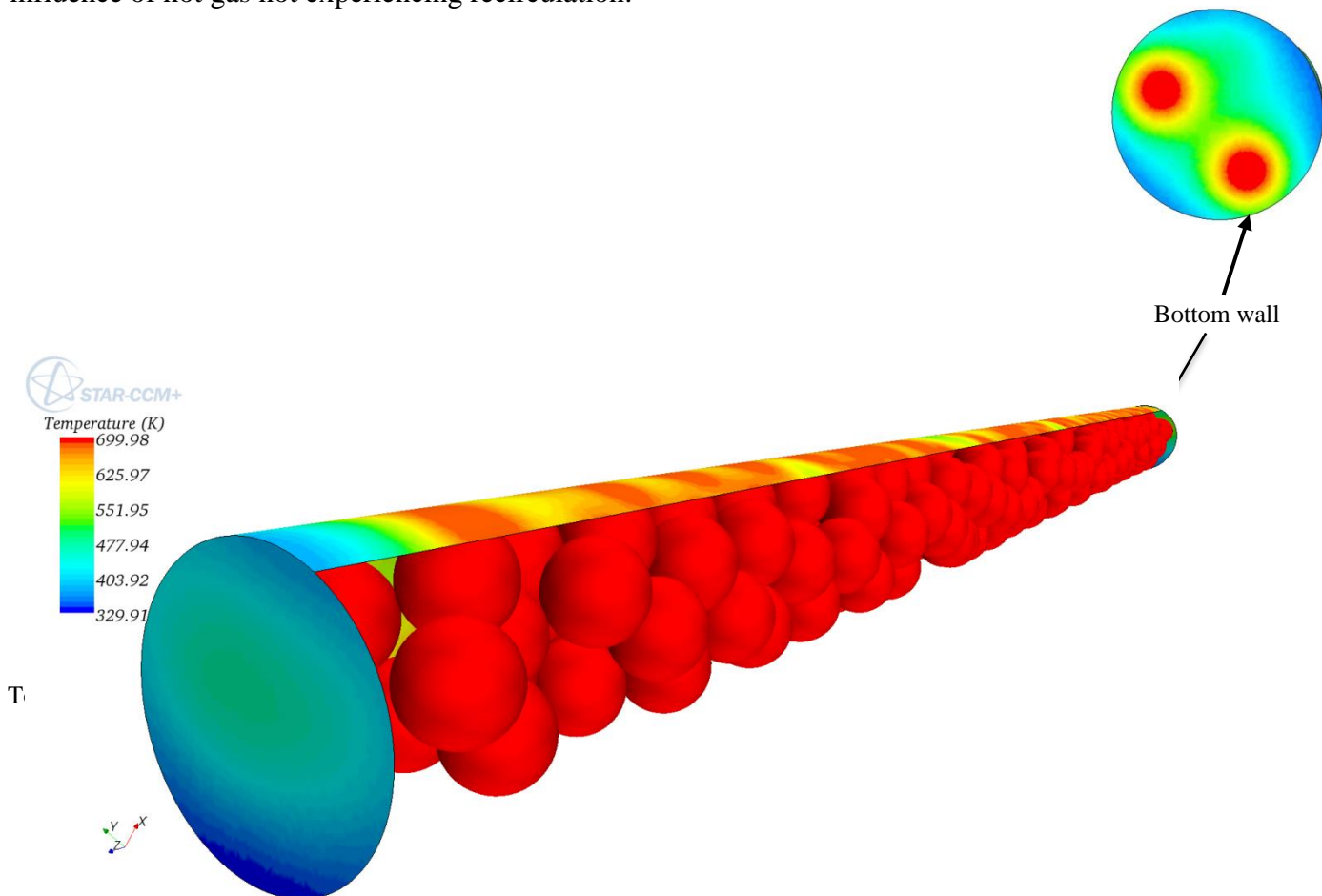


**Figure 6.7** Temperature contour plot for packed beds in helium environment contained in an enclosed slender cylindrical tube

This can be confirmed by the heat spread out on the top wall surface, which is non-uniform because one side of the surface received more heat than the other and this is proved to be true by the velocity vector plot.

The two red contours on the bottom wall located at the extreme right of the modelled diagram indicate the influence of just two particle point contacts on the bottom wall surface. The yellow/green/blue contour is an influence of heat spread out from the two heated point contacts, which were assisted by the hot gas neighbouring the wall boundary. Packed particle temperature was measured using the commercial code along the axial and radial direction to determine temperature uniformity along the directions. The hot helium gas helped to improve the conduction heat transfer from the coated particle fuel to the cladding tube walls, thereby creating a heat spread out on the walls of the tube. Fig. 6.8 illustrates the particle temperature along the axial length to be uniform except for a slight drop for the first particle in contact with the bottom wall, which could be due to heat loss to contacting the bottom wall through conduction.

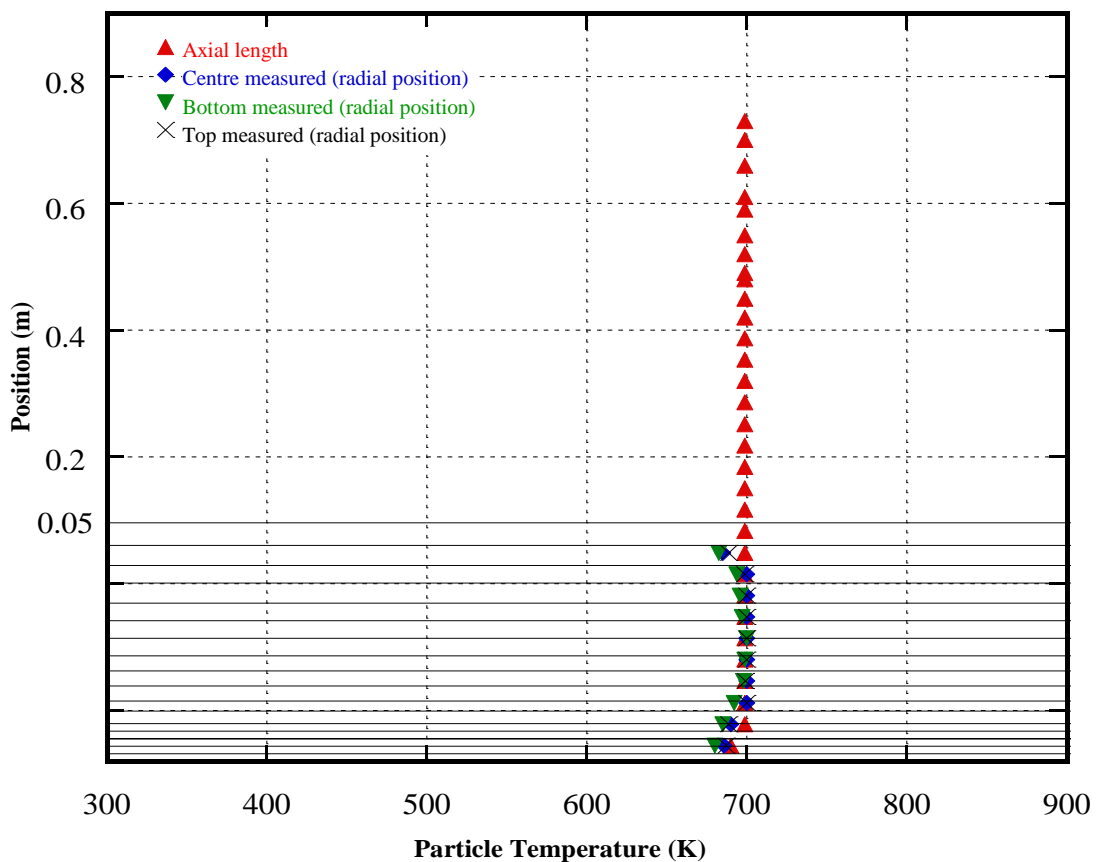


**Figure 6.8** Particle temperature profile along axial and radial positions

Likewise, the particle temperature along the radial direction for the three locations examined is relatively uniform except for a slight drop for particles in contact with the side walls. This could also be attributed to heat loss to contacting walls on both sides through conduction. The heat transfer coefficient is a quantitative characteristic of convective heat transfer between a gas medium (a fluid) and the solid (particle) surface immersed in the fluid. A plot of increasing fluid temperature rise against particle-to-fluid heat transfer coefficient is depicted in Fig. 6.9. The graph shows a sudden initial rise in heat transfer coefficient followed by a plunge after the gas had gained some substantial heat and later a gradual drop until around 600K when a rise in the heat transfer coefficient started developing again. The initial rise in heat transfer coefficient could be attributed to a sudden high heat input on particle surfaces due to nuclear fission reaction. The initial sudden high heat input created a sharp increase in fluid density resulting in initial high convective fluid velocity (see Fig.6.6a). The graph in Fig. 6.9 is related to the graph in Fig. 6.11 because the sharp rise in the heat transfer coefficient is a function of the initial high flow around the particles. As fluid temperature rose, flow recirculation began to develop at various locations while convective fluid velocity was on the decline (see Fig. 6.6b). This transformed into a decreasing heat transfer coefficient, as shown in Fig. 6.9.

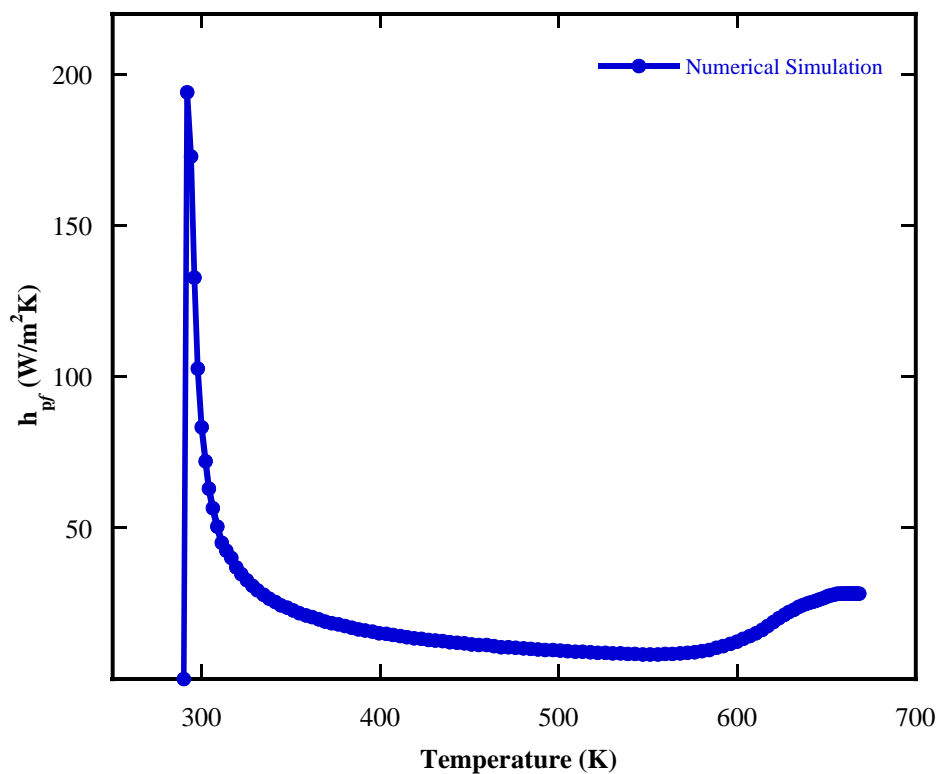


**Figure 6.9** Effect of convective fluid velocity on particle-to-fluid heat transfer coefficient

At the initial heating stage of the gas by the particles, convective fluid velocity was on the rise due to reducing gas density at an increasing gas temperature. As gas temperature increased, convective fluid velocity started dropping due to reducing buoyancy force acting on the gas. The surrounding water on the outside of the tube prevented a condition of local thermal equilibrium from being reached in the medium. While the dimensionless Reynolds number governs the flow regime in forced convection, the flow regime in natural convection is governed by the dimensionless Grashof number, which represents the ratio of the buoyancy force to the viscous force acting on the fluid. The initial rise and a later drop in Grashof number, as depicted in Fig. 6.10, was due to a surge in the buoyancy force acting on the gas at start-up caused by sudden high heat input on particles surfaces. As partially warm gas mixed with the cold gas, the gas temperature dropped and the buoyancy force equally dropped leading to the fall in Grashof number shortly after starting up. The Grashof number increased again as the gas average temperature rose and increased while it approached the surface temperature of the particles.

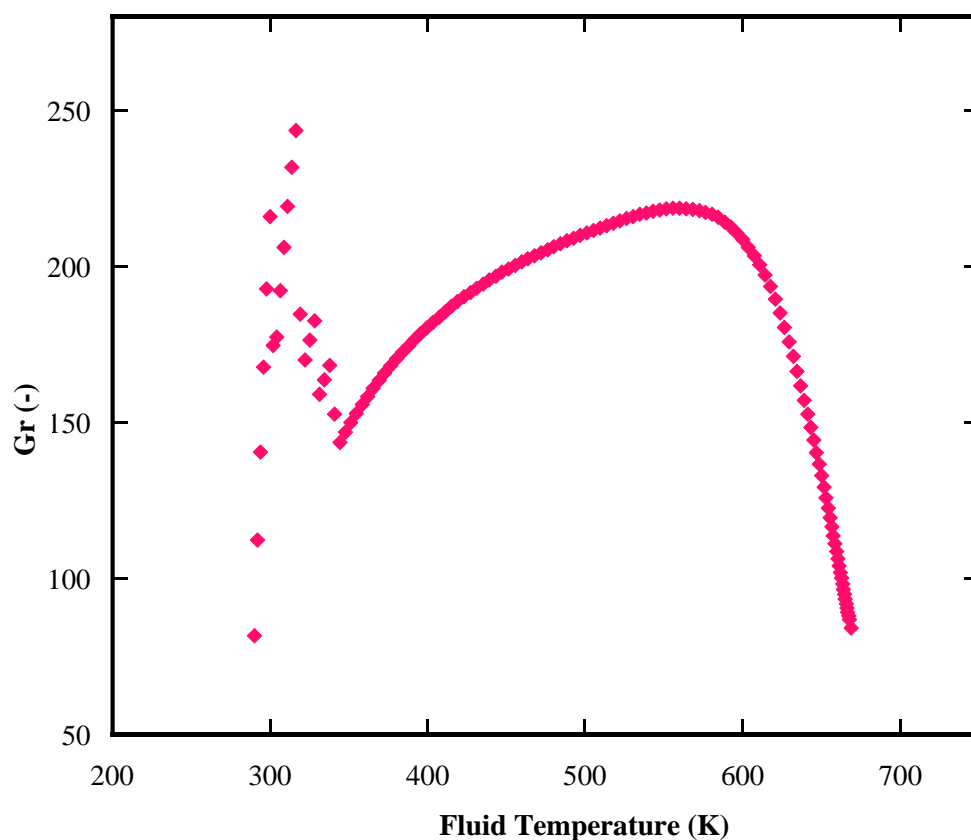
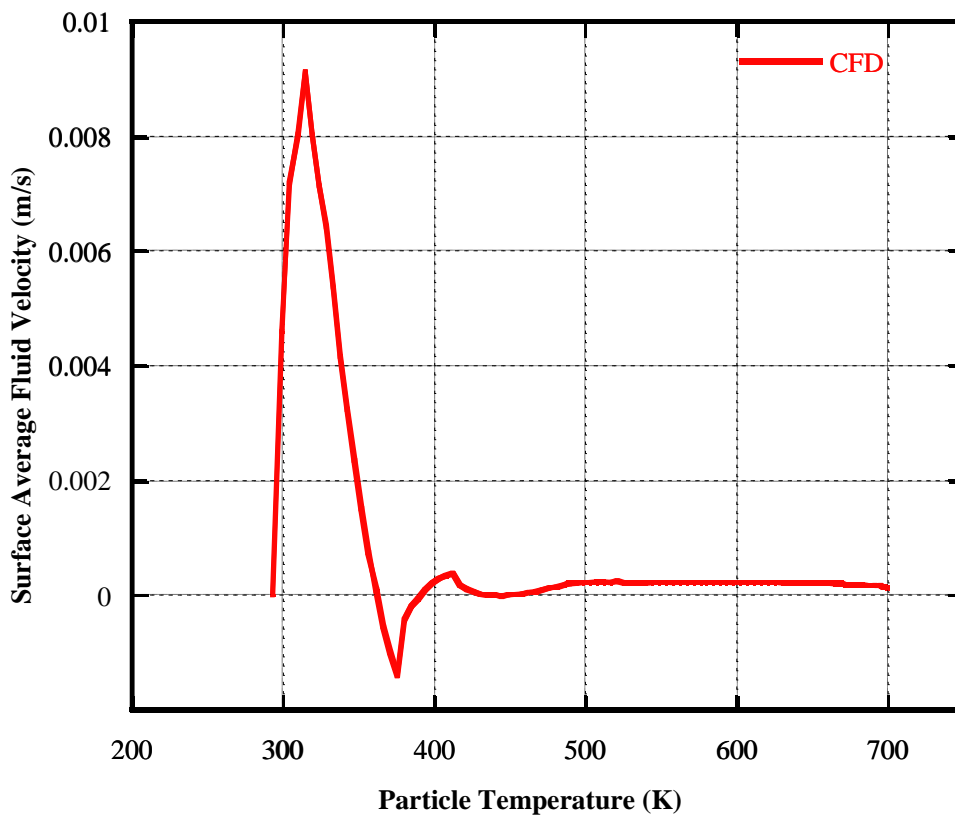


Figure 6.10 Effects of fluid temperature on Grashof number

A turning point was reached as the gas temperature approached the surface temperature of the particles when the buoyancy force began to drop due to low temperature difference between the particles and gas temperature. It should be noted that the heat transferred from the cladding wall to the surrounding water prevented the medium from reaching a point of local thermal equilibrium (LTE) hence the possibility of the Grashof attaining a zero value was ruled out. Even though the tube was tightly closed at both ends, initial bulk gas movement was observed in the medium. Fig. 6.11 shows a sharp rise in surface average gas velocity occurring due to a sharp fluid temperature rise caused by a sudden high heat input on particle surfaces immediately after the fission reaction began. The initial sharp rise in the convective surface average gas velocity was responsible for the initial sharp rise in the particle-to-fluid heat transfer coefficient observed in Fig. 6.9. The graph in Fig. 11 is related to that in Fig. 9 because  $h_{pf}$  is a function of the flow around the particle surfaces. The rise was short-lived as the gas velocity was seen to drop abruptly before rising again to a fairly stable value as the simulation progressed.



**Figure 6.11** Surface average fluid velocity against particle temperature along packed bed full height

This could be caused largely by the tendency of the gas towards attaining a uniform temperature as it gained heat. In heat transfer, at a boundary (surface) within a gas, the Nusselt number ( $Nu$ ) is the ratio of convective to conductive heat transfer across the boundary. In the graph depicted in Fig. 6.12, a gradual increase in Nusselt number is observed as gas average velocity rose due to increasing gas temperature. The Nusselt number in Fig. 6.12 is seen to rise even though gas average velocity dropped; this could be attributed to flow recirculation developing at different locations in the bed. As the gas temperature approached the particle temperature, flow recirculation diminished and the Nusselt number dropped. Cooling by the water surrounding the tubes would cause the Nusselt number to rise again; and a point of total equilibrium would be reached.

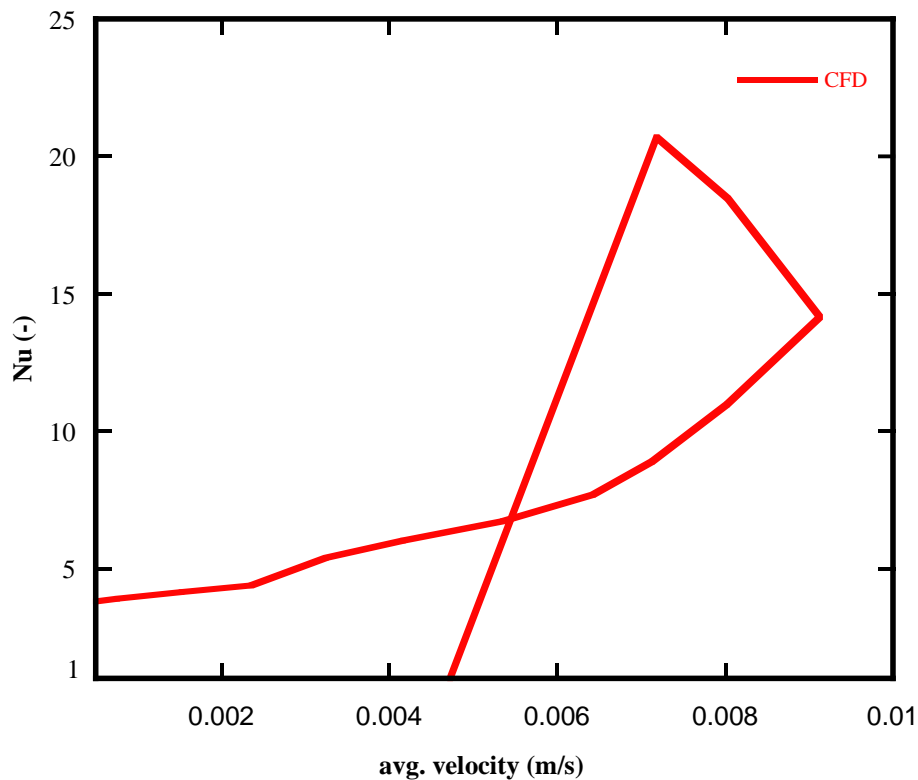


**Figure 6.12** Nusselt number against surface average gas velocity

The Rayleigh number is a dimensionless term used in the calculation of natural convection heat transfer in a medium; it is associated with buoyancy-driven flow. Its value in this investigation was determined from the thermophysical properties of the particle test sample and heated helium gas. The Rayleigh number depicted in Fig. 6.13 increased sharply immediately after the gas gained heat and experienced some instability as the temperature increased.

The initial increase in  $Ra$  could be due to a surge in buoyancy force, thereby creating an initial rise in convective surface average gas velocity, as can be seen in Fig. 6.12. As the temperature difference dropped, the Rayleigh number fluctuated due to convectional current fluid flow. As the temperature difference increased steadily, the Rayleigh number experienced a gradual rise. It can be noticed that as the gas temperature approached the particle surface temperature, a declining temperature difference was established in the medium necessitating a drop in the buoyancy force, which relatively gave rise to a sharp fall in the Rayleigh number. The plot in Fig. 6.14 depicts the changes in the Nusselt number with respect to the heat transfer between the heat-generating particles and the hot gas. At an early stage of the gas temperature rise, an increase in Nusselt number was experienced

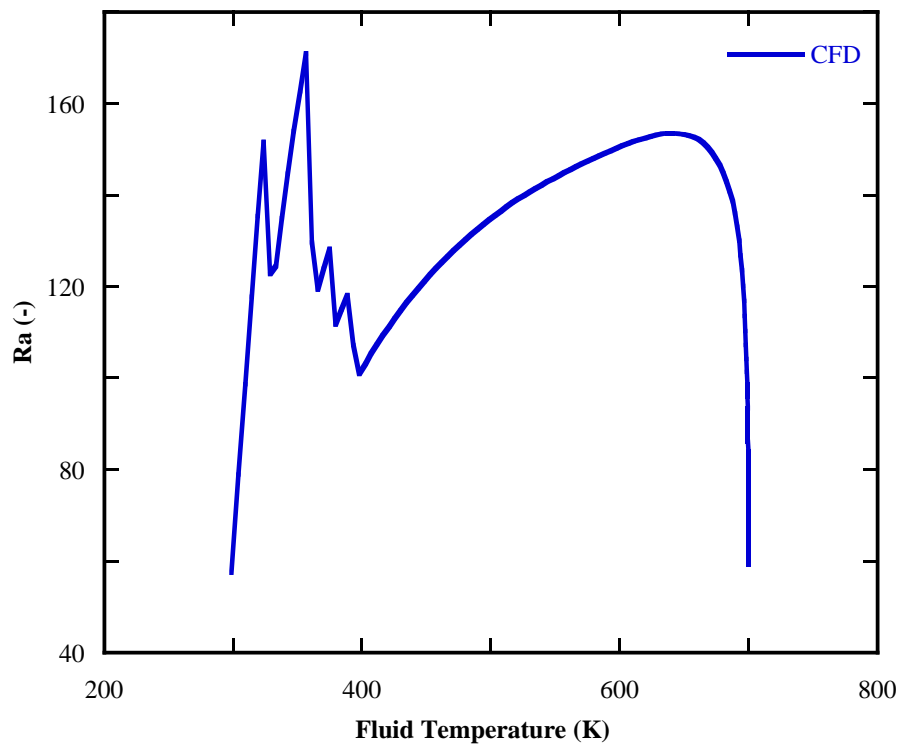


**Figure 6.13** Variation of Rayleigh number with gas temperature

A further gas temperature rise resulted in a small decline in Nusselt number due to recirculation. After a while, the Nusselt number is observed to increase as the gas temperature increased with decreasing Rayleigh number due to a lowering buoyancy force that was developing in the medium.

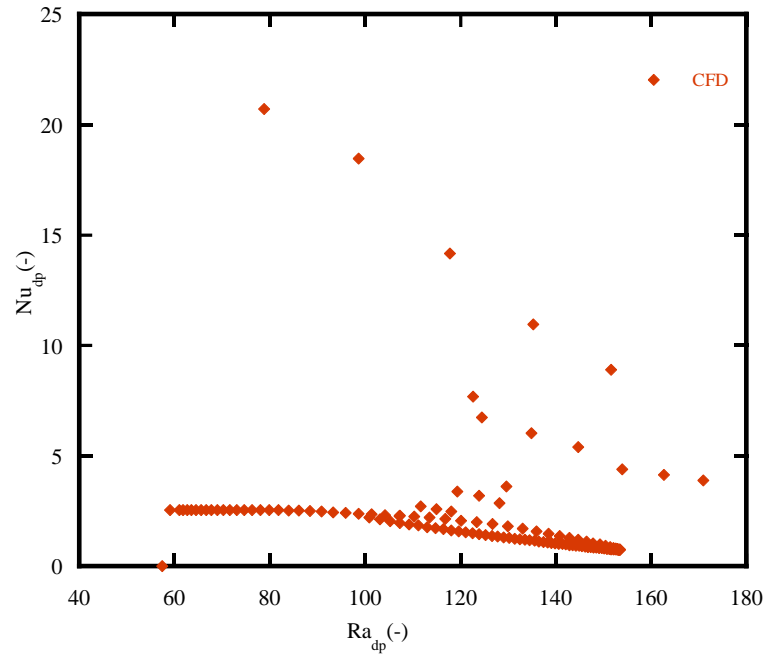


**Figure 6.14** Nusselt number against Rayleigh number for particle-to-fluid heat transfer

## 6.8 Comparison of Experimental Evaluation, Theoretical and CFD Results

Before the three approaches used are compared, it is worth mentioning that Eq. (6.3) was applied to the CFD approach in the determination of  $h_{pf}$  and  $Nu_{dp}$ . It should also be noted that the experimental and theoretical analysis approaches are for fluid-to-particle heat transfer while the CFD approach is for a particle-to-fluid heat transfer mimicking the new fuel design. In comparing the three approaches, it can be seen through the smooth curves in Fig. 6.15 that the heat dissipation process in the medium under experimental investigation was relatively calm compared with the heat dissipation experienced during the numerical CFD simulation approach, which showed some uneven initial heating in the medium. The three approaches experienced substantial increase in the Nusselt number as medium temperature increased with each displaying different profiles. A combination of the basic unit cell (BUC) model and CFD best expresses the heat transfer phenomenon taking place in the media and the heat transfer characteristics obtained from this combined process can be said to be reasonable.

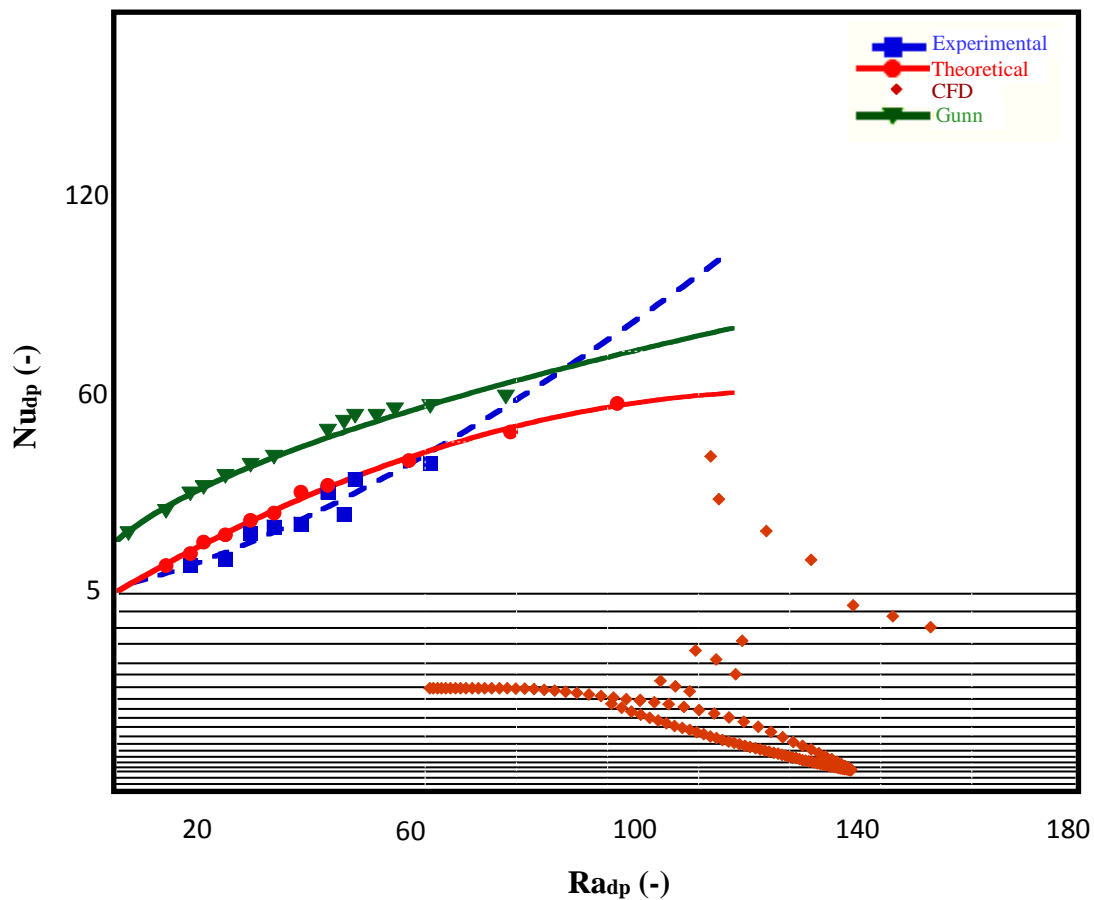


**Figure 6.15** Nusselt number against Rayleigh number

## 6.9 Conclusion

Computational fluid dynamics (CFD) has proved to be a reliable tool for fixed bed reactor design [133], through the resolution of 3D transport equations for mass, momentum and energy balances. Solution of these equations has enabled the velocity and temperature profiles within the mimicked cladding to be attainable. With the establishment of an adequate refined mesh, the temperature contours, velocity vectors and graphs depicted the results of qualitative features in the medium after simulation. These results presented in various modes illustrate the relationships among the heat transfer coefficient, fluid temperature and velocity in the medium. The hot helium gas through the heat gained from particles greatly assisted in accelerating the heat transfer and heat spread-out along the wall surfaces; only a little fraction of the heat on particle surfaces was conducted to the walls through point contacts. A non-uniform temperature distribution on the walls through such point contacts was established. The development of

recirculation at different parts in the medium enhanced heat transfer to the fluid and made the thermal layer thicker. The graphs of different characterising parameters used in the study revealed the transport and heat transfer phenomenon taking place in the medium. The walls of the geometrical model were not made adiabatic but environment to mimic the high thermal conductivity/low thermal resistance properties of the cladding tube (SiC). The medium was prevented from attaining the local thermal equilibrium (LTE) condition by the cooling water surrounding it.

# 7

## Conclusions and Recommendations

---

### 7.1 Conclusions

This PhD work is a contribution to global research to make water-cooled reactors safer. An innovative nuclear fuel design was proposed and investigated at the University of Pretoria, Department of Mechanical and Aeronautical Engineering. The proposal is to load these coated particles into the fuel tubes instead of conventional fuel pellets. The particles will be submerged in a helium gas that will transfer the heat to the surface of the tube. The heat transfer from these particles to the tube wall is investigated as part of the research. Part of the heat transfer is by means of natural convection, which forms a major focus of the investigation.

Three (3) types of analysis were performed in the process of investigating natural convection heat transfer characteristics from heated microspheres in a slender cylindrical geometry. These are experimental model, theoretical model and a CFD simulation. Contributions from this research output to existing knowledge in water-cooled reactors and randomly packed beds are; (i) introduction of elements of passive safety measures utilised in HTR into the traditional fuel configuration of light-water reactors, (ii) heat transfer characteristics in porous media should not only be associated and resolved through media flow (transport) because very limited and complex flow recirculation may exist in some media, which is the case in this study, (iii) The main limitation of heat transfer models in packed beds is the poor knowledge of flow patterns within them; the use of modelling and simulation tools in the study makes it possible to define not only spatial distribution of involved species, but also temperature and velocity profiles within the bed.

Carried out in the first analysis was an experimental investigation of fluid-to-particle natural convection heat transfer characteristics in packed beds heated from below. Captured data readings from the experiment were analysed and heat transfer characteristics in the medium evaluated by applying the first principle heat transfer concept. In the second analysis, a basic unit cell (BUC) model developed was used for the theoretical analysis, the model was applied to determine the *heat transfer coefficient,  $h$ , Nusselt number,  $Nu$ , Grashof number,  $Gr$ , Reynolds number,  $Re$ , and Rayleigh number,  $Ra$* , of the medium. The model is an application of conservative heat transfer energy balance within any unit cell in the medium; it related the convective heat transfer effect of the flowing fluid with the conduction and radiative effect at the finite contact spot between adjacent unit cell particles. As a result, the model could account for the thermophysical properties of sphere particles and the heated gas, the interstitial gas effect, gas temperature, contact interface between particles, particle size and temperature distribution within the particles achieved by using finite volume method (FVM) in the investigated medium. Although the heat transfer phenomenon experienced in the experimental set-up was a reverse case of the proposed fuel design, the study with the achievement in the validation with the Gunn correlation aided in developing the appropriate theoretical relations required for evaluating the heat transfer characteristics in the proposed nuclear fuel design.

In the third analysis, numerical simulation mimicking the ideal nuclear fuel design using a commercial code gave good display of contours and graphic illustration of the heat transfer performance anticipated in the proposed design. Existing relationships of fluid temperature, particle surface temperature and convective fluid velocity illustrated through the numerical simulation provided substantial information on the nature of flow phenomena expected in the proposed medium. Heat transfer characteristics in simulated medium mimicking the proposed medium portrayed slightly different graphical profiles compared with the medium investigated experimentally in the study. The reason could be the mode of heating in the medium and the level of unsteady heat transfer between contacting particles compared with the transient heat transfer obtained in the experiment. The heat transfer coefficient and other heat transfer characteristics parameters used in the study were influenced by the relationships of convective gas velocity, fluid and particle surface temperature difference.

The concept of using particle nuclear fuel to enhance safety in water-cooled reactors is an innovative idea. Apart from the passive safety system advantage the proposal has over the traditional nuclear fuel requiring active safety system, the risk of a rod break in case of some

accident is expected to be lower. The ability of coated fuel particles to contain fission products in the proposed design will make filling the cladding tube to the top with coated fuel particles possible compared with the traditional nuclear fuel system, which has provision for plenum in the cladding. Filling the cladding tube with coated fuel particles is expected to be quicker and easier to do than filling the cladding with the traditional nuclear fuel. Although the traditional nuclear fuel is expected to have a higher packing density in the tube than the proposed fuel design, the reduction in the fuel content can be made up by merely increasing the enrichment proportionally. On the other hand, higher fuel enrichment in the proposed nuclear fuel will provide higher burn-up, which is another advantage of the proposed design over the traditional nuclear fuel. Production cost of the proposed coated fuel particles is expected to be cheaper compared with the traditional nuclear fuel (fuel pellet).

Although this study covered a large part of convective heat transfer in packed beds, it focused on the convective heat transfer between particles and gas at the bulk region for a homogeneous bed. The wall-to-fluid convective heat transfer experiment was not done in this study. The wall to-fluid convective heat transfer is expected to differ from the pebble-to-fluid convective heat transfer due to the very large porosity gradient close to the wall (near-wall region). The heat transfer characteristics in the proposed design would presumably be influenced by spots (locations) experiencing recirculation due to higher interstitial temperature expected at such spots.

An aspect ratio of  $A = 19.54$  was used in the modelling due to problems arising from computational time but the aspect ratio for the cladding tube was expected to be as high as 200.00.

## 7.2 Recommendations for Further Work

Further work can be done in the near-wall region to investigate the influence of the region on the overall heat transfer performance in the medium. Thermal radiation is a heat transfer mechanism that occurs in packed beds at high temperatures; the phenomenon is a complex problem. The study considered thermal radiation between bed particles only. Further work should account for thermal radiation between the bed particles and interstitial gas, and between interstitial gas and the bed wall.

## Conclusions and Recommendations

The effect of aspect and diameter ratios on the heat transfer performance in porous media needs to be investigated in future work to evaluate their effects on the proposed design. Although a porous region was modelled to validate the experimental results, future work can apply the direct numerical simulation approach to equally validate the experimental results. Further simulation work can be carried out to investigate the neutron flux distribution inside the cladding tube containing the proposed nuclear fuel. The resultant heat distribution obtained from such simulation can be compared with this present result. The heat transfer performance from outer walls of the cladding tube to the surrounding cooling water can also be investigated by CFD simulation can be included as part of the further work to be carried out for the proposed design.

## References

- [1] Nuclear reactor [http://en.wikipedia.org/wiki/Nuclear\\_reactor](http://en.wikipedia.org/wiki/Nuclear_reactor) (accessed May 1, 2014).
- [2] J. Newman, *Physics of the Life Sciences*. Springer, New York, 2008.
- [3] IAEA – LWR, Technical Working Groups on Advanced Technologies for LWRs and HWRs (TWG-LWR and TWG-HWR), Retrieved 2009.
- [4] Y. Wakatsuki, New radioactive water leak at Japan's Fukushima Daiichi plant, [cnn.com](http://www.cnn.com). Archived from the original on 2014.
- [5] P. Lipsy, K. Kushida, T. Incerti, The Fukushima disaster and Japan's nuclear plant vulnerability in comparative perspective. *Environmental Science and Technology*, **47**
- [6] O.O. Noah, J.F. Slabber, J.P. Meyer, Investigation of natural convection heat transfer phenomena in packed beds: Lead-way toward new nuclear fuel design. *ASME J. Nuclear Engineering and Radiation Science*, **1**(4), 2015, 041014-12.
- [7] A.R. Balakrishnan, D.C.T. Pei, Heat transfer in gas-solid packed bed systems, 2 & 3. The conduction mode. Overall heattransfer rates in adiabatic beds. *Ind. Eng. Chem. Process Des. Dev.*, **18**(1), 1979, 40-48.
- [8] A. Buonanno, Y. Chen, M. Vallisneri, Particle physics and cosmology: the fabric of spacetime, *Phys. Rev. D*, **69**, 2003, 104017.
- [9] M. Bahrami, M.M. Yovanovich, J.R. Culham, Effective thermal conductivity of rough spherical packed beds. *Int. J. Heat Mass Transfer*, **49**(20), 2006, 3691-3701.
- [10] W. van Antwerpen, C.G. du Toit, P.G. Rousseau, A review of correlations to model the packing structure and effective thermal conductivity in packed beds of mono-sized spherical particles. *Nuclear Engineering and Design*, **240**(7), 2010, 1803-1818.
- [11] M. Kaviany, *Principles of Heat Transfer in Porous Media*, 2<sup>nd</sup> edition, Springer-Verlag, New York, 1995.
- [12] D.A. Nield, A. Bejan, *Convection in Porous Media*, 3<sup>rd</sup> edition, Springer Science + Business Media, Inc 2006.
- [13] K. Kugeler, *HTR Technology. Study guide*, Potchefstroom: North-West University, 2009.

- 
- [14] A. Koster, H.D. Matzner, D.R. Nicholisi, PBMR design for the future. *Nuclear Engineering and Design*, **222**, 2003, 231-245.
- [15] KTA, Reactor core design of High Temperature Gas-Cooled Reactors, Nuclear Safety Standards Commission, KTA standards, (1978, 1983, 1981) 3102.1, 3102.2, 3102.3.
- [16] H.T. Aichlmayr, The Effective Thermal Conductivity of Saturated Porous Media. Master's thesis, University of Minnesota, 1999.
- [17] D. Vortmeyer, J. Schuster, Evaluation of steady flow profiles in rectangular and circular packed beds by a variational method. *Chemical Engineering Science*, **38**(13) 1983 1691-1699.
- [18] R.P. Zou, A.B. Yu, The packing of spheres in a cylindrical container: the thickness effect. *Chemical Engineering Science*, **50**, 1995, 1504-1507.
- [19] R.F. Benenati, C.B. Brosilow, Void fraction distribution in beds of spheres. *A.I.Ch.E. Journal*, **8** (3), 1962, 359-361.
- [20] M.L. Hunt, C.L. Tien, Non-darcian flow, heat and mass transfer in catalytic packed-bed reactors. *Chemical Engineering Science*, **45**(13), 1990, 55-63.
- [21] L.H.S. Roblee, R.M. Baird, J.W. Tierney, Radial porosity variations in packed beds. *A.I.Ch.E. Journal*, **4**(13), 1958, 460-464.
- [22] J.S. Goodling, R.I. Vachon, W.S. Stelpflug, S.J. Ying, Radial porosity distribution in cylindrical beds packed with spheres. *Powder Technology*, **35**, 1983, 23-29.
- [23] G. Gordon, C.G. du Toit, Comparison between the experimental and numerical determination of the radial variation in the porosity in the cylindrical packed beds. In *Proceedings at the Fourth South African Conference on Applied Mechanics*, Johannesburg, 2004.
- [24] K. Gotoh, W.S. Jodrey, E.M. Tory, Variation in the local packing density near the wall of a randomly packed bed of equal spheres. *Powder Technology*, **20**(13) 1978, 257-260.
- [25] A. Griveau, Modelling and transient analysis for the Pebble Bed Advanced High-temperature reactor (PB-AHTR). M.S. PROJECT REPORT, University of California at Berkeley, Department of Nuclear Engineering, 2007.
- [26] A. de Klerk, Voidage variation in packed beds at small column to particle diameter ratio. *AICHE Journal*, **49**, 2003, 2022-2029.
- [27] G.E. Mueller, Radial void fraction correlation for annular packed beds. *AICHE Journal*, **45**, 1999, 234-246.
- [28] C.G. du Toit, Radial variation in porosity in annular packed beds. *Nuclear Engineering and Design*, 2008, 3073-3079.

- [29] G.E. Mueller, Radial void fraction distribution in randomly packed fixed beds of uniformly sized spheres in cylindrical containers. *Powder Technology*, **72**, 1992, 269-275.
- [30] J. Theuerkauf, P. Witt, D. Schwesig, Analysis of particle porosity distribution in fixed beds using the discrete element method, *Powder Technology*, **165**, 2006, 92-99.
- [31] J.S. Goodling, M.S. Khader, Co-ordination number distribution of spherical particles in a packed cylindrical bed. *Powder Technology*, **44**, 1985, 53-55.
- [32] D.P. Haughey, G.S.G. Beveridge, Structural properties of packed beds: a review. *Canadian Journal of Chemical Engineering*, **47**, 1969, 130-140.
- [33] J. Rumpf, *Chem.-Ing.-Techn.*, **30**, 1958, 144.
- [34] H.P. Meissner, A.S. Micheals, R. Kaiser, Crushing strength of zinc oxide agglomerates. *I&EC Process Design and Development*, **3**, 1964, 202-205.
- [35] K. Ridgeway, K.J. Tarbuck, Voidage fluctuations in randomly-packed beds of spheres adjacent to a containing wall. *Chemical Engineering Science*, **23**(9), 1968, 1147-1155.
- [36] M. Suzuki, K. Makino, M. Yamada, K. Iinoya, A study on the coordination number in a system of randomly packed, uniform-sized spherical particles. *International Chemical Engineering*, **21**(1), 1981, 482-488.
- [37] D. Kunii, J.M. Smith, Heat transfer characteristics of porous rocks. *AIChE Journal*, **6**(1), 1960, 71-78.
- [38] M. Kaviany, *Principles of Heat Transfer in Porous Media*. Springer-Verlag, New York, 1991.
- [39] W.W.M. Siu, S.H.-K Lee, Effective conductivity computation of a packed bed using constriction resistance and contact angle effects. *International Journal of Heat and Mass Transfer*, **43**, 2000, 3917-3924.
- [40] S.H.-K. Lee, S.C.-H. Ip, A.K.C. Wu, Sphere-to-sphere radiative transfer coefficient for packed sphere system. *Proceedings of ASME International Mechanical Engineering Congress and Exposition*, New York, 2001, pp. 105-110.
- [41] O.O. Noah, J.F. Slabber, J.P. Meyer, Natural convection heat transfer phenomena in packed bed systems. *Proceedings of ASME International Mechanical Engineering Congress & Exposition*, Montreal, Canada, November 14-20, 2014.
- [42] H.F. Niessen, B. Stöcker, Data Sets of SANA Experiment, 1994-1996, JUEL-3409, Forschungszentrum Jülich, (1997).

- [43] H. Nabielek, W. Schenk, W. Heit, A.W. Mehner, D.T. Goodin, The performance of high-temperature reactor fuel particles at extreme temperatures. *Nuclear Technology*, **84**, 1989, 62-81.
- [44] C.W. Lapwood, F.T. Roger, Convection currents in a porous medium. *Journal of Applied Physics*, **16**, 1945, 367-370.
- [45] V. Prasad, F.A. Kulacki, M. Keyhani, Natural convection in porous media. *Journal of Fluid Mechanics*, **150**, 1985, 89-119.
- [46] E.R. Lapwood, Convection of a fluid in a porous medium. *Proc. Camb. Phil. Soc.*, **44**, 1948, 508-521.
- [47] N. Wakao, S. Kaguei, T. Funazkri, Effect of fluid dispersion coefficient on particle-to-fluid heat transfer coefficients in packed beds: correlation of Nusselt number. *Chemical Engineering Science*, **34**, 1979, 325-336.
- [48] D.J. Gunn, Transfer of heat or mass to particles in fixed and fluidised beds. *International Journal for Heat and Mass Transfer*, **21**(8, 18), 1978, 467-476.
- [49] V. Gnielinski, Equation for the calculation of heat and mass transfer during flow through stationary spherical packings at moderate and high Peclet numbers. *International Chemical Engineering*, **21**(18), 1981, 378-383.
- [50] German Nuclear Safety Standards Commission, Reactor Core Design of High-Temperature Gas-Cooled Reactors. Part 2: Heat Transfer in Spherical Fuel Elements, Tech. Rep. KTA 3102.2 (1983) 18.
- [51] E. Achenbach, Heat and flow characteristics of packed beds. *Experimental Thermal and Fluid Science*, **10**(18), 1995, 17-27.
- [52] A.G. Dixon, Heat transfer in fixed beds at very low tube-to-particle diameter ratio. *Industrial Engineering & Chemical Research*, **36**, 1997, 3053-3064.
- [53] S.W. Churchill, H.H.S. Chu, Correlating equations for laminar and turbulent free convection from a vertical plate. *Int. J. Heat Mass Transfer*, **18**, 1975, 1323-1329.
- [54] A.R. Balakrishnan, D.C.T. Pei, Heat transfer in gas-solid packed bed systems, 1. A critical review, *Ind. Eng. Chem. Process Des. Dev.*, **13**, 1979, 441.
- [55] D.T. Wen, T.N. Cong, Y. He, H. Chen, Y. Ding, Heat transfer of gas-solid two-phase mixtures flowing through a packed bed. *Chemical Engineering Science*, **62**, 2007, 4241-4249.
- [56] S. Messai, E.G. Mohammed, J. Sghaier, A. Belghith, Experimental study of the convective heat transfer coefficient in a packed bed at low Reynolds numbers, *Thermal Science*, **18**(2), 2014, 443-450.

- [57] W.E. Ranz, W.R. Marshall, Evaporation from drops, Part II. *Chemical Engineering Progress*, **48**, 1952, 173-180.
- [58] S. Messai, J. Sghaier, A. Belghith, Drying modeling of a packed bed of porous particles in superheated steam and humid air. *Porous Media*, **14**(2), 2011, 169-177.
- [59] E. Tsotsas, E-U. Schlünder, Heat transfer in packed beds with fluid flow: Remarks on the meaning and the calculation of a heat transfer coefficient at the wall, *Chemical Engineering Science*, **45**, 1990, 819-837.
- [60] S. Whitaker, Forced convection heat transfer correlations for flow in pipes, past flat plates, single cylinders, single spheres, and for flow in packed beds and tube bundles. *AIChE Journal*, **18**, 1972, 361-371.
- [61] N. Wakao, Particle-to-fluid transfer coefficients and fluid diffusivities at low flow rate in packed beds. *Chemical Engineering Science*, **31**, 1976, 1115-1122.
- [62] K. Jafarpur, M.M. Yovanovich, Laminar free convective heat transfer from isothermal spheres: a new analytical method. *Int. J. Heat Mass Transfer*, **35**(9), 1992, 2195-2201.
- [63] S.W. Churchill, R. Usagi, A general expression for the correlation of rates of transfer and other phenomena. *A.I.Ch.E. J.*, **18**, 1972, 1121-1132.
- [64] S.W. Churchill, Comprehensive theoretically based, correlating equations for free convection from isothermal spheres. *Chem. Eng. Commun.*, **24**, 1983, 339-352.
- [65] M.J. Chamberlain, Free convection heat transfer from a sphere, cube, and vertically aligned bi-sphere. M.Sc. thesis, University of Waterloo, Waterloo, Ontario, Canada (1983).
- [66] D. Royston, Heat transfer in the flow of solids in gas suspensions through a packed bed. *Industrial & Engineering Chemistry Process Design and Development*, **10**, 1971, 145-150.
- [67] K. Ichimiya, A new method for evaluation of heat transfer between solid material and fluid in a porous medium. *ASME Journal of Heat Transfer*, **121**, 1999, 978-983.
- [68] K. Vafai, C.L. Tien, Boundary and inertia effects on flow and heat transfer in porous media. *Int. J. Heat Mass Transf.*, **24**, 1981, 195-203.
- [69] W.M. Kays, M.E. Crawford, *Convective Heat and Mass Transfer*. McGraw-Hill, New York, 1993, 136-140.
- [70] A.A. Adeyanju, K. Manohar, Theoretical and experimental investigation of heat transfer in packed beds. *Research Journal of Applied Science*, **4**(5), 2009, 166-177.

- [71] T.E.W. Schumann, Heat transfer: a liquid flowing through a porous prism. *J. Heat Transfer*, **5**, 208-212.
- [72] O.A. Saunders, Heat transfer in the flow of gas through a bed of solid particles. *J. Iron Steel*, **141**, 1940, 291-296.
- [73] W.M. Kays, A.C. London, *Compact Heat Exchanger*. McGraw-Hill, New York, 1964.
- [74] G.O.G. Lof, R.W. Hawley, Unsteady state heat transfer between air and loose solids. *J. Ind. Eng.*, **40**(6), 1948, 1061-1070.
- [75] M. Leva, M. Grummer, Concentration and temperature profiles in a tubular reactor. *Ind. Chem. Eng. Fundam.*, **40**, 1948, 747-753.
- [76] M. Riaz, Analytical solution for single and two phase models of packed bed thermal storage systems. *J. Heat Transfer*, **99**, 1977, 489-492.
- [77] C.P. Jefferson, Prediction of break through curves in packed beds: application of single parameter models. *AIChE J.*, **18**(2), 1972, 409-416.
- [78] W.E. Ball, Heat transfer properties of a packed bed: determination by a frequency response technique. *Dissertation Abstract*. **19**, 1958 494.
- [79] C.L. Norton, Pebble heater: new heat transfer unit for industry. *J. Am. Ceramic Soc.*, **29**, 1946, 187-193.
- [80] R.M.G. Meek, The measurement of heat transfer coefficients in packed beds by the cyclic method. *Int. Heat Transfer Development*, ASME, New York, 1961.
- [81] R.C. Bradshaw, J.E. Myers, Heat and mass transfer in fixed and fluidized beds of large particles. *AIChE. J.*, **9**, 1963, 590-599.
- [82] J.H. Harker, E.J. Martyn, Energy storage in gravels beds. *J. Inst. Energy*, **58**, 1985, 94-99.
- [83] H. Bouguettaia, J.H. Harker, Energy storage in packed beds of spheres containing palm oil. *J. Inst. Energy*, **64**, 1991, 89-94.
- [84] J.J. Barker, Heat transfer in packed beds. *Indus. Eng. Chem. Process Design Develop.*, **57**(4), 1965, 43-51.
- [85] A.F. Chechetkin, *High Temperature Heat Carriers*. Pergamon Press. Oxford, 1963.
- [86] A. Bejan, I. Dincer, S. Lorente, A.F. Miguel, A.H. Reis, *Porous and Complex Flow Structures in Modern Technologies*. Springer, New York, 2004.
- [87] A. Bejan, The boundary layer regime in a porous layer with uniform heat flux from the side. *Int. J. Heat Mass Transfer*, **26**(2), 1983b, 1339-1346.

- [88] J.E. Weber, The boundary-layer regime for convection in a vertical porous layer. *Int. J. Heat Mass Transfer*, **18**, 1975b, 569-573.
- [89] A. Bejan, On the boundary layer regime in a vertical enclosure filled with a porous medium. *Lett. Heat Mass Transfer*, **6**, 1979, 93-102.
- [90] J.S. Huenefeld, O.A Plumb, A study of non-Darcy natural convection from a vertical heated surface in a saturated porous medium. *ASME 20th National Heat Transfer Conf. Paper 81-HT-45*, 1981.
- [91] O.O. Noah, J.F. Slabber, J.P. Meyer, Experimental evaluation of natural convection heat transfer in packed beds contained in slender cylindrical geometries. *Proceedings of the 5<sup>th</sup> International Conference on Applications of Porous Media*, Romania, 2013, 301-316.
- [92] J.R. Lamarsh, A.J. Baratta, *Introduction to Nuclear Engineering*, 3<sup>rd</sup> edition, Prentice Hall Upper Saddle River, New Jersey, 2001.
- [93] W. van Antwerpen, *Modelling the Effective Thermal Conductivity in the Near-Wall Region of a Packed Pebble Bed*, Ph.D. thesis, North-West University, Potchefstroom, South Africa, 2009.
- [94] C.K. Chen, C.L. Tien, Conductance of packed particles in vacuum, *J. Heat Transfer*, **95**, 1973, 302-308.
- [95] M.M. Yovanovich, Apparent conductivity of glass micro-particles from atmospheric pressure to vacuum, ASME Paper 73-HT-43. ASME-AIChE, Heat Transfer Conference, Atlanta, Ga, 1973.
- [96] W. van Antwerpen, P.G. Rousseau, C.G. du Toit, Multi-sphere unit cell model to calculate the effective thermal conductivity in packed pebble beds of mono-sized spheres, *Nuclear Engineering and Design*, **247**, 2012, 183-201.
- [97] S.P. Timoshenko, J.N. Goodie, *Theory of Elasticity*. Article 140, McGraw-Hill, 1970,
- [98] M.M. Yovanovich, E.E. Marotta, Thermal spreading and contact resistances, in: A. Bejan, D. Kraus (Eds.). *Heat Transfer Handbook*, John Wiley and Sons Inc., Hoboken, New York, USA, (Chapter 4), 2003, 261-393.
- [99] M. Bahrami, J.R. Culham, M.M. Yovanovich, Thermal joint resistance of non-conforming rough surfaces with gas-filled gaps. *AIAA J. Thermophysics Heat Transfer*, **18**(3), 2004, 326-332.
- [100] J.E. Hoffmann, Validation and verification of CFD simulation at PBMR, *Proceedings of the Fourth South African Conference on Applied Mechanics*, Johannesburg, **2**, 2004, 19.
- [101] K. Robold, Wärmetransport im inneren und in der randzone von kugelschüttungen, Tech. Rep. 1976, *Kernforschungsanlage Jülich GmbH*, 1982, 19.

- [102] P. Zehner, E.U. Schlünder, Wärmeleitfähigkeit von schüttungen bei mäßigen Temperaturen, *Chemie Ingenieur Technik*, **42**, 1970, 933-941.
- [103] IAEA TECDOC-1163, Heat transport and after heat removal for gas cooled reactors under accident conditions, International Atomic Energy Agency, 2000.
- [104] G. Breitbach, H. Barthels, The radiation heat transfer in the HTR core after failure of the afterheat removal system, *Nuclear Technology*, **49**(1), 1980, 392-399.
- [105] R. Bauer, E.U. Schlünder, Effective radial thermal conductivity of packings in gas flow. Part 2: Thermal conductivity of the packing fraction without gas flow, *Int. Chem. Eng.*, **18**(2), 1978, 189-204.
- [106] C.-L. Tien, Thermal radiation in packed and fluidized beds, *J. Heat Transfer*, **110**(4b), 1988, 1230-1242.
- [107] M. Kaviany, B.P. Singh, Radiative heat transfer in porous media, *Adv. Heat Transfer*, **23**, 1993, 133-186.
- [108] A. Shams, F. Roelofs, E.M.J. Komen, E. Baglietto, Quasi-direct numerical simulation of a pebble bed configuration: Part 1: Flow (velocity) field analysis, *Nuc Eng. Des.*, **263**, 2013, 473-489.
- [109] T. Zeiser, P. Lammers, E. Klemm, Y.W. Li, J. Bernsdorf, G. Brenner, CFD calculation of flow, dispersion and reaction in a catalyst filled tube by the lattice Boltzmann method, *Chemical Engineering Science*, **56**, 2001, 1697-1704.
- [110] F. Augier, F. Idoux, J.Y. Delenne, Numerical simulation of transfer and transport properties inside packed beds of spherical particles, *Chemical Eng. Sc.*, **65**, 2010, 1055-1064.
- [111] H.P.A. Calis, J. Nijenhuis, B.C. Paikert, F.M. Dautzenberg, C.M. van den Bleek, CFD modeling and experimental validation of pressure drop and flow profile in a novel structured catalytic reactor packing. *Chemical Engineering Science*, **56**, 2001, 1713-1720.
- [112] S.J.P. Romkes, F.M. Dautzenberg, C.M. van den Bleek, H.P.A. Calis, CFD modeling and experimental validation of particle-to-fluid mass and heat transfer in a packed bed at very low channel to particle diameter ratio. *Chemical Engineering Journal*, **96**, 2003, 3-13.
- [113] O.R. Derkx, A.G. Dixon, Determination of the fixed bed wall heat transfer coefficient using computational fluid dynamics, *Numerical Heat Transfer, Part A*, **29**, 1996, 777.
- [114] S.A. Logtenberg, A.G. Dixon, Computational fluid dynamics studies of fixed bed heat transfer, *Chem. Eng. Process*, **37**, 1998, 7-21.

- [115] S.A. Logtenberg, A.G. Dixon, Computational fluid dynamics simulations of fluid flow and heat transfer at the wall-particle contact points in a fixed-bed reactor, *Chemical Engineering Science*, **54**, 1999, 2433-2439.
- [116] M. Nijemeisland, A.G. Dixon, Comparison of CFD simulations to experiment for convective heat transfer in a gas-solid fixed bed. *Chemical Engineering Journal*, **82**, 2001, 231-246.
- [117] P.A. Cundall, O.D.I. Strack, A discrete numerical model for granular assemblies, *Geo-Technique*, **29**, 1979, 47-65.
- [118] CD-Adapco, CCM+ User Guide 7.02. Setting Material Properties Methods, 2012 pp. 2463.
- [119] J.Y. Delenne, M.S. El Youssoufi, F. Cherblanc, J. Be´net, Mechanical behavior and failure of cohesive granular materials, *International Journal for Numerical and Analytical Methods in Geomechanics*, **28**, 2004, 1577-1594.
- [120] F. Soulie, F. Cherblanc, M.S. El Youssoufi, C. Saix, Influence of liquid bridges on the mechanical behaviour of polydisperse granular materials, *International Journal for Numerical and Analytical Methods in Geomechanics*, **30**, 2006, 213-228.
- [121] V. Richefeu, M.S. El Youssoufi, F. Radjaï, Shear strength properties of wet granular materials, *Physical Review E*, **73**, 2006, 051304.
- [122] M.P. Allen, D.J. Tildesley, *Computer simulation of liquids*, Oxford University Press, Oxford, 1986.
- [123] P.R. Spalart, Strategies for turbulence modelling and simulations, *International Journal of Heat and Fluid Flow*, **21**, 2000, 252-263.
- [124] M. Shur, P. Spalart, K. Squires, M. Strelets, A. Travin, Three dimensionality in Reynolds-averaged Navier-Stokes solutions around two-dimensional geometries, *AIAA Journal*, **43**, 2005, 1230-1242.
- [125] G. Beavers, D.D. Joseph, Boundary conditions at a naturally permeable wall, *J. Fluid Mech.*, **30**, 1967, 197-207.
- [126] D.K. Gartling, C.E. Hickox, R.C Givler, Simulation of coupled viscous and porous flow problems, *Comp. Fluid Dyn.*, **7**, 1996, 23-48.
- [127] B. Alazmi, K. Vafai, Analysis of fluid flow and heat transfer interfacial conditions between a porous medium and a fluid layer, *International Journal of Heat and Mass Transfer*, **44**, 2001, 1735-1749.

- [128] N. Massarotti, P. Nithiarasu, O.C. Zienkiewicz, Natural convection in porous medium-fluid interface problems: a finite element analysis by using the CBS procedure, *Int. Journal of Numerical Methods for Heat & Fluid Flow*, **11**(5/6), 2001, 473-489.
- [129] D.A. Nield, A. Bejan, *Convection in Porous Media*, Springer Verlag, New York, NY, 1992.
- [130] S.V. Patankar, *Numerical Heat Transfer and Fluid Flow*. Hemisphere Publishing Corporation, New York, USA 1980.
- [131] H. Huang, J. Ayoub, Applicability of the Forchheimer equation for Non-Darcy flow in porous media, *SPE Journal*, 2008, 112-122.
- [132] S. Ergun, Fluid flow through packed columns, *Chem. Eng. Prog.*, **48**(2), 1959, 89-94.
- [133] A. Guardo, M., Coussiratb, F., Recasensa, Larrayoza, M.A., CFD study on particle-to-fluid heat transfer in fixed bed reactors: convective heat transfer at low and high pressure. *Chemical Engineering Science*, **61** 2006, 4341-4353.
- [134] A. Polson, 2006, Private Communication.

# Appendix A: Calibrations, Experimental Uncertainty and Measurement of Force for Loading

## A.1 Thermocouple Calibration and Experimental Uncertainty

T-type thermocouples were used in measuring: 1) the temperature distribution within the test particles, 2) the temperature of the gas at the interstice close to the test sample particle, 3) the temperature of the hot gas entering the bed at the wire gauze and its temperature leaving the bed at the top.

All the thermocouples used in the experiment were calibrated using the set-up in Fig. A-1. The thermocouples were calibrated from a reference temperature of 18 °C to 51 °C at an interval of 2 °C using the PolyScience Circulating Bath (see Fig. A-2). The thermocouples were systematically arranged at one end and taped to a slender wooden rod before being dipped into the bath while the other end was fixed to the armature multiplexer card before inserting into the data logger. The logger was attached to the computer system for display and storage of data acquired. At each reference temperature, the corresponding thermocouple temperature at each channel was captured/scanned. A graph of all reference temperatures against corresponding scanned temperature was plotted for each thermocouple card channel and a linear equation generated (see Fig. A-3).

An uncertainty analysis was done to determine the experimental uncertainty associated with each thermocouple. Using Eq. (A.1), the statistical variance,  $U(\mathbf{x}_{i,statistical})$ , for each thermocouple was calculated (see Table A-1):

$$U(\mathbf{x}_{i,statistical}) = \sqrt{\frac{\sum_i^N (\mathbf{x}_i - \bar{\mathbf{x}})^2}{N}} \quad (\text{A. 1})$$

where  $x_i$  is the reference temperature value and  $\bar{x}$  the corresponding measured temperature of N sample points. The uncertainty for the data logger that was used  $U(x_{i,instrument})$  is  $\pm 1$  °C.

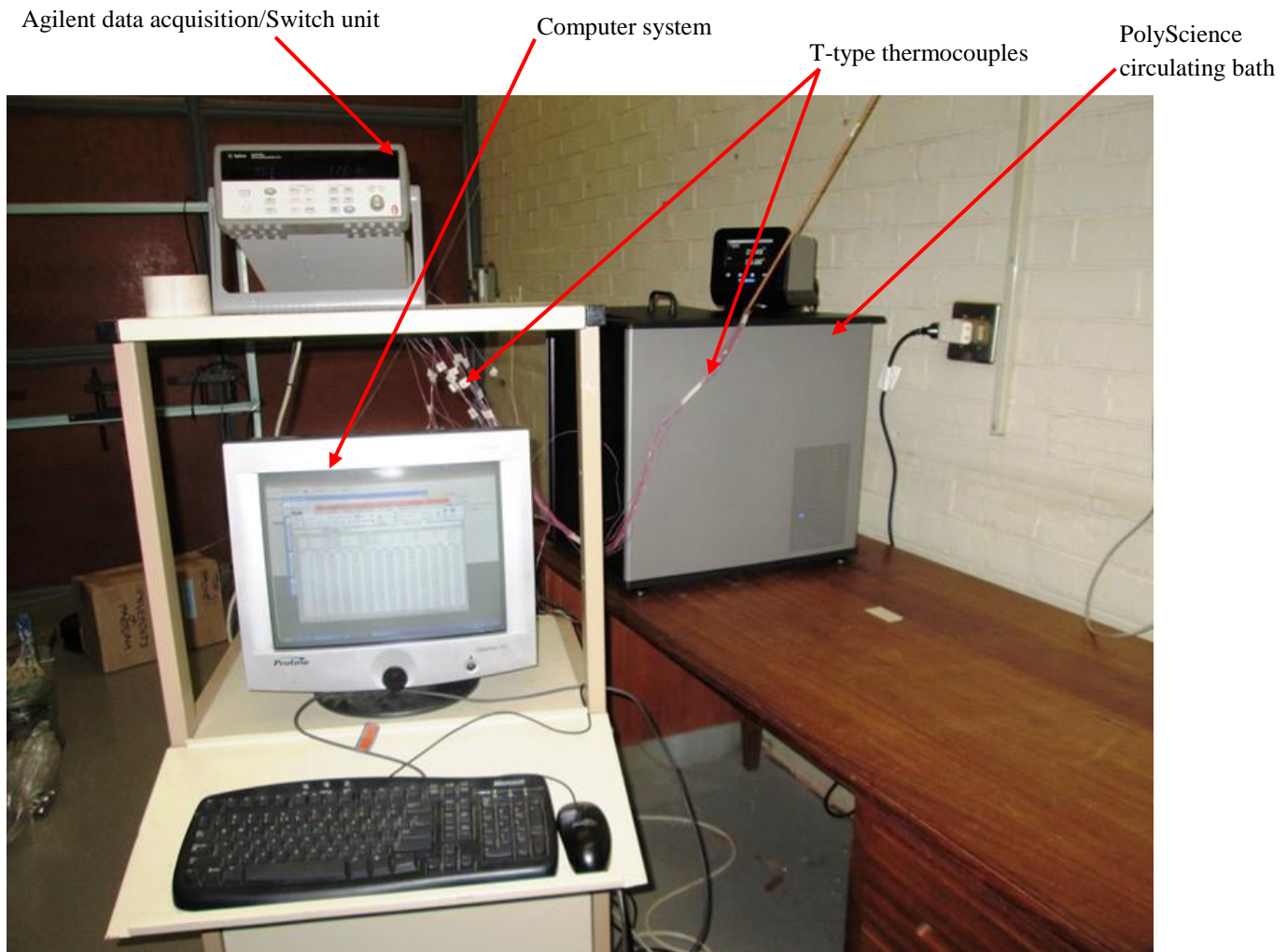


**Figure A-1** Thermocouple calibration set-up

To combine the uncertainty of both the thermocouples and the data logger, Eq. (A.2) is used. The equation calculates the measured experimental uncertainty  $U(x_{i,exp})$ . The result of the two equations can be found in Table A-1.

$$U(x_{i,exp}) = \sqrt{[U(x_{i,statistical})]^2 + U(x_{i,instrument})^2} \quad (\text{A.2})$$



**Figure A-2** PolyScience circulating bath (PD20R-30-A12E) used for calibration

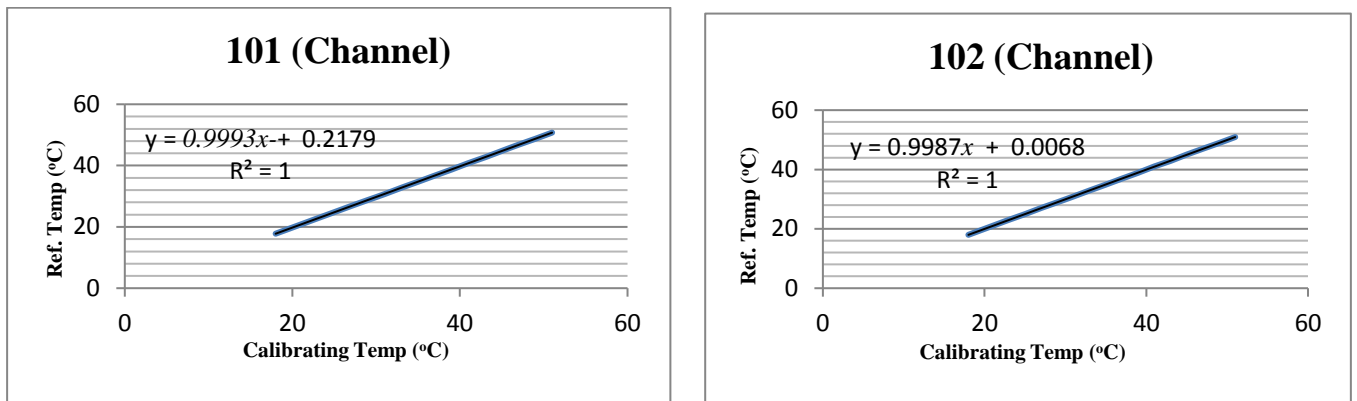


**Figure A-3** Linear equation for each thermocouple at the card channel

**Table A-1:** Statistical results for thermocouples

Name	Channel	Type	$U(x_{i,statistical})$	$U(x_{i,exp})$
T101	101	T-Type	0.3368	1.06
T102	102	T-Type	0.0705	1.0025
T103	103	T-Type	0.0889	1.0039
T104	104	T-Type	0.2257	1.0252
T105	105	T-Type	0.4444	1.0943
T106	106	T-Type	0.6702	1.2038
T107	107	T-Type	0.6133	1.1731
T108	108	T-Type	0.5693	1.1507
T109	109	T-Type	0.5748	1.1534
T110	110	T-Type	0.5396	1.1363
T111	111	T-Type	0.4172	1.0835
T112	112	T-Type	0.4681	1.1041
T113	113	T-Type	0.366	1.0649
T114	114	T-Type	0.3262	1.0519
T115	115	T-Type	0.2677	1.0352
T116	116	T-Type	0.1725	1.0148
T117	117	T-Type	0.1357	1.0092
T118	118	T-Type	0.6018	1.1671
T119	119	T-Type	0.4835	1.1108
T120	120	T-Type	0.2019	1.0202
T201	201	T-Type	0.1475	1.0108
T202	202	T-Type	0.5568	1.1446

## A.2 Pressure Transmitter

Two WIKA pressure transmitters model A-10 (see Fig A-4) of 0 – 2.5bar measuring range, about 5VDC power supply output and 0.25% non-linearity were used for pressure measurement in the medium. The pressure transmitters were connected to silicon tubes on one end while the other ends were positioned at the entry of the bed (at the wire gauze) and at the top of the bed. The ambient temperature and pressure were 20.5 °C and 86.6kPa respectively.

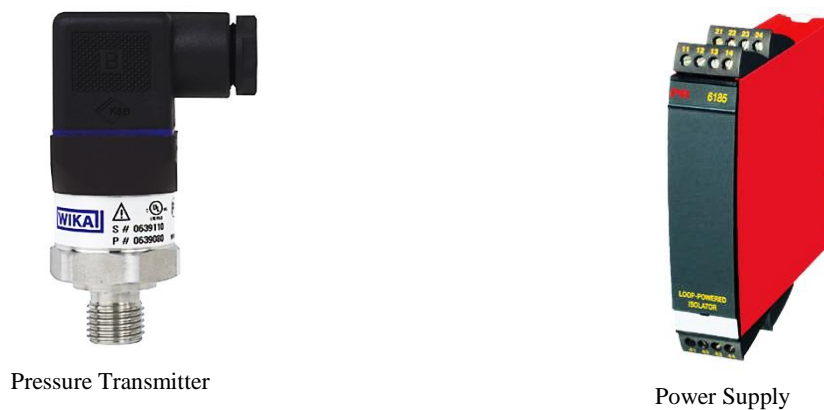


**Figure A-4** Pressure transmitter (PT) used

**Table A-2:** Calibration data for pressure transmitter

Name	Channel	Type	Pressure (Pa)					
			0.0	1000	2000	3000	4000	5000
PT <sub>1</sub>	219	Transducer	0.218V	0.965V	1.724V	2.495V	3.246V	4.010V
PT <sub>2</sub>	220	Transducer	0.135V	0.839V	1.610V	2.381V	3.147V	3.888V

A linear equation was fitted through the data in order to calculate the pressure for any given voltage (volts). The equations are:

$$PT_1 = 1313.8V_1 - 267.32 \quad (\text{A.3})$$

$$PT_2 = 1320.5V_1 - 148.25 \quad (\text{A.4})$$

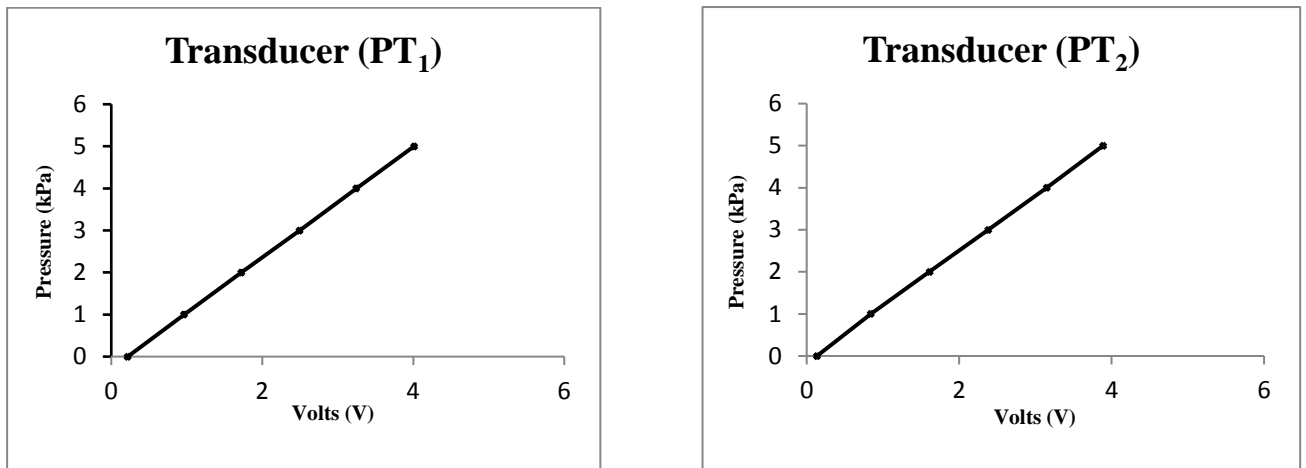


**Figure A-5** Linear equations fitted to pressure transducer data

### A.3 Contact Force Distribution

The same numerically packed bed data set used for calculating the radial porosity and coordination number was used to calculate the average contact force on each pebble as a function of pebble bed depth. [134], who generated the numerically packed bed, treated the contact region as two springs that compressed against each other (Fig. A-6). The combined stiffness between two spheres can be calculated by:

$$k = \frac{k_1 k_2}{k_1 + k_2} \quad (\text{A. 5})$$

where  $k$  is the combined stiffness between Spheres 1 and 2. The deformation depth,  $\omega_o$ , can be calculated using:

$$\omega_o = d_p - d_F \quad (\text{A. 6})$$

where  $d_p$  is the pebble diameter and  $d_F = d_p - \omega_o$  the distance between the two pebble centres due to an external force acting on the pebbles.

The contact force can then be calculated by:

$$F = \omega_0 k \tag{A.7}$$

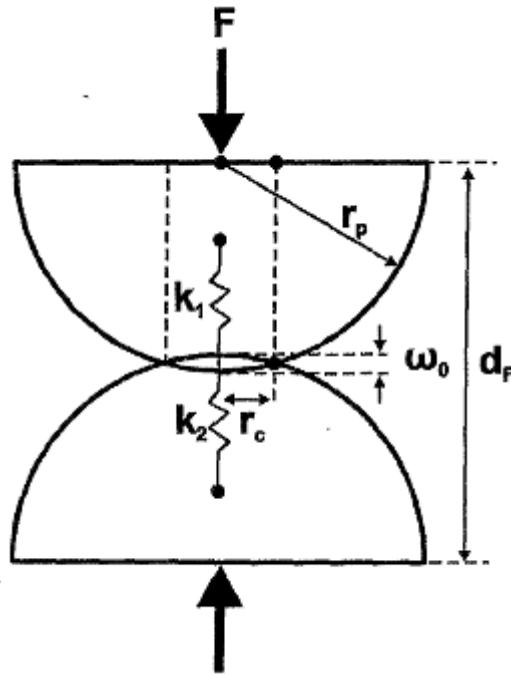


**Figure A-6** Spring representation of contact force calculations

The distance between spheres in contact for the numerically packed bed was calculated using a program in C++ while the contact force between each pebble was then further calculated on an Excel spreadsheet. A further analysis was done calculating an average contact force as a function of depth. This was achieved by calculating an average contact force for pebble centres falling in increments of  $1/4 d_p$  increasing in height. The result is presented in Fig. A-7 and a linear curve fit obtained, given by:

$$F = 72.307(Z_{depth}) + 7.8716 \tag{A.8}$$

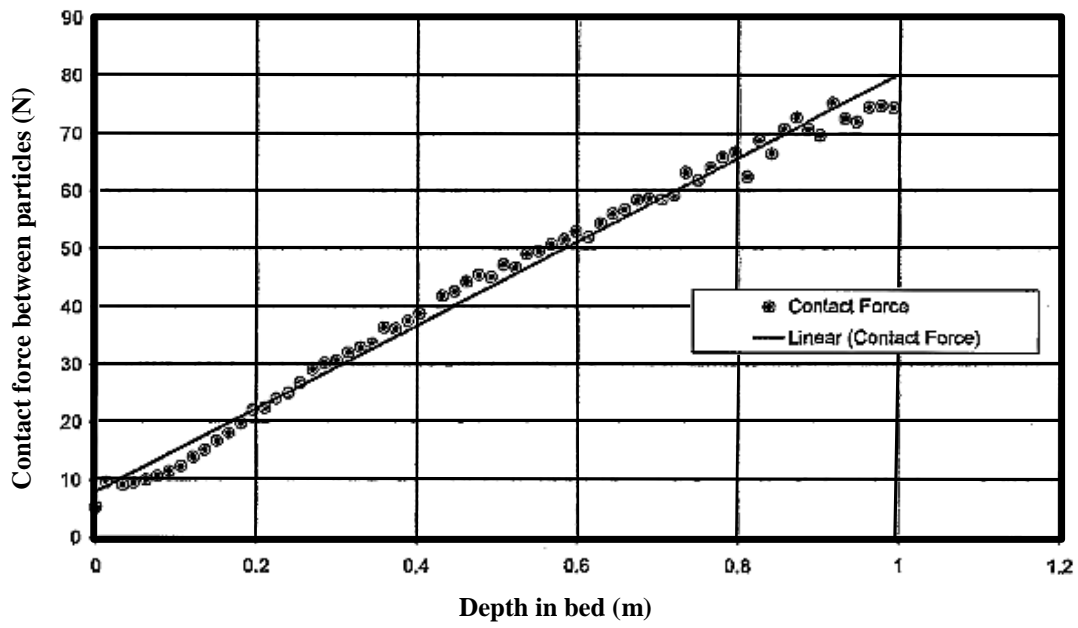


**Figure A-7** Contact force as a function of height in the test facility

# Appendix B: Programming Codes, Discrete Element Method and Discretisation Scheme

## B.1: MATLAB Codes

The temperature distribution within each test particle was determined experimentally at three nodal points through the instrumented thermocouples. The temperatures were validated numerically using the discretisation method. A finite volume method implicit scheme at a time-step of two seconds was applied to validate the experimental captured temperature (see Fig. 5.5). The validation showed a good agreement with experimental temperature reading.

The discretisation method enables temperatures at many nodal points on the test particles to be determined. This may be difficult to obtain experimentally. Applying the finite volume method for the discretisation process is time-consuming when solving for temperature at each node hence the use of MATLAB was found appropriate to facilitate the rate at which results were generated. A programme in MATLAB was written to perform the discretisation exercise for each particle for a given number of nodes.

### Codes for calculating the temperature distribution within test particles

```
%% Heat equation subject to periodic boundary condition
function heat_trial
clear all
%clc
global lambda m periodic c1
periodic = 0;
%nonperiodic = 0;
T = .5;
a = 0;
b = 0.01746;
m = 2;
x = linspace(a,b,m+1); % equal spacing
dx = x(2)-x(1);

c1 = [37.087106 35.54573 33.47026]; %constant initial condition
```

```

%f = @(z)c1*z.^0; % function handle for initial condition
y(1,:) = c1;%f(x(2:m)); % stting the initial conditon
lambda = 0.5;
dt = dx^2*lambda;
n = round(T/dt);
q = 0;
for j = 2:n+1
    y(j,:) = y(j-1,:) + rhs(y(j-1,:)) + q;
end
temp = y(n+1,:);%[c1(1) y(n+1,:) c1(3)];
figure(1)
plot(x,temp,'o-')
figure(2)
mesh(y')
save data
function Y = rhs(v)
global lambda m periodic c1
i = 2;
c = 15.6/(7831*456);
if periodic
    Y(1) = c*lambda*(v(m) -2*v(1) + v(2));
    Y(i) = c*lambda*(v(i-1) -2*v(i) + v(i+1));
    Y(m+1) = c*lambda*(v(m) -2*v(m+1) + v(2));
else
    v0 = c1(1);
    vm = 33.47025;
    Y(1) = c*lambda*(v0 -2*v(1) + v(2));
    Y(i) = c*lambda*(v(i-1) -2*v(i) + v(i+1));
    Y(m+1) = c*lambda*(v(m) -2*v(m+1) + vm);
end
end
  
```

## B.2: Visual Basic Codes

When centroid (x, y, z) coordinate points were exported to the CAD (SolidWorks) environment, the diameter of the particles was increased by 0.5% of their original diameter to enable particle-to-particle and particle-to-wall contacts. To perform this task, a programme in visual basic was run in the macro tool of SolidWorks, this allowed the coordinate points to be displayed on the CAD environment before a sketch-driven pattern operation was performed.

### Codes for visual basic run in the macro of a cad package

```

Sub main()
Set swApp = Application.SldWorks
Set Part = swApp.ActiveDoc
swApp.ActiveDoc.ActiveView.FrameState = 1
Dim skPoint As Object
Open "C:\Users\User\Documents\Practice For Sketch Driven pattern\Paper
Journal xyz Centroid plot txt.txt" For Input As #1
Part.SketchManager.Insert3DSketch True
  
```

```

Do While Not EOF(1)
Input #1, X, Y, Z
Set skPoint = Part.SketchManager.CreatePoint(X / 1000, Y / 1000, Z / 1000)
Loop
Close #1
Part.ShowNamedView2 "*Isometric", 7
Part.ViewZoomtofit2
End Sub
  
```

### B.3: Discrete Element Method (DEM)

The amount of injected particles is controlled by the porosity limit property. During the raining process, a loose (and non-physical) packing was generated. The forces at the point of contact were modelled as a pair of spring-dashpot oscillators; one representing the normal direction and the other the tangential direction of force with respect to the contact plane normal vector. The force  $\vec{F}_c$  between two spheres described by Eq. (B.1) has a normal part  $\vec{F}_n$  due to the presence of contacts between particles and a tangential part  $\vec{F}_t$  due to friction (see Fig. B-1a). The two parts are expressed by Eqs. (B.2) and (B.3):

$$\vec{F}_c = \vec{F}_n + \vec{F}_t \quad (\text{B.1})$$

For the force law between a pair of contacting particles, a linear-elastic approximation [110] is used:

$$\vec{F}_n = (-k_n \delta + 2\alpha \sqrt{mk_n} \dot{\delta}) \frac{C_i \vec{C}_j}{\|\vec{C}_i \vec{C}_j\|} \text{ for } \delta < 0 \quad (\text{B.2})$$

and  $\vec{F}_n = 0$  otherwise.  $\delta = \|\vec{C}_i \vec{C}_j\| - \frac{1}{2}(d_i + d_j)$  is the gap (see Fig. B-1b) or the overlap between the two contacting particles  $i$  and  $j$  (Fig. B-1a),  $k_n$  is the normal stiffness,  $m = m_i m_j / (m_i + m_j)$  is the reduced mass and  $\alpha \in [0, 1[$  is a damping parameter, which controls energy dissipation due to inelastic collision [110]. Since there is an interest in the equilibrium state, the parameter  $\alpha$  has a very weak influence on the final results, but high values of  $\alpha$  reduce the simulation time. For the friction, the classical Coulomb law was used and expressed as a non-linear relation between the friction force  $\vec{F}_t$  and the sliding velocity  $\vec{\delta}_t$  with a viscous regularisation around the zero velocity:

$$\vec{F}_t = -\min\{\beta_t \|\dot{\delta}_t\|, \mu_c \|\vec{N}\|\} \frac{\dot{\delta}_t}{\|\dot{\delta}_t\|} \quad (\text{B.3})$$

where  $\beta_t$  is the tangential viscosity parameter and  $\mu_c$  is the coefficient of friction [110], values of some of these parameters are displayed in Table B.1. Similar force laws were used to compute the interactions of the grains with the top and upper plates and with the inner wall of the cylindrical column [121].

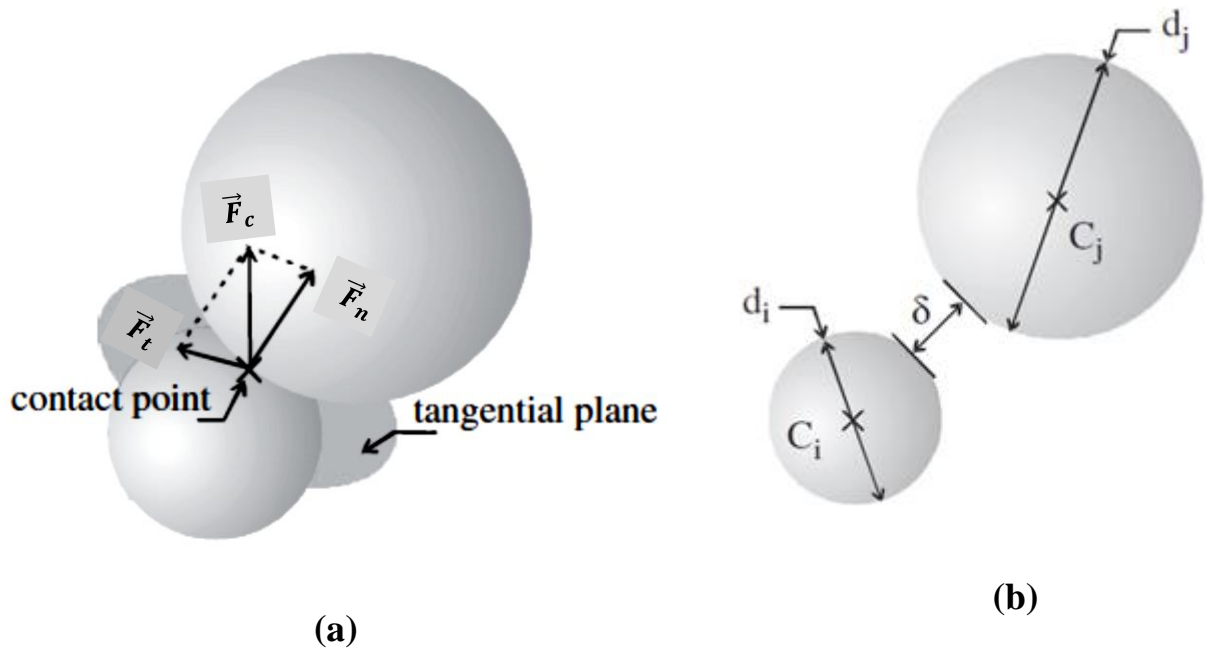


**Figure B-1** (a) contact force components between particles (b) Geometrical parameters and gap between two particles [110].

Given the local interaction laws, the algorithm for the simulation of a collection of particles follows the following general scheme: (1) At each time step, the displacements of the particles are used to compute the forces between grains and with boundary walls. (2) The accelerations are determined by means of the equations of motion from forces acting on the particles. (3) The “velocity verlet” scheme [122] is used for the integration of the equations of motion over a time step in order to calculate the particle displacements. (4) The grain positions are updated according to the calculated displacements. The friction between particles and the inner wall of the cylindrical mould is neglected. The simulation was stopped when a dense packing was formed and the particles fitted to the cylindrical geometry (Fig. 6.1).

**Table B-1** Parameters for DEM packing

Parameter	Value
Normal stiffness, $k_n$	$10^6$ N/m
Interparticle friction coefficient, $\mu_c$	0.3
Density of particles, $\rho_p$	$2250 \text{ kg/m}^3$
Damping coefficient, $\alpha$	0.7
Tangential viscosity, $\beta$	1Ns/m
Time step	$1.7835 \times 10^{-5}$ sec

For the study, 171 densely packed uniformly sized particles with packing ratio of 0.58 were generated for the simulation. The construction of wall-to-particle and particle-to-particle contact points is also an important subject in the process of developing a geometrical model. Previous work in literature reports the emulation of contact points (leaving small gaps between surfaces and assuming zero velocity in the gap) to avoid convergence problems [116].

#### B.4: Discretisation Scheme

In CFD analysis, each type of discretisation method (FVM, FDM and FEM) used should yield the same solution if the grid is fine enough, but some methods are more suitable than others. In the selection of discretisation methods, efficiency, accuracy and special requirements (i.e. shock wave tracking) are some factors that should be considered. Higher order numerical methods usually predict higher order of accuracy for CFD, but are more likely unstable due to less numerical dissipation. Stability is attained if the method adopted does not magnify the errors that appear in the course of the numerical solution process. A finite volume discretisation method was used in this work. The solution domain was subdivided into a finite number of small control volumes corresponding to the cells of a computational grid.

Discrete versions of the integral form of the continuum transport equations were applied to each control volume. The objective was to obtain a set of linear algebraic equations, with the total number of unknowns in each equation system corresponding to the number of cells in the grid. With non-linear equation, iterative techniques that rely on suitable linearisation strategies must be employed. The resulting linear equations are then solved with an algebraic multigrid solver. Considering the general governing equation given in Eq. (B.4), which consists of the transient term, convective term, diffusion term and the source term respectively, the

discretisation approach for individual term differs. The transient term is only included in transient calculations, it is not generally used as a device to obtain a steady-state solution. The Implicit Unsteady solver in STAR-CCM+ offers two temporal discretisation options: first-order and second-order. The first-order temporal scheme, also referred to as Euler Implicit, discretises the unsteady term using the solution at the current time level,  $n + 1$ , as well as the one from the previous time level,  $n$ . This is expressed in Eq. (B.5):

$$\frac{\partial(\varepsilon\rho\phi)}{\partial t} + \nabla \cdot (\varepsilon\rho\vec{v}\phi) = \nabla \cdot (\varepsilon\Gamma\nabla\phi) + \varepsilon S_\phi \quad (\text{B.4})$$

$$\frac{d}{dt}(\rho\kappa\phi V)_0 = \frac{(\rho_0\phi_0)^{n+1} - (\rho_0\phi_0)^n}{\Delta t} V_0 \quad (\text{B.5})$$

The second-order temporal scheme expressed by Eq. (B.6) discretises the unsteady term using the solution at the current time level,  $n + 1$ , as well as those from the previous two time levels,  $n - 1$ .

$$\frac{d}{dt}(\rho\kappa\phi V)_0 = \frac{3(\rho_0\phi_0)^{n+1} - 4(\rho_0\phi_0)^n + (\rho_0\phi_0)^{n-1}}{2\Delta t} V_0 \quad (\text{B.6})$$

On the first time-step of a second-order temporal simulation, a first-order discretisation is used since only two time levels are available. The convective term at a face is discretised using the expression in Eq. (B.7), where  $\phi_f$  and  $\dot{m}_f$  are the scalar values and mass flow rates at the face respectively, and  $\mathbf{G}$  is the grid flux computed from the mesh motion:

$$[\phi\rho(\mathbf{v} \cdot \mathbf{a} - \mathbf{G})]_f = (\dot{m}\phi)_f = \dot{m}_f\phi_f \quad (\text{B.7})$$

The manner in which the face value  $\phi_f$  is computed from the cell values has a profound effect on the stability and accuracy of the numerical scheme. Several schemes are commonly used, some of which are first-order upwind, second-order upwind, central differencing, bounded central differencing and blended upwind/central.